UNIVERSITY OF CALIFORNIA,
IRVINE

OPTIMAL SOLAR PV, BATTERY STORAGE, AND SMART-INVERTER ALLOCATION IN ZERO-NET-ENERGY MICROGRIDS CONSIDERING THE EXISTING POWER SYSTEM INFRASTRUCTURE

DISSERTATION

submitted in partial satisfaction of the requirements
for the degree of

DOCTOR OF PHILOSOPHY

in Mechanical & Aerospace Engineering

by

Laura Martinez de Novoa

Dissertation Committee:
Professor Jack Brouwer, Ph.D., Chair
Professor Kia Solmaz, Ph.D.
Professor Michael Green, Ph.D.

2020

DEDICATION

To

my parents, husband, and friends

my love and gratitude,

for seeing my happiness **as their own**

some wisdom:

Wherever you go. ***There you are***

~Confucius

and optimism:

It is possible for ordinary people to choose to be ***extraordinary***

~Elon Musk

TABLE OF CONTENTS

LIST OF FIGURES

LIST OF TABLES

ACRONYMS

AC	Alternating Current
ACPF	Alternating Current Power Flow
AEC	Advanced Energy Community
AWG	American Wire Gauge
BESS	Battery Energy Storage System
C&I	Commercial and Industrial
CAISO	California Independent system Operator
DC	Direct current
DER	Distributed Energy Resource
DERopt	Distributed Energy Resource Optimization
DG	Distributed Generation
DLPF	Decoupled Linearized Power Flow
DOE	Department of Energy
DSO	Distribution System Operator
EES	Electric Energy Storage
ETAP	Electric Transient Analysis Program
EUI	Energy Use intensity
GHG	Greenhouse Gas
LP	Linear Program
MILP	Mixed Integer Linear Program
MV/LV	Medium Voltage / Low Voltage
NEC	National Electric Code
NEM	Net Energy Metering
O&M	Operation and Maintenance
OPF	Optimal Power Flow
P2G	Power to Gas
PCC	Point of Common Coupling
PF	Power Factor
PV	Photovoltaic
REES	Renewable Electric Energy Storage
RPF	Reverse Power Flow
RTE	Round Trip Efficiency
SAIDI	System Average Interruption Duration
SAIFI	System Average Interruption Frequency
SCE	Southern California Edison
SOFC	Solid Oxide Fuel Cell
SOS	Special Ordered Set
TC	Transformer constraints
TIGER	Transmission Integrated Grid Energy Resource
TMY	Typical Meteorological Year
TOU	Time-of-Use

VVO	Volt-Var Optimization
ZNE	Zero Net Energy

ACKNOWLEDGMENTS

I would like to express my sincere and genuine gratitude to my committee chair, **Professor Jack Brouwer**, for being much more than an academic advisor, but a true mentor, advocator, and friend. Who has always believed in me, and allowed me to do so as well. Whose passion for clean energy inspires positivity and hope. His teachings and guidance shaped my research and made this work possible.

My gratitude also goes to **Professor Scott Samuelsen**, for precious teachings such as *Buford* — the social-political impacts of technology and innovation and Seabiscuit— a horse for his time. Also, for his leadership in the Advanced Power and Energy Program, whose impacts on the development of clean energy transcend globally and will continue to do so for many years beyond.

I would also like to thank my committee members, **Professor Kia Solmaz**, for all her teachings in optimization techniques, which gave me the first-principles understanding that served as the foundation for my optimization work. Also, for being a great role model for strong women in academia. **Professor Michael Green** whose expert knowledge in electric power systems have much supported and guided this work.

In addition, a thank you to all industry professionals that were also mentors and advisors: **Russ Neal**, who worked closely with APEP to provide valuable technical guidance on power systems. **Roberto Analco**, from ETAP, who provided me guidance on power flow state estimation, **Jerry Thode**, from Southern California Edison, who provided expert insights in the utility industry, and **Sarah Walinga**, from Tesla, who taught me so much about smart inverters.

I am immensely grateful for **all my dearest APEP friends**, who always created a great community to belong to. I will cherish our memories forever.

I am also especially grateful for the infinite support from my husband, **Greg Alesso**, for the emotional support only one that has married to a Ph.D. will ever understand. Thanks for reminding me to take breaks to pet **Momo** every so often, and not letting me work too hard.

Lastly, I am (and will eternally be) grateful to **Prof. Valerie Sheppard,** who taught me how to master life from the eyes of abundance, happiness, and wholeness. Whose teachings were just (or perhaps, more) important than any other technical course I've attended during my academic career at UC Irvine. I am profoundly grateful our paths have crossed.

VITA

Laura Martinez de Novoa

2008 - 2014 B.S. in Energy Engineering
Universidade Federal do ABC, Sao Paulo, Brazil

2014 - 2016 M.S. in Mechanical Engineering
Advanced Power and Energy Program, *University of California, Irvine*

2016 - 2020 Ph.D. in Mechanical Engineering
Advanced Power and Energy Program, University of California, Irvine

Sum. 2016 Internship – Power systems: automation, protection, and communications applications engineering
Schweitzer Engineering Laboratories, Irvine

Sum. 2018 Internship – Power systems: inverter and solar PV modeling
Tesla Inc., Palo Alto

Fall 2019 Internship - Powerwall (residential battery storage) applications engineering
Tesla Inc., Palo Alto

Spr. 2016 Teaching Assistant
MAE 118/218 Sustainable Energy.
Instructor: Dr. Brian. Tarroja

FIELD OF STUDY

Optimal allocation (size and siting) of distributed Energy Resources (DER), focusing on smart-inverter connected solar PV, battery storage within a microgrid for achieving high renewable energy penetration.

PUBLICATIONS

Dynamics of an integrated solar photovoltaic and battery storage nanogrid for electric vehicle charging
L Novoa, J Brouwer
Journal of Power Sources 399, 166-178

Optimal renewable generation and battery storage sizing and siting considering local transformer limits
L Novoa, R Flores, J Brouwer
Applied Energy 256, 113926
**Also recommended to special edition: Progress in Applied Energy.*

Optimal DER Allocation in Meshed Microgrids with Grid Constraints
L Novoa, R Flores, J Brouwer
Applied Energy (manuscript submitted)

Transmission Integrated Grid Energy Resources to Enhance Grid Characteristics
L Novoa, R Neal, J Brouwer
Applied Energy (manuscript submitted)

Optimal solar inverter sizing considering Volt-Var droop-control and PQ control for voltage regulation
L Novoa, R Flores, J Brouwer
Applied Energy (manuscript submitted)

Transformer Infrastructure upgrades for PEV Charging in a solar PV plus storage microgrid
L Novoa, R Flores, J Brouwer
Applied Energy (manuscript to be submitted)

Google Scholar Profile

ABSTRACT OF THE DISSERTATION

OPTIMAL SOLAR PV, BATTERY STORAGE, AND SMART-INVERTER ALLOCATION IN ZERO-NET-ENERGY MICROGRIDS CONSIDERING THE EXISTING POWER SYSTEM INFRASTRUCTURE

By

Laura Martinez de Novoa

Doctor of Philosophy in Mechanical & Aerospace Engineering

University of California, Irvine, 2020

Professor Jack Brouwer, Chair

In response to climate change and sustainability challenges, various incentive programs have promoted solar photovoltaic (PV) economic feasibility and interconnection into the low voltage electrical distribution system. However, the existing power system infrastructure can only accommodate a limited amount of PV generation before reverse power flow (PV generation flowing back into the distribution network) becomes an issue. This limits the ability to achieve Zero Net Energy (ZNE) behind individual meters and in whole communities since ZNE communities typically require large PV deployments. In parallel, district-level energy systems, such as Advanced Energy Communities (AEC) microgrids— electrically contiguous areas that leverage the clustering of load and generation by integrating multiple utility customer-owned Distributed Energy Resources (DER) — that include battery storage, offer a great prospect for integrating high levels of solar PV into the built environment.

Designing the least-cost and technically feasible system to serve a district load has been a challenge to utilities and city planners. Battery energy storage and smart-inverter

technologies emerge in this context to enable higher penetration of solar PV by locally regulating voltage and controlling active and reactive power flows. However, there is no straight forward way nor a practical rule or consensus on how to size such assets optimally.

This work proposes a Mixed Integer Linear Program (MILP) optimization to determine the least-cost DER portfolio consisting of inverter-connected solar PV and battery storage. It also allocates it in a multi-node electrical grid and dispatches it considering the existing electric infrastructure limits (transformer capacities and nodal voltage magnitudes). Novel linearization techniques such as polygon relaxations are used to limit otherwise non-linear apparent power flows at transformers. A novel Alternating Current (AC) decoupled linearized power flow is also integrated into the MILP optimization. Moreover, for the first time, smart-inverter droop-control functions are included in the DER optimal allocation problem. Results show that such comprehensive MILP is achievable and tractable for a 115-node AEC.

1 Introduction

Within an Advanced Energy Community microgrid, DER assets allow for most of the energy demand to be generated and consumed internally. External energy transfers enter the community if local production is insufficient. Excess electricity is exported to the wide-area electricity grid.

Optimally designing AEC to serve commercial, and industrial loads, while minimizing cost and maximizing the penetration of solar PV, has been a challenge to Distribution System Operators (DSO) and city planners. Moreover, a significant share of AEC project success depends upon achieving an adequate allocation of DER such as PV and battery storage resources while considering the existing urban power system infrastructure to support and enhancing the overall utility grid network characteristics.

We first attempt to demonstrate the local impacts of inverter-connected DER in the local power systems that it is integrated. We are interested in the challenges associated with the grid integration of large-scale PV deployments into the existing power system infrastructure. From the results of worst-case steady-state simulations, presented in Chapter 4 utility distribution transformer overloads are visibly the worst negative impact of a large deployment of solar PV. Over voltage excursions showed to be another major limiting factor to large PV deployments. These results drove the development of novel t*ransformer constraints* to limit the reverse power flow at the transformer level (limiting the total apparent power injection at that node), as described later in Chapter 5. And also an AC Decoupled Linearized Power Flow (DLPF) formulation to constrain nodal voltages, as described in Chapter 6

In chapter 5, a Mixed Integer Linear Program optimization is proposed to decide the best DER portfolio, allocation, and dispatch, for an AEC that achieves ZNE and islanding while respecting electrical grid operational constraints, with a focus on distribution transformer overloads. The main strategies to avoid transformer overloads were found to be careful sizing and siting of

battery energy storage and also optimally re-distributing PV throughout the community, which increased the ability of the electric infrastructure to support a PV deployment that is 1.7 times larger than the existing transformer capacity without the need for infrastructure upgrades.

In Chapter 6, a new approach to model the linearized power flow in distributed energy resources allocation and dispatch optimization is developed here. The model uses the Decoupled Linearized Power Flow(J. Yang, Zhang, Kang, & Xia, 2016) approach. DLPF has the advantage of being suitable for meshed networks, while the majority of current models use LinDistFlow, which is only suitable for radial networks. First, a validation is provided for the DLPF voltage magnitude and branch power (in kVA) solutions against LinDistFlow and the true AC power flow (ACPF) solution for a meshed benchmark network, a 33-node system. Then, the DER allocation and dispatch problem are formulated as a MILP and DLPF and LinDistFlow are used to model constraints on the electric power network infrastructure that limits voltages to ANSI C84 standard limits. The implementation of DLPF developed here improves the accuracy of nodal voltage calculation for meshed networks. The LinDistFlow solution fails to capture true under and over voltages; it also underestimates the optimal PV and battery storage capacities when compared to the DLPF solution.

Advanced inverter controls are a recent requirement for providing voltage support on distribution feeders with large PV deployments and high reverse power flow. These control functions, especially those that involve locally injecting or absorbing reactive power, require appropriate inverter sizing to accommodate for the reactive power support. The industry had historically adopted an AC/DC ratio smaller than one, which limits the inverter potential for reactive power support when at full Direct Current (DC) output —and when most needed. Optimal Volt-Var control (VVO) strategies have been devised, yet, currently, most commercial inverters adopt droop-control functions (which provide a more equitable share of reactive power regulation between customers). There is no consensus on how to size inverters optimally, in order to provide the necessary amount of reactive power compensation when in droop-control. In Chapter 7, a MILP for optimal DER investment planning is developed to optimally size inverters that can equitably provide voltage support for a ZNE microgrid with high PV penetration. Results show that the optimal AC/DC ratio is location-specific and ranges from 0.83 to 1.5. We also find a correlation between inverter AC/DC ratio and maximum nodal over-voltage and provide a curve fit model for optimal inverter sizing.

1.1. Research goals

The goal of the current research is to optimize the allocation (sizing and siting) and dispatch of inverter-connected solar PV and battery storage to minimize cost and guarantee power quality in distribution feeders of a grid-connected, or islanded, urban microgrid that requires large deployments of renewable solar PV, and often, zero-net-energy.

1.2. Objectives to meet goals

1. Continuously review the literature on DER optimal allocation, dispatch, smart inverters, zero-net energy microgrids, advanced energy communities, and related topics.

2. Determine the ability of baseload inverter-connected DER to regulate voltage on a constrained system.

3. Develop and verify a steady-state power flow model of a distribution feeder of an urban microgrid with high penetration of solar PV. Determine the solar PV hosting capacity of the existing microgrid infrastructure, considering existing service transformers and voltage limits. Model battery energy storage and smart-inverters with reactive power support into the model to improve solar PV hosting capacity.

4. Implement power system infrastructure constraints into an existing single-node, time-series MILP optimization framework for DER allocation in a ZNE microgrid. Constraints focus on service transformer capacity limits and AC power flow for limiting nodal voltage excursions. Determine optimal DER allocation in a ZNE microgrid under these constraints.

5. Implement Smart Inverter *Volt/Var* and *optimal PQ* control functions into the optimization framework. Determine optimal inverter sizing and abstract a practical model from the simulations.

1.3. Approach

This dissertation encompassed six key tasks, one for each objective described previously. This section describes how each task, and specific activities, maps to the chapters constituting this dissertation.

Task 1: Background (Chapter 2)

An extensive, continuous **literature review** on the topics below was made throughout this research. Relevant concepts were extracted and summarized in a background chapter to familiarize the reader with the following concepts:

- DER hosting capacity of power systems
- DER and voltage control
- Optimization methods applied to renewable, distributed energy systems, and power flow modeling
- Smart-inverter functions
- Advanced energy communities

Task 2: Determine baseload DER ability to regulate voltage on constrained systems (Chapter 3)

- Model a generation-constrained transmission system to investigate and demonstrate the ability of an inverter-connected DER to locally regulate voltage
- Carry out steady-state load flow simulations for different DER deployments, operating at a unity, *i.e.*, pure active power injection) and leading power factor, *i.e.*, having a combination of active and reactive power injection.
- Determine best DER placement that achieves greater grid benefits
- Determine impacts on overall system steady-state voltage stability

Task 3: Create an urban microgrid test case with high PV penetration. Develop a steady-state power flow model to identify and quantify main impacts in existing power system infrastructure. Implement battery energy storage and smart-inverters into the steady-state model to mitigate impacts (Chapter 4)

- Create a real-world microgrid test case. Characterize an existing urban district power system in Southern California through satellite imagery and on-site surveys.
- Model the high voltage (230 kV) transmission and medium/low voltage (12kV / 480/240/120 V) distribution feeders, with a high penetration of inverter-connected solar PV. Model any existing grid-support equipment, such as shunt capacitor banks, or load tap-changing transformers.
- Perform worst-case steady-state load flow simulation to identify and quantify the negative impacts on the existing power system infrastructure. Determine the (minimum) PV hosting capacity.
- Judiciously size and site battery energy storage and smart-inverters operating at a fixed power factor to eliminate negative impacts and increase the test case PV hosting capacity

Task 4: Implement power flow and distribution transformer constraints into a time-series MILP optimization framework for DER investment planning. Determine the optimal DER allocation (Chapter 5 and Chapter 6)

- Starting from an existing MILP optimization model, namely DERopt (R. J. Flores, 2016). Implement additional decision variables and constraints relevant to microgrid operations, such as export to the utility grid, and zero-net-energy constraints.
- Formulate and implement linearized AC power flow constraints (Decoupled Linearized Power Flow) into exiting optimization model
- Incorporate other relevant grid constraints into the optimization model, such as transformer capacity constraints and nodal voltage constraints.

- Use the model to determine optimal DER allocation for the test case.

Task 5: Implement smart inverter functions into the MILP optimization framework. Determine optimal smart inverter capacity for minimizing voltage deviation (Chapter 7)

- Model within a MILP framework two smart inverter controls Volt-Var and optimal PQ.
- Optimally size the solar PV inverter to minimize voltage deviations caused by solar PV in high penetrations.
- Abstract an approximated model for AC/DC inverter sizing from simulations

1.4. Structure of this dissertation

Chapter one *Background* intends to provide introductory first-principles knowledge to the reader that is unfamiliar with some of the concepts that will be explored here. Chapters three through seven map directly to the tasks outlined. Each chapter has its own applicable introduction, literature review, gaps found in current literature, contributions, and results. A summary section at the end of each chapter identifies the major points and insights from the results. Lastly, Chapter 8 Conclusions consolidates all the most relevant findings and provides the main conclusions of this work.

It is worth mentioning that the results and analysis of most chapters of this dissertation were submitted to prestigious peer-reviewed journals, as mapped by the table below. Chapter 5 was recommended by the editor in Chief of Applied Energy to a special edition *Progress in Applied Energy*.

Chapter 3:	**Transmission Integrated Grid Energy Resources to Enhance Grid Characteristics** L Novoa, R Neal, J Brouwer Applied Energy (manuscript submitted, in review process)
Chapter 5:	**Optimal renewable generation and battery storage sizing and siting considering local transformer limits** L Novoa, R Flores, J Brouwer Applied Energy 256, 113926
Chapter 6:	**Optimal DER Allocation in Meshed Microgrids with Grid Constraints** L Novoa, R Flores, J Brouwer Applied Energy (manuscript submitted Dec 2019)
Chapter 7:	**Optimal solar inverter sizing considering Volt-Var droop-control and PQ control for voltage regulation** L Novoa, R Flores, J Brouwer Applied Energy (manuscript to be submitted early 2020)

2 Background

2.1. DER hosting capacity

Hosting capacity is defined as the maximum level of additional DER penetration that an existing electric power system can accommodate while maintaining acceptable system performance (Bollen & Hassan, 2011). Grid performance can be analyzed concerning "performance indices", which depend upon applicable technical standards, local network configuration and operation, which will vary regionally (Schwaegerl, Bollen, Karoui, & Yagmur, 2005). These indices refer to different aspects of power supply, such as power quality, short circuit contribution, power system protection, reliability, and safety (Stetz, 2014). Figure 2.1 illustrates the concept of hosting capacity, where a given performance index limit was exceeded above acceptable deterioration limit. In a hosting capacity study, however, not only one but a combination of performance indices is likely to be considered, characterizing it as a multi-dimensional problem; once one given limit is exceeded the maximum hosting capacity is reached.

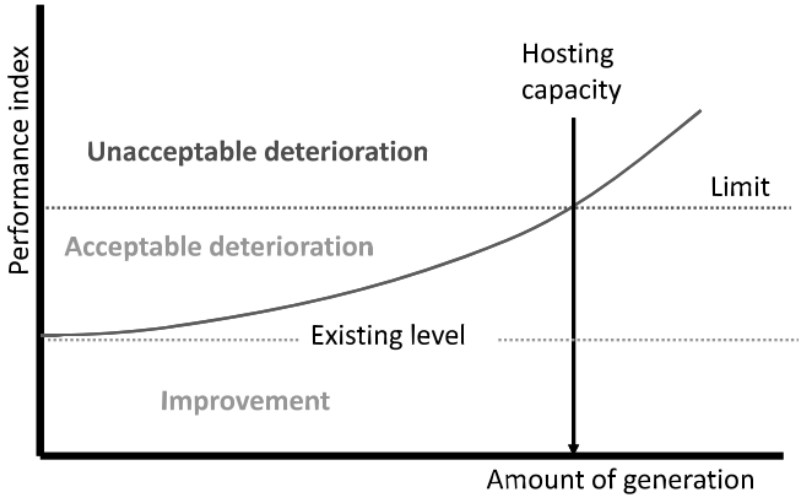

Figure 2.1 – Definition of hosting capacity (when a performance index is exceeded) (Bollen & Hassan, 2011).

In general, the three primary criteria used in hosting capacity analysis are (Electric Power Research Institute (EPRI), 2015; EPRI; APS, 2017; EPRI, Smith, & Rogers, 2015; Southern California Edison, 2016):

- Voltage excursions, which is limited by the absolute overvoltage magnitude, or a percent deviation from the nominal value.
- Equipment overloads (or thermal limits) which are limited by current flows, and thus, power flows allowed through equipment, such as transformers and cables.
- Protection, which examines whether the addition of DER interferes with the ability of existing protection schemes to identify and respond to abnormal conditions. One example is when DER is located

In a hosting capacity analysis, these indices are usually evaluated under a worst-case scenario for example, during a severe reverse power flow event; which occurs when a low load condition is associated with significant PV generation, thus, the power is that is not consumed locally is exported. In an RPF condition, the receiving bus voltage rises above nominal 1 per unit (P.U.)

The boundedness of these constraints should also be evaluated in practical terms. Thus, the analysis nature (i.e., steady-state vs. time-domain) plays a vital role in how conservative the hosting capacity results are. Steady-state worst-case type analysis often results in over-conservative limits, i.e., it is designed for a condition that only happens during one hour in the entire year, and most times, over-voltage or overloading issues might be acceptable within a short period. These nuances are often captured by time-series simulations (Christos, 2016)

Hosting Capacity is heavily influenced by the DER allocation within the system. Thus, one can also define a Minimum and Maximum hosting capacity (Electric Power Research Institute (EPRI), 2015), which depicts the more/less optimal DER allocation. In other words, at the same DER penetration level, different DER allocation (sizes and siting) deployments across the system can cause different impacts, perhaps because some locations have more voltage rise headroom, or are close to the head (beginning) of a feeder, where the total impedance is lower. Figure 2.2.illustrates the concept of minimum and maximum hosting capacity.

In this work, optimal allocations of DER will aim to maximize the total hosting capacity of a low voltage microgrid, which will be further discussed in section 2.3.

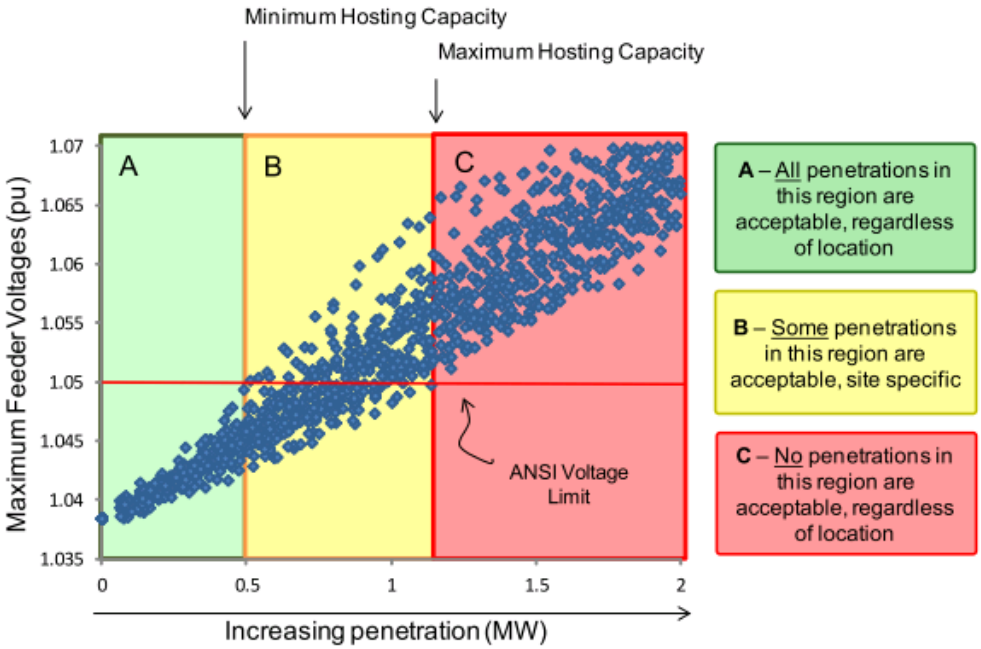

Figure 2.2 – Concept of Minimum and Maximum Hosting Capacity. Source: (Electric Power Research Institute (EPRI), 2015)

2.2. Voltage challenges caused by DER

To illustrate the prevalent technical challenge caused by high penetrations of DER that are Distributed Generators (DG), we refer to power flow concepts. The voltage excursion caused by DG is illustrated in Figure 2.3 (Christos, 2016; Mahmud, Hossain, & Pota, 2011; Stetz, 2014). Considering a two-bus system with a load and a DG unit, it will likely export power to the upstream distribution grid (P and Q). In order to do so, it has to operate at a higher voltage than the voltage at the sending end. For Kirchhoff's Law of Voltage (KLV), we can express the voltage phasor at the sending end ($\hat{V}_S$), or the grid voltage as:

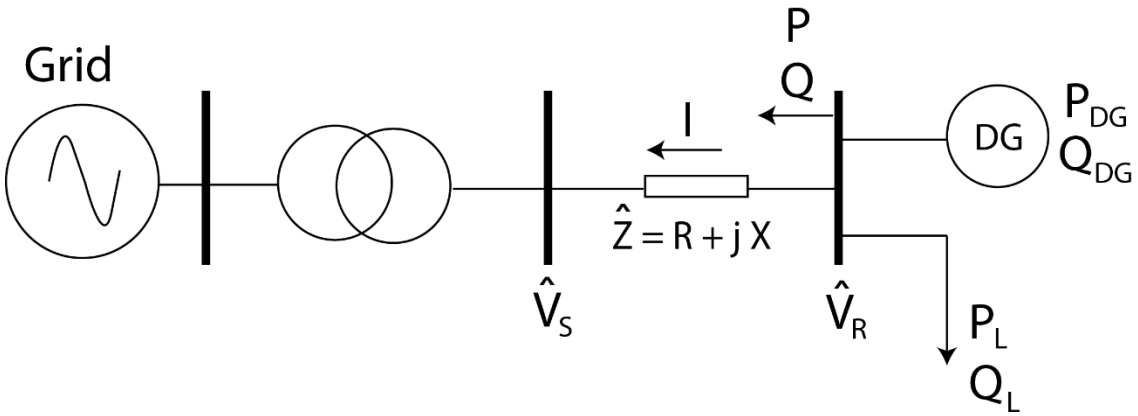

Figure 2.3 – Two-bus distribution system with DG and a load. Adapted from (Mahmud et al., 2011)

$$\hat{V}_S = \hat{V}_R - \hat{I}\,Z \tag{1}$$

$$\hat{Z} = R + jX \tag{2}$$

Where $\hat{V}_S$ is the voltage at the receiving end, where the load and DG are connected, $\hat{I}$ is the current phasor flowing through the line.

The complex power flowing through the network can be expressed as, where P and Q are the active and reactive power respectively.

$$\hat{S} = P + jQ = \hat{V}_S \hat{I}^{*} \tag{3}$$

From which we can write

$$\hat{I} = \frac{P - jQ}{\hat{V}_S} \tag{4}$$

Thus, we can readily define the voltage difference (raise or drop) ΔV between the receiving and sending end as:

$$\Delta V = \hat{V}_R - \hat{V}_S = \hat{I}\,Z = \left(\frac{P - jQ}{\hat{V}_S}\right)(R + jX) = \frac{RP + XQ}{\hat{V}_S} + j\frac{XP + RQ}{\hat{V}_S} \tag{5}$$

Since the voltage drop between the sending and receiving end is small, the voltage drop can be approximated by the real part of Eq. (5), also, if the sending end voltage is taken as the reference bus voltage, its angle is zero. Thus, it equals to the sending voltage magnitude.

$$\hat{V}_S = V_s \tag{6}$$

Moreover, we can finally write

$$\Delta V \approx \frac{RP + XQ}{V_s} \tag{7}$$

Moreover, writing the active and reactive power flows $P = P_{DG} - P_L$ and $Q = \pm Q_{DG} - Q_L$

$$\Delta V \approx \frac{R(P_{DG} - P_L) + X(\pm Q_{DG} - Q_L)}{V_s} \tag{8}$$

Some important observations can be drawn from Eq. (8):

- V_s can be considered a stiff, source, and therefore, constant.
- As the DG active power output P_{DG} increases, ΔV increases
- As the load active P_L and reactive Q_L power consumption increases, ΔV decreases
- The DG can absorb $(-Q_{DG})$ or inject $(+Q_{DG})$ reactive power.

- If DG absorbs reactive power, ΔV decreases (equivalent to operating at a lagging PF)
- If DG injects reactive power, ΔV increases (equivalent to operating at a leading PF)

The distribution system's resistance R and reactance X can be reduced (typically by costly line upgrades) in order to reduce the voltage rise.

Voltage rises are likely to occur when DG is exporting power. The legacy power system networks were designed to handle unidirectional passively (radial) power flows from the centralized generation resources to the high voltage transmission system, and finally to the medium and low voltage distribution system, where commercial, industrial, and residential loads are connected. Extreme RPF events pose a significant technical challenge to the current grid paradigm and limit the PV hosting capacity of a circuit. In this work, ways to increase PV hosting capacity by locally controlling active and reactive power flows, using smart-inverter advanced functions, and more specifically, how to optimally parameterize these functions will be proposed.

2.3. Optimal DER allocation in a microgrid environment

Microgrids are defined as clusters of load, generation, and storage resources, that can operate autonomously (independent of the main electric grid, i.e., islanded) or grid-connected. Moreover, the notion of a microgrid also entails a certain level of advanced control capabilities, which assure system reliability during islanded operations (Hatziargyriou, 2014). Microgrids provide a platform to integrate DER into the medium and low voltage distribution network, with focus on meeting loads with local generation (Kwasinski, Weaver, & Balog, 2017). DER include distributed generation, including, but not limited to microturbines, solar PV and fuel cells (FC), and wind turbines and also storage systems such as batteries, power-to-gas (P2G), flywheels, ultra-capacitors, to mention a few.

To allocate DER in any system, pure analytical techniques, and, more recently, optimization and artificial intelligence hybrid techniques have been used. The approach of allocating DER in a Microgrid environment is no different from allocating it in a grid-connected system, only the goals of the system and constraints might be different to capture the goals of a microgrid environment, for instance, ZNE, islanding, enhanced reliability, among others.

There are in the current literature a large number of different solution methodologies to the DG allocation problem, which can be broadly categorized in (1) sensitivity/pure analytical, (2) classical optimization, and (3) artificial intelligence techniques (Arabali, Ghofrani, Bassett, Pham, & Moeini-Aghtaei, 2017), and also (4) hybrid intelligent (Pesaran H.A, Huy, & Ramachandaramurthy, 2017)

Sensitivity/pure analytical methods represent the system in a mathematical model and compute its direct numerical solution. These techniques are fast, simple, accurate, and easy to implement, but can only be applied to small-scale systems. Techniques used in this approach are Eigenvalue Based-Analysis (EVA), Index method (IMA), Sensitivity Based Method (SBM) and Point Estimation Method (PEM). (Arabali et al., 2017).

Classical optimization methods are used to minimize (or maximize) a given goal, or cost function, subjected to given technical/operational constraints (equality and inequality constraints). These methods are useful for continuous and differentiable domains and are characterized by relatively slower convergence rates and computational times. These techniques involve Optimal Power Flow (OPF), Linear Programming (LP), Mixed Linear Integer Programming (MILP), Mixed Non-linear Integer Programming (MINLP), Dynamic Programming (DP), Sequential Quadratic Programming (SQP), and Ordinal Optimization (OO). (Arabali et al., 2017).

Artificial intelligence (meta-heuristic) techniques are usually applied to solve complex nonlinear optimization problems through intelligent techniques methodology inspired by natural phenomena. Some challenges often associated with this technique involve premature convergence, local optima, and unstable results. Such techniques are the Genetic Algorithm (GA), Fuzzy Logic (FL), Particle Swarm Optimization (PSO), Artificial Bee Colony (ABC), Tabu Search (TS), and Ant Colony Search (ACS). (Arabali et al., 2017). For further reading on these techniques, and many other hybrid intelligent methods, (Rezaee Jordehi, 2016), and (Pesaran H.A et al., 2017), are recommended, which are a comprehensive review compendium all these existing approaches.

A number of practices have been used for DER allocation in energy systems. The most simplistic one involves allocating a single specific type of DER, such as solar PV, or wind, in a single node according to a particular optimization goal and constraints. This analysis is usually performed in

an “aggregate approach”, and it is static, or steady-state. Several “enhancements” to this approach were developed in subsequent studies, such as (1) optimizing a portfolio (mix) of DER, and allocating it (2) including heating and cooling demands in the load elements (3) incorporating the time-coupling of DG and load (and sometimes it’s inherent uncertainty) in a time-domain, dynamic simulation (4) considering electric power grid constraints, in a multi-node approach, (5) considering electric energy storage, and lastly, (6) considering smart-grid technologies to achieve better grid performance. However, most studies in the literature to date only implement one or two of the improvements mentioned above, but not all of them.

2.4. Optimization formulations applied to DER allocation

Optimization problems for DER allocation are typically non-linear, highly constrained, multi-objective, mixed-integer, multi node, thus, finding a near-global optimal solution is challenging (Rezaee Jordehi, 2016). DER type, location, real and reactive power outputs are the standard decision variables computed. In the following section, typical formulations for steady-state (static) DG allocation problems found in the recent literature are reviewed. Time-domain (dynamic) optimizations follow a similar formulation, but compute a decision variable for each time-step t, increasing the problem dimension significantly.

2.4.1. Objective function

The optimization problem is built to minimize (or maximize) an objective function that is formulated using a group of parameters in a logical manner that translates a single objective or a weighted multi-objective (WMO) (Arabali et al., 2017).

$$minimize\ f(x) = \alpha\ x_1 + \beta\ x_2 + \cdots + \gamma\ x_n \tag{9}$$

Where $x_1, x_2\ , and\ x_n$ are individual objectives and $\alpha, \beta, and\ \gamma$ are weight factors (the sum of weight factors should always equal to one).

The most common objective function goals in the existing research works are listed below:

- Cost

The costs of DER allocation involve construction/investment (capital cost), financial (principal and interest), O&M (facility management, regular maintenance fuel, and equipment

replacement). Nonetheless, there are also possible financial returns from surplus energy sales, reduction of emission of pollutants, infrastructure upgrade deferrals, and potential tax credits.

An approach shown in (Arabali et al., 2017) formulates the objective function for cost as:

$$\max f_{cost} = C_D + C_e - C_{DG} - C_l \quad (10)$$

Where: $C_D = \sum_{i=1}^{T} T_{\max i} * C_w * F_V * P_{\sum Dg_i}$ is the generated income, where T is the number of years, $T_{\max i}$ is the annual average operating hours for the DG. F_V is the ratio of average output and the rated power of the DG, and $P_{\sum Dg_i}$ is the power produced by the DG unit . C_w is the grid electricity price. $C_e = \sum_{i=1}^{T} T_{\max i} * C_c * F_V * P_{\sum Dg_i}$ are the emission reduction benefits, where C_c is the conventional fuel generation environmental costs $C_{DG} = \sum_{i=1}^{T} T_{\max i} * \partial * C_{DG_j} * P_{\sum Dg_i}$ are the investment costs, where C_{DG_j} is the cost of an individual equipment, $\partial = \frac{r*(1+r)^t}{(1+r)^t-1}$ is the average cost factor of a DG fixed investment, r is the annual profit, t are the planning years $C_l = \sum_{i=1}^{T} \beta_i * c_i * T_{\max i} * P_{\sum Dg_i}$ are the O&M costs, where c_i is the unit capacity factor, β_i is the O&M cost per unit of power

- System Active Power Losses

When optimally sized and placed, DG can reduce system losses by 10-20% (Arabali et al., 2017). The power loss formulation usually focuses on reducing branch power, and most times, active power losses. The exact loss or the "i-squared" loss which is calculated from the branch current, can be formulated as in (Sultana, Khairuddin, Aman, Mokhtar, & Zareen, 2016). It is worth pointing out that not only instantaneous, but accumulated losses over time, such as daily losses or annual losses can also be the focus of the minimization. Equation (11) refers to the exact active power loss flowing from branch i to branch j (Arabali et al., 2017) and Equation (12) refers to the copper losses caused by branch current I_{bi} passing through a resistor R_{bi} (Prakash & Khatod, 2016). Another approach is to calculate the power loss index (Prakash & Khatod, 2016) as in Equation (13), which calculates the % reduction in copper losses after DG is placed, which is a quantity that should be maximized.

$$min\ f_{losses} = P_L = \sum_{i=1}^{N}\sum_{j=1}^{N}\left[\alpha_{ij}\left(P_iP_j + Q_iQ_j\right) + \beta_{ij}\left(Q_iP_j - P_iQ_j\right)\right] \quad (11)$$

$$\alpha_{ij} = \frac{R_{ij}}{V_i V_j}\cos(\delta_i - \delta_j)$$

$$\beta_{ij} = \frac{R_{ij}}{V_i V_j}\sin(\delta_i - \delta_j)$$

$$P_L = \sum_{i=1}^{N} |I_{bi}|^2 \; R_{bi} \tag{12}$$

$$P_{L_i} = \left(1 - \frac{Re\left\{P_{L_{afterDG}}\right\}}{Re\left\{P_{L_{beforeDG}}\right\}}\right) X\ 100\% \tag{13}$$

- Voltage profile excursions

Voltage profile improvement i.e., maintaining bus voltages $\overline{V_i}$ as close to their nominal operation value $\overline{V_{nom}}$ is also commonly chosen as an optimization goal. One approach is to calculate the Voltage Profile Index (VPI) (Arabali et al., 2017). When included in the objective function, the VPI penalizes the size-location pair that gives higher voltage deviations from the nominal value, as written in Equation (14).

$$VPI = \max\left(\frac{|\overline{V_{nom}}| - |\overline{V_i}|}{|\overline{V_{nom}}|}\right)\ i = 1, \dots, n \tag{14}$$

- Emissions from grid and DER

Emission goals can be translated into economic revenues originated from emission reductions. One of such approaches was already shown in Equation (9) C_e . In another approach shown in (Falke, Krengel, Meinerzhagen, & Schnettler, 2016), the total emissions of CO_2 equivalent are computed. The total emissions include both emissions caused by manufacturing ($E_i^{production}$) and operation ($E_i^{operation}$) of each DG i, and are minimized, as shown in Equation (15). A Life Cycle Analysis (LCA) are likely necessary to be applied to the DER technologies to obtain $E_i^{production}$.

$$\min f_{CO_{2eq}} = \sum_{i=1}^{N}\left[E_i^{production} + E_i^{operation}\right] \tag{15}$$

One approach to calculate operation emissions based on power output is shown in (Basu, Bhattacharya, Chowdhury, & Chowdhury, 2012)

$$E_i^{operation} = \sum_{i=1}^{N} \left[\alpha_i + \beta_i + P_{DG_{i_{max}}} + \gamma_i {P_{DG_{i_{max}}}}^2 \right] \quad (16)$$

Where $\alpha_i , \beta_i, and\ \gamma_i$ are CO_2 or NO_x emission coefficients of the ith DER determined by a least-squares fit on equipment data of emissions vs power output.

- Reliability

Multiple analyses had shown that a DG reduced both the magnitude and duration of failures, directly by being available when the central generation was not or indirectly by reducing stress on the system components, so the individual system component reliability is increased. Also by locally reducing load and enabling feeder tie operations that were avoided due to high-load conditions, (Arabali et al., 2017). The System average interruption frequency index (SAIFI) indicates how often an average customer is subjected to sustained interruption over a predefined time interval:

$$SAIFI = \frac{Total\ Number\ of\ Customer\ Interruptions}{Total\ Number\ of\ Customers\ Served} = \frac{\sum \lambda_i N_i}{\sum N_i} \quad (17)$$

Where $\lambda_i$is the failure rate, and N_i is the number of customers of load point i. (Arabali et al., 2017)

Another index, the System average interruption duration index (SAIDI) indicates the total duration of interruption an average customer is subjected to for a predefined time interval:

$$SAIFI = \frac{Sum\ of\ Customer\ interrupstion\ Duration}{Total\ Number\ of\ Customers\ Served} = \frac{\sum U_i N_i}{\sum N_i} \quad (18)$$

Where U_i is the annual outage time (Arabali et al., 2017). These indices can be included in the cost function to penalize solutions that are unreliable.

- DER hosting capacity, DG penetration

It is worth mentioning that the vast majority of previous literature work is mainly focused on minimizing cost and copper losses. Another interesting optimization objective, which will be

significantly explored in this work, is to maximize the installed capacity of DG installed in the network, for increasing total renewable energy penetration into the existing power system.

$$\max f_{DG_{capacity}} = \sum_{i=1}^{N} P_{DG_i} \tag{19}$$

A comprehensive list of many other possible objective functions is provided in (Pesaran H.A et al., 2017), as illustrated in Figure 2.4.

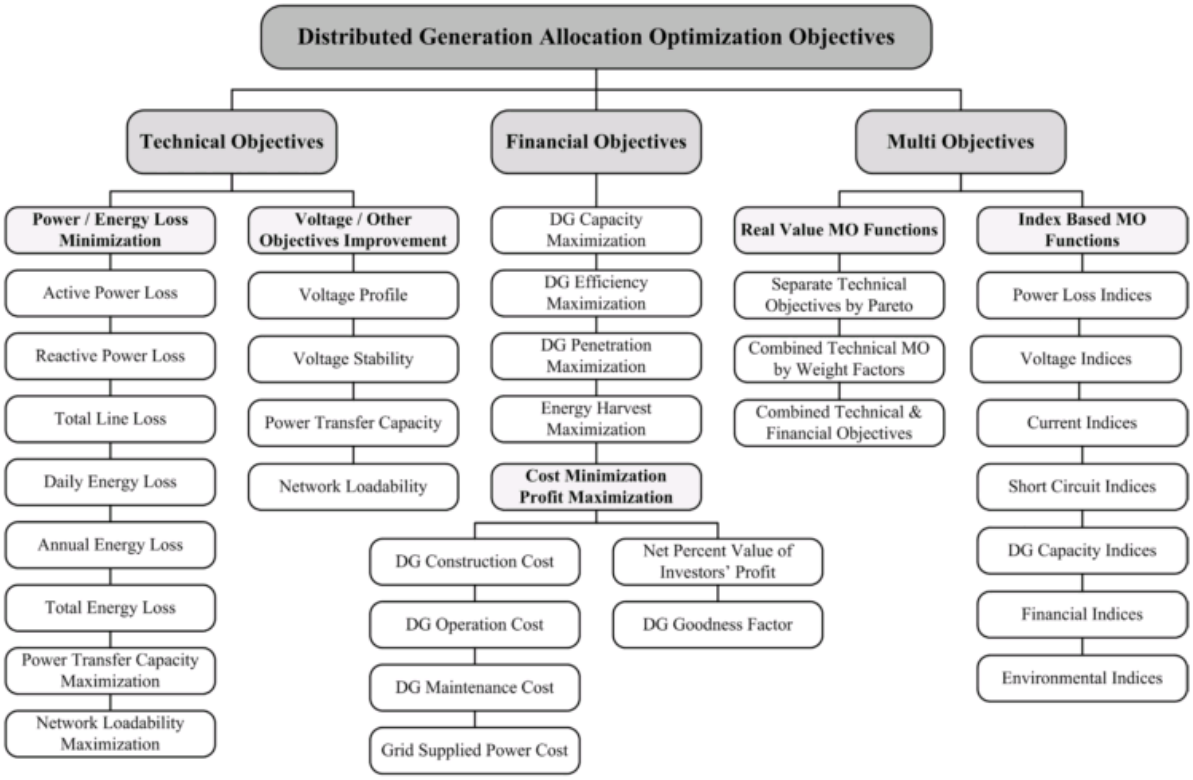

Figure 2.4 – DG allocation Optimization Objectives . (Pesaran H.A et al., 2017)

2.4.2. Constraints

As in a typical optimization formulation, the objective function for the DG allocation problem should satisfy given equality $h_i(x) = 0$ or inequality $g_i(x) \leq 0$ constraints such as:

- Voltage constraints

The voltage at the ith V_i bus should always stay within upper and lower limits $\underline{V_i}$ and $\overline{V_i}$ respectively, as shown in (20) (Arabali et al., 2017). Limits for voltage are usually taken as the (ANSI, 2005)

$$\underline{V_i} \leq |V_i| \leq \overline{V_i} \tag{20}$$

- Current (thermal) constraints (line and transformer)

The apparent power flowing from branch i to branch j (S_{ij}) should not exceed the maximum rated power the circuit or transformer can withstand $S_{ij\,max}$, as shown in Equation (21) (Arabali et al., 2017)

$$S_{ij} < S_{ij\,max} \tag{21}$$

- Power Balance

At each node, the power generated from the DG at each node i, (P_{G_i} and Q_{G_i}) plus losses ($P_L, and\ Q_L$) should equal the active and reactive load et each node (P_{D_i} and Q_{D_i}), as shown in Equation (22) (Arabali et al., 2017). If the system is grid-connected and allows for import and export, these decision variables can be included as shown in Equation (24).

$$\sum_{i=1}^{N} P_{G_i} + P_L = \sum_{i=1}^{N} P_{D_i}$$
$$\sum_{i=1}^{N} Q_{G_i} + Q_L = \sum_{i=1}^{N} Q_{D_i} \tag{22}$$

$$\sum_{i=1}^{N} P_{G_i} + P_L + P_{grid_{import}} = \sum_{i=1}^{N} P_{D_i} + P_{grid_{export}} \tag{23}$$

- Storage constraints

Battery storage can be modeled in the case of a time-domain dynamic simulation, which will account not only for power but energy balances. An approach to model storage was shown in (Mashayekh, Stadler, Cardoso, & Heleno, 2016), and can be written as shown in Equations (24), (25), and (26).

$$SOC_{n,s,t} = (1 - \phi_s) * SOC_{n,s,t-1} + SIn_{n,s,t} - SOut_{n,s,t} \tag{24}$$

$$\underline{SOC_s} \leq SOut_{n,s,t} \leq \overline{SOC_s} \tag{25}$$

$$\begin{aligned} SIn_{n,s,t} &\leq Cap_{n,s} * \overline{SCRt_s} \\ SOut_{n,s,t} &\leq Cap_{n,s} * \overline{SDRt_s} \end{aligned} \tag{26}$$

Where:

$SIn_{n,s,t}$ = Energy input to storage technology s at node n, kWh

$SOut_{n,s,t}$ = Energy output from storage technology s at node n, kWh

$Cap_{n,s}$ = Installed capacity of continuous technology k at node n, kW or kWh

$\underline{SOC_s}/\overline{SOC_s}$ = Min/max state of charge for storage technology s, %

$\overline{SCRt_s}/\overline{SDRt_s}$ = Max charge/discharge rate of storage technology s, kW

In the case of storage, the power/energy balance equation will need to also include the power charge/discharge from the battery, modifying the active power portion of Equation (22) to include storage would result in:

$$\sum_{i=1}^{N} P_{G_i} + P_L + SOut_{n,s,t} = \sum_{i=1}^{N} P_{D\,i} + SIn_{n,s} \tag{27}$$

- Power Flow

The power flow equations are active and reactive power balance equations at each node. An approach used by (Arabali et al., 2017) uses the AC nonlinear power flow equations as constraints, where P and Q generated by the DG are P_{G_i} *and* Q_{G_i} . V_i and V_j are the voltages at nodes i and j and δ_i *and* δ_j are the respective voltage angles $|Y_{ij}|$ and θ_{ij} represent the admittance magnitude and angle from the admittance matrix.

$$\begin{aligned} P_{G_i} - P_{D_i} - \sum_{j=1}^{N} |V_i||V_j||Y_{ij}| \cos(\delta_i - \delta_j - \theta_{ij}) = 0 \\ Q_{G_i} - Q_{D_i} - \sum_{j=1}^{N} |V_i||V_j||Y_{ij}| \sin(\delta_i - \delta_j - \theta_{ij}) = 0 \end{aligned} \tag{28}$$

- Power imported from the grid

It is often necessary to limit the power provided by the network P_{grid}. Otherwise, for most cost-based objective functions, the load is likely going to be supplied fully by power imported from the grid, which is cheaper, and the optimization problem returns zero DER installed capacity.

$$0 \leq P_{grid} \leq \overline{P_{grid}} \tag{29}$$

- Space and area

Available space for DER installation is a constraint often overlooked in the literature, but essential for obtaining more realistic results. An approach suggested by (Y. Yang, Zhang, & Xiao, 2015b) is directly applied to PV systems and rooftop area. $N_{PV,n}$ is the installed capacity of the PV system in building l. $Area_{PV}, j$ is the area occupied by each kW of the PV panel and $MaxRoof_l$ is the roof area space of building l.

$$N_{PV,l} * Area_{PV} \leq MaxRoof_l \tag{30}$$

- Power factor (PF)

DG units are usually operated in PQ mode with a constant power factor. However, in some studies, the DER was allowed to operate to export or import reactive power. An approach shown in (Prakash & Khatod, 2016), an inequality constraint was set to bound the operating PF of the DG from 0.8 to unity.

$$0.8 \leq PF_{DG,j} \leq 1 \tag{31}$$

The PF can also be controlled by setting a fixed PF value and optimizing the amount of reactive power output/absorbed by the DG, as shown in (Arabali et al., 2017)

$$Q_{G_i} \leq P_{G_i} \sqrt{PF^{-2} - 1} \tag{32}$$

A comprehensive list of many other possible objective functions is provided in (Pesaran H.A et al., 2017), as illustrated in Figure 2.5.

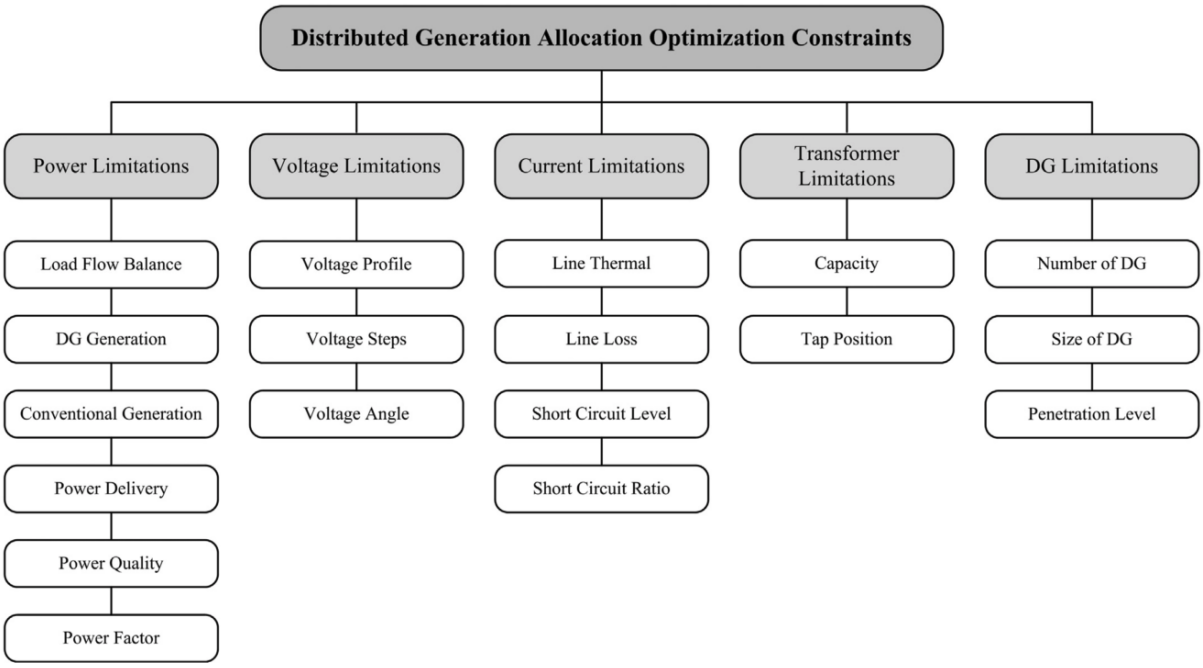

Figure 2.5 – DG Allocation Optimization Constraints (Pesaran H.A et al., 2017)

2.4.3. Optimal power flow

The first optimal power flow problem was proposed in 1962 by J. Carpentier (Carpentier, 1979). Since then, many authors have contributed to the development of the central problem formulation to apply OPF to many different applications. The OPF problem is simply an optimization formulation, i.e., a minimization or maximization of an objective function having it constrained within a set of equality and inequality constraints that describe the power flows across the system nodes and determine the power system operational limits. These equality and inequality conditions define the feasible region for the OPF problem. Most times, these formulations are nonlinear and non-convex (Abdi, Beigvand, & Scala, 2017). OPF formulations are widely used for the economic dispatch of generators, i.e., optimize generation to reduce cost. Nonetheless, OPF formulations have been gaining attention and applied to other goals such as minimize losses, regulate voltage and maximize DER penetration.

The decision variables of an OPF control the solution space dimension, thus, for n decision variables the dimension of the solution space will be n. Examples of such variables may include active power generation of all nodes (Except slack bus), reactive power injections for voltage

regulation equipment, voltages across the system node, tap settings in the transformers, and so forth.

A sample OPF problem, as taken from (Zhang, 2013) can be expressed as:

$$\text{minimize } f(P_1, P_2, \dots, P_n) \tag{33}$$

$$\text{subject to } h_i(x) = 0 \qquad i = 1, \dots, m \tag{34}$$

$$g_j(x) \leq 0 \qquad j = 1, \dots, r \tag{35}$$

Where (33) is the cost function, usually defined on the real power outputs, Equation (37) represents the equality constraints, usually expressed by the physical load flow equations, and equation (38) represents the inequality constraints that typically define system operating limits.

The OPF problem is usually solved using Newton-type methods, which have a non-guaranteed convergence to a local minimum (Zhang, 2013). Various other methods have also been proposed, such as Distributed and Parallel OPF (DPOPF), Multiphase OPF (MOPF), linearization approaches, iterative approaches, unbalanced three-phase OPF (TOPF), Alternating Direction Method of Multipliers (ADMM). Each of these methodologies is summarized in (Abdi et al., 2017), and also have their computational performances compared.

Amongst some of the challenges/recommendations identified in the field of OPF applied to microgrid and smart-grids (Abdi et al., 2017) (Ehsan & Yang, 2017)are:

- The increased dimension of the optimization problem, especially when considering distribution systems at a lower voltage level.
- The unbalance nature of loads
- The integration of energy storage, which requires a dynamic time-series simulation, or Optimal Energy Flow (OEF)
- The incorporation of uncertainties of renewable generation
- Hybrid techniques combining analytic metaheuristic and computations methods should be explored

2.5. Smart-inverter functions

The main smart-inverter functions to be considered in this work and summarized in this section were initially proposed in the "ERPI, Common Functions for Smart Inverters – Phase 3" report (Electric Power Research Institute (EPRI), 2014). This report was the result of a collaborative industry and utility work facilitated by EPRI. It proposes a core set of key smart-inverter functions that will facilitate higher DG penetration without affecting system power quality or reliability. These functions are considered mandatory in California under Rule 21, and in other utilities with the IEEE Standard 1547-2018.

2.5.1. Fixed power factor

This function provides a mechanism to regulate the DER's power factor to a pre-set fixed value. Attention is needed for the sign convention used, as illustrated in Figure 2.6, there are two different sign conventions typically used in industry:

1. IEC: Generated or Supplied active power is positive. Demanded active power be negative.

2. IEEE: leading (capacitive, producing Var) PF is positive and lagging (inductive, absorbing Var) PF is negative.

Also, a PF of +1.0 and -1.0 are essentially the same (zero Vars).

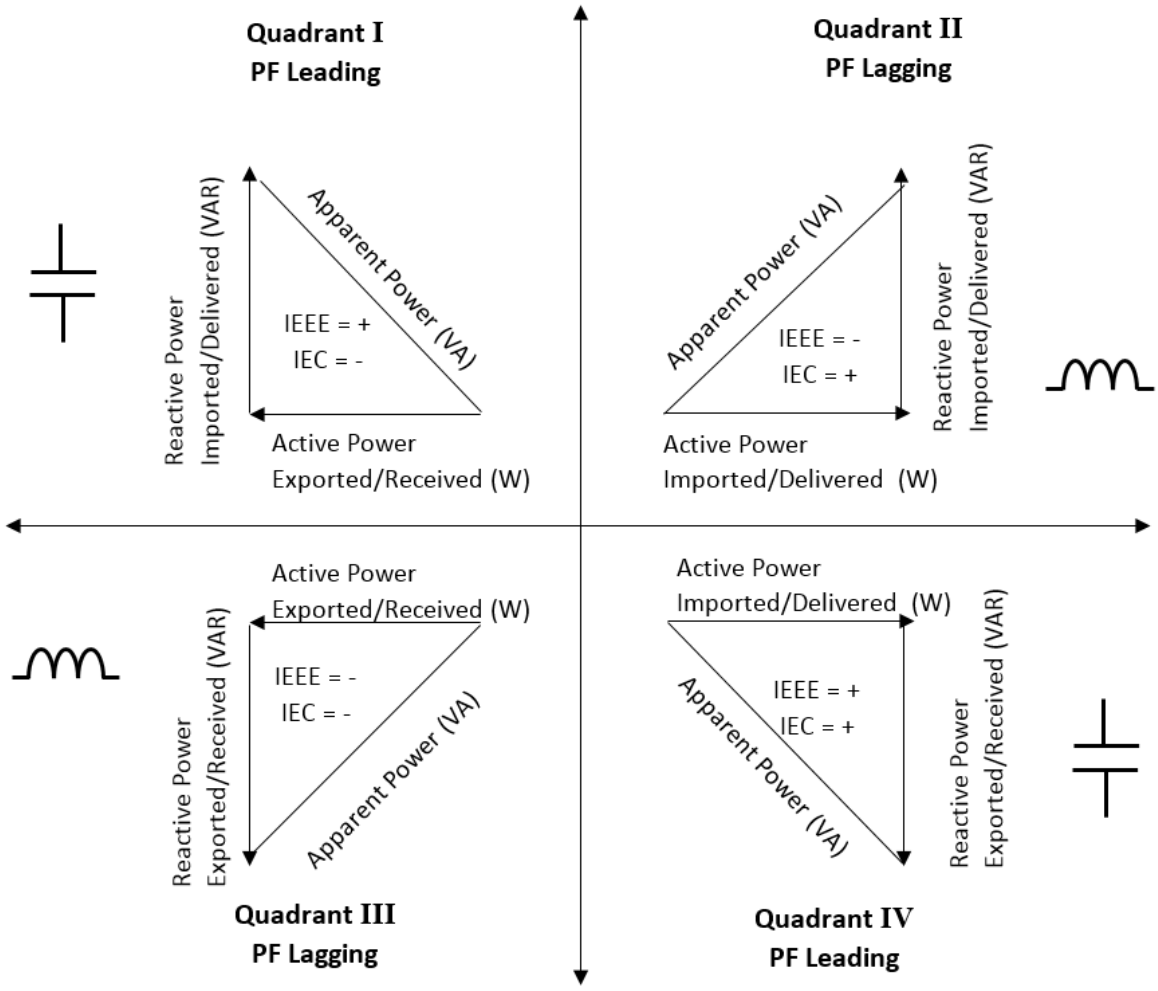

Figure 2.6 – IEC and IEEE power factor sign convention. Adapted from (Electric Power Research Institute (EPRI), 2014)

2.5.2. Volt-Var

A smart inverter with a Volt-Var function controls reactive power, Var, to regulate local voltage. The function uses a "configurable curve", i.e., a two-dimensional X-Y array, which defines a linear function of the desired Volt-Var behavior. Vars are the controlling variable and Volts are the variable to be controlled. The Y-axis is the percent available Vars, in other words, the power capacity that the inverter can provide at a given moment without limiting its Watt output, which usually takes priority. Also, the array X-values are defined as the "Percent Voltage", as defined in Equation (36), which is the voltage value but expressed in percentage of the Reference Voltage ($Vref$).

$$Voltage\ (\%) = \frac{Voltage}{Vref}\ x\ 100\% \tag{36}$$

Figure 2.7 illustrates a typical Volt-Var function. The four points, P1 through P4, indicate the desired percentage available Var level (Q1 through Q4) for a given voltage value in percentage of $Vref$ (V1 through V4). Noting that P2 and P3 represent a "dead-band", which a corresponding Var output of 0%, or 0 Var. In addition, expressing the points in the curve as percentages allows the use of the curve for many different DERs without having to adjust for local conditions such as nominal voltage.

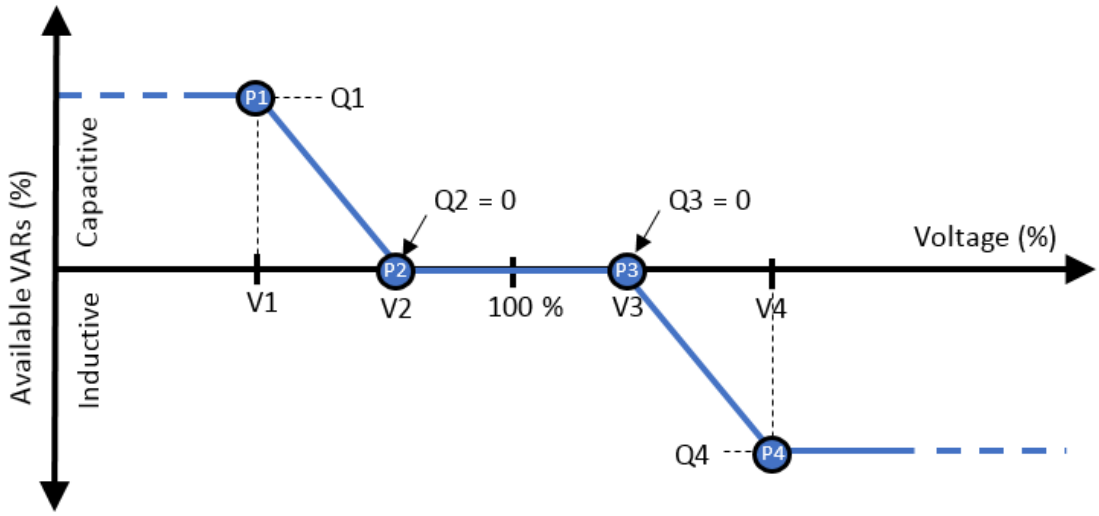

Figure 2.7 – Example Volt-Var function curve. Adapted from (Electric Power Research Institute (EPRI), 2014).

Different manufacturers can have different Volt-Var behavior characteristics such as a horizontal line or two points forming a ramp. In some cases, it might also be desired to have a hysteresis behavior. The hysteresis adds the benefit of avoiding any unnecessary fluctuations, for instance, as can be observed in Figure 2.8 the same amount of Vars Q3 = Q5 is outputted when the voltage decreases from V3 to V5.

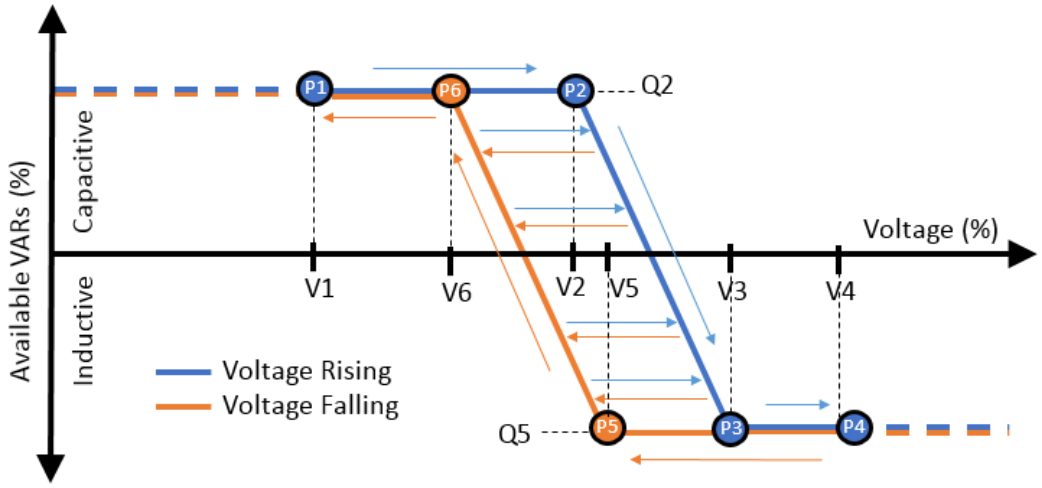

Figure 2.8 – Example of Volt-Var function curve with hysteresis. Adapted from (Electric Power Research Institute (EPRI), 2014).

Lastly, these curves should be implemented as "modes", so a single inverter can have many modes pre-programmed, which can be interchanged by a signal broadcast, or also scheduled over time.

2.5.3. Volt-Watt

An inverter with a Volt-Watt function is able to reduce its Watt output gradually in order to achieve a target voltage level at the PCC. The specific need for such a function arises from cases where a high PV penetration at low loads can cause feeder overvoltage. This function adopts the same "configurable-curve" approach as the Volt-Var function. An example of such a curve is shown in Figure 2.9, where a horizontal line extends across the lowest voltage, V1, and to the highest voltage, V3, until an operational limit is reached. The horizontal axis is expressed in percent of $Vref$. The vertical axis is the inverter's Maximum Watt output, also in percentage. Thus, for a system with nominal 480 V, and the function settings are V2 = 105% and V3 = 110%, the Watt reduction would begin for voltages above 504 V and be reduced to zero at 528 V.

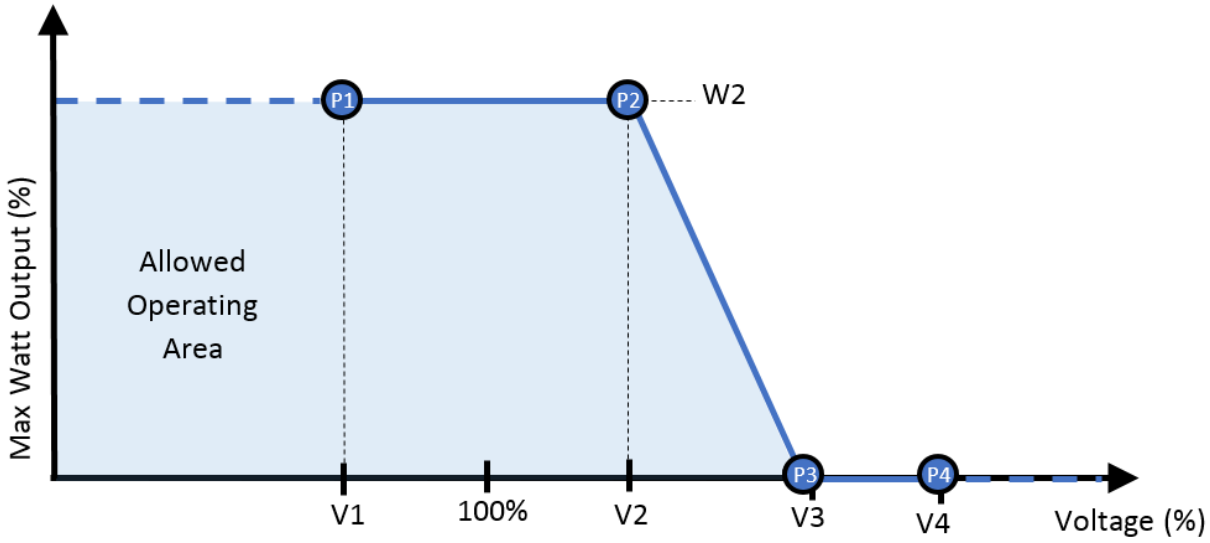

Figure 2.9 – Example of Volt-Watt function curve. Adapted from (Electric Power Research Institute (EPRI), 2014).

There is a separately defined function designed for systems containing energy storage: the Absorbed Volt-Watt function. There are two proposed ways to limit the rate of charging power, the Low-Pass Filter Limiter, where $\omega = 2\pi f$ and τ is the time-constant of the filter, defined in Equation (37) and Figure 2.10.

$$\left|\frac{Output}{Input}\right| = \frac{1}{\sqrt{1+(\omega\tau)^2}} \quad \longleftrightarrow \quad Output = Input * (1 - e^{-\frac{t}{\tau}}) \tag{37}$$

Frequency Domain — Time Domain

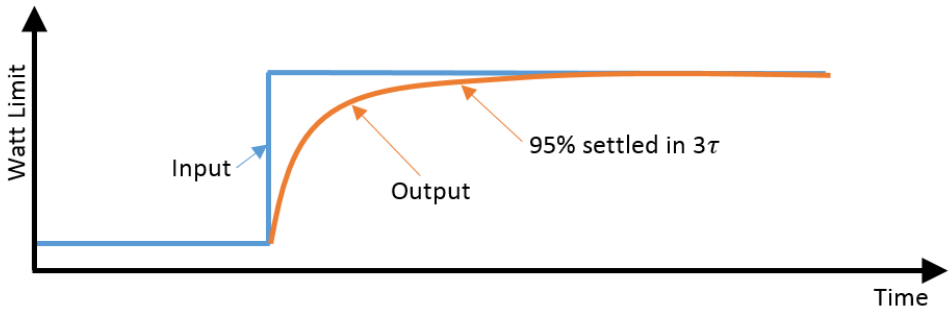

Figure 2.10 – Low Pass Filter Limiter Example. Adapted from (Electric Power Research Institute (EPRI), 2014).

There is also the Rate of Change Limiter, defined in Equation (38), which establishes a maximum value for the rising and falling rates of the Watts limits.

$$\frac{dWattLimit}{dt} \leq Rise\ Limit \qquad \frac{dWatt\ Limit}{dt} \geq Fall\ Limit \tag{38}$$

- Interactions between Volt-Var and Vol-Watt

The interaction between the Volt-Var and Volt-Watt functions is direct and intentional. In all functions described so far, Watts must take precedence over Vars regardless of voltage, and it might be that an inverter that is producing its full Watt capacity does not have any extra Vars to offer. Nonetheless, in most cases, there is a sufficient margin between the inverter VA rating and the peak PV array output (W); therefore, there is enough room for significant Vars production. The combined operation of both functions allows for the reduction of Watts when there is a local voltage rise, also enabling more Vars production.

To clarify the combined operation described above, consider the following two scenarios. In the first one (Figure 2.11), the PV active power output, in blue, is 100% of the inverter limit. This means that the available Var output, in yellow, is zero until the Watts are reduced by the Volt-Watt function. As the voltage increases so does the ability to produce Vars.

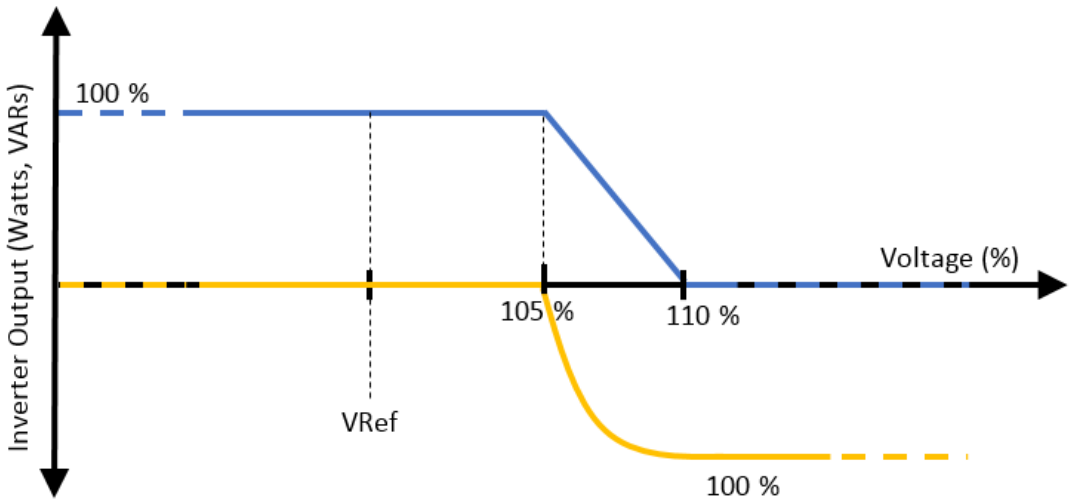

Figure 2.11 – Interaction between Volt-Var and Volt-Watt – Scenario 1. Adapted from (Electric Power Research Institute (EPRI), 2014).

In the second scenario, shown in Figure 2.12, the PV active power output, in blue, is only 80% of the maximum inverter output. Thus, there is a maximum available Var output capacity of 60%, in yellow, (from the constant VA circle) until the Volt-Watt function reduces the Watts.

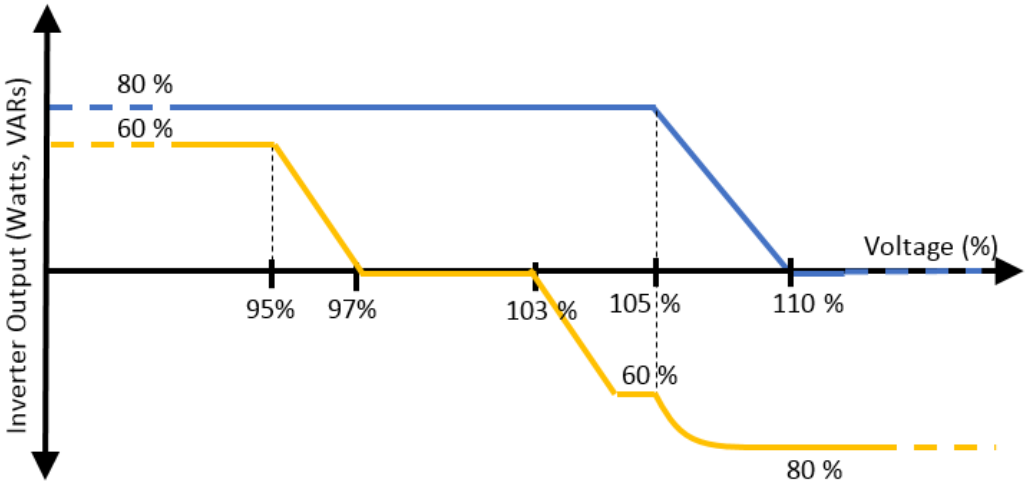

Figure 2.12 – Interaction between Volt-Var and Volt-Watt – Scenario 2. Adapted from (Electric Power Research Institute (EPRI), 2014).

3 Baseload DER ability to regulate voltage on generation-constrained systems

Highlights

- Large-scale baseload DER is deployed to support a constrained transmission system
- A combined active/reactive power injection is ideal for voltage regulation
- Placing DER on the bus with the lowest voltage achieves greater overall grid benefits
- DER deployment enhances the overall system steady-state voltage stability

This chapter presents a steady-state power flow analysis that investigates and demonstrates the ability of an inverter-connected DER to locally regulate voltage in a real-world transmission (500/230/66 kV) power system that is generation-constrained, that is, it has a generation deficit and therefore an unbalanced generation/load. A MW-scale DER operating as baseload (that is, able to output constant power) is able to output a combination of active and reactive power, by operating at a fixed (leading/lagging) power factor.

Power flow simulations are carried out for different DER deployments. Results show that DER can reduce line losses and provide local voltage support. The allocation of only three DER systems operating at a 0.7 leading power factor or as a pure reactive source is able to maintain all system nodal voltages 0.98 p.u. or above when it otherwise would have dropped to near 0.92 p.u. when the systems main power source, a 2.0 GW nuclear plant, went off-line. The best DER placement is proven to be always at the weakest point in the system (at the end of the circuit, at the lowest voltage bus) as opposed to being distributed across nearby buses. Moreover, the DER deployment enhances the overall system steady-state voltage stability

3.1.Approach

In this chapter, high-temperature fuel cells are proposed as the distributed energy resource and are referred from this point forward in the text as *TIGER* (Transmission Integrated Grid Energy Resources). The practical potential of fuel cell distributed generation was earlier recognized in numerous studies (Bauen, Hart, & Chase, 2003; Bischoff, 2006; Cragg, 1996; Das, Das, & Patra, 2014; Dufour, 1998; Krumdieck, Page, & Round, 2004; Tarman, 1996; Toonssen, Woudstra, & Verkooijen, 2009). The attractiveness of this power source stems from the following features:

- The high-availability factor: a TIGER station's power output is constant, non-intermittent, and only dependent on fuel supply. Thus, most of the challenges associated with highly dynamic and unpredictable DER no longer apply for TIGER stations.
- The high efficiencies achieved in small-scale systems, which can be further increased with combined heat and power applications.
- The high energy density and availability of sufficient land in many substations or nearby transmission ROW
- The modular design allowing tailored power output and enhanced load following capabilities
- The inverter-based connection, which provides flexibility for reactive power compensation and minimal short circuit contribution
- Low noise and pollutant emissions favoring siting and permitting within urban areas
- The resulting short lead times for construction and commissioning.

These features lead to another benefit, namely the ability to site TIGER stations where they can provide grid benefits such as improving voltage profiles and reducing transmission line losses. In TIGER stations, all of the produced active and reactive power is transferred to the grid through an inverter, which allows for a flexible power output that can be adjusted to supply active and reactive power as needed. In the stationary fuel cell market, there are now a number of commercially available, next-generation multi-megawatt systems, several of those are the result from the U.S. distributed generation Fuel Cell Program (Mark C. Williams & Maru, 2006), (M.

C. Williams, Strakey, & Singhal, 2004). Moreover, various utilities in the U.S. and Korea are deploying such systems as large-scale fuel cell power parks (Curtin & Gangi, 2015).

There is a common concern regarding the capabilities of fuel cells to operate dynamically, providing adequate load following. Appropriate thermal management is a typical challenge, which can be accomplished well for low temperature fuel cell systems such as proton exchange membrane or phosphoric acid fuel cells, but is more challenging for high-temperature fuel cells such as solid oxide or molten carbonate fuel cells. If thermal management is not accomplished well dynamic temperature excursions could lead to accelerated cell degradation. The benefits of TIGER stations evaluated in this paper assume a typical steady-state baseload operation, but it is known that the actual grid is dynamic. Meaningful research progress has been made in achieving a superior load-following capability for stationary fuel cell systems. In (Barelli, Bidini, & Ottaviano, 2016) an SOFC was able to respond to a 46% step down in power, this should be sufficient to meet the part-load operation requirements for a transmission substation.

The key points this chapter will investigate are the ability of TIGER stations to assist in supporting the local voltage profile of regions with poor load/generation balance, the ability to reduce resistive line losses, and optimal TIGER placement, when operating at a unity power factor, 0.7 leading power factor, and at pure reactive power injection. We will also investigate the effects on the system steady-state voltage stability using P-V curve analysis methods.

3.1. Model Development and Assumptions

The test case used for this analysis is a real-world transmission system located in Southern California. Figure 3.1 illustrates the geographical location of its primary substations, transmission lines, and corresponding voltage levels. An “A” substation is one where the transformer high voltage winding is connected at 230 kV, and an “AA” substation is one connected at 500 kV. The test case is bounded by the dashed lines and it is referred to here as the *SONGS system*.

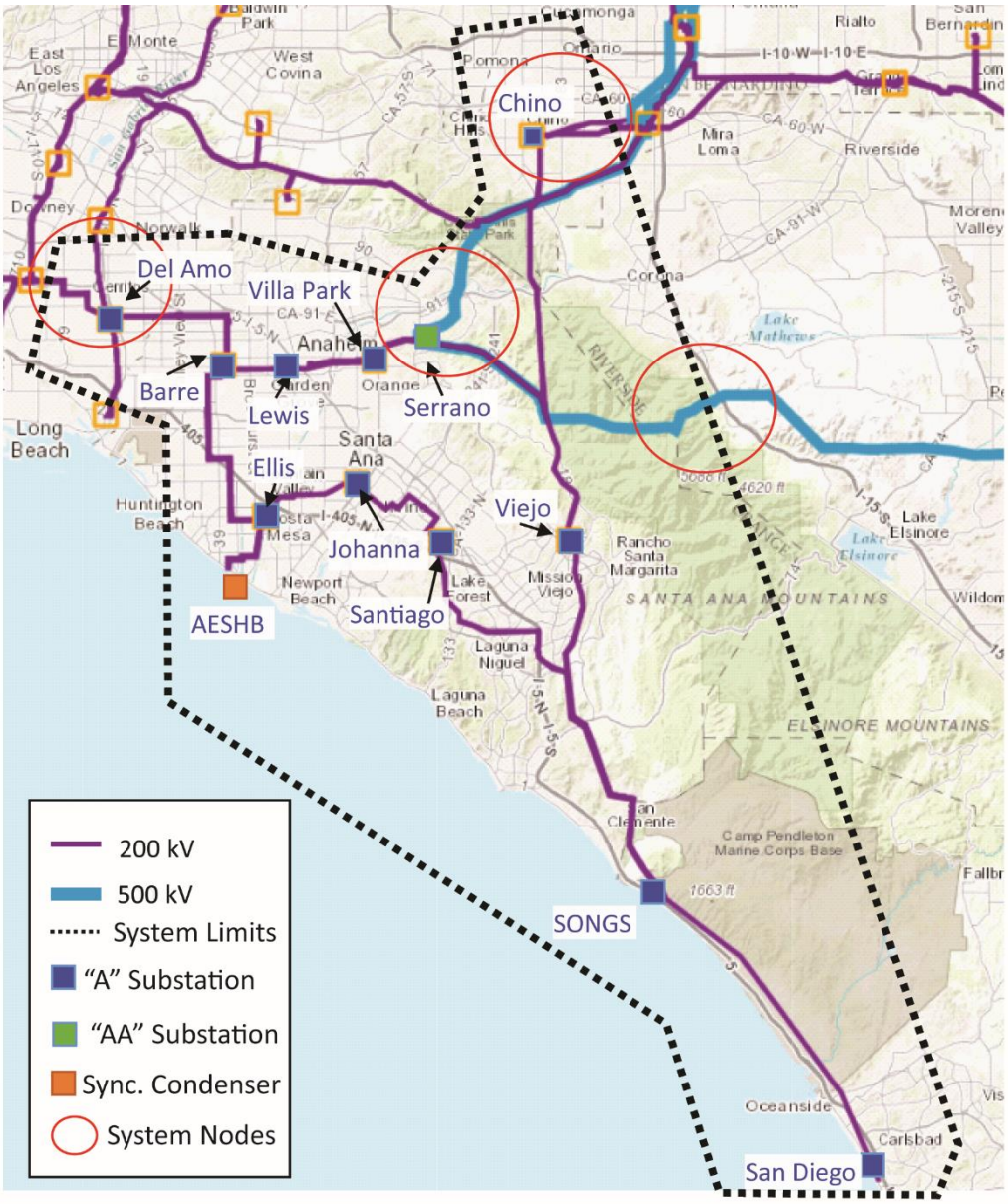

Figure 3.1 – Southern California Main Transmission substations and system boundary for SONGS System. (Southern California Edison (SCE), 2016a)

A steady-state power flow model of the *SONGS system* was developed in *PowerWorld™*, an industry standard power flow simulation software, to solve for the steady-state power flows and nodal voltages. Figure 3.2 illustrates a simplified one-line diagram of the model. There are thirteen 230 kV buses, two synchronous generators, one at the system slack bus and other located at the SONGS bus, and one synchronous condenser, which corresponds to two generator units retired in 2013 that currently operate as synchronous condensers to provide voltage support to the area ("AES Uses Synchronous Condensers for Grid Balancing," n.d.).

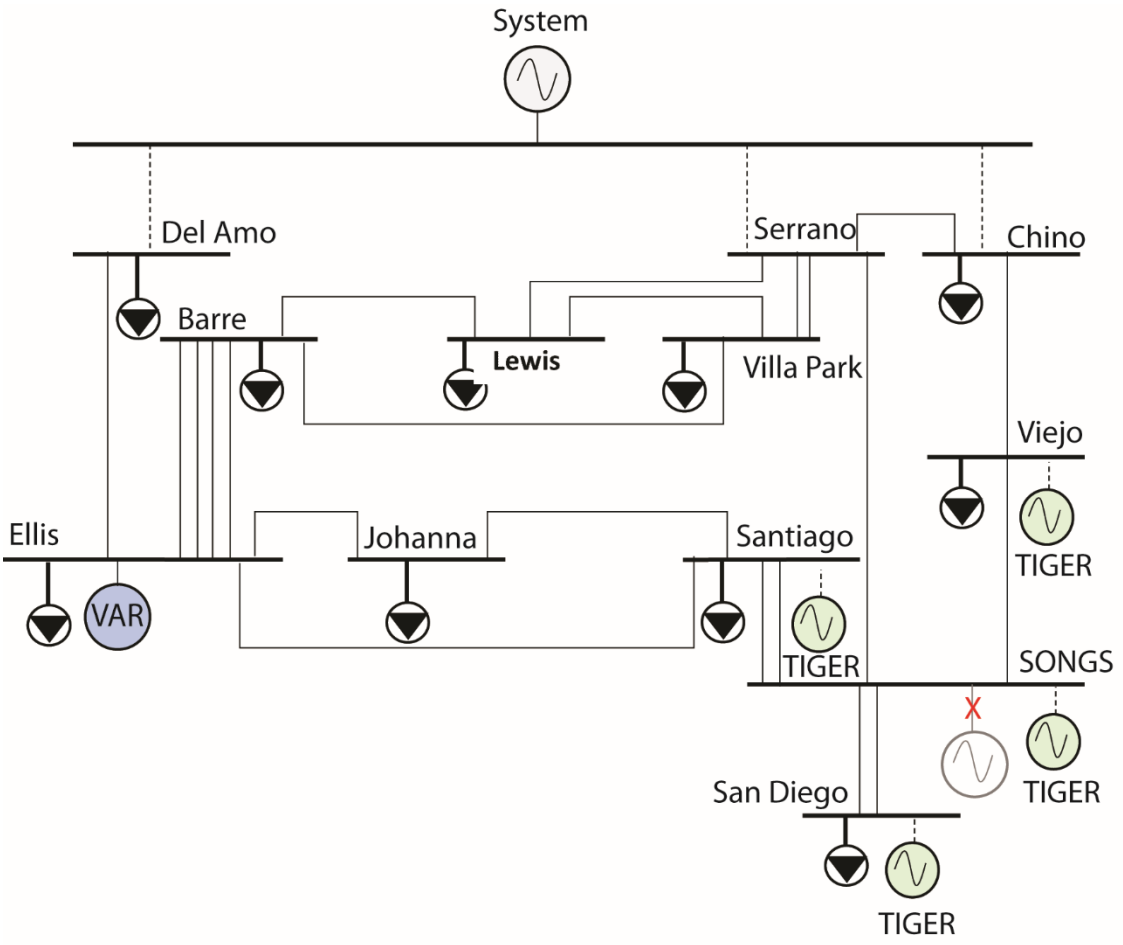

Figure 3.2 – One-line diagram of SONGS system

Loads were modeled as constant power (PQ) and having a unity power factor. Demand values on the 230/66 kV transmission substations were taken from the 2017 peak load forecast contained in the CAISO 2015-2016 Transmission Plan (California ISO, 2016), and shown in Table 3.1. Interconnection studies in this area have identified total current distributed generation at those substations, in MW (Southern California Edison (SCE), 2016a).

The base values for the per-unit calculations used were S_{base} = 100 MVA, V_{base} = 230 kV, thus using equations (39) and (40) (Grainger & Stevenson, 1994), we calculated that Z_{base} = 529 Ω, and I_{base} = 251 A.

$$Z_{base} = \frac{V_{base}^2}{S_{base}} \tag{39}$$

$$I_{base} = \frac{S_{base}}{\sqrt{3}V_{base}} \tag{40}$$

The boundaries of the test case, as shown in Figure 3.1 are the 230 kV buses at Serrano, Del Amo, and Chino. These points were modeled as Thevenin equivalent reactances assuming a short circuit duty of 50 kA at Del Amo and Chino substations and 63 kA at Serrano. For these boundary lines, the short circuit per-unit (p.u.) impedance values used were Z_{pu} = 0.005, for Del Amo and Chino buses and Z_{pu} = 0.004 for Serrano. San Diego was modeled as a 700 MW load assuming SONGS would typically meet this amount of power flow toward SDG&E service territory.

Table 3.1– Substation 2017 Peak Load forecast

Substation Name	Load Forecast - 2017 (MW)	Total Distributed Generation
Barre	723	-
Chino	741.3	-
Del Amo	545.2	-
Ellis	700	450 MVar[1]
Johanna	461	-
Lewis	657	-
Santiago	879	-
Viejo	378	-
Villa Park	737	-
SONGS	-	2,200 MW
San Diego	700	-

[1] Source (AES California, n.d.)

Line lengths were obtained from Southern California Edison's DERiM map (Distributed Energy Resource Interconnection Map), publicly available at (Southern California Edison (SCE), 2016a). Line impedance was obtained from the following assumptions:

- All conductors are assumed to be Aluminum Steel Reinforced (ASCR)
- 230 kV lines
    - Lapwing conductor: 1590 kcmil, R = 0.0622 Ω /mile, and X = 0.364 Ω /mile
    - 140 feet height vertical single-circuit transmission tower layout
    - 20 feet spacing between phases
    - Transposed lines

- Reliability Must Run (RMR) capacitor banks, usually deployed at the 230kV level to compensate the inductance of the transmission lines were not modeled since the goal is to determine the ability of TIGER stations alone to regulate voltage.

3.2. Scenarios

Table 3.2 summarizes all scenarios considered. For each scenario, a steady-state power flow simulation was performed. Base Case 1 and Base Case 2 (no TIGER stations) represent the test case before and after the main generation source is retire. The "TIGER with pure active power injection" scenarios aim to study the ability of TIGER station to provide local voltage support. Incremental 100 MW TIGER stations were allocated at the nodes with the lowest steady-state-voltage in the Base Case 2 (San Diego, SONGS, Viejo and Santiago) as described in Table 3.2.

To study the effects of reactive power injection by TIGER stations, i.e., the "TIGER with MVar injection" scenarios, the same "TIGER with pure active power injection
" scenarios were simulated with two additional TIGER operating conditions: (1) each TIGER station operated at a 0.7 constant leading power factor. And (2) the TIGER stations were operated with pure reactive power injection.

Table 3.2 – Scenario Description

<table>
<tr><td>Base Cases</td><td colspan="3">Base case 1: Main generation source online</td></tr>
<tr><td></td><td colspan="3">Base case 2: Main generation source offline</td></tr>
<tr><td>TIGER with pure active power injection (unity power factor)</td><td>1 TIGER
Santiago
SONGS
San Diego</td><td>2 TIGER
San Diego + SONGS
SONGS + Viejo
SONGS + Santiago
Santiago + Viejo
2 x San Diego</td><td>3 TIGER
SD + SONGS + Viejo
SONGS + Viejo + Santiago
3 x San Diego</td></tr>
<tr><td rowspan="2">TIGER with MVar injection (leading power factor)</td><td colspan="3">Previous TIGER scenarios, having each a 100 MVA inverter operating at 70 MW /70 MVar (0.7 PF lead) output</td></tr>
<tr><td colspan="3">Previous TIGER scenarios, having each a 100 MVA inverter operating at 100 MVar (pure MVar injection)</td></tr>
</table>

3.3. Results and Discussion

3.3.1. Voltage profiles

To capture the effect of TIGER size upon voltage support, i.e., the effect that each given MW has in voltage profile improvement, an index is here presented, namely, the "Voltage Improvement Index", VII. This index was based on similar indices already presented in the literature (Chiradeja & Ramakumar, 2004; Gil, El Chehaly, Joos, & Cañizares, 2009). For calculating the VII, the per-unit voltage at a given bus i after TIGER placement (V_{pu_i}) is subtracted from the per-unit voltage at a given bus i before TIGER placement ($V_{pu_{i_o}}$) and then divided by the voltage in the base case. The result is then divided by the TIGER penetration ($TIGER_{pen}$) defined in Equation (41), which is the percentage of the load met by TIGER at a given bus. For instance, a VII of 0.5 indicates that the bus voltage improved 0.5% per 1% TIGER penetration increase, and a higher VII implies there are higher voltage improvements per MW installed. This index was calculated for the deployments of TIGER in the San Diego bus, and its trend is shown in Figure 3.3

$$TIGER_{pen} = 100 \times \frac{\sum P_{TIGER_i}}{Load_i} \tag{41}$$

$$VII = \frac{100 \times \frac{V_{pu_{i_o}} - V_{pu_i}}{V_{pu_{i_o}}}}{TIGER_{pen}} \tag{42}$$

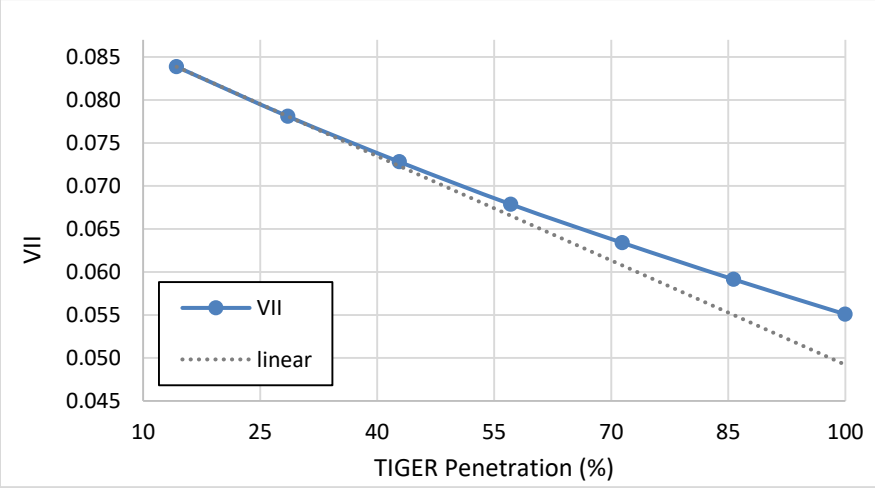

Figure 3.3 – Voltage improvement index, VII vs. TIGER penetration (%)

By analyzing the VII, it is clear that there are diminishing returns associated with the addition of TIGER station capacity to support system voltage, as VII goes progressively down with TIGER penetration in a non-linear fashion. This is consistent with prior work suggesting that at low penetrations of DER, these indices are relative linearly additive, and as the DER penetration increases, VII becomes non-linear (Gil et al., 2009).

To achieve further voltage improvements, this analysis also considers reactive power injection. This is possible since TIGER stations are connected to the grid through switching power electronics inverters. Considering a 100 MVA rated inverter, the total output can be (1) up to 100 MW, (2) or any combination of MW and MVar that respects the apparent power rating. A combination of 70 MW and 70 MVar output, corresponding to a leading power factor of 0.7, is evaluated here, or (3) pure 100 MVar of reactive power. Reactive power injection in this system is intuitive since long transmission lines have a high X/R ratio, i.e., the ratio of its reactance to its resistance; thus, they are a reactive power sink. The results shown in Figure 3.5 capture that TIGER stations operating at a 0.7 leading PF (i.e., a combination of active and reactive power injection) achieved a higher overall rise in voltage profiles of the buses that needed voltage support compared to pure active power or pure reactive power injection (illustrated in Figure 3.5(b)). These results agree with the results obtained in (Hessenius, Ang, & Hamilton, 2006).

The advantage of using a 0.7 power factor is clear because, as one might expect, voltages rely on power flows, active and reactive. If the local demand for active power increases, this demand must be met by an increased amount of power, and current, flowing through transmission lines. Meeting these demands locally will reduce these flows and regulate local voltages. Also, it is known from voltage regulation fundamentals that operating at a leading power factor will increase the receiving end voltage (Grainger & Stevenson, 1994).

To illustrate these facts, consider a two-bus system, shown in Figure 3.4, comprised of a 200 MW load that is fed by a remote System generator (slack) through a transmission line with impedance $Z = 0.01R + j0.1X$ p.u., with the load also locally supplied by a 100 MVA TIGER. When the TIGER operates at unity power factor, it will offset 100 MW of active power flow from the upstream system, but the transmission line still acts as a reactive power sink. In the 0.7 leading PF case, less load is displaced, but now the TIGER bus is a reactive power source, which will increase the local voltage. In the pure reactive power injection case, the load now needs to

be fully met by the upstream remote generator; moreover, 100 MVar is injected back to the System upstream and the terminal voltage again increases.

Looking again at the voltages in Figure 3.4, one can infer that pure reactive power injection seems the most attractive solution for regulating voltage, however, reactive power compensation is only effective over short distances, whereas active power will flow higher upstream. This effect can be observed by the comparison of the leftmost graphs in Figure 3.5 where the 0.7 leading PF case shows an overall better voltage regulation, *i.e.*, the difference between receiving end and sending end voltage magnitudes, for the entire system. Thus, a combination of active and reactive power injection is found to regulate voltage more effectively than only active power in systems like the SONGS system with long power lines.

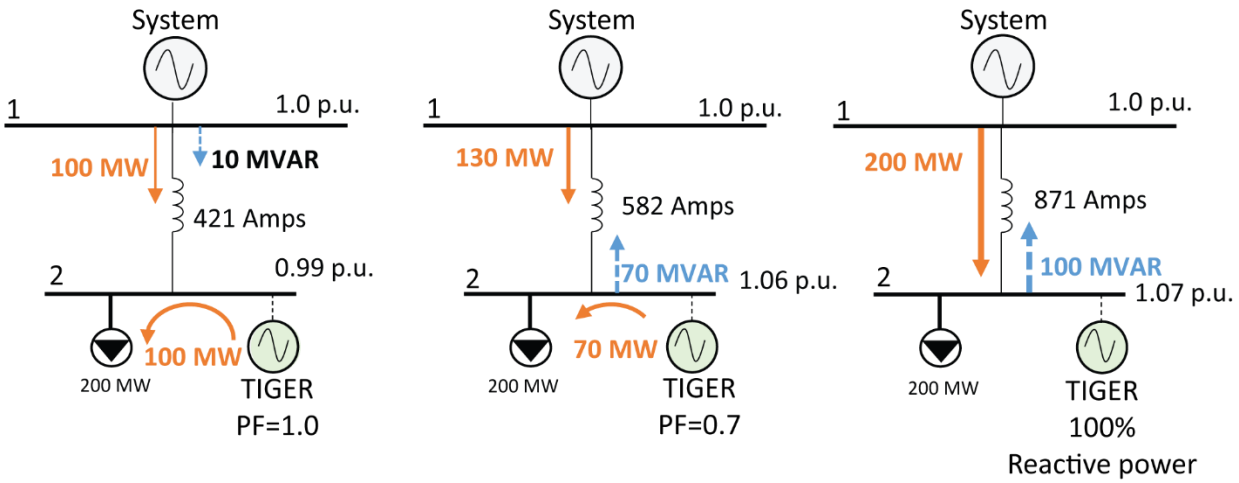

Figure 3.4 – TIGER Power Factor and resulting power flows

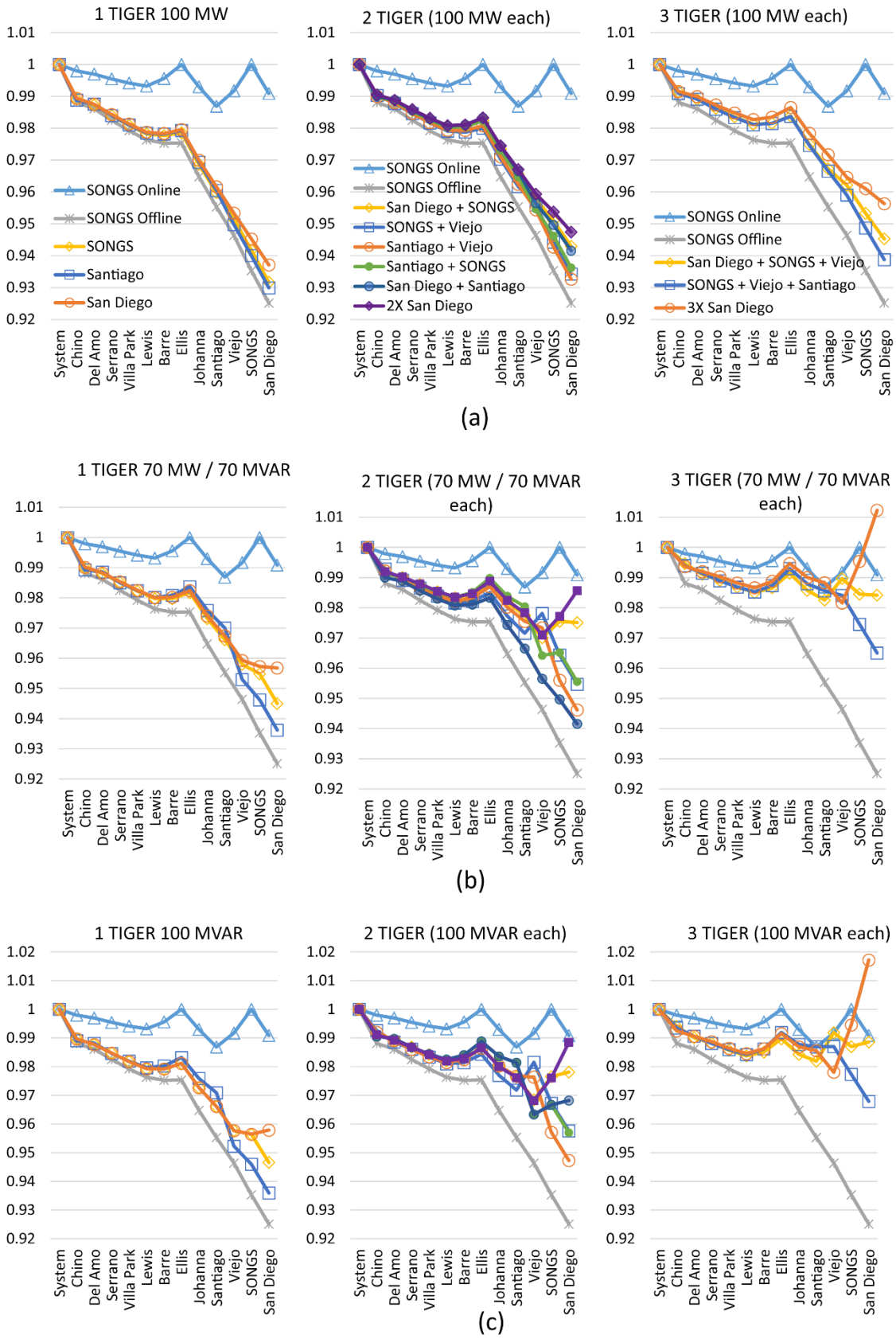

Figure 3.5 – (a) 100 MW TIGER. (b) 70 MW/70 MVar TIGER. (c) 100 MVar TIGER

3.3.2. Steady-State voltage stability

Voltage stability typically involves determining the operating point at which a system reaches its so-called voltage collapse. There have been extensive efforts in the literature devoted to identifying optimal placement of DER to improve local voltage stability, which is likely in the weakest bus in the system (Abdel-Akher, Ali, Eid, & El-Kishky, 2011; Angelim & Affonso, 2016; H. Chen, Chen, Shi, & Duan, 2006; P. Chen, Member, Malbasa, & Kezunovic, 2013; Ranjan & Das, 2003). The primary focus of the current analysis, is not, however, optimal DER placement. Here, we start from the point that we already know the weakest bus in the system, namely, the San Diego bus, which is fed by two long lines that transfer power from the system all the way down to the local loads in San Diego. Thus, we focus rather on how adding a TIGER station at the weakest bus affects the system's voltage stability. Though several other papers have already evaluated this subject, few have compared the effects of different operating power factors on voltage stability. Besides, in this work, we also consider pure reactive power injection. The SONGS system was divided into two regions. One region is considered the "Source" (all buses upstream San Diego) while the other is considered the "Sink" (San Diego) and several steady-state power flow simulations were carried out increasing the amount of power transfer between the injection groups until the system in each case reached the point of voltage collapse. The power transfer increase is determined by an increase in the load at the San Diego bus and a corresponding increase in generation from the system slack bus (within the Source).

For each simulation, the system bus voltages are plotted against the system total power Shift as defined by Equation (43) i.e., the amount of power the Source injection group added to its normal operation, ΔP, to meet San Diego load growth plus the added power losses, $\Delta Losses$.

$$Shift = \Delta P + \Delta Losses\ [MW] \tag{43}$$

These results are usually plotted in what is known as a P-V curve analysis, where the maximum Shift obtained before the point of voltage collapse is of particular interest. A higher maximum shift implies that more power can be transferred from Source to Sink before the voltage collapses, and is associated with a more stable system.

The scenarios simulated in these analyses include (1) Base case (no TIGER), (2) one 100 MW (unity power factor), (3) one 70 MW /70 MVar (0.7 leading PF), and (4) one 100 MVar (pure reactive power injection) TIGER stations placed solely at the San Diego bus (Bus 13). Figure 3.6

illustrates the P-V curves for all system buses and Figure 3.7 provides a comparison between the P-V curves for the San Diego bus for each of the scenarios. The obtained values for Maximum Shift, Maximum Load, and Initial Voltage at the San Diego bus are summarized in Table 3.3.

Table 3.3 – P-V analysis summary: San Diego bus Maximum shift, Maximum Load Growth, Initial voltage, and Total System Losses.

Scenario	Maximum Shift (MW)	Max load at San Diego (MW)	Total System Losses (MW)	Initial Voltage (p.u.)
Base Case	790	1,400	90	0.925
Unity PF	900	1,500	100	0.937
0.7 leading PF	930	1,525	105	0.957
Pure reactive power injection	880	1,450	130	0.958

In the Base Case, without any TIGER station support, a maximum shift of 790 MW is achieved, which means that the system voltages remain stable (the solution converges) even if the loads at the San Diego bus increased from 700 MW to 1,400 MW, which is a 700 MW load growth plus 90 MW in line losses. For a 100 MW TIGER station operating at unity power factor, the maximum shift increases to 900 MW, and, as expected, this means that the system can accommodate 800 MW of load growth at San Diego up until 1,500 MW, plus 100 MW in line losses. The maximum shift can be further increased to 930 MW if the TIGER station is operated at a leading 0.7 power factor and the load that can be accommodated slightly rose to 1,525 MW, which implies an 825 MW load growth, noting that when a combination of active and reactive power is involved, the load growth is not just the linear addition of initial load and TIGER station local active power injection. We attribute this to the positive effect reactive power injection has in supporting voltage: the initial terminal voltage at the San Diego bus is improved from 0.937 p.u. (unity PF) to 0.958 p.u. (0.7 leading PF). Thus, an increased Maximum Shift is allowed before the voltage collapses. The same voltage benefit is observed when the TIGER station injects purely reactive power. However, as discussed in the previous section, this scenario comes at the expense of increased line losses, which will offset the voltage benefits and reduce the Maximum Shift achieved in this scenario to 880 MW, the lowest of all TIGER scenarios.

In summary, the potential for a TIGER station operating with a leading power factor of 0.7 for enhancing the system voltage stability is higher than that for a TIGER operating with a unity power factor. Also, pure active power operation demonstrated the smallest improvement in voltage stability.

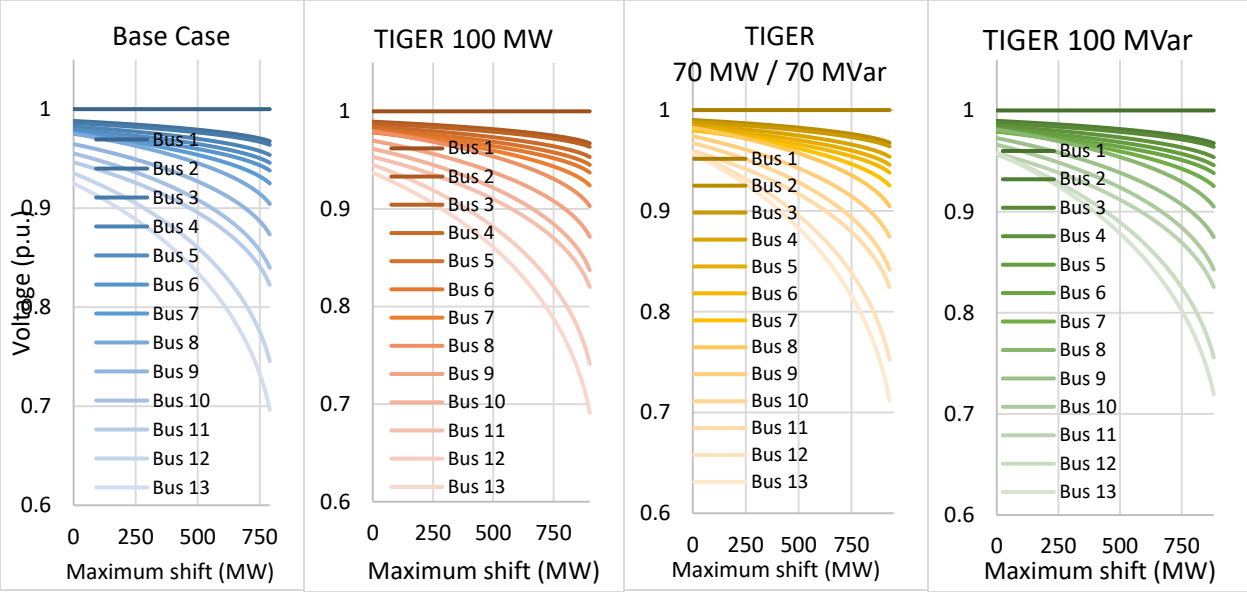

Figure 3.6 – P-V curves for TIGER @ San Diego - variable power factors

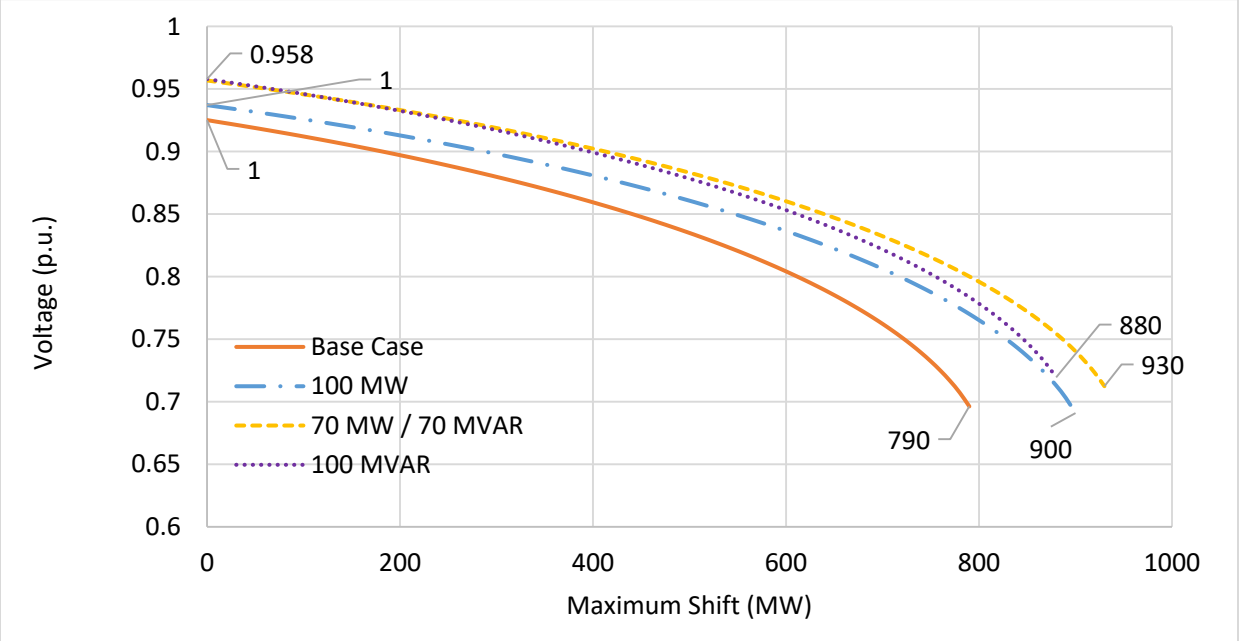

Figure 3.7 – P-V curve at San Diego bus

3.4. Summary

This chapter evaluated how baseload DER, such as TIGER stations, large-scale fuel cells integrated at transmission substations, affect voltage profiles, line losses, and voltage stability of a system affected by the loss of a significant part of its power generation. The Southern California SONGS system was used as a case study; nonetheless, we regard this analysis to be

representative of similarly constrained systems. One of the major distinguishing features of this analysis is that several other studies have investigated the impacts of distributed generation in transmission systems, but few have analyzed inverter-connected DER capable of operating within a range of power factors.

As seen from the results, the installation of only three TIGER stations operating at 70 MW/70MVar or 100MVar each was able to maintain voltages throughout at 0.98 p.u. or above, when it otherwise had dropped to near 0.92 p.u. when the 2.0 GW nuclear plant went off-line. Moreover, the deployment of a single TIGER station operating at 70 MW/70MVar or at 100 MVar was able to maintain voltages throughout at 0.95 p.u. or above.

Regarding baseload DER impact in voltage profiles, we found that:

- The location that best contributes to an overall voltage improvement is at the bus with the lowest voltage. There are also diminishing returns in the system voltage improvement per MW of TIGER stations deployed.
- In systems with long lines, reactive power injection is, in fact, more effective to raise voltage profiles than active power injection. The combined active/reactive power injection scenario is found to be most attractive for voltage regulation; thus, the 0.7 leading PF case shows an overall better voltage regulation for the entire system.

Concerning line loss reductions, we found that:

- There is a clear trend of diminishing returns in loss reduction per MW of local generation installed. Thus, line loss reduction and DER size do not scale linearly.
- The best locations proved to be the weakest points in the system, i.e., at buses with the lowest terminal voltages, as opposed to the buses with the highest loads.
- As expected, when operating at a leading power factor, i.e., injecting reactive power, the resistive losses increased.

Finally, in terms of voltage stability:

- The potential for a TIGER station operating with a leading power factor of 0.7 for enhancing the system voltage stability is higher than that for a TIGER station

operating with a unity power factor, while pure active power operation demonstrated the smallest improvement in voltage stability.

4 Steady-state power flow analysis of the impacts of large solar PV deployments in an urban power system

Highlights

- A novel, real-world urban community microgrid test case is developed from site surveys of the existing urban infrastructure
- Large PV deployments (the economically-optimal) overload most of the transformer infrastructure, from up to 400% of existing rated capacity.
- Limiting PV adoption to not overload the existing transformer infrastructure also avoids overvoltage deviations above 1.02 per unit.

The primary objective of this chapter is to describe the development of a power system test case that is representative of a real-world urban community microgrid. We then use this test case to identify potential challenges associated with large-scale PV deployments into this system

A neighborhood in Huntington Beach, CA known as Oak View and illustrated in Figure 4.1, is chosen for this purpose. The test case is then modeled in a steady-state load flow software. Worst-case steady-state load flows are simulated for peak load operation and for the following PV deployment scenarios: (1) High-Penetration (optimal) PV, which deploys the optimal solar PV capacity that minimizes cost over the project lifetime (2) Realistic PV (transformer-constrained), which represents a scenario where PV deployments are constrained by transformer size and local demand. (3) High-Penetration (optimal) PV +battery energy storage and smart-inverter, which adds to scenario 1 distributed battery electric energy storage systems and smart inverters capable of reactive power compensation.

From the characterization of the Oak View power system until the test case and steady-state model development and finally, the result analysis, a significant understanding of challenges on grid integration of PV in high-penetration was obtained. Below is a summary of the significant results and findings.

The worst reverse power flow event occurs on a sunny weekend in spring, where temperatures were mild, and load demand is lower. For this specific test case, the worst-case RPF occurred during the Easter Sunday of April 2015, at 1:00 PM.

There are locations in the feeder more prone to challenges in hosting DER. As seen from the results, impacts on the 66 kV level are negligible, *i.e.*, no 66 kV feeders or substation transformer is overloaded nor registers over voltage problems. Moreover, over voltages and transformer overloads are, in general, more likely to occur at the lower voltage 480V, 277 V, 208 V or 120/ 240 V level, at the secondary buses. Additionally, over voltages are exacerbated as PV is deployed further away from the substation. Line overloads are more likely to happen at the head of the feeder (closest to the substation) since at this point all the RPF currents from radial branches add up.

Judiciously siting the DER can be challenging, especially given the discrete nature of the power and energy ratings at which DER components (PV panels, battery storage, transformer, and feeders) scale-up. The analysis approach of this chapter points to the lack of an integrated tool to optimize the DER size and siting while considering system dynamic (time-series) operation and the resultant power flows, voltages, and branch currents at the electric grid network and related infrastructure. The integration of these constraints in the DER allocation problem formulations is essential for a practical and comprehensive hosting capacity evaluation, especially when including battery storage and smart inverters. Ideally, the optimization suite would simultaneously account for all constraints and compute a unique final solution.

The results from this chapter provide key insight into how a high-penetration of solar PV in an urban power system negatively affects utility equipment, especially transformers. These results inspired the further development of this work regarding the devising of additional constraints often overlooked in typical optimal DER allocation analysis. These extra constraints aim to limit the reverse power flow at the transformer level (limiting the total apparent power injection at that node). These novel constraints applied to transformer nodes are discussed in Chapter 5

Additionally, results from this chapter regarding how voltage excursions are another major limiting factor to large PV deployments, point to the need of a linearized power flow formulation (that is also suitable for meshed networks) to accurately describe (and limit) the impact of these deployments. Chapter 6 describes the development of a linearized decoupled power flow formulation that can be integrated into a MILP for DER optimal allocation.

The following sections of this chapter provide details concerning the test case and steady-state power flow model development, the design scenarios studied, and the results obtained.

4.1. Test Case

The Oak View community has over 300 buildings, of which, 280 are multi-family homes. Remaining buildings are destined for commercial and industrial activities, including a waste processing facility, small commercial shops, a large manufacturing facility, a primary and an elementary school, a community center, and a public library.

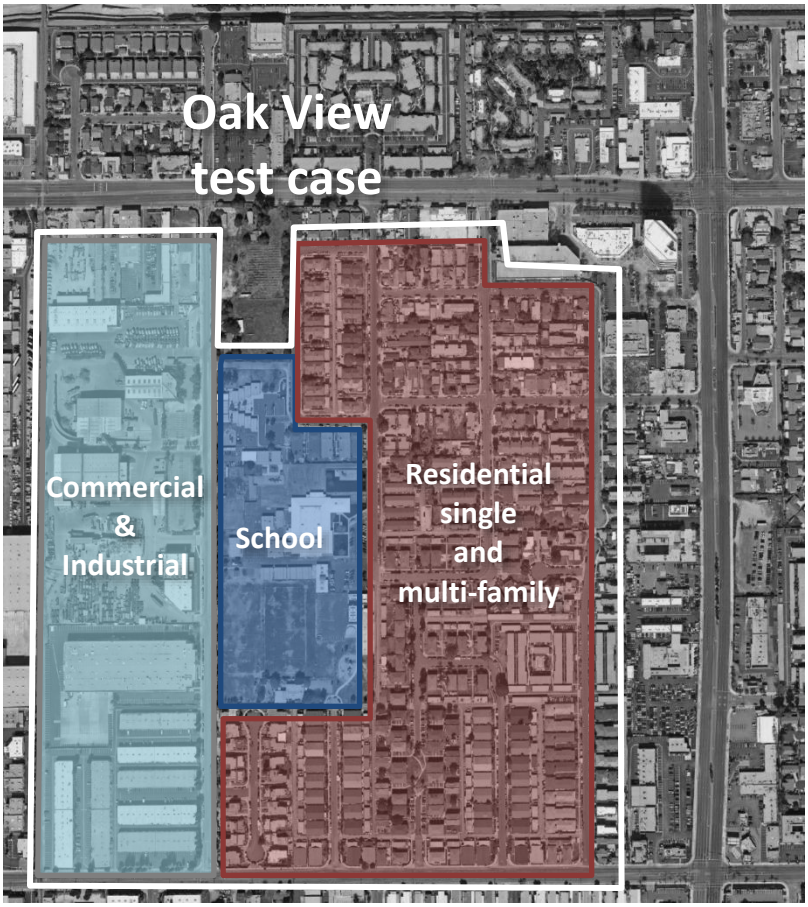

Figure 4.1 – Oak View community, used as the test case, and its different building sectors: Commercial and Industrial, School, and Residential

4.1.1. Power system characterization

An extensive survey to characterize relevant substations and circuits surrounding Oak View was performed using a tool provided by the local electricity utility, the DERIM (Distributed Energy Resources Interconnection Map) *ArcGIS*© database (Southern California Edison (SCE), 2016b). DERIM provides the precise geographical location of sub-transmission and distribution substations and circuits throughout the utility's service territory.

4.1.2. 66/12 kV substation (Ocean View)

Oak View is powered by two 10 MVA transformers at the Ocean View substation, which step-down voltage from the 66 kV sub-transmission to the 12 kV distribution voltage level (Southern

California Edison (SCE), 2016b). Figure 4.2 shows an aerial view of the Ocean View substation obtained from *Google Earth Pro*© (Google Inc., 2017).

Figure 4.2 – View of Ocean View Substation from Google Earth.

4.1.3. 66 kV sub-transmission circuits and neighboring substations

Five 66 kV sub-transmission circuits create a network between Ocean View and six other neighboring 66/12 kV substations: Ellis, Bolsa, Barre, Trask, Brookhurst, and Slater. Figure 4.3 illustrates these feeders and respective lengths, measured using a Google Earth toolbox.

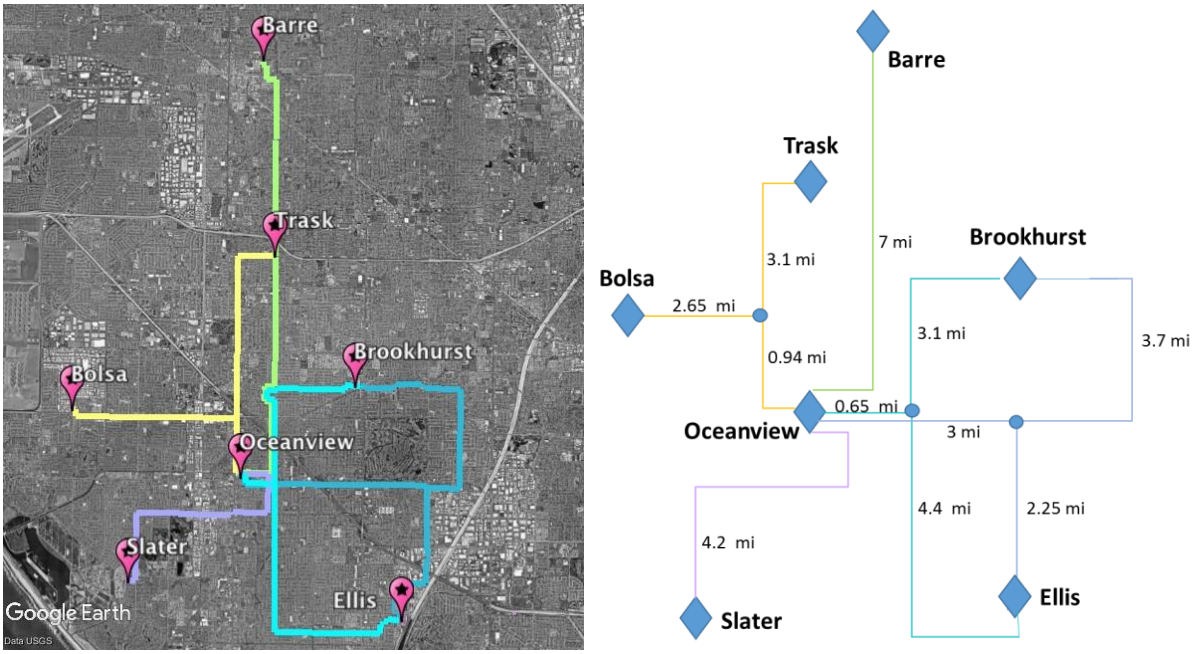

Figure 4.3 – 66 kV circuits from Ocean View substation. Source: DERIM circuits exported to Google Earth

4.1.4. 12 kV distribution circuits (from Ocean View)

Seven 12 kV distribution circuits originate from Ocean View and deliver electricity to Oak View and the surrounding area (Figure 4.4). They are named Smeltzer, Bushard, Beach, Bishop, Heil, Standard, and Wintersburg. The Oak View residential customers are fed by Smeltzer 12 kV, and a few north-west commercial customers are fed by Standard 12 kV.

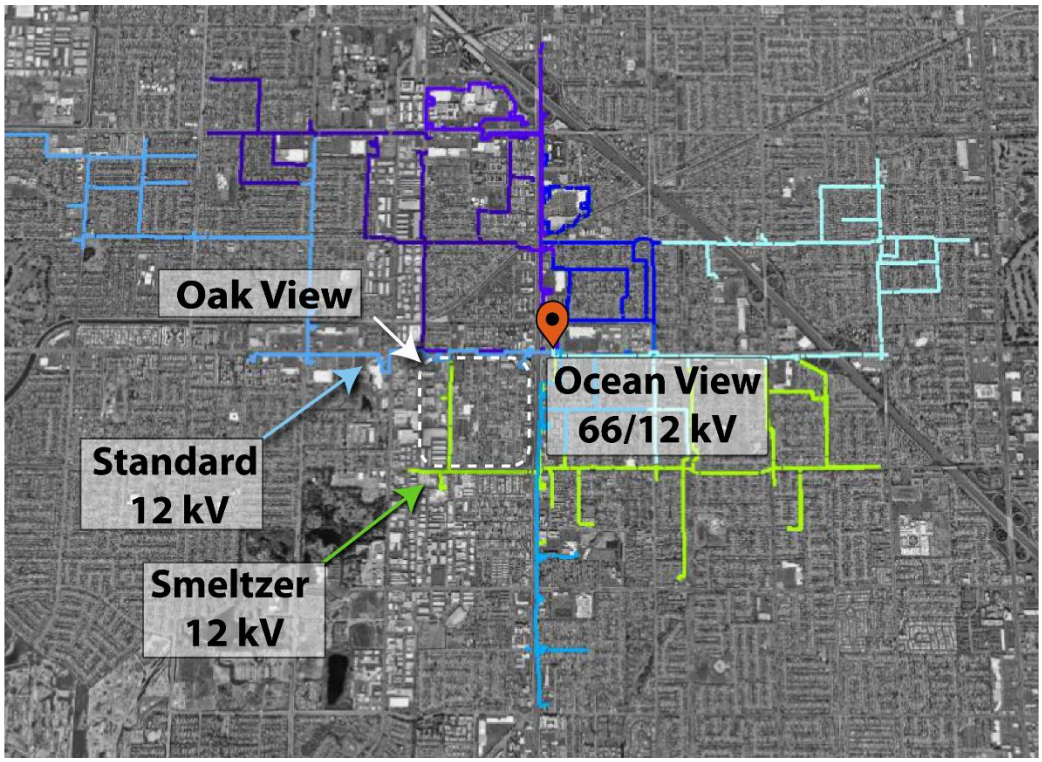

Figure 4.4 – 12 kV circuits from Ocean View Substation. Source: DERIM circuits exported to Google Earth.

4.1.5. Service transformers and low voltage distribution circuits

At the time of model development, not all circuit branches that serve Oak View were mapped in DERIM. Thus, the remaining 12 kV circuit branches that originate from both Smeltzer and Standard feeders were identified through a site survey. Figure 4.5 shows these branching circuits in pink. The Smeltzer and the Standard circuits (as mapped in DERIM) are shown in lime green and light blue, respectively. The pink branch circuits terminate on the primary side of distribution service transformers, which are either pole-top, pad-mounted, or underground, depending on the customer type, load, and service voltage.

The local distribution transformer infrastructure used in Oak View was also identified through a site survey. Examples of pole-top and pad-mounted transformers are illustrated in Figure 4.6. In total there are 35 single-phase service transformers, which feed the residential loads and 14 three-phase service transformers, which feed the school, commercial, and industrial loads. Figure 4.5 identifies and maps all transformers.

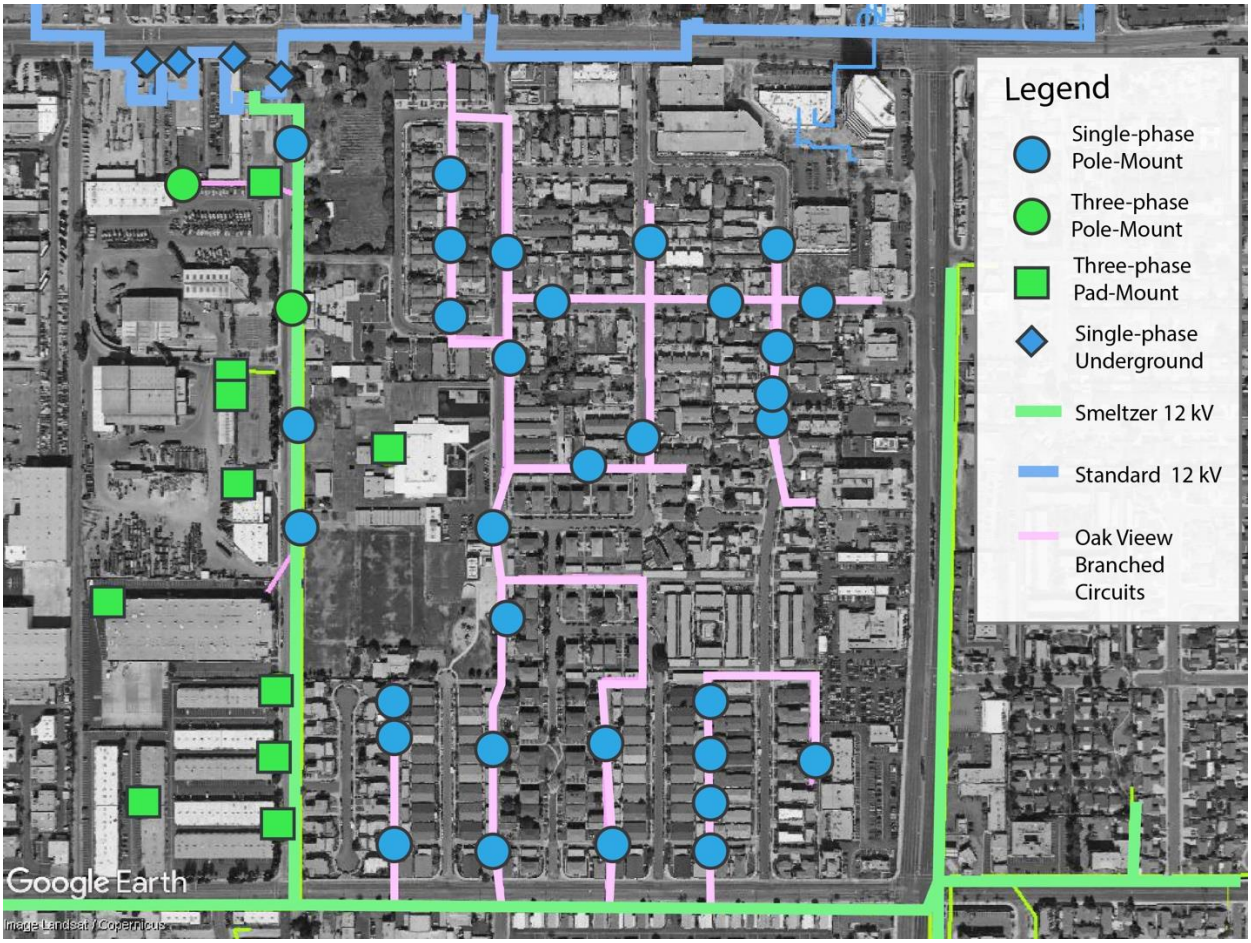

Figure 4.5 – Oak View circuits and Transformers. Source: DERIM circuits exported to Google Earth.

(a) (b)

(c)

Figure 4.6 – Oak View pole-top service transformers (a) single-phase 25 kVA (left) (b) three-phase 75 kVA pole top (right) (c) three-phase 300 kVA pad mounted.

Transformer voltage and load ratings were determined through communication with SCE distribution city planners, and through site visits. The transformer rated parameters are shown in Table 4.1, which also shows the estimated maximum and minimum loads aggregated by each transformer. These loads were estimated by first calculating total annual building energy consumption using Energy Use Intensity (EUI) surveys kWh/ft^2 multiplied by building areas surveyed on *Google Earth*. The national EUI surveys used as reference include the Residential Energy Consumption Survey (RECS) (EIA n.d.), the Commercial Buildings Energy Consumption Survey (CBECS) (EIA n.d.), and the Manufacturing Consumption Survey (MECS) (EIA n.d.). Full details on building demand modeling are presented in Brouwer *et al.*(R. Flores et al., 2018). Since in this analysis we are interested in power flows, not energy totals, once the estimated energy consumption is calculated, a "flat" (average) load profile is obtained by dividing the annual energy total by 8,760 hours/year. Then, a peak and valley factor, calculated based on the DOE synthetic load profiles, are applied to these profiles to determine the minimum and maximum hourly demand.

Table 4.1 – Oak View transformer infrastructure – voltage and power ratings, and maximum/ minimum loads fed by a transformer

#	Customer	Voltage	Max Load (kVA)	Min Load (kVA)	Rating (kVA)
Single-Phase					
1	Residential	120/240	19	10	25
2	Residential	120/240	15	9	25
3	Residential	120/240	15	8	25
4	Residential	120/240	14	8	25
5	Residential (Solteros Apt.)	120/240	39	22	100
6	Residential	120/240	37	21	50
7	Residential	120/240	37	20	50
8	Residential	120/240	36	20	50
9	Residential	120/240	25	14	100
10	Residential	120/240	43	24	50
11	FRC + Lib.	120/240	31	17	37.5
12	El School	480, 120/240	14	11	75
13	Residential	120/240	12	7	15
14	Residential	120/240	31	17	50
15	Residential	120/240	29	16	50
16	Residential	120/240	42	23	50
17	Residential	120/240	22	12	25
18	Residential	120/240	23	13	25
19	Residential	120/240	40	22	50
20	Residential	120/240	29	16	50
21	Residential	120/240	19	11	50
22	Residential	120/240	9	5	15
23	Residential	120/240	12	6	15
24	Residential	120/240	25	14	37.5
25	Residential	120/240	48	27	50
26	Residential	120/240	27	15	37.5
27	Residential	120/240	76	42	100
28	Child Day Care	120/240	9	5	15
29	Discount Tire	120/240	20	18	25
30	El School (East)	120/240	17	13	25
31	Residential	120/240	57	32	75
32	Residential	120/240	54	30	75
33	Residential	120/240	38	21	50

34	Building Materials	120/240	32	12	75
35	WILLY'S Auto	120/240	50	18	75
3-Phase					
1	Ind. Offices	120/208	50	18	75
2	Ind. Offices	120/208	101	36	150
3	Ind. Offices	120/208	101	36	150
4	Ind. Offices	120/208	142	51	150
5	Zodiac	480Y/277	838	302	1500
6	Pre-School	120/208	34	12	75
7	El School	480Y/277	94	52	300
8	El School	480/208Y,120	20	16	75
9	Republic 1	480Y/277	121	43	150
10	Republic 2	480Y/277	23	8	50
11	Republic 3	480Y/277	326	117	350
12	Republic 4	480Y/277	69	25	100
13	Republic 5	480Y/277	117	42	150
14	HBC + Disc Tire	120/208	114	41	150

4.1.6. Current generation and projected load

The DERIM database (Southern California Edison (SCE), 2016b) provides information on the current existing generation and projected (2018) load at the substations and 12 kV feeders as well as feeder lengths.

Table 4.2 – 66/12 kV Substations – Existing generation and projected load [16] .

Substation (66/12 kV)	**Total Existing Generation (MW)**	**Projected Load (MW)**
Ocean View	3.13	49.20
Barre	3.35	75.50
Brookhurst	3.30	44.80
Bolsa	2.90	40.00
Ellis	3.95	42.50
Slater	4.42	50.50
Trask	5.58	86.10

Table 4.3 – 12 kV Feeders – Existing generation and projected load [16].

Feeder (12 kV)	Total Existing Generation (MW)	Projected Load (MW)	Length (mi)
Smeltzer	0.39	7.77	6.29
Standard	0.40	9.37	2.98
Bushard	0.63	8.25	6.13
Beach	0.12	3.56	2.76
Bishop	0.08	7.96	2.7
Heil	0.66	6.46	4.25
Wintersburg	0.84	8.93	4.1

4.2. Model development and assumptions

A steady-state power flow model was developed in ETAP© (Operation Technology Inc., 2017), which is a commercially available power flow software. ETAP utilizes iterative numerical solver methods to solve the traditional power flow problem, as defined in (Grainger & Stevenson, 1994). The load flow results are nodal voltages, currents, and branch active and reactive power flows. ETAP has a graphical interface that offers a quick and easy development platform for modeling spatially-resolved electric circuits. Moreover, it specifies the exact circuit location of any voltage or rated power capacity limits violation.

The dashed lines of Figure 4.7 define the geographical boundaries that are assumed for this analysis. The model starts at the high voltage sub-transmission level (66/12 kV) and comprises the 66/12 kV neighboring substations, 12 kV feeders, and the Oak View community test case. Figure 4.8 illustrates the one-line diagram of the model in the ETAP environment. Thus, the Oak View test case is a sub-network (highlighted in pink) connected to the main-area electric grid network.

To model the current load and generation at each 66/12 kV substation and 12 kV feeder, default load and generator ETAP “blocks” are connected to each substation. The load and generation magnitudes are based on the current generation and projected load values from DERIM (Table 4.2 and Table 4.3, respectively

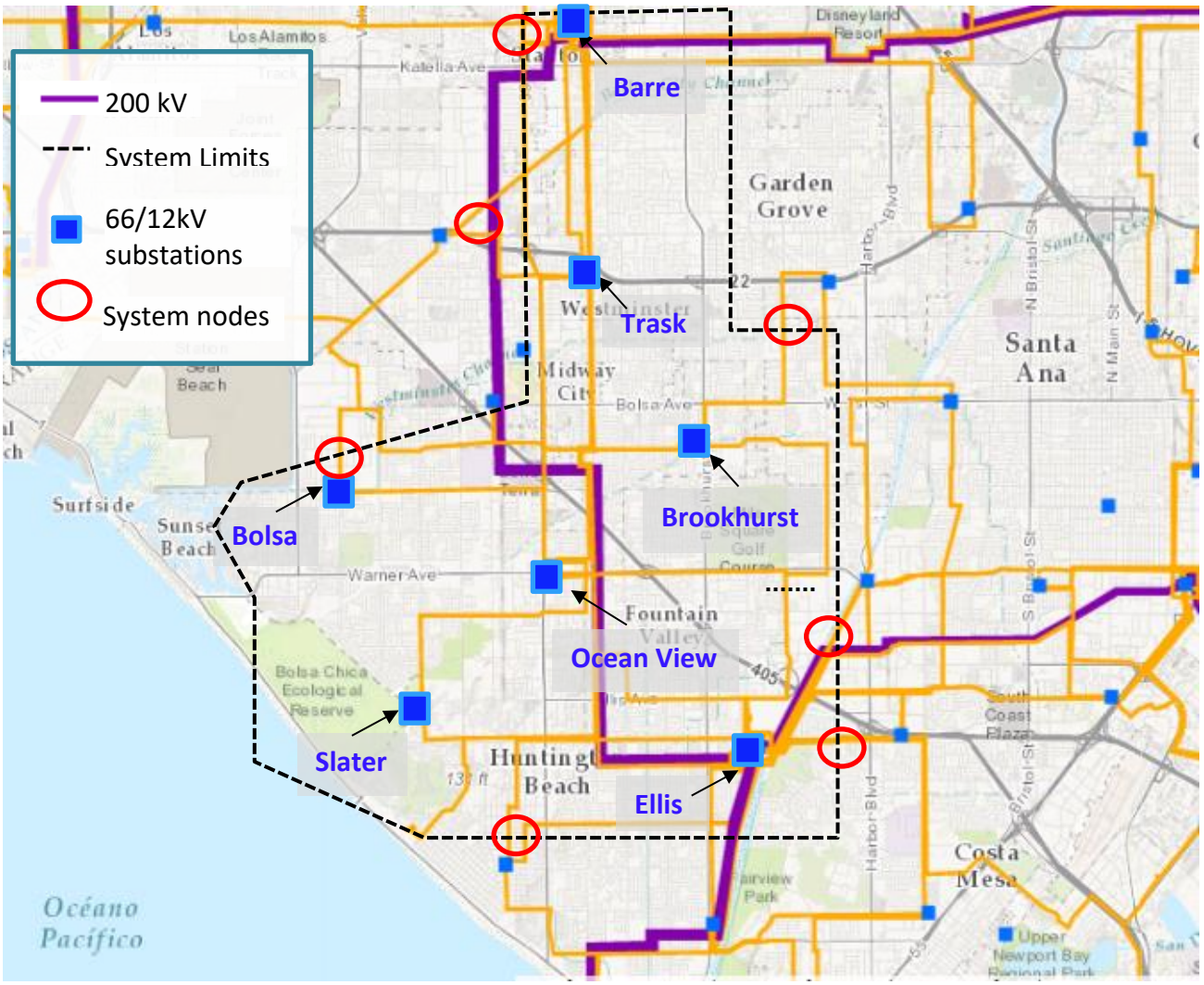

Figure 4.7 – Power Flow system boundaries geographical location of substations, 66 kV, and 12 kV lines. Source: (Southern California Edison (SCE), 2016b)

The base values used for the per-unit calculations are S_{base} = 100 MVA, V_{base} = 230 kV, thus using equations (44) and (45) (Grainger & Stevenson, 1994), it follows that Z_{base} = 529 Ω, and I_{base} = 251 A.

$$Z_{base} = \frac{V_{base}^2}{S_{base}} \quad (44)$$

$$I_{base} = \frac{S_{base}}{\sqrt{3}V_{base}} \quad (45)$$

The boundaries of the system are the 230 kV buses at Bolsa, Trask, Barre, Brookhurst, Ocean View, Ellis, and Slater, as shown in Figure 4.7. These points are modeled as Thevenin equivalent

reactances, assuming a short circuit duty of 50 kA at all substations. For these boundary lines, the short circuit impedance values used are Z_{pu} = 0.0023.

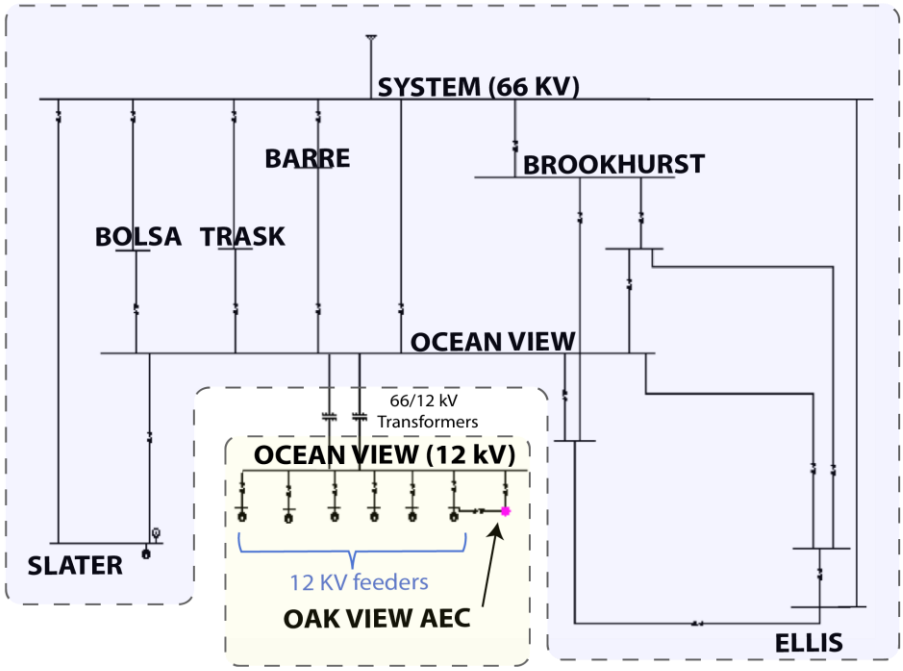

Figure 4.8 – High voltage 66/12 kV one line

For the low voltage Oak View model, we limit our analysis to one single circuit. Therefore, without loss of generality, we combined Standard and Smeltzer circuits by adding loads from Standard at the end of Smeltzer (nodes 38, 44, and 28, as shown in Figure 4.9.

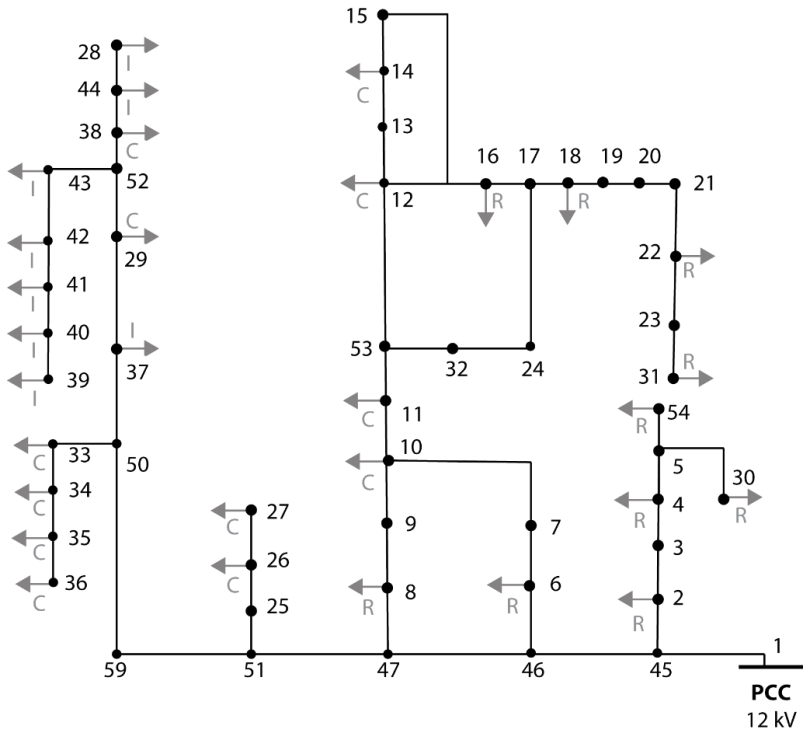

Figure 4.9 – Oak View test case low voltage system network graph. Triangles represent load clusters connected to transformer nodes. Load types are residential (R), commercial (C) and industrial (I).

4.2.1. Loads and PV systems

4.2.2. Residential

For modeling residential systems, the three-phase 12 kV overhead distribution feeders are converted into a single-phase, three-wire (two lines and one neutral, known as split-phase) connection. Utilities alternate between the phases used in these connections: AB, BC, or CA, to avoid load unbalances. The same approach is used in this chapter.

In the split-phase configuration, the service transformers' secondary winding is center-tapped (each section has the same number of windings, and consequently, the same voltage) and the center tap is connected to a grounded neutral. In this flexible wiring configuration, there are two output secondary voltages: 240 V between the two hot phases (L1 and L2) and 120 V between one phase and the neutral (center tap), in other words, the phase, (or line-to-ground) voltage is half the line-to-line voltage. This configuration is useful in a residential application since lights and small plug loads are connected to 120 V, while large appliances such as air conditioners,

dish, and clothes washers, and dryers, are connected to 240 V. A wiring diagram for this type of connection is shown in Figure 4.10.

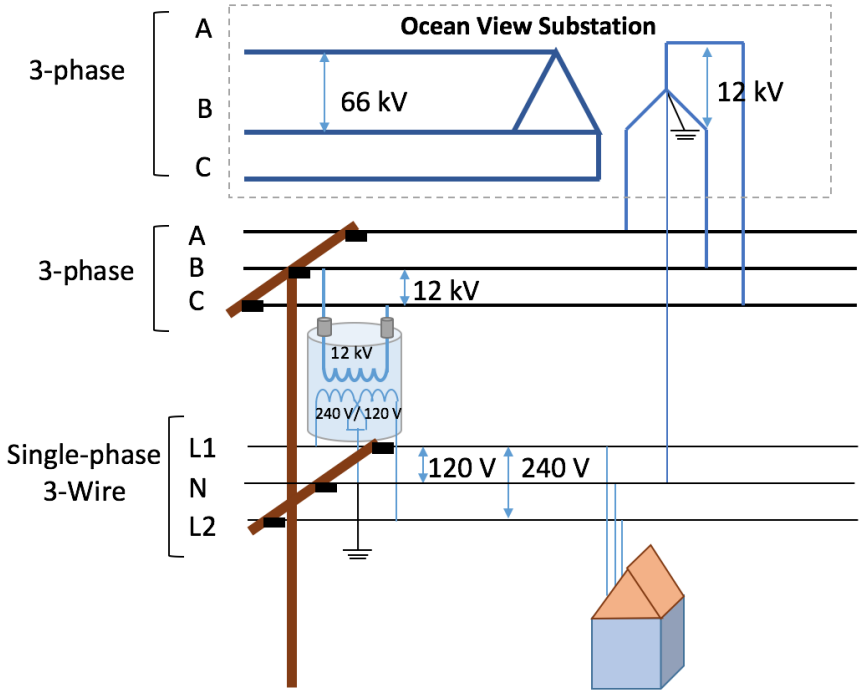

Figure 4.10 – Wiring diagram for sub-transmission and distribution voltages.

Figure 4.11 shows the circuit schematics of a typical residential PV installation. The PV arrays are grouped into strings of 10 up to 15 modules and connected in parallel in a junction box. The junction box then feeds the DC side of the inverter (PV+ and PV-). The AC side of the inverter outputs the PV power in a single-phase three-wire (L1, L2, N) connection that ties into the home's main service panel, which is also the point of connection to the distribution grid.

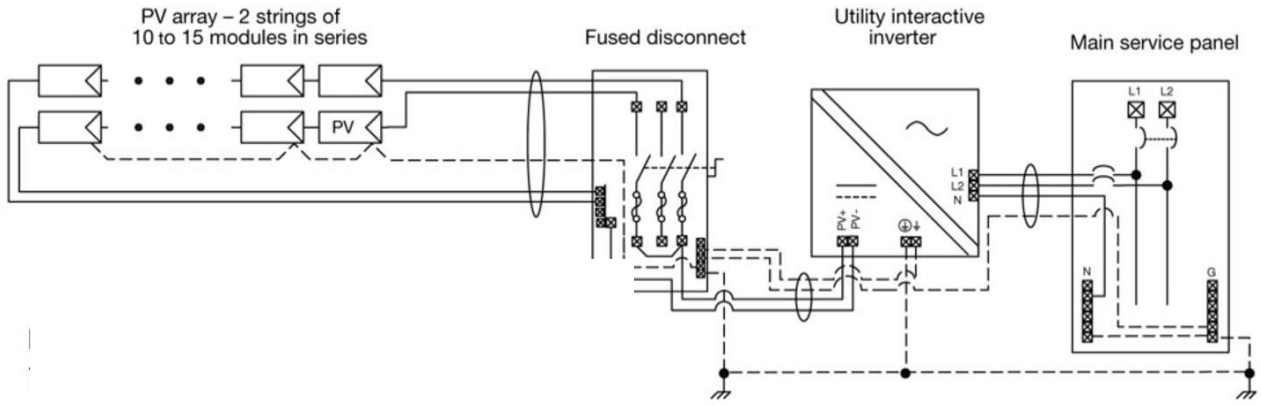

Figure 4.11 – Typical Residential PV installation (Solar Pro & Berdner, 2008)

Due to a limitation on ETAP's solar PV panel and inverter model blocks, which only support three-phase connections, the residential PV installations were modeled as AC current sources. It is expected that this workaround does not affect the accuracy of the steady-state power flow simulations. Nonetheless, this approach still poses the drawback of not having an inverter component explicitly modeled to account for efficiency losses. However, converter efficiencies are usually high (>96%); thus, the expected error is negligible.

Figure 4.12 illustrates a typical residential PV installation modeled in the ETAP environment. The 12kV 3-phase distribution line originates from the 12kV circuit. A phase-splitter splits phases A and B, which is used in the single-phase service. A single-phase transformer transforms the 12kV distribution voltage into the 240/120V residential voltage. In the main service panel, the multi-family building loads are connected in parallel with the PV array, at 240V. The dashed lines enclose the aggregate system, i.e., an aggregation of multi-family building loads and PV arrays, modeled behind each service transformer. All other residential buildings are modeled following this approach.

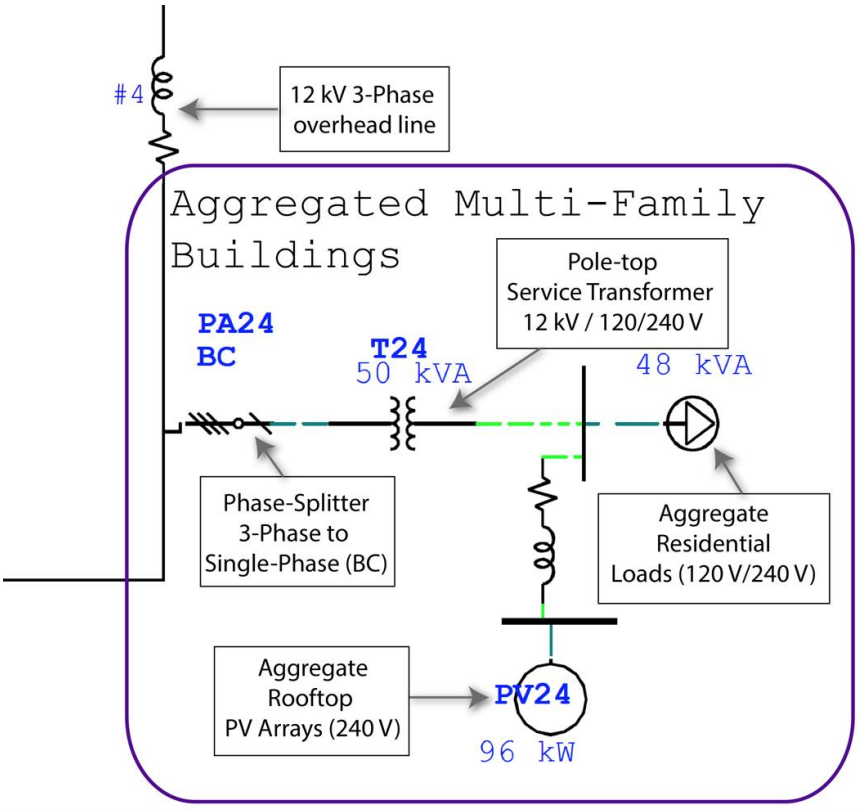

Figure 4.12 – Example of ETAP model for a typical residential installation

4.2.3. Commercial & industrial

Commercial and Industrial (C&I) customers are serviced with three-phase power. The service transformer voltage ratings depend upon customer needs. Typical three-phase voltage levels used by Southern California Edison are 480/277 V for large-scale customers and 120/208 V for smaller-scale customers. Figure 4.13 illustrates a typical C&I installation modeled in ETAP. The three-phase transformer steps down the voltage from 12 kV to 480/277 V in a wye configuration. A three-phase load is connected to the secondary of the transformer, and on the same bus, the three-phase inverter and PV array system are also connected. A central inverter approach is used for the PV installation.

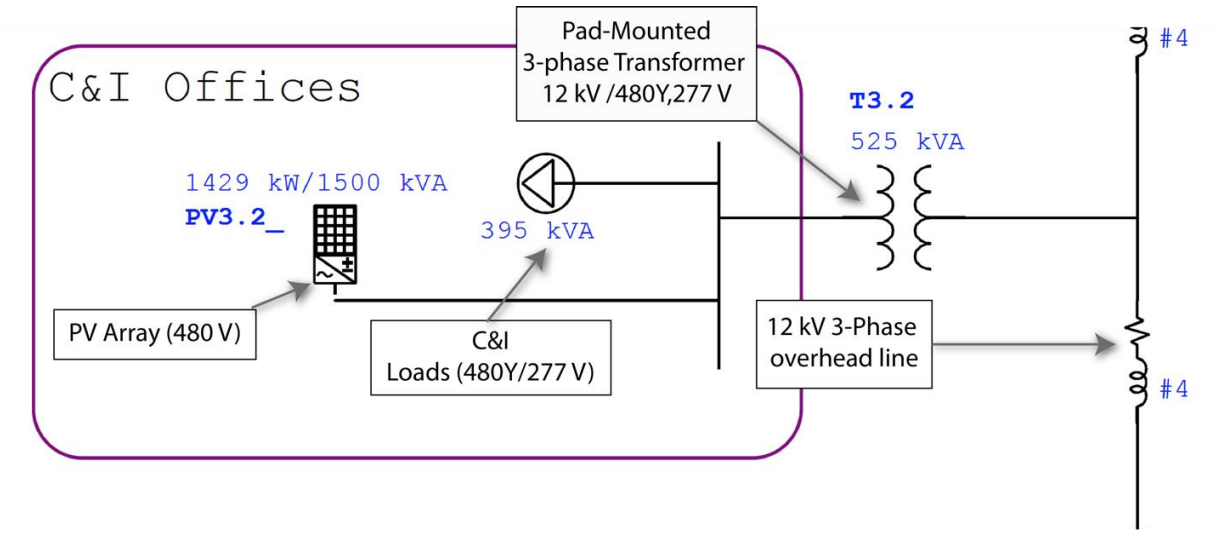

Figure 4.13 – Example of ETAP model for a typical C&I installation

4.2.4. Conductor sizing

The conductor American Wire Gauge (AWG) sizing methodology followed the recommendations made in the National Electric Code (NEC) (National Fire Protection Association (NFPA) n.d.). Section 222.5 regulates that overhead spans serving 1,000 V and above shall not be smaller 4 AWG, for bare aluminum conductors on air. Moreover, Section 230.23 regulates that for service spans, the conductors shall not be smaller than 6 AWG aluminum.

Hence, for the three-phase 12kV lines, 4 AWG is used, while for the 240/120V service connections, 6 AWG is used. The sizes of the conductors are shown in Figure 4.12 and, right next to the respective conductor (shown as "#6" or "#4). Nonetheless, there are instances where the wire AWG was increased to accommodate a local load demand that would create a circuit overload condition for that specific branch. For the PV AC output, three conductors are used, one for each phase (A, B, and neutral). These conductors provide the thermal limit for the PV power flows.

4.2.5. Worst-case reverse power flow

A reverse power flow condition is created when the PV generation surpasses the local load, resulting in power flowing from the local PV node towards the upstream distribution system. The worst reverse power flow event occurs typically on sunny, cold days in spring, particularly on

weekends, when the load is even lower. RPF causes the voltages at the substation and local nodes to rise above nominal 1 p.u.

The worst-case steady-state simulations in this chapter simulate the system at the worst-case RPF since it is the operation point that limits the system voltage-based hosting capacity. To identify the exact time in the year when the worst-case RPF happens, an "RPF Factor" was calculated; The maximum value of the RPF Factor indicates the time where worst-case RPF happens.

For calculating the RPF we assumed a real-world times-series aggregated demand profile for a distribution substation in Southern California and a normalized hourly PV generation profile, obtained from a PV system installed in at UC Irvine. For each hour of the year, the load demand was subtracted from the PV generation. The worst-case RPF happens during Easter Sunday, on 04/05/2015 at 1:00 PM. Figure 4.14 shows how the load demand on Easter Sunday was much lower compared to the rest of the year, this can be attributed to the mild temperatures in spring, which reduces the need for AC cooling, and also the fact that it was a holiday. Moreover, by observing Figure 4.15, during this same day there was significant PV generation during compared to the rest of the year, typical of clear sunny spring days. Therefore, 04/05/2015 at 1:00 PM is the snapshot in time chosen for all worst-case steady-state simulations in this analysis.

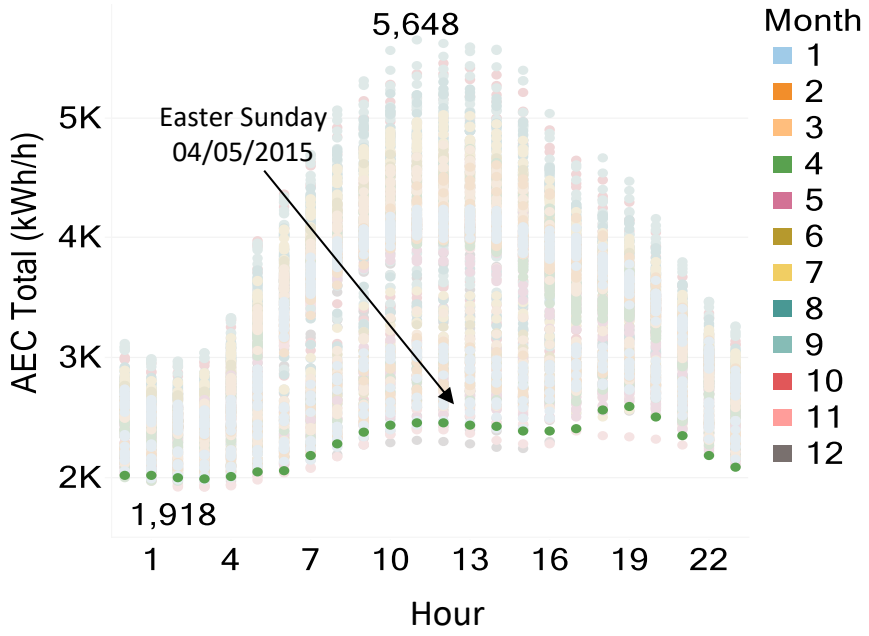

Figure 4.14 – Oak View annual load profile distribution - Highlight shows load profile on 04/05/205 (Easter Sunday). Colors show detail about month

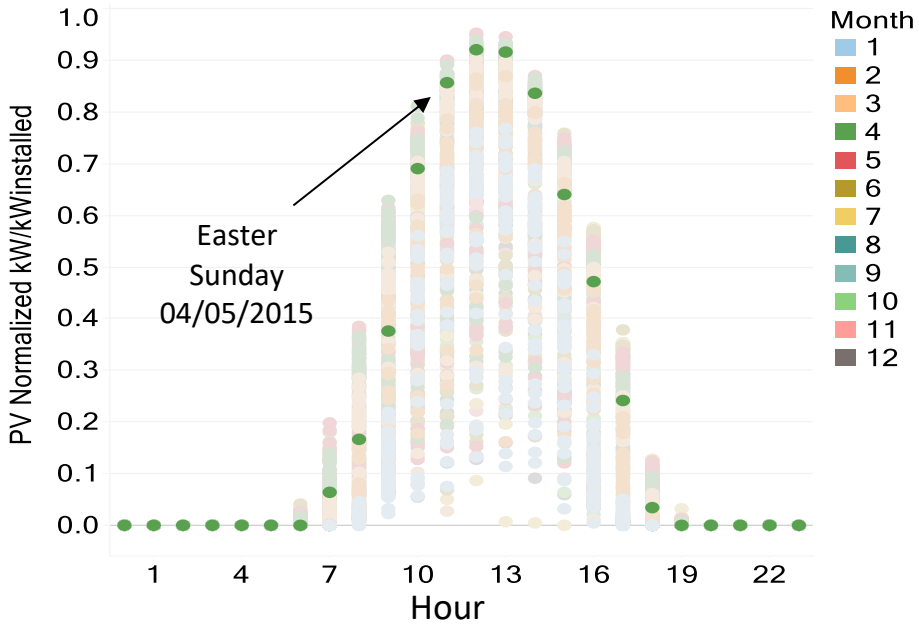

Figure 4.15 – Normalized PV generation profile for a system in Southern California, at UC Irvine. Highlight shows data for Easter Sunday 04/05/2015. Colors show details about month

4.3. Scenarios

Four scenarios were created to represent the real operational conditions of the Oak View test system. Table 4.4 provides a detailed description and goals of each scenario. The Peak load scenario was simulated during the worst-case evening peak, which happened on October 11th, 2015 at 6 PM. The remaining scenarios were simulated during the worst-case reverse power flow as identified in the previous session, which occurred on Easter Sunday of April 2015 at 1 PM.

Table 4.4 – Scenarios simulated in the steady-state power flow model

Scenario Name	**Description**
Peak Load / No PV generation	Simulates a period of high congestion: the residential evening peak demand hour. Oak View loads are modeled as the peak values and PV generation is zero (no generation in the evening).
High-penetration (optimal PV)	Simulates a large PV deployment (8.8 MW), or the optimal amount of solar PV that minimizes the total project lifetime costs (fixed and operational) while meeting operational constraints. The amount of PV deployed is calculated using *Homer Pro*©.

Realistic PV (transformer-constrained)	Simulates a reduced PV deployment (6.3 MW) constrained to avoid transformer overloads and bus overvoltages. the PV array size connected to a given transformer must add up to 90% of the transformer rating plus the minimum load connected to that transformer
Optimal PV + EES + Smart-Inverter	Simulates the optimal PV capacity and also an (oversized) electric energy storage (EES) capacity associated with smart-inverter Var injection function, which can assist the system during the worst-case RPF. This scenario aims to investigate the potential of battery energy storage and smart-inverter technology on improving local power quality; Battery storage aims to remove the worst-case reverse power flow, i.e., charge to absorb excess power, and the smart inverter aims to absorb reactive power (operate at a lagging power factor) to reduce over voltages.

4.4. Results and Discussion

Table 4.5 provides the capacity and voltage ranges, in % of rated capacity and per-unit, taken as marginal and critical. Here, only critical values are considered inappropriate, whereas marginal values are acceptable even though they are not ideal for regular power system operation.

Table 4.5 – Critical and Marginal Limits for Loading and Bus Voltage

	Critical	Marginal
Loading (%)		
Bus	100	95
Cable	100	95
Line	100	95
Transformer	100	95
Generator	100	95
Inverter	100	95
Bus Voltage (p.u.)		
Over Voltage	1.05	1.02
Under Voltage	0.95	0.98

4.4.1. Peak Load

The *Peak Load* scenario provides a validation of the Oak View test case. Its results provide a starting point for any necessary power system infrastructure upgrades, such as transformer TAP settings, reactive power compensation, and adjustments to conductor AWG sizing to remove any critical voltage excursions and cable overloads. These upgrades are made under the assumption that the current real-world system has a good power quality. Thus, 31 MW of distributed capacitor banks were added to the model to correct the low voltages at the terminal buses of the 12 kV feeders originating from Ocean View, as to approximate 1.0 p.u. Also, the TAP of the secondary of a 3-phase transformer, which feeds one of the industrial loads, was increased to 2.5. Moreover, six Smeltzer circuit segments needed to be upgraded from 4 AWG (which is capable of handling 63.4 A, at 12 kV). The circuit segment closer to the Ocean View substation was upgraded to 3/0 AWG to handle a 140 A, at 12 kV incoming current to feed all peak loads. Likewise, five other adjacent segments were upgraded to 2/0 and 1/0 AWG, according to the current flow they needed to handle (averaging 100 Amps).

Figure 4.16 shows the system voltage profile, staring at the 66 kV System node, and all the way down to the Oak View secondary nodes. Buses are ordered by distance from the System node. The 66 kV system operates within the desired voltage margins. The 12 kV system, however, operates mostly below marginal limits. One can notice how under voltages are aggravated as the distance from the System node increases. There were no instances of a transformer or cable overload for this scenario.

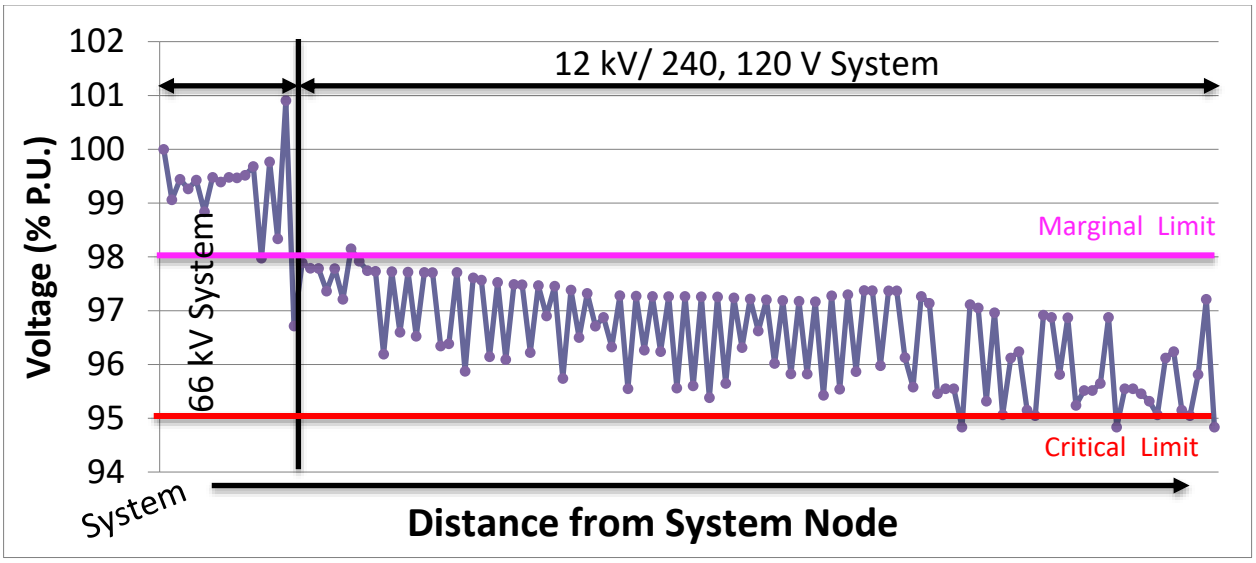

Figure 4.16 – Peak Load Scenario – Voltage Profile for 66 and 12 kV systems

Figure 4.17 illustrates a PV installation in a utility customer bus and highlights a primary and a secondary bus. Primary buses connect to the primary side of the transformers, at the high voltage level (12 kV). Secondary buses are connected to the secondary side of the transformer, at the lower voltage levels (480, 208 V if 3-phase and 240/120 V if single-phase). Utility customer loads are connected to the secondary bus.

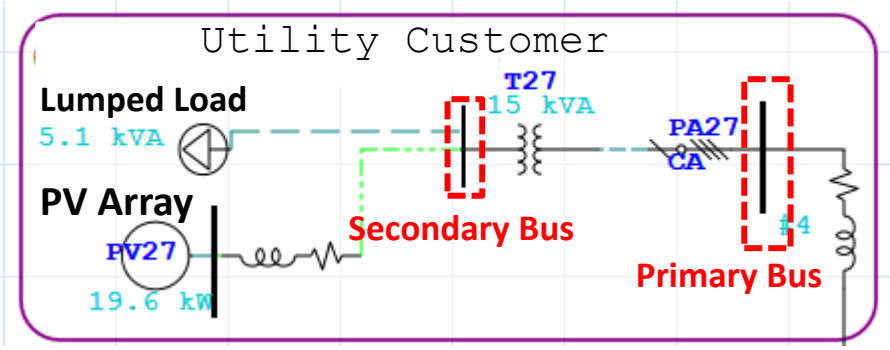

Figure 4.17 – Example of Primary, Secondary (NET) and PV buses at the Oak View test case

4.4.2. High-penetration (optimal PV)

This scenario, in which we will refer to as *Optimal PV*, simulates a large PV deployment, which is the optimal solution to the *DER allocation problem*, *i.e.*, the system size that reducing overall project costs. Our initial attempt to solve the optimal DER allocation problem uses a commercial software for optimal energy systems design, *HOMER Pro*© (HOMER Energy LLC, 2017). The software sizes distributed energy assets for grid-connected or islanded loads to minimize cost.

The user indicates the types of generation technologies intended for the project, the hourly load profile to be met, and the location-specific weather database. A MILP optimization computes the best design, *i.e.*, the DER and inverter capacities to match the direct current power output of the DER systems to the alternating current power load requirements. To analyze the grid impacts of large PV deployments, the DER capacities are judiciously allocated withing the Oak View test case and a steady-state load flow was performed in ETAP.

4.4.3. Optimal set of DER to serve the Oak View test case

Figure 4.18 shows where the Oak view community modeled in HOMER. The system is grid-tied, and the DER are solar PV and battery electric energy storage (EES).

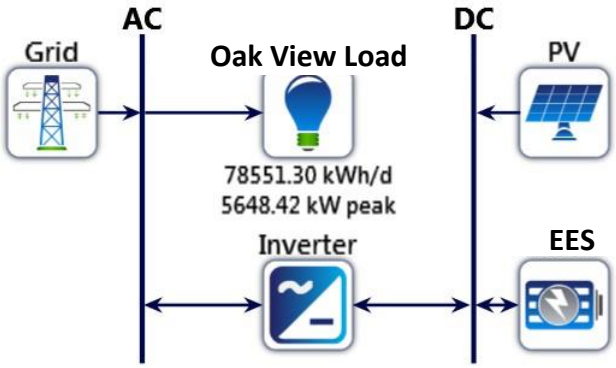

Figure 4.18 – HOMER Pro© *Modeling Environment – Oak View DER assets and connections*

A synthetic load profile is used to represent the aggregate Oak View load (McDonald, 2017)—which includes residential, commercial, and industrial loads. Table 4.6 lists the parameters of the DER technology considered. The electric energy storage chemistry assumed here is Lithium-ion, since the storage needs are short-term and highly-cyclic. Li-ion batteries provide a combination of technical advantages that make them attractive for grid-scale applications, such as a high energy density (~200 Wh/kg), a long lifetime (~10,000 cycles), a high cycle efficiency (85-90%), and a suitable depth of discharge (10%)(Zakeri & Syri, 2015). Besides, the recent growing adoption of Li-ion batteries for ancillary services in improving grid stability and reliability, as well as recent improvements in its manufacturing, materials, and processing is reducing its final levelized cost of energy. A four to one energy to power ratio, *i.e.*, a fully charged EES can be fully discharged at full power for four hours, is assumed. The weather database used is NREL's TMY3, using data from the weather station located in Long Beach (NREL, n.d.). The utility rate structure assumed is the SCE TOU 8-B, and grid exports for revenue are not allowed.

Table 4.6 – DER technology parameters assumptions

Technology	**Manufacturer**	**Unit Size**
PV Panel	Canadian Solar C26X 325P (Solar, 2017)	325 W
EES	Tesla Power Pack 2 (Tesla, 2017)	50 kW/ 210 kWh
Weather Database	TMY3 (NREL, n.d.)	--

Table 4.7 – DER technology cost assumptions

Technology	**Capital ($/kW)**	**Fixed O&M ($/kW/year)**	**Variable O&M ($/MWh)**	**Fuel Cost ($/MMBtu)**	**Lifetime (years)**
Solar PV	2,500	15	N/A	N/A	25
EES	500	22 – 27.50	N/A	N/A	15

Table 4.8 – Oak View test case DER Optimal Design computed by HOMER Pro

Technology	***Ratings/Units***	**Total Energy (kWh/year)**
PV	8,823 kW	14,667,696
EES	62 units	2,705,520
	2,800 kW	
	11,759 kWh	
Inverter	4,129 kW	
Grid Import	4,500 kW (peak)	15,226,784
Grid Sales	Not allowed	0
Excess Electricity (Curtail)	451,153 kWh	
Net Grid Purchases	15,226,784 kWh	

Figure 4.19 shows the dynamic operation of the DER optimal design as computed by HOMER Pro. The following observations can be made:

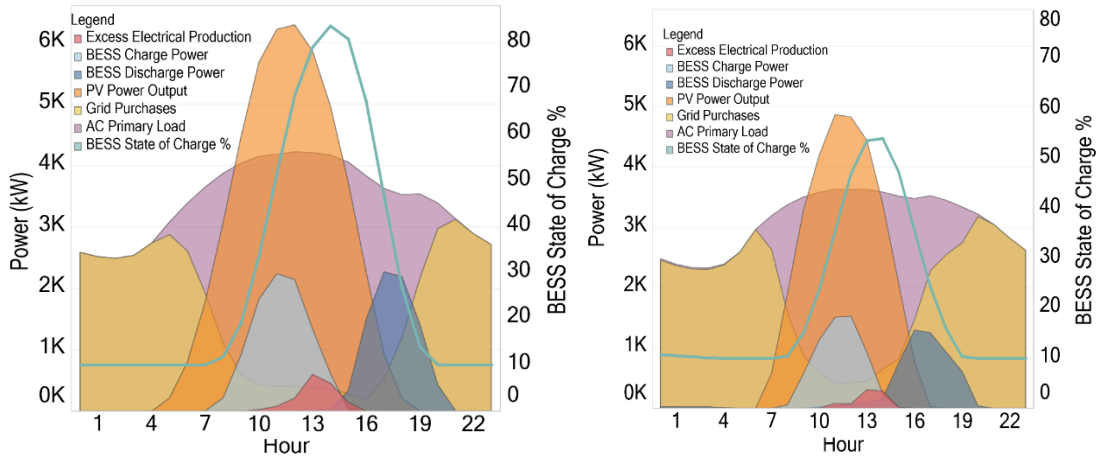

Figure 4.19 – Oak View hourly dynamics in summer (left) and winter (right). BEES = battery energy storage.

- The EES charges daily with solar PV generation. It also discharges daily to meet the evening peak demand. The EES performs a complete cycle (charges and discharges fully) daily.
- There is some excess solar PV generation from 10 AM to 16 PM (red shaded area). All excess PV is ultimately curtailed since the system cannot store energy (EES is fully charged) nor export power beyond the grid export limit.
- Grid purchases are limited to 4.5 MW. Initially, grid imports were set to equal the Oak View peak load. This limit then was progressively decreased until an unfeasible solution was reached. Thus, a 4.5 MW grid import capacity was the lowest feasible capacity required to meet the peak demand.

4.4.4. Allocation of optimal PV in the Oak View test case

For the *Optimal PV* scenario, the *Realistic PV* scenario is used as a starting point. All solar PV installation are equally scaled up by a factor of 1.4 (8,823 kW/6,277 kW). Using this approach, however, due to area constraints (i.e., the suitable available area for PV deployment), there is a 1,028 kW PV capacity shortage that can't be allocated. This remaining capacity is then judiciously allocated to the larger rooftops, mostly at customers located at the C&I corridor, who are also connected at a higher service voltage level and usually behind bigger transformers.

The voltage profiles of the Oak View test case under this scenario are shown in Figure 4.20, Figure 4.21, and Figure 4.22. One can notice that no critical over voltages occur. In fact, for all primary buses and most of the secondary buses, there are no overvoltage conditions at all. It is at

2 of the secondary buses that (marginal) overvoltages occur. Nonetheless, for this scenario, most of the transformers are overloaded; 43 critical transformer overloads range from 107 to 491% of rated capacity. Besides, five lines are critically overloaded from 105% to 169% of the rated capacity. These line overloads occur at the head of the Smeltzer circuit. Table 4.9 summarizes these results.

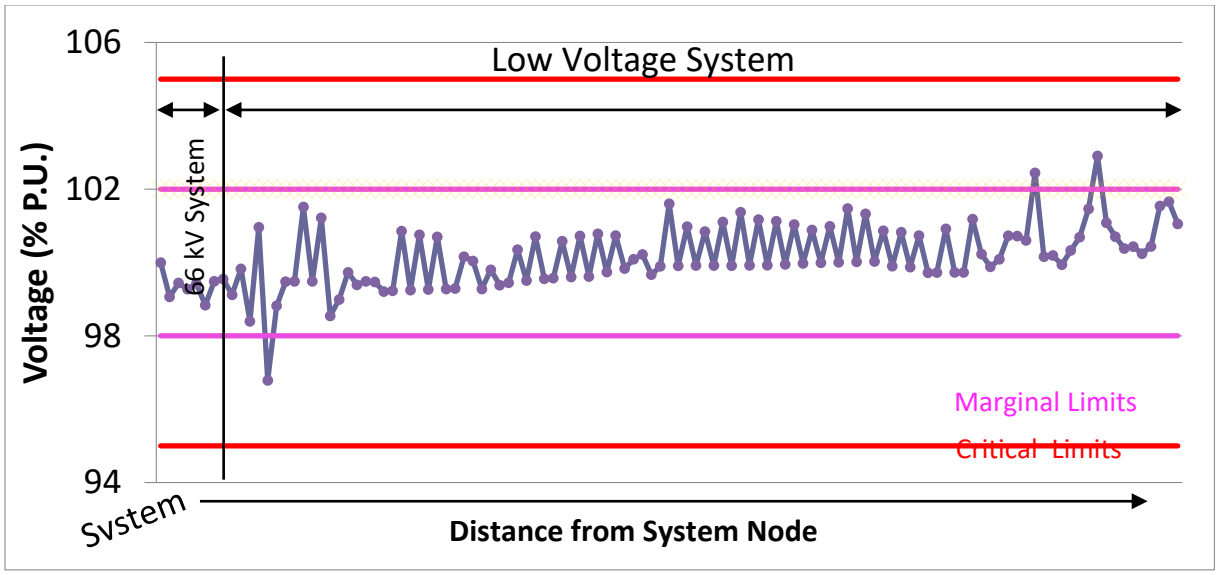

Figure 4.20 – Optimal PV Scenario - Voltage Profile for 66/12 kV system

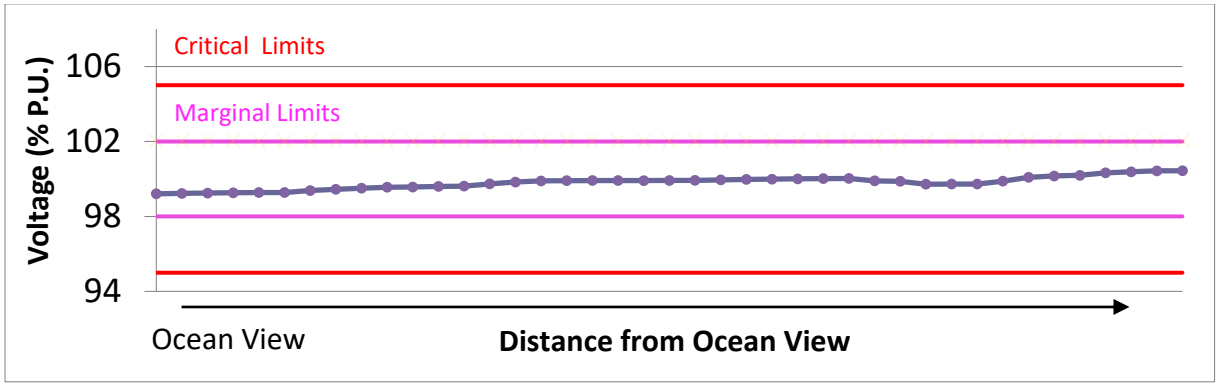

Figure 4.21 – Optimal PV Scenario - Primary Buses Voltage Profile

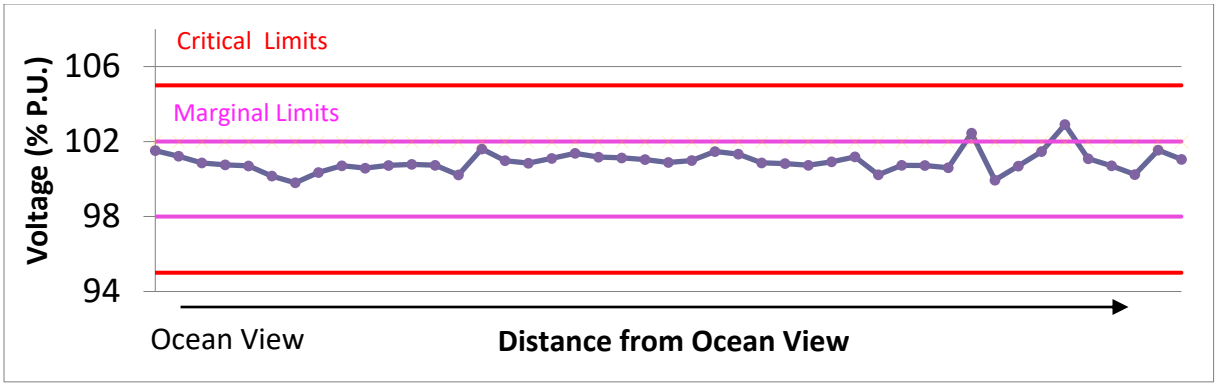

Figure 4.22 – Optimal PV Scenario – Secondary Buses Voltage Profile

Table 4.9 – Optimal PV Scenario - Events

Summary	Count	Min (%)	Avg. (%)	Max (%)
Transformer Overloads				
Critical	43	107	124	491
Marginal	0	--	--	--
Line Overloads				
Critical	5	135	150	169
Marginal	0	--	--	--
Over Voltages				
Critical	0	--	--	--
Marginal	2	102.6	102.8	103.0

In sum, in this scenario, the power system is severely overloaded. It realistically represents the current challenge of increasing the PV penetration in urban power systems.

4.4.5. Realistic PV (transformer-constrained)

The *Realistic PV* scenario aims to reduce the PV deployed at the test case as to never overload transformers during a reverse power flow event. The approach is to size the PV capacity to equal the transformer capacity plus 90% of the *minimum* load demand at that transformer, as shown in Equation (46). The 90% is used as a "security factor", since a reverse power flow condition that equals to 100% of the transformer rated capacity is not desirable.

$$Realistic\ PV\ (kVA) = Transformer\ Rating\ (kVA) + 0.9 * Minimun\ Load\ (kVA) \quad (46)$$

This approach is less conservative than the approach typically adopted in other hosting capacity analysis. For example, in (Electric Power Research Institute (EPRI), 2015), the PV rated power in kW is always less or equal than the transformer kVA, therefore, it does not consider the fact that local loads are contributing to absorbing some PV power, and in turn, reduce RPF. The total amount of PV deployed in the *Realistic PV* scenario is **6,277 kW**, which is 30% smaller than the *Optimal PV* scenario (8,823 kW). It is also only 42% of the maximum area-limited PV potential (14,661 kW).

The results from the *Realistic PV* scenario show that this approach eliminates all transformer overloads, and also critical overvoltages issues. One marginal over voltage above 1.02 p.u. still occurs at a secondary bus, as seen in Figure 4.25.

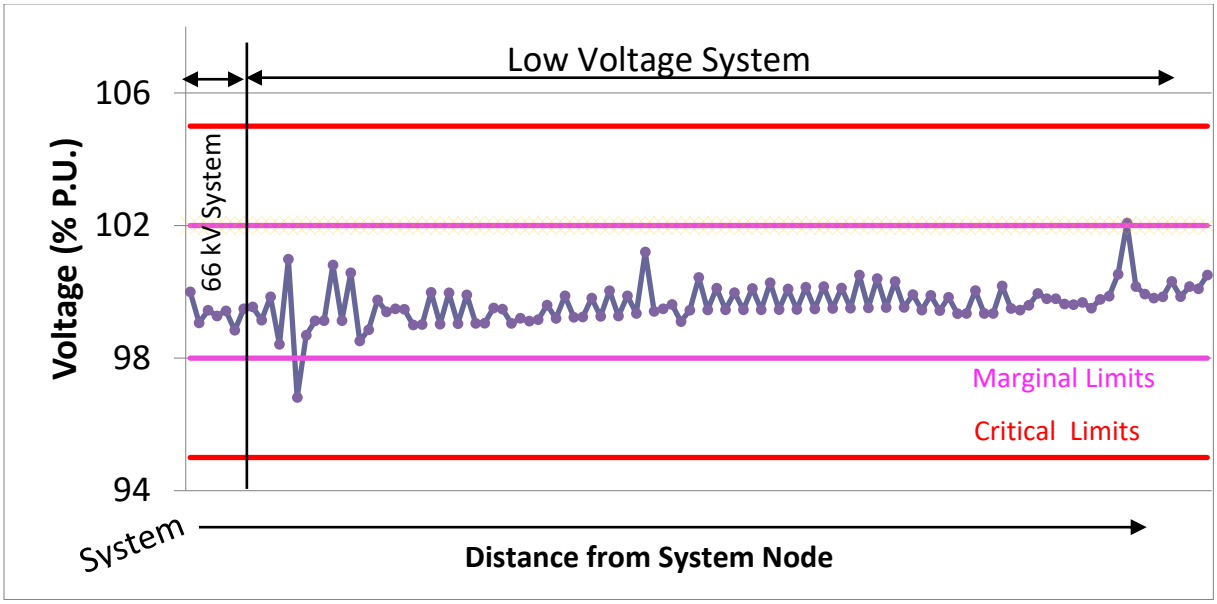

Figure 4.23 – Realistic PV Scenario - Voltage Profile for 66/12 kV system

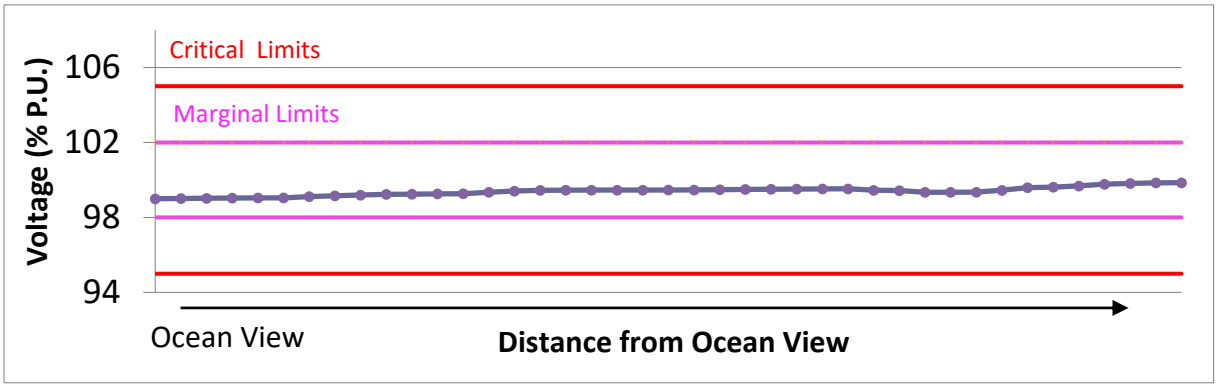

Figure 4.24 – Realistic PV Scenario - Primary Buses Voltage Profile

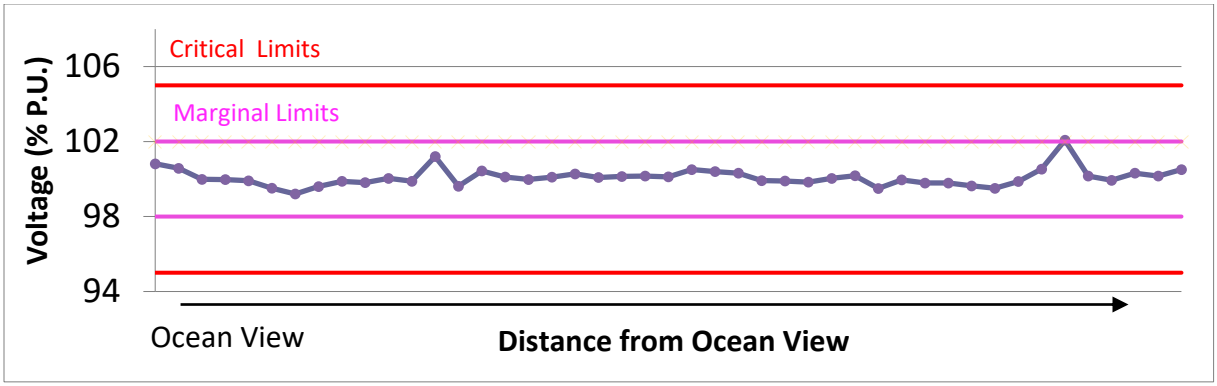

Figure 4.25 – Realistic PV Scenario – Secondary Buses Voltage Profile

Table 4.10 summarizes the critical and marginal events for the Realistic scenario. As carefully intended, there are no transformer overloads, and there is only one occurrence of a marginal overvoltage, which occurs at one secondary node. Nonetheless, there are still 4 line overloads (three critical and one marginal), which mostly occur near the head of the Smeltzer 12 kV feeder and the point where the currents originating from RPF at branches circuits adds up. The critical overloads range from 103 to 114 % of rated conductor capacity.

Table 4.10 – Realistic PV Scenario – Events

Summary	Count	Min (%)	Avg. (%)	Max (%)
Transformer Overloads				
Critical	0	N/A	N/A	N/A
Marginal	0	N/A	N/A	N/A
Line Overloads				
Critical	3	103	107	114
Marginal	1	96	96	96
Over Voltages				
Critical	0	-	-	-
Marginal	1	102	102	102

4.4.6. Optimal PV + EES + Smart inverter (Fixed PF)

This scenario aims to eliminate some of the negative power quality events observed in the High-penetration (*Optimal PV*) scenario, such as critical transformer and line overloads, and undesirable over voltages. The strategy is to use battery electric energy storage, modeled as constant PQ loads, to absorb the excess solar PV generation and alleviating RPF events. Moreover, the local control of reactive power is also explored by enabling the solar PV inverter

to operate at a fixed power factor, *i.e.*, absorbing or delivering reactive power. For this, it is necessary to couple two aspects of power system modeling: (1) the dynamic operation of battery storage, *i.e.*, charging and discharging energy balances, and (2) steady-state power flows. Figure 4.26 shows the daily dynamics of the solar PV, load, and battery energy storage for the high-penetration (*Optimal PV*) scenario, where the optimal amount of storage recommended by HOMER Pro 2,800 kW/11,759 kWh is also deployed. One can see from the battery charging/discharging dynamics that the EES is already fully charged (100% SOC) on 04/05/2015 at 1:00 PM, which is when our worst-case steady-state power flow simulation is performed. Hence, the EES does not assist with absorbing excessive PV during the worst-case RPF. In other words, the EES system does not add value to reduce overloads and overvoltages.

Hence, here we investigate the effects of having a larger (oversized, compared to the optimal design) EES system that would be able to contribute to absorbing excess PV at the worst-case RPF. A simple energy balance is performed on April 5th, 2015, accounting for solar PV production and hourly load demand. The EES is then sized to have enough energy capacity to charge with all the excess PV generation that occurs at 1:00 PM. The required EES size is determined to be **7,200 kW and 30,238 kWh**. Note that because power and energy rating are coupled, the power rating of the EES is significantly oversized, since the EES requirements are based on its energy capacity, and the Tesla Powerpack 2 offers a power-to-energy ratio of one to four (210 kWh/50kW). These values are then used as inputs in HOMER, which simulates the battery operation for one year, from which we can get the SOC and charging power at the worst-case RPF: 85% SOC and a 4,232 kW charging rate. Note that the charging power is only 60% of total EES rated power capacity, this charging power is used in the steady-state power flow simulation. Figure 4.27 illustrates the dynamic operation of the resulting design.

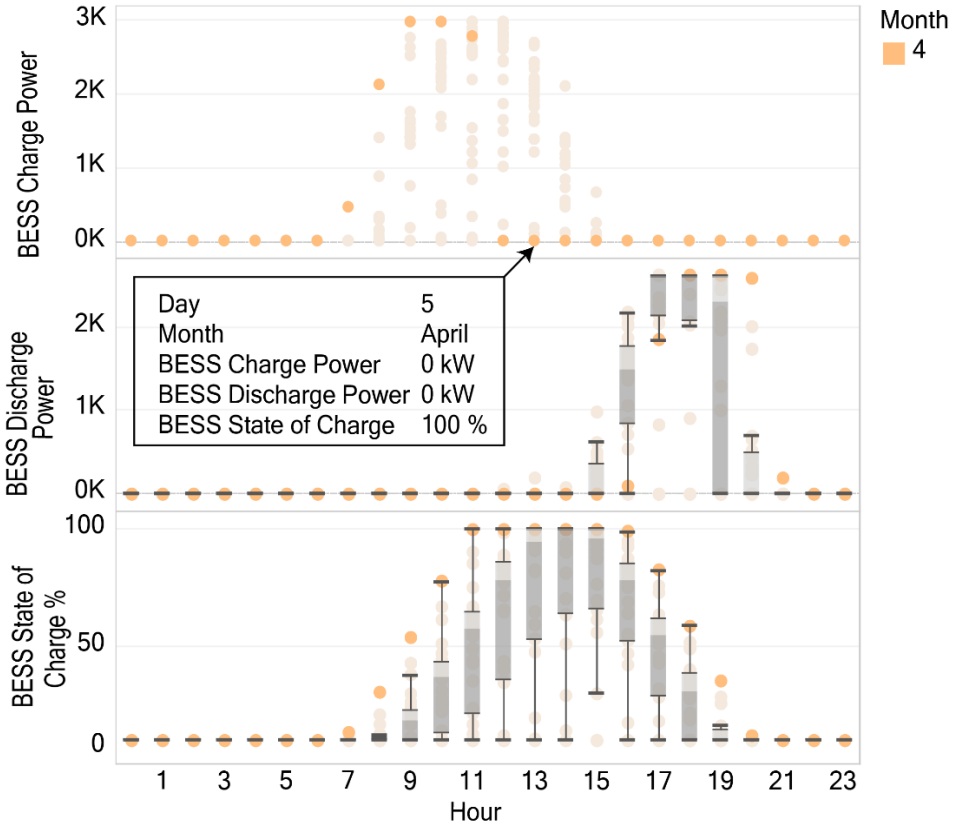

Figure 4.26 – Battery storage (BESS) Charge Power, Discharge Power, and State of Charge for the entire month of April 2015. Points highlighted show values for the specific day April 5th.

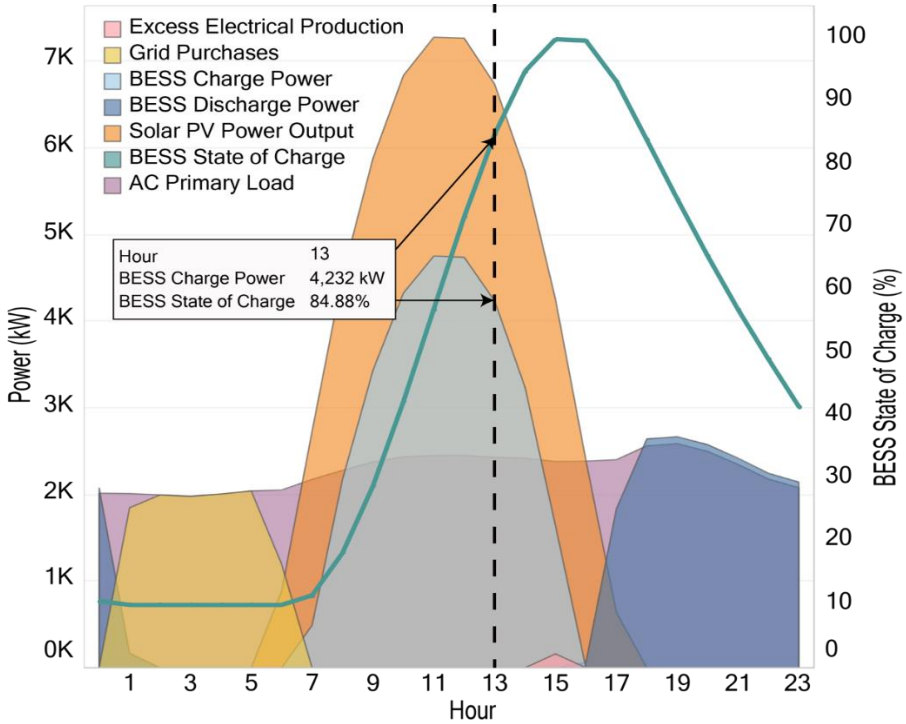

Figure 4.27 – Optimal PV + battery (BESS) design. .Battery rating is 7,200 kW/30,238 kWh. Battery will have around 85% SOC at 1:00 PM, and will charge at a 4,232 kW rate.

Having the total required EES calculated, we judiciously allocate the EES at the C&I corridor. Residential EES are avoided due to barriers such as high investment cost associated with a lack of financial incentives/market mechanisms to such systems, besides backup power.

Manually allocating EES throughout the Oak View test case is an iterative process. The approach taken is to match EES charging power with the local transformer net-load (*i.e.*, PV generation minus total load behind the given transformer). For this, the net-load at every C&I transformer is calculated. The required charging power is always 60% of the EES rated capacity, as observed in Figure 4.27. Thus, the net load is divided by a factor of 0.6 to obtain the EES rated power needed. Another assumption considered here is that EES rated capacities are discrete values. The discrete value used in this analysis is based upon the Tesla Powerpack 2 rating of 50 kW. Thus, each EES system needs to be a multiple of 50 kW. Thus, the final EES values are all rounded up to the closest multiple of 50.

After the EES is sized for all C&I customers using this methodology, the amount is compared to the amount required in the energy balance analysis (7,200 kW). The EES capacity allocated is short by 150 kW. This means that more EES would need to be judiciously deployed at other locations. For this, we also need to define the maximum allowed EES charging load that can be supported by each transformer. This amount equals the transformer net-load plus 90% of the transformer's rated power. This way, the transformer imports equal to only 90% of its rated capacity. Therefore, the remaining 150 kW are judiciously allocated at the transformers that could host new EES charging loads, at 50 kW increments. Table 4.11 shows these values for every transformer where EES is allocated. The "EES minimum rated power" equals the rated power that zeros-out the transformer's net-load. The "EES maximum rated power" equals the EES rated power that causes an import that equals 90% of the transformer's rated power. The "EES rated power" is the final EES system discrete size that is allocated to each transformer.

Table 4.11 – Optimal PV + EES Scenario - EES capacity allocated at AEC transformers

Transformer	Customer	EES minimum rated power (kW)	EES maximum rated power (kW)	EES rated power (discrete) (kW)
11	FRC + Library	71.9	134.4	100
7	Elementary School	571.4	1071.4	600

27	Child Day Care	28.7	53.7	50
28	Discount Tire	45.4	87.1	50
1	Ind. Offices	143.1	255.6	150
2	Ind. Offices	324.4	549.4	350
3	Ind. Offices	286.1	511.1	300
4	Ind. Offices	1,264.5	1,489.5	1,300
3	Zodiac	1,892.8	4,142.8	2,050*
4	Pre-School	142.8	255.3	150
9	Republic 1	286.4	511.4	300
10	Republic 2	95.2	170.2	100
11	Republic 3	668.9	1,193.9	700
12	Republic 4	190.8	340.8	200
13	Republic 5	260.7	485.7	300
6	Building Materials	48.2	160.7	50
8	WILLY'S	143	255.5	150
9	HBC + Disc. Tire	286.3	511.3	300
TOTAL				**7,200 kW**

*EES added to match the required capacity of 7,200 kW.

Figure 4.28 illustrates how EES is modeled in ETAP. A 1,300 kVA (1,300 kW) EES is deployed at transformer 4 and eliminates the overload condition. Note that the EES charges at 790 kW, which is 60% of its rated power capacity plus wiring losses. Once the EES charging loads are added, however, it creates a marginal under voltage condition at the secondary bus. To counteract this problem, the PV inverter at this bus is set to operate at a 98% leading power factor, *i.e.*, the inverter injects reactive power to increase the local voltage. Thus, for all other five instances of marginal under voltages created by elevated EES charging loads, the PV inverter power factor is manually adjusted to correct the local voltage to close to 1 per unit.

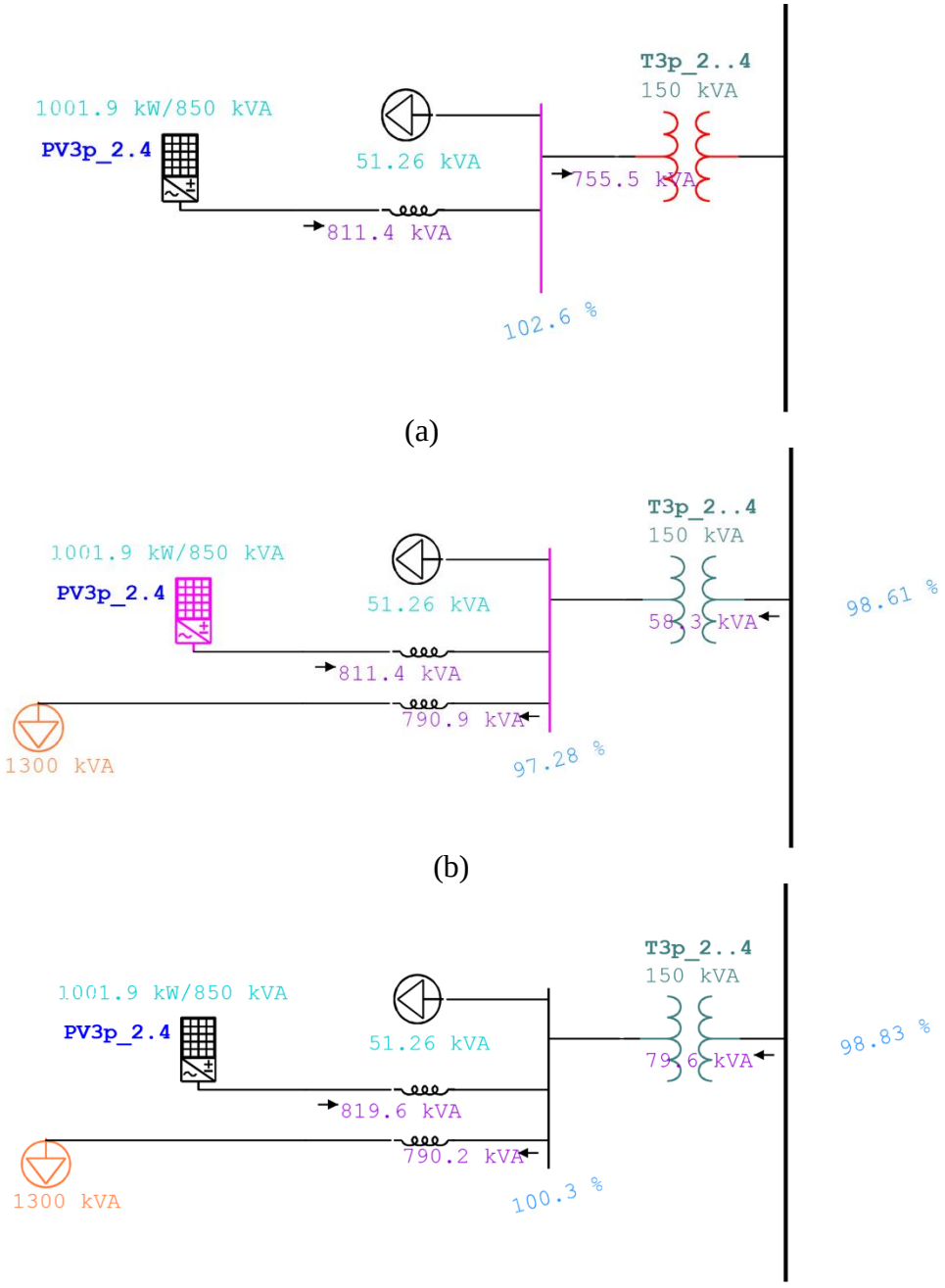

Figure 4.28 – EES storage deployed behind an overloaded transformer. (a) A 150 kVA transformer is overloaded (red) due to a 755 kVA reverse power flow, (b) A 1,300 kVA EES load is deployed to charge at 791 kVA, causing an under voltage of 97.28 % per unit at the secondary node. (c) Smart-inverter Fixed-PF functionality (98% PF leading) corrects the voltage to 100.3 % per-unit.

The voltage profiles of this scenario are captured by Figure 4.29, Figure 4.30, and Figure 4.31 which compare the voltage profiles of the previous scenarios: High-penetration (*Optimal PV*) and *Optimal PV + EES + Volt-Var* compensation. One clear observation is that even though EES is initially deployed to eliminate transformer overloads, it also has a positive impact on reducing marginal overvoltages, especially on secondary buses, as seen in Figure 4.31. As seen in Table

4.12, a significant number (28) of overloads still occur in this scenario, in the residential areas, where no battery energy storage.

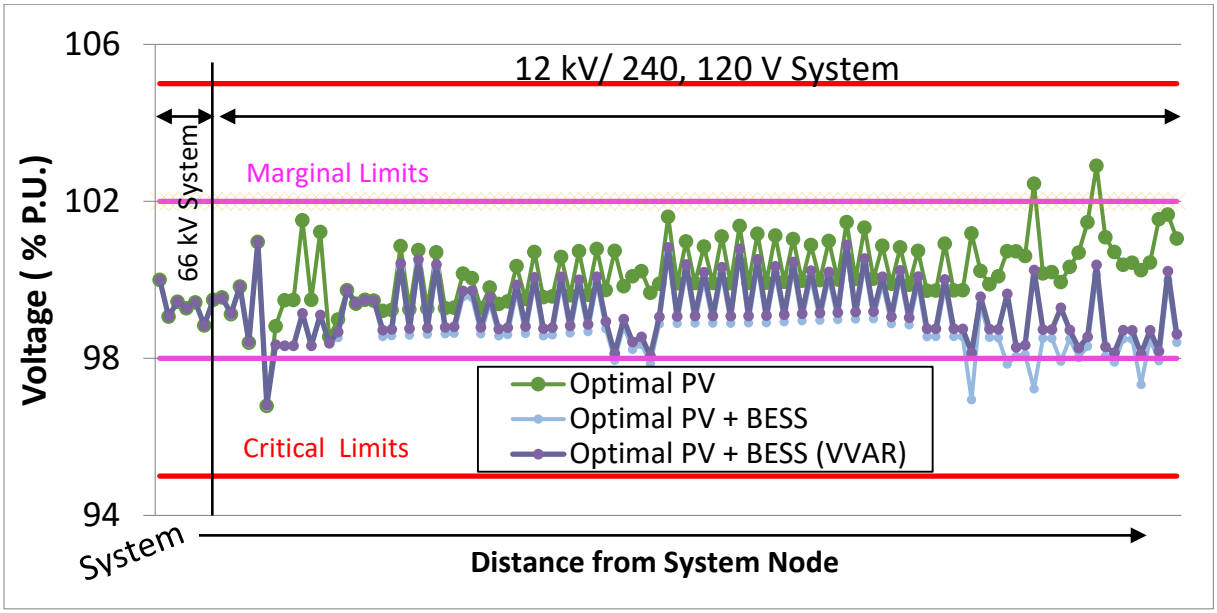

Figure 4.29 – Optimal PV (with and w/o battery (BESS)) comparison- Voltage Profile for 66/12 kV system

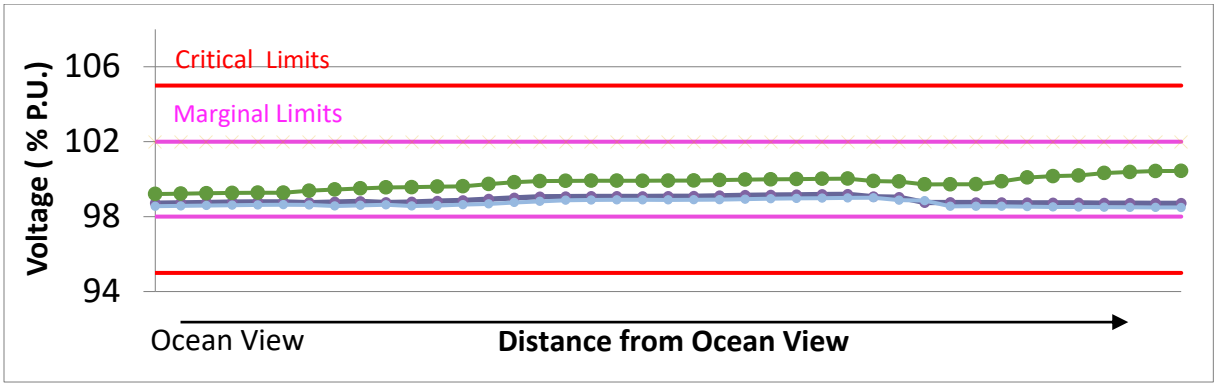

Figure 4.30 – Optimal PV (with and w/o battery) comparison - Voltage Profile for Primary buses

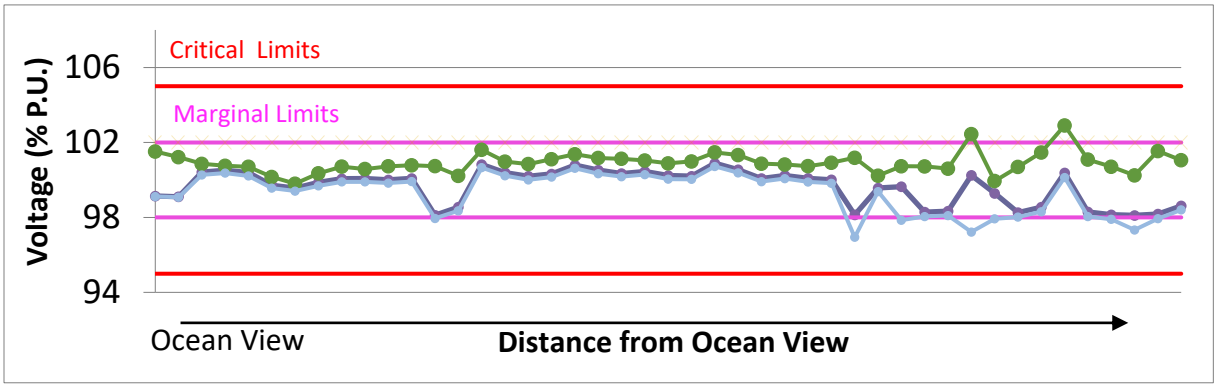

Figure 4.31 – Optimal PV (with and w/o EES) comparison - Voltage Profile for Secondary buses

Table 4.12 – Optimal PV + EES + VVar Scenario events

Summary	Count	Min	Avg.	Max
Transformer Overloads				
Critical	28	107	115	120
Marginal	0	--	--	--
Line Overloads				
Critical	0	--	--	--
Marginal	0	--	--	--
Over Voltages				
Critical	0	--	--	--
Marginal	0	--	--	--

4.5. Summary

- A real-world urban neighborhood microgrid test case was developed from site surveys on the existing urban infrastructure.
- Transformer overloads were visibly the worst negative impact of large deployment of solar PV. For the *Optimal PV* scenario, an 8,823 kW solar PV deployment overloads 43 transformers up until around 400% rated capacity and causes two over voltages above 1.02 per-unit besides causing four line overloads.
- By limiting PV deployment to not overload the existing transformer capacity, the total PV deployment is reduced to 6,277 kW (a 30% reduction), and one marginal overvoltage of 1.02 p.u. occurs.
- At all the locations deployed, EES not only avoided transformer overloads but also eliminated marginal overvoltages.
- For the optimal sizing of battery energy storage, a time-series simulation was necessary to account for charging/discharging dynamics and energy storage capacity (SOC).

5 Optimal Solar PV and Battery Storage Sizing and Siting Considering Local Transformer Limits

Highlights

- An optimization for DER allocation incorporates utility transformer constraints
- A polygon relaxation models the apparent power flow through power transformers
- TOU, NEM, and wholesale rates are modeled for each utility customer type
- A novel, renewable energy battery storage is modeled to export under NEM rates

5.1. Literature Review

A significant challenge involving DER integration into the utility grid network is to allocate (*i.e.*, to assign an amount or portion of a resource) to a particular recipient node, which entails both sizing and siting these resources into the existing electric distribution grid. Ideally, DER allocation and dispatch can be done, so that no additional distribution infrastructure upgrade is required. Known issues caused by DER, specifically PV systems when installed in high-penetration, include but are not limited to voltage rise during low load periods, and reverse power flow, that is, a flow of power from a section of a radial circuit towards the main distribution substation, which increases electric power losses and creates issues in protection equipment (Jahangiri & Aliprantis, 2013),(von Appen, Braun, Stetz, Diwold, & Geibel, 2013). Solving the problems mentioned above is essential to promote an increase in the PV hosting capacity of urban district systems, which are rising to be one of the most effective ways to integrate not only PV but a suite of DER into a local distribution grid. Thus, the types of DER, their allocation within the system, as well as their operation and dispatch have to be carefully

chosen to improve the overall system performance while meeting customer demand. Judicious and systemic DER deployment (allocation and dispatch) is recommended over random deployment (Prakash & Khatod, 2016) and is essential to enable the very high PV penetrations required for ZNE.

Simultaneously, there has been much recent interest in developing the concept of Advanced Energy Communities — electrically contiguous areas that leverage the clustering of load and generation by integrating multiple utility customer-owned DER (Electric Power Research Institute (EPRI), 2017). Within an AEC, DER assets allow for most of the energy demand to be generated and consumed internally. External energy transfers enter the community if local production is insufficient. Excess electricity is exported to the wide-area electricity grid. AEC can operate grid-connected or as islanded microgrids (for resiliency purposes) under certain circumstances of containing a sufficient DER to match the loads and a microgrid controller, AEC and microgrids may share typical DER and local control resources and electric infrastructure topology. Moreover, AEC facilitate the integration of clean and innovative DER technologies into the existing utility grid infrastructure, minimizing the need for upgrades while maximizing the local renewable generation hosting capacity to provide environmental, societal, and utility benefits (Electric Power Research Institute (EPRI), 2017).

The present chapter evaluates a piece of the broader AEC vision, assuming total electrification of community energy demand as ZNE developments are expected to be introduced (Electric Power Research Institute (EPRI), 2016). Moreover, we only consider PV and battery storage as our DER. Nonetheless, the analysis and models developed can be easily extended to include a broader variety of DER.

For most AEC, the ultimate goal is to allow for ZNE operation. To achieve ZNE operation, a big challenge is how to increase the hosting capacity, *i.e.,* the maximum DER penetration for which the power system infrastructure operates satisfactorily (Electric Power Research Institute (EPRI), 2015), in urban distribution systems. Historically, DSOs have employed rules-of-thumb for DER integration. The “15% rule” only allows for DER penetration below 15% of the local maximum load (Palmintier et al., 2016). Various other DSOs have employed (and some still employ) similar rules of thumb. For example, in Canada, DG deployment shouldn’t exceed 60% of the transformer rating at the main substation. In Portugal, the total DG ratings should be lower than

25% of the medium voltage/low voltage (MV/LV) transformer rating. In Spain, the total DG ratings should be lower than 50% of the MV/LV transformer rating and lower than 50% of the thermal limit of the affected feeders. In Italy, the total DG ratings should be lower than 65% of the MV/LV transformer rating and lower than 60% of the thermal limit of the affected feeders (Ismael, Abdel Aleem, Abdelaziz, & Zobaa, 2019). These conservative and somewhat arbitrary rules are practical but impose a limit on achieving high-penetration of renewable generation and ZNE.

In California, DSOs have been required to provide a high-level hosting capacity analysis of their medium-voltage circuits with some utilities developing interactive GIS map tools, such as DERIM maps (Southern California Edison (SCE), 2016b). However, the DER allocation in the lower voltage (<12 kV) portion of the circuit, specifically regarding distribution transformer constraints, has not been addressed.

Given the need of deploying PV in high penetrations to meet AEC ZNE goals, a significant share of AEC project success depends upon achieving an adequate allocation of DER such as PV and battery storage resources while supporting and enhancing the overall utility grid network characteristics. There have been numerous state-of-the-art optimization approaches applied to the development of computational tools for the investment planning and operation of DER. In district systems, DER allocation can be performed optimally to maximize benefits to the utilities, project owners, and customers. These benefits include, but are not limited to: minimizing project cost, minimizing power system electric losses, maximizing renewable penetration, minimizing carbon emissions, maximizing the PV hosting capacity, or achieving zero-net-energy operation.

The underlying DER allocation problem is typically non-linear, highly constrained, multi-objective, mixed-integer, and multi-modal. Thus, finding a global optimal solution is challenging (Rezaee Jordehi, 2016). Known optimization techniques used in the literature include, but are not limited to linear programming (LP), mixed integer linear programming, mixed integer non-linear programming (MINLP), dynamic programming (DP), sequential quadratic programming (SQP), ordinal optimization (OO), cone programming (CP), and heuristic methods such as genetic algorithms (GA) and particle swarm optimization (PSO) (Arabali et al., 2017).

Amongst the most common approaches are MILP formulations, in which only some variables are constrained to be integers, while other variables are allowed to be continuous. Integer programs

can model many practical situations, such as scheduling, and resource allocation(Conforti, Cornuéjols, & Zambelli, 2014) due to their flexibility in modeling constraints involving binary or integer decisions (yes or no, and on or off behaviors)There is also a wide availability of robust commercial solvers, that allow control and awareness of the optimality gap between optimal and integer solution(Mansini, Ogryczak, & Speranza, 2015). MILP algorithms can be solved in polynomial time, that is, computing time is defined by a polynomial function of the instance size, therefore, the MILP computational burden increases significantly with the scale of the problem, typically requiring the program developer to balance model complexity with tractability(Mansini et al., 2015).

The most straightforward DER allocation problem involves allocating a single specific type of DER at a single node, according to a particular optimization goal and a set of constraints. This analysis is usually performed by aggregating all loads and generation together (*i.e.*, "aggregate approach") and assuming the lossless transfer of energy between nodes. A number of enhancements to this approach were developed in subsequent literature, such as (1) optimizing a portfolio (mix) of DER(Ren & Gao, 2010), (2) considering the time-coupling of generation and load in a time-domain, dynamic simulation (Falke et al., 2016; R. J. Flores & Brouwer, 2018a; Huang, Zhang, Yang, Wang, & Kang, 2017; Ren, Zhou, Nakagami, Gao, & Wu, 2010; Stadler, Groissböck, Cardoso, & Marnay, 2014) (3) siting DER on different nodes of a network (Basu et al., 2012), (4) incorporating electricity grid constraints (Mashayekh et al., 2017; Morvaj, Evins, & Carmeliet, 2016; Qiu, Zhao, Yang, Wang, & Dong, 2018; Y. Yang et al., 2015b; Y. Yang, Zhang, & Xiao, 2015a), (6) energy storage (Grover-Silva, Girard, & Kariniotakis, 2018), (5) DER uncertainty (Grover-Silva, Heleno, et al., 2018; Z. Wang, Chen, Wang, Kim, & Begovic, 2014), and (7) smart-grid technologies (Chanda & De, 2014; Santos, Fitiwi, Shafie-khah, Bizuayehu, & Catalão, 2016).

5.1.1. Related Work

Many dynamic optimization approaches for DER allocation already exist where the objective function is to allocate DER and also dispatch DER such that cost is minimized, or other multi-objective formulation. A few examples of such analyses are listed below:

Falke *et al.*(Falke et al., 2016) developed a multi-objective optimization for the design of a district electricity and heat supply system to minimize annual costs (investment, demand, and operation) of energy supply and CO_2 emission equivalents. The decision variables included the heating network connections, DER types, sizes, and operation. The problem was decomposed into three sub-problems (heating network, DER, and energy efficiency measures design, and DER operation) and solved iteratively to reduce computational complexity. The solution approach involved the heuristic spanning tree method (Kruskal's method), an evolutionary algorithm, and a deterministic operation simulation.

Flores *et al.* (R. Flores & Brouwer, 2017) developed a MILP model to minimize the cost of energy while limiting greenhouse gas (GHG) emissions. The decision variables used were DER type, size, and operation. Two primary technology scenarios were explored (DER including storage with and without electrical export). Li *et al.* (Li, Roche, Paire, & Miraoui, 2017) decomposed the DER allocation problem into a leader-follower problem. The leader problem was a genetic algorithm to search for the best sizing values of each component to minimize cost. Each candidate solution was then fed into the follower problem, a MILP, which was used to solve the DER sizing and obtain the optimal energy management strategy.

In many publications that use these optimization strategies, authors did not include grid constraints (voltage at nodal buses, power flows through distribution lines and transformers), and assumed that the grid infrastructure has an unlimited capacity. Results from these studies are optimal for a distributed energy system comprised of a single node but may lead to suboptimality or infeasibility when applied to a distribution grid network (Mashayekh et al., 2016). Moreover, single-node, aggregate modeling approaches do not allow for DER siting and can under-estimate DER capacities and project costs, since they do not account for the electrical distribution grid infrastructure and its constraints and internal losses (Mashayekh et al., 2016). All previously mentioned literature sources do not include simultaneous optimization of (1) DER size and location, (2) DER operation, and (3) impact on the local power system infrastructure. Four recent studies, however, were found to address these sub-problems simultaneously.

Mashayekh *et al.* (Mashayekh et al., 2017) used a MILP approach to determine optimal technology mix, size, placement, and dispatch in a multi-energy (electric, heating, and cooling) microgrid, using a multi-node, time-series approach. The objective (minimize cost or CO_2

emissions) was constrained by linearized power flow (LinDistFlow) constraints, nodal voltage constraints, and linearized apparent power constraints for cable current limits. The DER simulated here were P-type (can only output active power), but the building loads were assumed to consume reactive power at a fixed power factor. An 18-node radial test system was used as a test case, where DER was limited to be installed only at three pre-defined nodes within the network.

Another study was presented by Morjav *et al.*(Morvaj et al., 2016) which described a framework for computing optimal DER size, location, and type, in an energy hub. Different combinations of a genetic algorithm and a MILP were compared. For the MILP formulation, the objective of minimizing cost and CO_2 emissions was constrained by linearized AC power flow equalities, voltage limits (±10%), and linearized current limits using a combination of linearization techniques including a first-order Taylor series approximation, and piece-wise linearization of the squared real and imaginary current components. The test case consists of 5 residential buildings connected on a radial network. The authors noted that a system with more buildings would be computationally intractable.

Additional recent work by Ehsan *et al.* (Ehsan & Yang, 2019) proposed a Mixed Integer Quadratically Constrained program for the optimal DER mix, siting, and sizing in multi-energy microgrids considering load and generation uncertainties. The objective of minimizing cost and carbon emissions is constrained by the simplified non-linear DistFlow formulation of voltage and line apparent power flow limits. The DER is PQ (active and reactive power) type, but with no S (apparent power) limit coupling of P and Q. The test case used was a 19-bus radial microgrid.

Lastly, a recent study by Alturki *et al.*(Alturki, Khodaei, Paaso, & Bahramirad, 2018) developed an optimization-based hosting capacity calculation using MILP for sizing and siting DG aiming to maximize the total DG deployments. Voltage limits were constrained as well as DG output and line capacities considering active and reactive power flows separately (*i.e.*, without considering the apparent power coupling). The IEEE-33 bus radial distribution grid was used as a test case. The near-optimal hosting capacity solution calculated by this method was found superior compared to traditional iterative hosting capacity calculation methods. While this study presented a brilliant strategy for maximizing PV penetration, the active and reactive power flow coupling was not captured.

The survey of current literature shows that the focus on modern multi-nodal DER allocation methods has been on ensuring feasible power flow between nodes while maintaining acceptable voltage levels. These previous approaches typically do not include:

- Limiting the power flow injections through distribution transformers; recent projects on large scale urban district systems (R. Flores *et al.*, 2018) suggest that transformer overloads will be a significant hurdle for DER integration into the urban low voltage network.
- The coupling between active (P) and reactive (Q) power in power flow constraints, due to its non-linear relationship ($S = \sqrt{P^2 + Q^2}$)
- Large-scale test cases. Current formulations typically use a large number of constraints involving binary and integer variables, which can make the problem computationally intractable. Hence, most test-cases in the literature consider only small and non-scalable grid networks.
- The variety of utility electricity tariffs that a mix of residential and commercial and industrial utility customers are subjected to, and the different markets where renewable DER can participate, namely Net-Energy-Metering (NEM) and wholesale.
- Explicit models of battery storage systems that can only charge from renewable sources, and in turn, meet utility requirements for exporting under NEM rates.
- The limited physical area available for a realistic DER deployment into the built urban environment.

5.1.2. Contributions

This chapter proposes a mixed integer linear program optimization to allocate PV and battery storage size and location across an AEC with complex existing distribution grid infrastructure. The objective is to minimize cost throughout the time-resolved dynamic operation of the system during a representative year using known load and solar insolation profiles. Desired operation goals such as Zero-Net-Energy and islanding as a microgrid for resiliency during unplanned grid outages are also modeled. The electrical distribution network is modeled in a multi-nodal approach, and the flows of both active and reactive power are taken into account. For a realistic

formulation of the DER allocation problem, minimum discretized DER sizes are enforced so that the global optimal solution can be guaranteed within a pre-defined optimality gap.

The present work adds to the previous literature by proposing a novel, yet straight-forward, approach to avoid distribution transformer overloads by constraining non-linear nodal apparent power injections with the use of polygon relaxations, which is less computationally intensive than piecewise-linearization since it does not need the addition of binary variables and special ordered sets.

In summary, the contributions of the current chapter are:

- The optimal DER allocation for a real-world electric distribution system, here defined as an Advanced Energy Community microgrid, considering its aggregated behavior as a grid-connected system or islanded, its diverse load profiles (residential, commercial and industrial) and limited physical space for DER deployment.
- Distribution transformer apparent (S) power flows are explicitly limited through a novel constraint, using a straightforward linearization method that allows for the test system to be scaled to more than 30 nodes;
- Electricity rates used to account for the realistic time of use (TOU) and demand rate structures for each individual residential, commercial, or industrial customer. Also, DER is allowed to take advantage of different market mechanisms such as NEM and wholesale rates, to add revenue streams;
- A novel storage concept is modeled, namely the Renewable-tied Energy Storage System (REES) *i.e.*, storage that charges exclusively from renewable solar PV energy, which is for that reason allowed to export electricity back to the utility grid under NEM rates; and
- District or community-wide operation goals such as Zero Net Energy and islanding are modeled.

5.2. Problem Formulation

The optimization formulation presented here builds upon the work presented in (R. Flores & Brouwer, 2017; R. J. Flores & Brouwer, 2018), namely the DERopt tool. We review the original problem formulation in Section 5.2.2 and 0 and expand upon the prior by introducing reactive power balances to the original formulation and transformer constraints with a polygon relaxation method, presented in Section 5.2.4.

5.2.1. Notation

The applicable model sets, Parameters, and Decision Variables

- $m \in M$: Set of all months
- $s \in S$: Set of all summer months ($S \subset M$)
- $t \in T$: Set of all hourly increments in month m
- $o \in O$: Set of all hourly increments during on-peak in summer month s ($O \subset T$)
- $p \in P$: Set of all hourly increments during mid-peak in summer month s ($P \subset T$)
- $b \in B$: Set of all buildings
- $x \in X$: Set of all transformers
- $j \in J_x$: Set of buildings that are connected to transformer x ($J \subset B$)
- $\lambda \in \Lambda$: Set of line segments for polygon relaxation

The applicable decision variables and parameters for the optimization model are shown in Table 5.1 and Table 5.2, respectively.

Table 5.1 – List of decision variables used in DERopt

Decision Variable	**Description**	**Units**
$P_{\text{import}_{t,b}}$	Power imported from the grid to building *b* at hour *t*	kW
$P_{\text{DC}_{m,b}}$	Maximum demand during month *m* at building *b*	kW
$P^{\text{on}}_{\text{DC}_{s,b}}$, $P^{\text{mid}}_{\text{DC}_{s,b}}$	Maximum on-peak and mid-peak demand during summer month *s* and building *b*	kW
S_{PV_b}	Solar PV capacity adopted at building *b*	kW
$P_{\text{PV BLDG}_{t,b}}$	Power generated by solar PV at hour *t* at building *b*	kW
$P_{\text{PV}_{\text{NEM},t,b}}$	Power exported under NEM rates at hour t from building *b*	kW
$P_{PV_{W,t,b}}$	Power exported under wholesale rates at hour *t* from building *b*	kW
S_{EES_b} , S_{REES_b}	EES/REES capacity adopted at building *b*	kWh
$e_{\text{EES}_{\text{t},b}}$, $e_{\text{REES}_{t,b}}$	EES/REES state of charge *t* hour *t* at building *b*	kWh

$P_{\mathrm{EES}_{\mathrm{ch},t,b}}$ $P_{\mathrm{REES}_{ch,t,b}}$	EES/REES charging power at hour *t* at building *b*	kW
$P_{\mathrm{EES}_{\mathrm{dch},t,b}}$, $P_{\mathrm{REES}_{dch,t,b}}$	EES/REES discharging power at hour *t* at building *b*	kW
$P_{\mathrm{REES}_{NEM,t,b}}$	Power exported from REES at NEM rates at hour t at building *b*	kW
n_{EES} , n_{REES}	Binary variable indicating EES/REES adoption at building *b*	n/a
$P_{T_x}, Q_{T_x}, S_{T_x}$	Active, Reactive, and Apparent Power flows through transformer *x* at hour *t*	kW/kVAr/kVA

Table 5.2 – List of parameters used in DERopt

Parameter	**Description**	**Units**	**Value**
$P_{\mathrm{BLDG}_{t,b}}$, $Q_{\mathrm{BLDG}_{t,b}}$	Power (active and reactive) demand at building *b*, at hour *t*	kW / kVAr	Based on URBANopt outputs
A_b	Area available for solar PV installation at building *b*	m^2	Based on methods described in Section
I_t	Normalized Average available insolation at hour *t*	kW/kWp	Taken from(White, 2016)
$C_{\mathrm{grid}_{t,b}}$	Utility electricity charge at hour *t* at building *b*	$/kWh	Southern California Edison Rate Structures
C_{DC_m}	Non-TOU demand charge in month *m*	$/kW	14.88
$\mathrm{C}^{\mathrm{on}}_{\mathrm{DC}_o}$, $\mathrm{C}^{\mathrm{mid}}_{\mathrm{DC}_s}$	On-peak and Mid-peak demand charge in summer month *s*	$/kW	23.74 (on) 6.55 (mid)
$C_{\mathrm{NEM}_{t,b}}$	Net energy metering price at which electrical utility purchases energy from building *b* at hour *t*	$/kWh	Energy charge $C_{grid,t}$ minus transmission and distribution cost
$C_{\mathrm{W}_{t,b}}$	Wholesale price at which electrical utility purchases energy from building *b* at hour *t*	$/kWh	0.03

C_{Cap}^{PV}	Capital cost for solar PV system	\$/kW	2000
$C_{\text{O\&M}}^{PV}$	O&M cost for solar PV system	\$/kWh	0.001
η_{PV}	Efficiency of PV at nominal conditions	%	18
$C_{\text{Cap}}^{\text{EES}}$, $C_{\text{Cap}}^{\text{REES}}$	Capital cost of EES/REES	\$/kWh	600
$C_{\text{O\&M}}^{\text{EES}}$, $C_{\text{O\&M}}^{\text{REES}}$	Cost to charge/discharge EES/REES	\$/kWh	0.001(R. J. Flores & Brouwer, 2018)
α	Retained EES/REES storage between hourly periods	%	99.99
$\eta_{\text{EES}_{ch}}$ $\eta_{\text{EES}_{dch}}$	EES/REES charging efficiency	%	90
$\eta_{\text{REES}_{ch}}$, $\eta_{REES_{dch}}$	EES/REES charging efficiency	%	90
$\overline{\delta}_{\text{EES}}$, $\overline{\delta}_{\text{REES}}$	Maximum EES/REES state of charge	% of purchased capacity	95
$\underline{\delta}_{\text{EES}}$, $\underline{\delta}_{\text{REES}}$	Minimum EES/ REES state of charge	% of purchased capacity	10
$\overline{\mu}_{\text{EES}}$, $\overline{\mu}_{\text{REES}}$	Maximum EES/ REES charging rate	% of purchased capacity	25
$\underline{\mu}_{\text{EES}}$, $\underline{\mu}_{\text{REES}}$	Maximum EES/ REES discharging rate	%of purchased capacity	25
$\overline{S}_{\text{EES}}$, $\overline{S}_{\text{REES}}$	Big M constant for EES/REES size	kWh	99,999
$\underline{S}_{\text{EES}}$, $\underline{S}_{\text{REES}}$	Minimum EES/REES size	kWh	13.5
$\bar{S}_{T_x}$	Power Rating of transformer *x*	kVA	Based on power system topology
PF	Building power factor	n/a	0.90 (Residential) 0.85 (C&I)
α_x	Transformer *x* p.u. loading	%	1
σ_b	Max PV installation coefficient at building *b*	kW/ft^2	0.005 (Residential)

			0.009 (C&I)
θ_i	Angle of segment *i* of polygon relaxation	degrees	Based on the number of polygon sides *L*
L	Number of sides for polygon relaxation	n/a	22

5.2.2. Objective Function

The objective function $J(x)$ is the sum of various individual cost components to be minimized. The cost parameters, defined by the C variables, include the cost of utility grid imports ($\mathrm{C_{grid}}$), demand charges ($C_{\mathrm{DC}}, C_{\mathrm{DC}}^{\mathrm{on}}, C_{\mathrm{DC}}^{\mathrm{mid}}$), the cost to purchase ($\mathrm{C_{cap}}$) and operate DER ($\mathrm{C_{O\&M}}$), and the revenue generated by exporting excess electricity to the grid under both NEM ($\mathrm{C_{NEM}}$) and wholesale rates ($\mathrm{C_W}$). The cost parameters are multiplied by the specific decision variables, which include the building hourly power flows (P variables for import, PV production, and battery charge and discharge), the maximum power demand over a month ($\mathrm{P_{DC}}$ variables), and the PV/EES/REES capacity adopted ($S_{\mathrm{PV}}, S_{\mathrm{EES}}$ and S_{REES}). All individual cost components are added through a specific time interval: t (hourly), m (monthly), or s (during summer months), and across all buildings b as follows in Equation (47). Therefore, the first line of the objective function captures the costs associated with purchase and sale of energy, the second line captures the cost associated with demand charges, and the third, fourth and fifth lines capture the cost associated with purchasing and operating the adopted DER.

$$
\begin{aligned}
J(x) \;=\; & \sum_{b=1}^{B}\left(\sum_{t=1}^{T} C_{\mathrm{grid}_{t,b}} P_{\mathrm{import}_{t,b}} - C_{\mathrm{NEM}_{t,b}}\left(P_{\mathrm{PV_{NEM},t,b}} + P_{\mathrm{REES_{NEM},t,b}}\right) - C_{W_t} P_{\mathrm{PV_{W},t,b}}\right. \\
& + \sum_{m=1}^{M} C_{\mathrm{DC}_m} P_{\mathrm{DC}_{m,b}} + \sum_{s=1}^{S}\left(C_{\mathrm{DC}_s}^{on} P_{\mathrm{DC}_{s,b}}^{on}\right) + \sum_{s=1}^{S}\left(C_{\mathrm{DC}_s}^{mid} P_{\mathrm{DC}_{s,b}}^{mid}\right) \\
& + C_{\mathrm{cap}}^{\mathrm{PV}} S_{\mathrm{PV}_b} + C_{\mathrm{O\&M}}^{\mathrm{PV}}\left(P_{\mathrm{PV_{BLDG},t,b}} + P_{\mathrm{PV_{NEM},t,b}} + P_{\mathrm{PV}_{W,t,b}}\right) \\
& + C_{\mathrm{cap}}^{\mathrm{EES}} S_{\mathrm{EES}_b} + C_{\mathrm{O\&M}}^{\mathrm{EES}}\left(P_{\mathrm{EES_{ch},\,t,b}} + P_{\mathrm{EES_{dch},\,t,b}}\right) \\
& \left. + C_{\mathrm{cap}}^{\mathrm{REES}} S_{\mathrm{REES}_b} + C_{\mathrm{O\&M}}^{\mathrm{REES}}\left(P_{\mathrm{REES_{ch},\,t,b}} + P_{\mathrm{REES_{dch},\,t,b}} + P_{\mathrm{REES_{NEM},\,t,b}}\right)\right)
\end{aligned}
\tag{47}
$$

The objective function is thus minimized subject to a set of equality and inequality constraints, and also integer constraints, lower l and upper u bounds, which limit strictly positive variables and Big M limits.

The MILP optimization problem is given by the following functions and constraints: Where $J(x)$ is the objective functions and A and B are the respective coefficient matrices for the x continuous decision variables and y integer decision variables. The problem is subjected to linear equality and inequality constraints, l and u upper and lower bounds, and integer constraints on y. The objective function is minimized subject to a set of equality and inequality constraints, and also integer constraints, which are detailed in the following sections.

$$\begin{array}{lll} \textbf{min} & J(x) & (47) \\ \boldsymbol{s.t.} & Ax + By \leq b & (49)\text{-}(69),(74) \\ & l \leq x \leq u & * \; l \text{ and } u \text{ are specific to variable} \\ & y \in \mathbb{Z}^n & \\ & y \geq 0 & \end{array} \tag{48}$$

5.2.3. General Constraints

In this optimization formulation, equality and inequality constraints are formulated to:

- Ensure the electrical energy balance within each building, *i.e.*, the electrical demand of the building, is entirely met at each time step while maintaining feasible operation;
- Set maximum and minimum generation output constraints for each DER;
- Control the operation of all electrical energy storage systems; and
- Limit the states of charge and charging rates for each battery system.

A concept similar to the Energy Hub, introduced in Morvaj *et al.*(Morvaj et al., 2016), is explored here, but only applied to electricity balances. Here, each building and its connected DER (PV, EES, and REES) represent a Building Energy Hub. Hence, the electricity needs of every building are to be met by an optimally sized combination of PV, EES, REES, and electricity imports. The model also makes the distinction between active (P), reactive (Q), and apparent (S) power flows. Considering active power, Equation (49) requires that at all times t, for every building b, the active electrical load ($P_{\mathrm{BLDG}_{t,b}}$) plus any EES charging ($P_{\mathrm{EES}_{\mathrm{ch}},t,b}$), is met through electricity imports ($P_{\mathrm{import}_{t,b}}$), currently available solar production sent to the building ($P_{PV\mathrm{BLDG,t},b}$), and the discharging of any EES or REES assets ($P_{\mathrm{EES}_{\mathrm{dch}}t,b}$ and

$P_{\mathrm{REES}_{\mathrm{dch}}t,b}$). Considering reactive power, Equation (50) requires that, the reactive electrical load of each building ($Q_{\mathrm{BLDG}_{t,b}}$), which will depend upon a fixed local power factor (PF) will be entirely met by utility reactive power imports ($Q_{\mathrm{import}_{t,b}}$). Note that no security or reliability margins are included in our formulation.

$$P_{\mathrm{import}_{t,b}} + P_{\mathrm{PV}_{\mathrm{BLDG},\,t,b}} + P_{\mathrm{EES}_{\mathrm{dch},\,t,b}} + P_{\mathrm{REES}_{\mathrm{dch},\,t,b}} = P_{\mathrm{BLDG}\,t,b} + P_{\mathrm{EES}_{\mathrm{ch},\,t,b}} \quad (49)$$

$$Q_{\mathrm{import}_{t,b}} = Q_{\mathrm{BLDG}_{t,b}} = \mathrm{P}_{\mathrm{BLDG}}\arctan(PF) \quad (50)$$

Equations (51), (52) and (53) relate electrical imports to both non-TOU and TOU demand charges. Where subscripts o and p are the set of all hourly increments during on-peak and mid-peak, respectively, in summer month s.

$$P_{\mathrm{import,t},b} \leq P_{DC,s,b} \quad (51)$$

$$P_{\mathrm{import,o},b} \leq P^{\mathrm{on}}_{\mathrm{DC},s,b} \quad (52)$$

$$P_{\mathrm{import,p},b} \leq P^{\mathrm{mid}}_{\mathrm{DC},s,b} \quad (53)$$

Solar PV adoption and operation constraints are shown in Equations (54) and (55). Equation (54) limits PV production by the PV capacity adopted (S_{PV_b}) and available insolation (I_t). Equation (55) limits the size of the PV adoption at each building according to the maximum available rooftop area (A_b) and the kW/ft^2 ratio (σ).

$$P_{\mathrm{PV}_{\mathrm{BLDG},\,t,b}} + P_{\mathrm{PV}_{\mathrm{NEM},\,t,b}} + P_{\mathrm{PV}_{W,\,t,b}} + P_{\mathrm{REES}_{\mathrm{ch},\,t,b}} \leq I_t S_{\mathrm{PV}_b} \quad (54)$$

$$S_{\mathrm{PV},b} \leq \sigma\,\mathrm{A}_b \quad (55)$$

Within electrical energy storage, the model considers two types of storage, (1) electrical energy storage, or EES, which can store imported utility electricity and excess renewable produced onsite and also (2) renewable electric energy storage, or REES, which is the storage exclusively supplied by renewable onsite PV. A distinction between EES and RESS is made because only energy storage exclusively charged using renewable energy is allowed to be exported to the grid under California NEM rates. Both the EES and REES share similar types of constraints. Equations (56) and (60) show the energy balance for the EES and REES respectively. The difference between EES and REES is the presence of the $P_{REES\,NEM\,dchrg,t,b}$ variable, allowing electricity export from any adopted REES. Note that wholesale import, *i.e.*, electricity imported

to the building, billed at wholesale prices, is not considered for REES charging since initial simulations indicated that this pathway is not economically attractive due to the REES round trip efficiency. Equations (57) and (61) limit the maximum state of charge by the installed capacity for the EES and REES, respectively. Equations (58) and (62) limit the maximum discharge rate by the size of the adopted battery, and Equations (59) and (63) limit charging to the battery for the EES and REES system, respectively. Equations (17) and (18) require that if EES and REES systems are adopted, a minimum system size is installed. The minimum battery size is based upon the popular Tesla Powerwall size of 13.5 kWh (Tesla, 2019). The variables $n_{EES,b}$ and $n_{REES,b}$ are binary variables, that is, integer variables that are restricted to values of 0 or 1.

$$e_{\mathrm{EES},t,b} = \alpha_{\mathrm{EES}} e_{\mathrm{EES}\,(t-1),\mathrm{b}} + \eta_{\mathrm{EES\,ch}} P_{\mathrm{EES\,ch},t,b} - \frac{P_{\mathrm{EES\,dch},t,b}}{\eta_{\mathrm{EES\,dch}}} \tag{56}$$

$$\underline{\delta}_{\mathrm{EES}} E_{\mathrm{EES},b} \leq e_{\mathrm{EES}\,,t,b} \leq \bar{\delta}_{\mathrm{EES}} E_{\mathrm{EES},b} \tag{57}$$

$$P_{\mathrm{EES\,dch},t,b} \leq \bar{\mu}_{\mathrm{EES}} S_{\mathrm{EES},b} \tag{58}$$

$$P_{\mathrm{EES\,ch},t,b} \leq \underline{\mu}_{\mathrm{EES}} S_{\mathrm{EES},b} \tag{59}$$

$$e_{\mathrm{REES},t,b} = \alpha_{\mathrm{REES}} e_{\mathrm{REES}\,(t-1),\mathrm{b}} + \eta_{\mathrm{REES\,ch}} P_{\mathrm{REES\,ch},t,b} - \frac{P_{\mathrm{REES\,dch},t,b} + P_{\mathrm{REES\,NEM},t,b}}{\eta_{\mathrm{EES\,dch}}} \tag{60}$$

$$\underline{\delta}_{\mathrm{REES}} E_{\mathrm{REES},b} \leq e_{\mathrm{REES}\,,t,b} \leq \bar{\delta}_{\mathrm{REES}} E_{\mathrm{REES},b} \tag{61}$$

$$P_{\mathrm{REES\,dch},t,b} + P_{\mathrm{REES\,NEM},t,b} \leq \bar{\mu}_{\mathrm{REES}} S_{\mathrm{REES},b} \tag{62}$$

$$P_{\mathrm{REES\,ch},t,b} \leq \underline{\mu}_{\mathrm{REES}} S_{\mathrm{REES},b} \tag{63}$$

$$\left(1 - n_{\mathrm{EES},b}\right) \underline{S}_{\mathrm{EES}} \leq S_{\mathrm{EES},\,b} \leq \left(1 - n_{\mathrm{EES},b}\right) \bar{S}_{\mathrm{EES}} \tag{64}$$

$$\left(1 - n_{\mathrm{REES},b}\right) \underline{S}_{\mathrm{REES}} \leq S_{\mathrm{REES},\,b} \leq \left(1 - n_{\mathrm{REES},b}\right) \overline{S}_{\mathrm{REES}} \tag{65}$$

Equation (66) constrains the value of exported electricity under NEM rates to the cost of imported electricity. Equation (67) imposes the ZNE operation, *i.e.*, total imports must be less than or equal to total exports by the end of the year.

$$\sum_{b=1}^{B}\sum_{t=1}^{T} C_{\text{NEM}t,b}\left(P_{\text{PV NEM},t,b} + P_{\text{REES NEM }t,b}\right) \leq \sum_{b=1}^{B}\sum_{t=1}^{T} C_{\text{grid},t,b} P_{\text{import}.t,b} \tag{66}$$

$$\sum_{b=1}^{B}\sum_{t=1}^{T} P_{\text{PV NEM},t,b} + P_{\text{PV W},t,b} + P_{\text{REES NEM },t,b} \leq \sum_{b=1}^{B}\sum_{t=1}^{T} P_{\text{import}.t,b} \tag{67}$$

5.2.4. Transformer Constraints and Polygon Relaxation

Here, we extend the formulation to a multi-node approach, where every Building Energy Hub (*i.e.*, building load and corresponding DER resources) is connected to spatially resolved nodes instead of a single physical (aggregated) node. The multi-node method allows for the modeling of the electric power distribution grid and the constraints involved with the physical power network and equipment.

The maximum amount of current limits the power capacity of a transformer at the rated voltage, so it does not exceed its design temperature. Ratings are specified in kilovolt-amperes (kVA), which corresponds to the total apparent power that can flow through transformer windings, which includes active (kW) and reactive (kVAr) power flows (Kurtz, Shoemaker, & Mack, 1997), as shown in Figure 5.2. Transformer overloads are typically acceptable for a short amount of time, and a typical transformer loading curve varies according to different ambient temperatures (U.S.Department of the Interior Bureau of Reclamation - Facilities Engineering Branch, 2000). Nonetheless, even short periodic overload conditions will affect the equipment lifespan and maintenance needs.

We assume a distribution transformer is connected to a given node in the network and serves one or a cluster of Building Energy Hubs. Figure 5.1 illustrates one such transformer T_x, which supplies only one Building Energy Hub, and its associated Solar PV and battery electric energy storage systems.

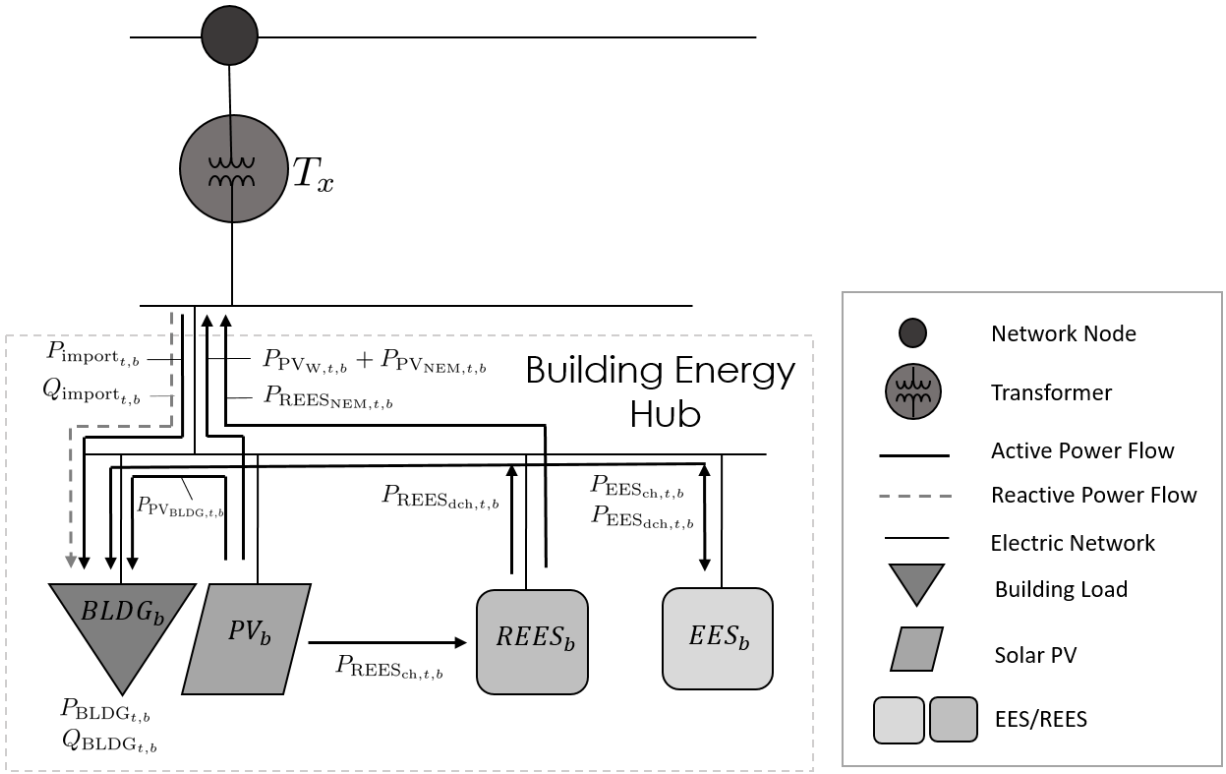

Figure 5.1 – Schematic of one Building Energy Hub used in the multi-nodal approach. Transformer T_x is one node, to which a cluster of buildings and DER are connected.

As shown in Figure 5.1, each building has a net energy flow of imports minus exports from solar PV and REES. The net real and reactive power flows for all building energy hubs that are connected to the same transformer are aggregated using Equation (68) and (69).

$$P_{\text{T}_x} = \sum_{j \in J_k} P_{\text{import}_j} - P_{\text{PVNEM}_j} - P_{\text{PV W}_j} - P_{\text{REES dch NEM}_j} \tag{68}$$

$$Q_{\text{T}_x} = \sum_{j \in J_k} Q_{\text{import}_j} \tag{69}$$

In Equations (70) and (71), for each time step, the absolute value of the apparent power flowing through a given transformer x, S_{Tx}, defined by the vector sum of active and reactive power, cannot exceed a given percentage (α) of its kVA rating ($\bar{S}_{T_x}$), where α is a coefficient used to allow under and overloading. Ultimately, all buildings and DER will have a transformer, or node, with such constraints associated with it.

$$S_{\text{T}_x} = \sqrt{P_{\text{T}_x}^2 + Q_{\text{T}_x}^2} \tag{70}$$

$$S_{\text{T}_x} = \alpha \bar{S}_{\text{T}_x} \tag{71}$$

Since a MILP method cannot directly capture the nonlinear constraints shown in Equations (70) and (71), a polygon relaxation of the apparent power circle shown in Figure 5.2 is performed. The method was inspired by Archimedes' π calculation process using polygons of an increased number of edges to approximate a circle(Archimedes (ed.Heath), 1897) . This particular approach was used as an effective method for modeling directional thrust for a ship (Erdal, 2015). First, a polygon with Λ sides is inscribed inside the circle created by Equation (70). A second circle with radius $s_{T_x} < \bar{S}_{T_x}$ can be inscribed within the polygon. In this case, the maximum s_{T_x} is defined by $s_{T_x} = \bar{S}_{T_x} cos\left(\frac{\pi}{\Lambda}\right)$, where increasing the number of sides L decreases the difference between maximum s_{T_x} and $\bar{S}_{T_x}$. Considering that the error as defined by the difference between s_{T_x} and $\bar{S}_{T_x}$ is given by Equation (72), absolute error can be reduced below 1% by setting the number of polygon sides Λ to 22. Using this approximation, power through a transformer can be written as Equation (73), and implemented directly into the MILP optimization model as Equation (74).

$$\epsilon = \overline{S}_{\mathrm{T}x} - s_{\mathrm{T}x} = \overline{S}_{\mathrm{T}x}\left(1 - \cos\frac{\pi}{\Lambda}\right) \rightarrow \Lambda \geq \frac{\pi}{\arccos\left(1 - \frac{\epsilon}{\overline{S}_{\mathrm{T}x}}\right)} \tag{72}$$

$$s_{\mathrm{T}x} = P_{\mathrm{T}x}\cos(\theta_\lambda) + Q_{\mathrm{T}x}\sin(\theta_\lambda) \quad , \quad \theta_\lambda = \frac{\pi}{\Lambda} + \lambda\left(\frac{2\pi}{\Lambda}\right), \quad \lambda = 0,1,\ldots,\Lambda - 1 \tag{73}$$

$$s_{\mathrm{T}x} \geq \begin{bmatrix}\cos(\theta_\lambda) & \sin(\theta_\lambda)\end{bmatrix}\begin{bmatrix}P_{\mathrm{T}x} \\ Q_{\mathrm{T}x}\end{bmatrix} \tag{74}$$

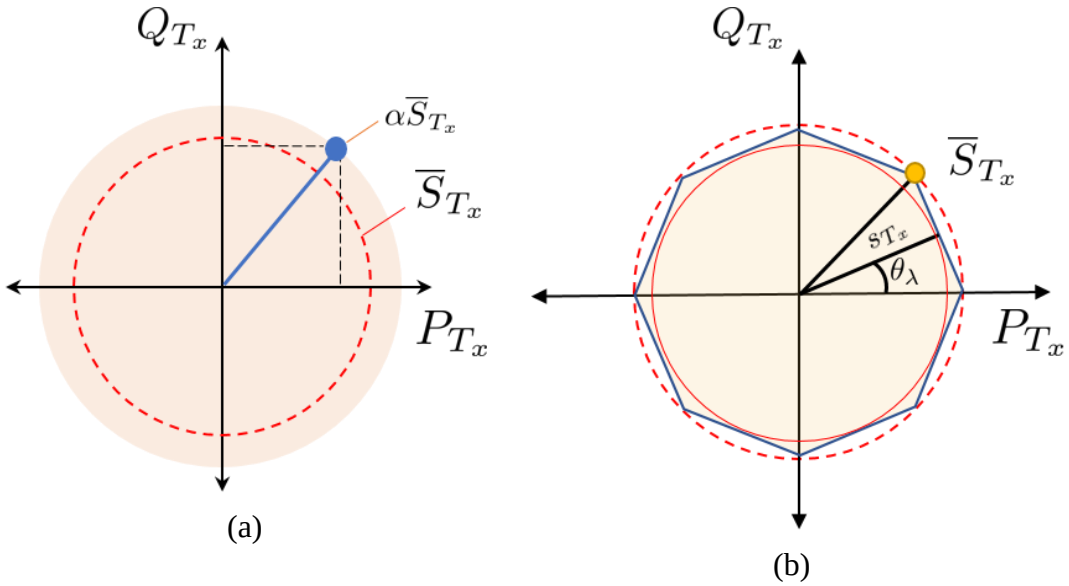

Figure 5.2 – (a) Operating regions for the transformer must be constrained so that $\alpha S_{T_x} = \sqrt{{P_{T_x}}^2 + {Q_{T_x}}^2}$ *and (b) Depiction of the polygon relaxation constraint*

Similar polygon relaxation techniques have been explored and used in recent literature (Ahmadi, Member, & Mart, 2015; Gholami, Shekari, & Grijalva, 2019; Mashayekh et al., 2017), but to the best of our knowledge, this concept has not been previously applied to limit transformer apparent power flows in a linear optimization.

5.3. Test Case

We use as test case the same system introduced in Chapter 4, a neighborhood in Huntington Beach, CA known as Oak View. The Oak View community includes over 300 buildings, including commercial and industrial operations, a primary school and library, and over 280 primarily multifamily homes. In this chapter, we take a step further and model the time-varying load demand as well as the time-varying PV resource, which are necessary inputs for the time-series MILP. A summary of both modeling and the description of assumed DER properties used in the current work are presented in this section.

5.3.1. Electrical Demand and Resource Modeling

Representative loads from the entire Oak View community building stock were selected from each of the three primary building sectors, namely, residential, commercial, and industrial. Detailed models of these buildings were developed in EnergyPlus (McDonald, 2017). The

outputs of these building models were used as inputs to the current DERopt optimization. Examples of a residential, commercial, and year-round industrial demand, colored by season, are presented in Figure 5.3.

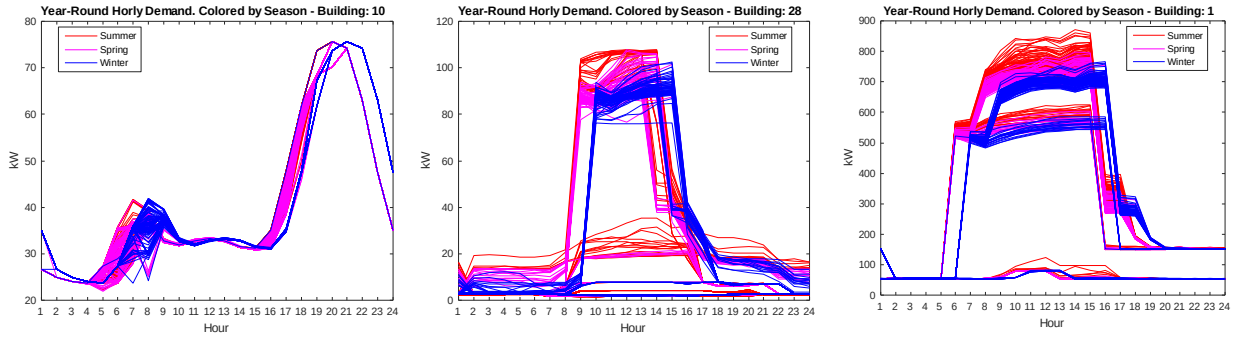

(a) (b) (c)

Figure 5.3 – Transformer-aggregated demand profiles for (a) Residential loads, (b) Commercial loads, and (c) Industrial loads. Color shows representative load variations for different seasons.

The building energy simulations produced hourly-resolved loads over an entire year. In order to pursue a tractable optimization model, the building annual energy datasets are reduced using the k-medoids methodology presented in Domíngues *et al.*(Domínguez-Muñoz, Cejudo-López, Carrillo-Andrés, & Gallardo-Salazar, 2011). The building energy simulation data was filtered to yield three representative days for each month. Finally, buildings behind a single transformer that are not subject to a demand charge were aggregated to reduce problem scale. Since the applicable Southern California Edison residential rates do not include a demand charge (Southern California Edison, 2019), most residential buildings were aggregated behind a single transformer. Thus, for residential loads, the terminology used here as "Building #" in fact refers to a cluster of residential buildings behind a single transformer.

Solar generation measured from a PV system installed at the University of California, Irvine was used as input (White, 2016). The annual generation profile dataset captures and seasonal and weather variations.

The maximum PV capacity for each building (or group of residential buildings) was determined using aerial images of the neighborhood and the PV software HelioScope (Folsom Labs, 2017). The maximum amount of PV *kWp* (kilowatts peak) that each rooftop in the Oak View community would be able to accommodate was determined considering rooftop geometry, set-backs and keep-outs determined by rooftop equipment, exhaust ports, and fire safety code

requirements. From this survey, the *kWp* installed/ft^2 coefficient (σ) was determined to be 0.009 *kWp* installed/ ft^2 for commercial and industrial buildings and 0.005 a *kWp* installed/ft^2 for residential buildings. A detailed list of all building load maximum demand, total energy demand, allowable PV area, in ft^2, the associated transformer number and its power rating, and building power factor is presented in Table 5.3.

Note that, in the Oak View case, the commercial and industrial rooftop area that is structurally capable of having a solar PV installation is relatively small in comparison to the loads in those same buildings. As a result, approximately 25% of some large industrial loads can be met through onsite solar PV. Prior to optimization, it is clear that community-scale ZNE in this particular community is only feasible when the remaining 75% is produced elsewhere in the community. Figure 5.4 illustrates results from this analysis, where C&I buildings 3,5, and 6 cannot meet their total annual energy demand with their own total annual onsite PV generation.

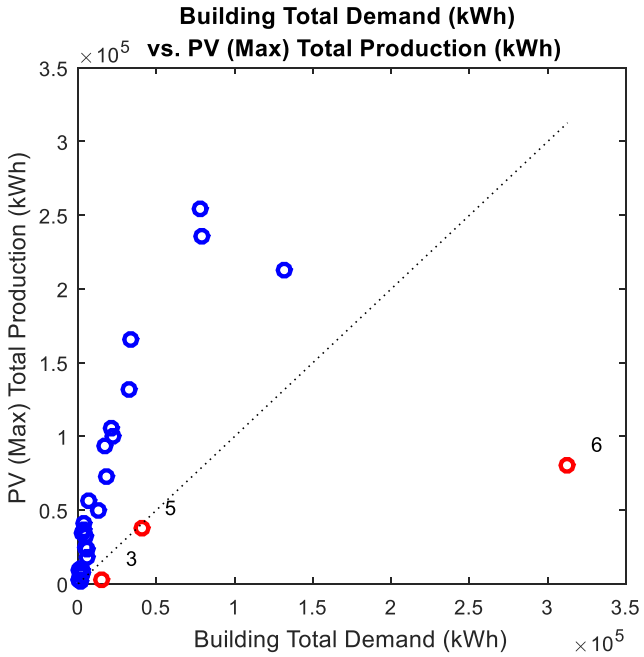

Figure 5.4 – Building total annual demand versus maximum total onsite yearly PV production, both in (kWh)

5.3.2. Electrical Distribution Infrastructure

Our AEC microgrid test system was developed based upon the real-world infrastructure installed in the Oak View neighborhood. The topology of the electrical power system, was already presented in Chapter 4, and is shown again in Figure 5.5 for completion. The Oak View AEC comprises single and multi-family residential buildings, a primary school, a library, a small park,

and some industrial and commercial properties. The power distribution system to support the community is a three-phase 12 kV feeder, which branches into single-phase, 240 V phase-to-phase (120 V phase-to-ground) circuits, for residential service and three-phase 480/277 V for commercial and industrial service.

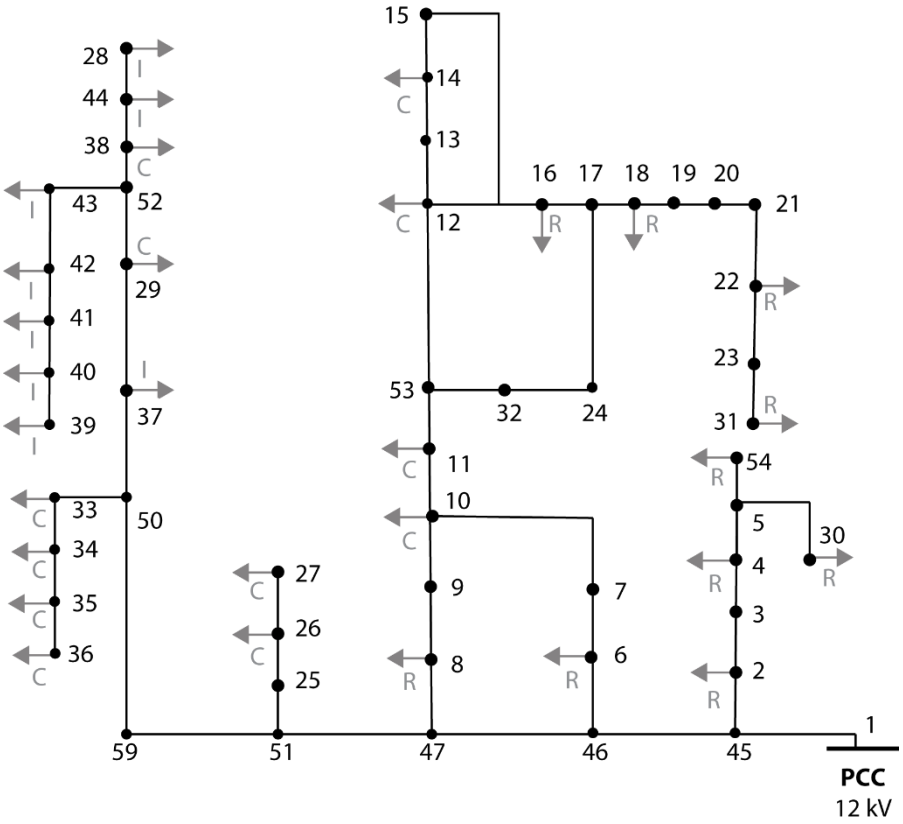

Figure 5.5 – Advanced Energy Community Low Voltage distribution grid network topology and load allocation (loads identified as residential, R, commercial, C, or industrial, I)

The test system is comprised of 54 nodes, 56 branches, 31 clustered building loads, and 30 transformers. The Slack bus is node 1, and it represents the PCC with the wide-area grid.

A load allocation was performed, using 31 representative buildings (and aggregated residential buildings), placing them in the nodes as shown in Figure 5.5 and scaling up their loads (clustering) to obtain a representative share of loads from each sector. For this community, electricity demand is 60% Industrial, 27% Residential and 13% Commercial. The distribution transformer kVA ratings, listed in Table 5.3 were sized to accommodate the aggregated loads served (*i.e.*, all power flows kept below 1.p.u. loading), taking into consideration the discretized ratings of transformers that are commercially available. We assume only rooftop PV is installed in the community.

Table 5.3 – AEC building loads, Maximum demand (kW), Total annual demand (kWh), Type, Rate Structure, Total Area (ft^2), Maximum rooftop PV installed (kW), Connected Transformer number, Transformer rating (kVA)

Building #	Max Load (kW)	Total (kWh)	Load Type	TOTAL Area (ft^2)	Max PV (kW)	PF	Transformer #	Transformer Rating (kVA)
1	872	2,743,640	I	140,086	1296	0.8	37	1250
2	27	78,338	I	23,843	221	0.8	40	37.5
3	100	327,587	I	1,892	18	0.8	28	150
4	18	57,404	I	22,673	210	0.8	44	25
5	170	840,106	I	24,575	227	0.8	39	250
6	1152	6,550,187	I	52,881	489	0.8	41	1500
7	5	8,066	I	6,278	58	0.8	42	25
8	27	99,994	I	21,403	198	0.8	28	37.5
9	21	68,847	I	27,140	251	0.8	43	37.5
10	76	350,279	R	114,103	573	0.9	2	100
11	420	1,585,376	R	308,880	1552	0.9	54	500
12	91	423,972	R	128,665	647	0.9	4	150
13	55	259,589	R	60,870	306	0.9	6	75
14	146	676,063	R	201,141	1011	0.9	30	200
15	6	24,338	R	1,719	9	0.9	18	25
16	138	655,735	R	159,390	801	0.9	22	200
17	90	449,899	R	121,954	613	0.9	8	150
18	10	48,347	R	11,620	58	0.9	31	25
19	81	374,790	R	88,777	446	0.9	16	100
20	24	98,388	C	16,109	149	0.85	29	37.5
21	24	35,067	C	3,987	37	0.85	34	37.5
22	9	12,180	C	1,624	15	0.85	27	25
23	49	56,530	C	4,867	45	0.85	35	75
24	30	36,350	C	5,441	50	0.85	14	37.5
25	74	109,745	C	11,990	111	0.85	38	100
26	35	47,181	C	4,419	41	0.85	10	50
27	79	120,429	C	15,379	142	0.85	33	100
28	108	143,182	C	36,866	341	0.85	12	150
29	779	1,655,836	C	155,232	1436	0.85	36	1000
30	9	12,288	C	1,572	15	0.85	26	25
31	20	38,001	C	6,691	62	0.85	11	25

5.3.3. Cost and Operational Assumptions

All DER cost and operational assumptions used are listed in Table 5.4. Our assumed capital cost for a battery storage system is based on the 2018 Lazard's Levelized Cost of Storage Analysis

report(Lazard, 2018b), and it is specific to Lithium-ion, behind-the-meter Commercial & Industrial projects with battery storage co-located with PV. Also, the cost is composed of the storage module, the balance of system, and related engineering procurement and construction costs. We also assume that the O&M fixed cost is embedded in the capital cost monthly payments, and the variable O&M costs are assumed from (R. J. Flores & Brouwer, 2018)

Table 5.4 – DERopt Cost and Operational Assumptions

Assumption	PV	EES
Capital Cost	2,000 $/kW (installed)(Lazard, 2018a)	600 $/kWh (installed)(Lazard, 2018b)
O&M Cost	0.001 $/kWh (generated) (R. J. Flores & Brouwer, 2018)	0.001 $/kWh (charged/discharged) (R. J. Flores & Brouwer, 2018)
Min SOC	-	0.1
Max SOC	-	0.95
Ramp rate	-	0.25 (% of capacity)
Efficiency	20%	90% (Charge/Discharge)
State of charge holdover	-	99.5%
Interest rate	8%	
Project lifetime	10 years	
Equity	20%	
Required Return	12%	

DERopt also captures electrical utility rates for all building and sector types and also captures the intricacies of exporting electricity, under NEM and wholesale rates. Under NEM rates, the utility customer can export electricity at the rate at which it is purchased, or retail rates, minus a non-bypassable charge (typically around $0.02 per kWh). However, a utility customer can only export as much electricity as it is imported. Moreover, the customer can only receive credits on their monthly bill, and cannot receive direct payment. In DERopt, if more electricity is exported than imported, the excess is not credited to the utility customer under NEM rates, but the customer is still able to sell electricity under wholesale rates, with values that are typically around $0.02 per kWh.

The utility electricity tariffs modeled in DERopt are based on Southern California Edison Time-of-Use (TOU) rates schedules as of 2018. For large C&I customers, Schedule TOU-8-B-2 kV to 50 kV for general service is adopted, and for residential customers, Schedule TOU-D-A for domestic service is adopted. Figure 5.6 illustrates the TOU rate schedules energy price ($/kWh) on the primary axis and demand charge ($/kW) on the secondary axis. Note that utility rates vary by season: Summer (from June to September, spanning 4 months) and Winter (from October to May, spanning 8 months) and also by day of the week (weekend versus weekday); for a given season and customer class, weekday rates are almost always more expensive than weekend rates. Moreover, in the TOU rate schedule assumed here, electricity prices can differ by up to nine-fold, which is the case for residential summer weekday on-peak rate versus off-peak rate. Demand charges are applied only to C&I customers and are also time-dependent. The differences in electricity price, driven by the TOU rate schedules, and demand charges strongly influence battery storage dispatch.

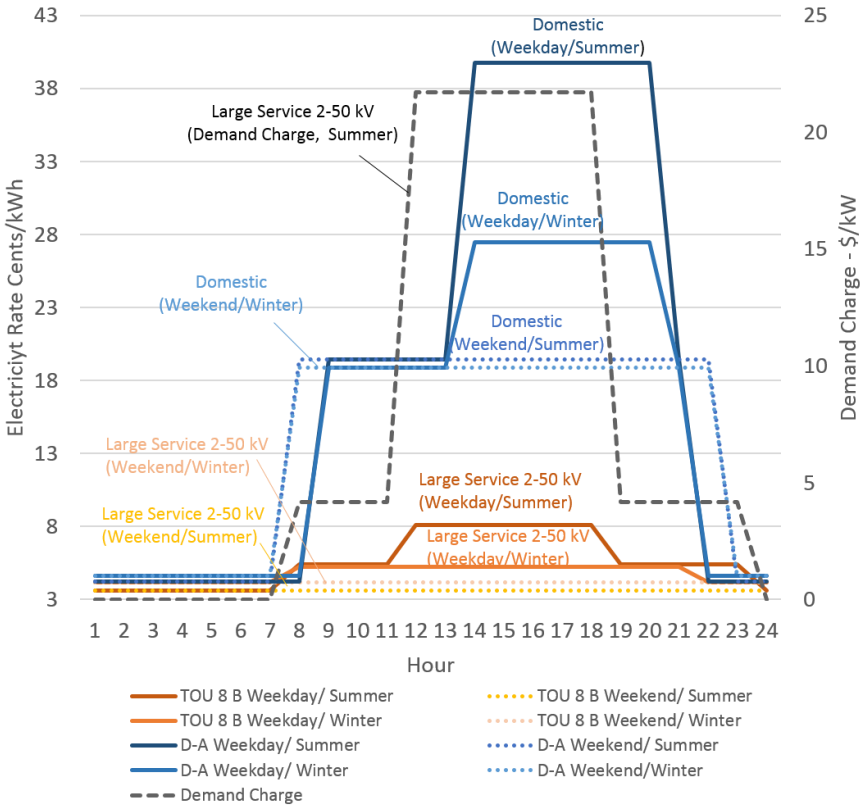

Figure 5.6 – Rate structures for utility electricity. Schedule TOU-8-B is used for large C&I utility customers, and Schedule D-A is used for residential utility customers. Color shows detail on different Schedules. Weekend rates are shown by dotted lines, and the secondary axis shows demand rates on dashed lines.

5.4. Results and Discussion

The optimization algorithm is implemented in MATLAB R2015a (The MathWorks Inc., n.d.) using the YALMIP R20181012 toolbox (Lofberg, 2005; Löfberg, 2019) and CPLEX v.12.8 (IBM, 2017) for the MILP solver. The k-medoids methodology reduces our dataset to 36 representative days for simulating the entire year; therefore, 864 hourly intervals are simulated. The hardware used for the optimization is an Intel Xenon CPU E5-2680 v2 @2.80 GHz server with 20 cores, 40 threads, and 32 GB of RAM. Simulation times average 280 seconds (with area and polygon transformer constraints, and around 41 minutes with island constraints. It is worth noting that piecewise linearization of the transformer constraints was implemented for the same scenarios and run times ranged from 25 to 30 minutes. Thus, polygon constraints are approximately 6 times faster.

The results presented in this section aim to identify the relevance and impacts of including transformer constraints (TC) in the design of AEC systems. To capture common district system and microgrid goals, two strategies are tested: (1) Zero Net Energy constrained, *i.e.*, to annually produce as much electricity as demanded, and (2) Islanding constraint, *i.e.*, to be able to meet critical loads under a non-planned utility grid network outage situation. The solar PV area constraint was also evaluated. Thus, the first set of scenarios simulated refers to ZNE operation with and without transformer constraints, the second set explores area constraints added to the first scenario set, and the third set employs the same constraints of the second set but explores a microgrid islanded operation instead of ZNE operation. The list of all scenarios simulated is given below:

1. **ZNE / ZNE + Transformer Constraints**: ZNE operation, constrained area for rooftop PV adoption, with or without transformer constraints;
2. **ZNE + Area Constraints / ZNE + Area Constraints + Transformer Constraints**: ZNE operation, constrained area for rooftop PV adoption, with or without transformer constraints;
3. **Island/ Island + Transformer Constraints:** Island operation, constrained area, with or without transformer constraint. It is assumed that critical loads are industrial and school, all other loads are shed. During islanding, there is no revenue for NEM and wholesale exports.

5.4.1. Using Optimization to Quantify and Eliminate Transformer Overloads

In all scenarios, excessive amounts of PV power (or REES discharge in some cases) export are the root cause for transformer overload. The degree to which these overloads exceed transformer ratings (without transformer constraints considered) is shown in the left panels of Figure 5.7, where each data point represents a transformer rated power capacity is plotted against its all-time maximum overload, *i.e.,* its maximum power injection recorded over the optimization timeframe. The x-axis was split into two data ranges: 25-500 kVA and 500-1500 kVA for better visualization of results. Overloaded transformers are shown in red and above the dotted line.

Out of a total of 30 transformers, the number of overloaded transformers was 13 for the first scenario, 17 for the second scenario, and 15 for the islanded scenario. The increase in transformer overloads when constraining the area points to the leveraging of the available physical area for PV deployment within the community, and the resulting increased PV adoption behind transformers feeding buildings with a larger rooftop area, namely transformers T11, T12, T29, T33, and T36. For almost all of those transformers, the maximum, area-constrained PV deployment is adopted (see Table 5.3 for maximum area-constrained PV deployment size and Table 2 in the Appendix, for transformer PV adoption) and these capacities lead to power production that is well beyond the transformer power ratings.

After transformer constraints are applied, the kVA flows through each transformer are forced to comply with their kVA power rating, and overloads are eliminated as shown in the right panels of Figure 5.7. All transformer overloads were eliminated by either reducing PV adoption, increasing battery energy storage adoption, or curtailing PV at the C&I buildings.

Figure 5.8 plots the net power flow through one given transformer, namely T54, over the optimization timeframe, before and after transformer constraints were applied; positive flows indicate exports to the grid. T54 is rated at 500kVA and feeds a large residential load cluster and hosts a large PV adoption that is in the MW order of magnitude (we refer the reader to Table 2 in the appendix for the detailed adoption values for all scenarios). Overloads, which occurred in the scenario without transformer constraints, are indicated by the solid red curve and are compared against the transformer-constrained operation, indicated by the dashed blue curve. Notice that high exports of excess PV generation cause overloads. These high exports, however,

are removed in the constrained scenarios through the adoption of battery energy storage, which "clips" the high PV exports by charging with the excess PV generation. Transformer constraints leveraged the adoption of 855 kWh of combined EES and REES for the ZNE case. For the area-constrained ZNE case, this adoption is even higher, at 2,332 kWh, to meet ZNE with a reduced PV adoption.

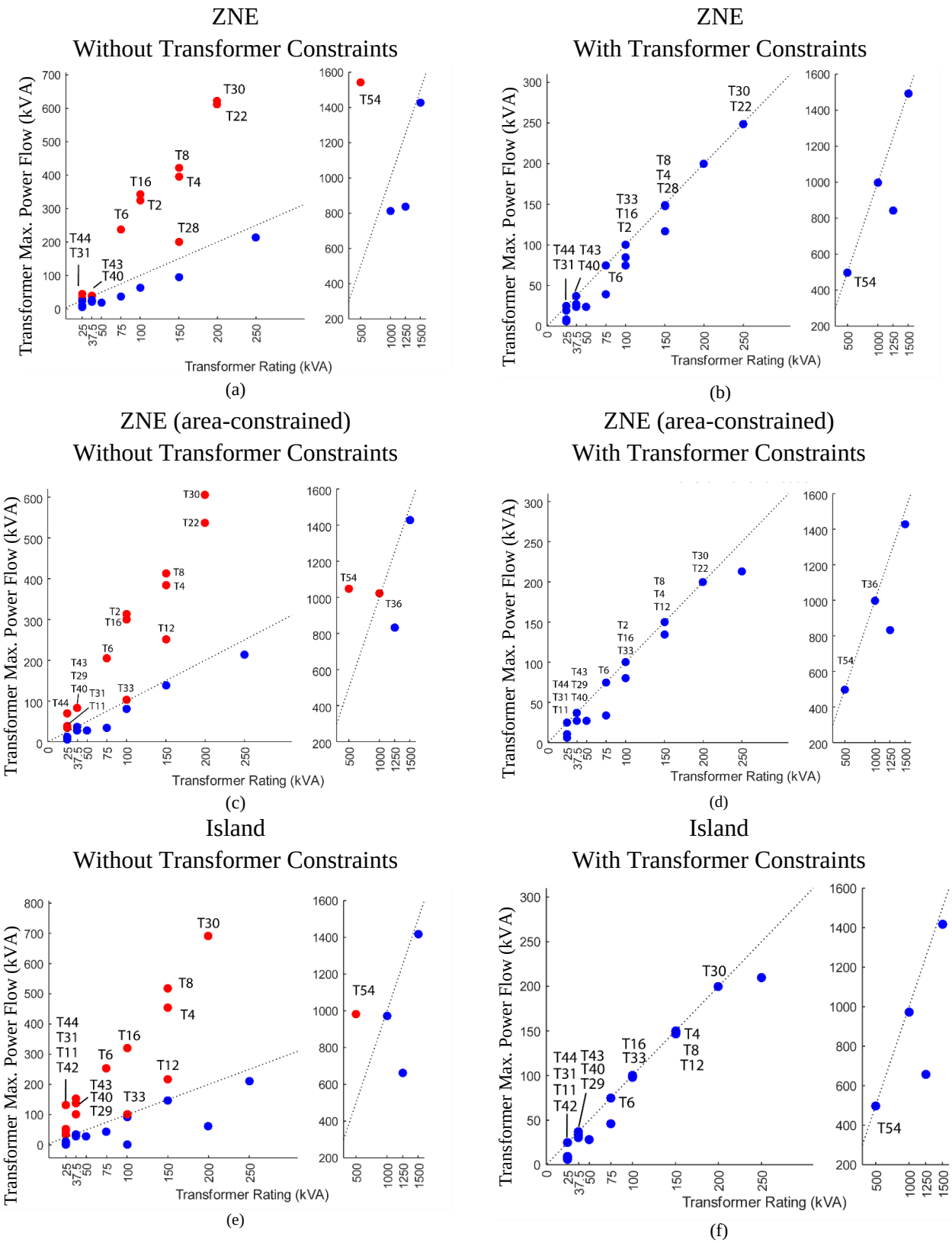

Figure 5.7 – Transformer overloads for (a) ZNE without transformer constraints and (b) ZNE with transformer constraints. (c) ZNE without transformer constraints and (d) ZNE with transformer constraints, (e) Island, without transformer constraints and (f) Island, with transformer constraints.

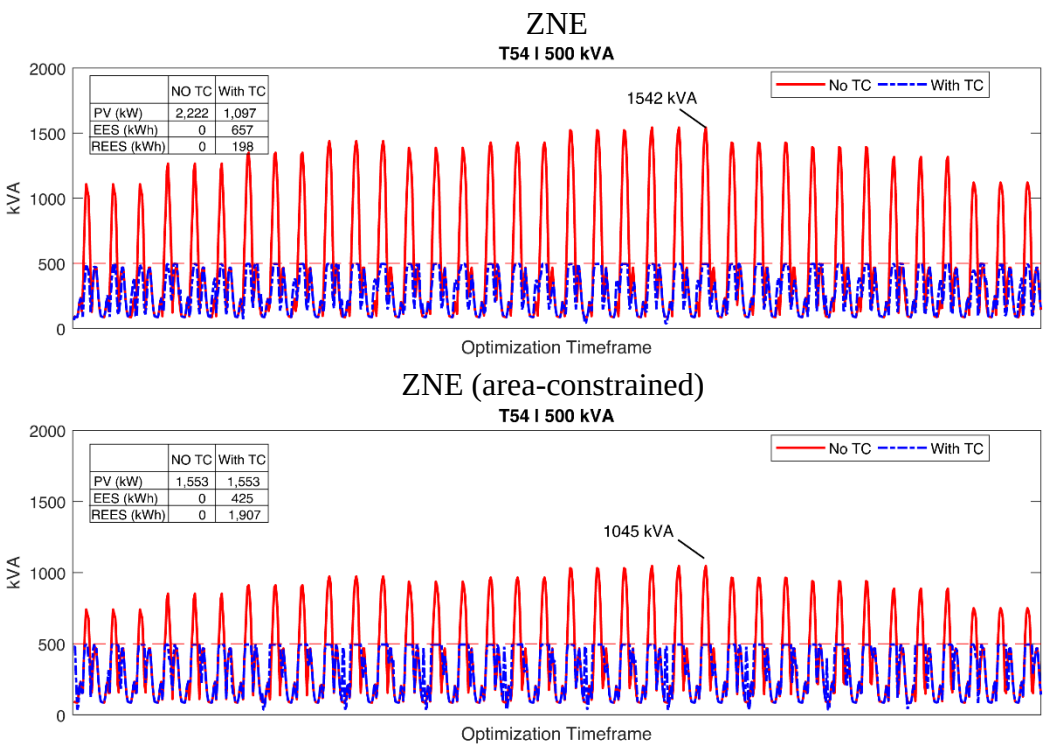

Figure 5.8 – Transformer 54 (500kVA) kVA power flows: comparison of before (solid red curve) and after (blue dashed curve) transformer constraints for ZNE (top), ZNE area-constrained (middle) and island (bottom) scenarios.

5.4.2. Impacts of Transformer Constraints on DER Allocation

Figure 5.9 compares the DER allocation in each individual building for each scenario set. Buildings 1 to 9 are industrial loads, buildings 9 to 19 are residential loads and buildings 20 to 31 are commercial loads. The first scenario set (Figure 5.9a) does not impose any constraints on the area available for PV installation. With no transformer constraints applied, PV is adopted in proportion to the magnitude of the building loads. Therefore, most (63%, or 6.7 MW) of the total community PV capacity is adopted in the residential sector, as our test case has a large number of residential loads, followed by the industrial sector (24%, or 2.53 MW), and commercial sector (13%, or 1.37 MW). This allocation, overloads local transformers, as shown in Figure 5.7. When transformer constraints are added, however, the PV capacity is redistributed leading to a shift of the PV capacity from the residential to the C&I sector, which has its typically larger transformer capacity leveraged to compensate for the reduction in PV on the residential sites, with smaller transformers. For instance, the PV adoption is reduced at Building 11, a cluster of residential buildings (from 2,222 kW to 1,096 kW) and increased at Building 6, an industrial site (from 894 to 2,766 kW).

After imposing area constraints for PV installation (Figure 5.9b), PV adoption becomes more evenly distributed across the buildings in the community, and little to no EES/REES is adopted. Intuitively, area constraints recommend PV system placement not at the buildings with larger loads but upon the buildings with available rooftop space. The constraint leverages the buildings in the residential and commercial sectors with enough area available for PV adoption to support the demand in the industrial sector, which cannot meet the energy demand using onsite PV. As discussed previously, this is often true for industrial building types, and regarding our test-case system, this fact is illustrated in Figure 5.4. Thus, these loads will likely depend upon energy imports from neighboring buildings, which reinforces the benefits of aggregating various loads as a community/microgrid if the goal is community-scale ZNE. As a result, the PV adoption in the vast majority of commercial and residential buildings equals to the maximum amount of area-limited maximum PV hosting capacity. For instance, PV adoption on Building 36, a cluster of commercial loads, is increased from 876 kW to 1,436 kW, the local area-constrained maximum PV capacity. This DER allocation, however, causes overloads, especially in residential transformers that are typically smaller in power capacity. When transformer constraints are added, transformer overloads are avoided through the adoption of EES/REES. REES storage is shown to be preferred (Figure 5.9) since discharge for grid export is allowed.

For the island case, a significant amount of storage is deployed to accomplish islanding even without transformer constraints. Nonetheless, excessive exports to meet neighboring loads also cause transformer overloads. Therefore, there is a shift from EES to REES investment since batteries are extensively required to export to neighbors.

In sum, all previous cases highlight the value of an optimal DER investment planning with transformer constraints, especially in area-constrained situations, where the local PV capacity must be high and can’t be reduced to meet ZNE goals, and storage must be deployed to avoid transformer overloads. The optimization can find the least cost allocation, where and how much DER should be installed, even though it might not have been the most obvious solution.

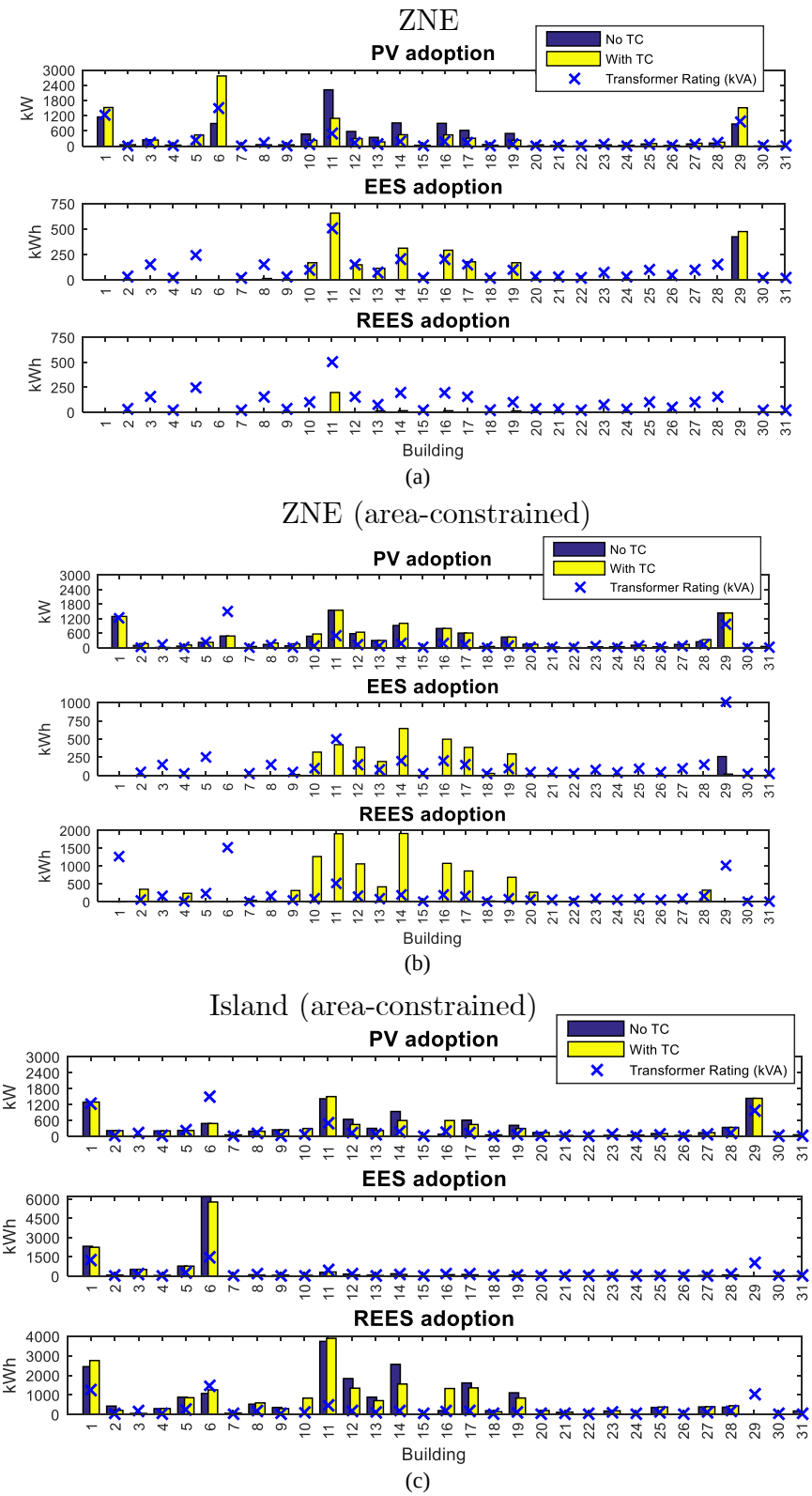

Figure 5.9 – Building DER allocation comparison with and without transformer constraintsfor scenarios: (a) ZNE, (b) ZNE (area-constrained), and (c) Island (area-constrained). Transformer kVA ratings are indicated by an x marker.

From the aggregate AEC perspective, for all scenarios, transformer constraints promote a slight increase in overall PV adoption, which is always accompanied by an increase in battery energy storage adoption. Table 5.5 lists the total DER adoption per DER type (PV, EES, and REES) for each scenario, where the trend described above is confirmed. At first, the increase in total PV adoption with transformer constraints may seem counterintuitive. We suspect that this increase is driven by the round-trip efficiency (RTE) of battery energy storage. A case run with 100% RTE for both EES and REES shows a marginal 1.4% increase in PV adoption, which confirms our guess. Moreover, from a design perspective, this trend is indeed reasonable, since the increased PV and battery storage capacity is (1) better sized to meet loads locally while avoiding large imports and exports that will result in transformer overloads, and (2) more distributed amongst buildings, as shown in Figure 5.9.

In total, for the area-unconstrained ZNE case transformer constraints add 101 kW of PV (1% increase), 2,104 kWh of EES (6 fold increase) and 254 kWh of REES (inexistent beforehand). For the area-constrained ZNE case, transformer constraints add 631 kW of PV (5.6% increase), 2,259 kWh of EES (12 fold increase), and 10,844 kWh of REES (inexistent beforehand). For the islanded case, transformer constraints do not significantly change the total PV and EES plus REES combined installed capacity; interestingly, PV and total storage capacities remain identical for practical purposes (ignoring differences below 10 kW/ 20 kWh). However, the locations of the DER resources change noticeably: the optimization reduces PV adoption in certain buildings, to remove transformer overloads while relocating storage (both EES and REES), and migrating 426 kWh of EES storage capacity to REES.

Table 5.5 – Total Building DER adoption for all scenarios

Scenario	DER Type	Total DER allocated	
		Without Transformer Constraints	With Transformer Constraints
ZNE (unconstrained)	**PV (kW)**	10,585	10,686
	EES (kWh)	424	2,528
	REES (kWh)	0	254
ZNE (area-constrained)	**PV (kW)**	10,580	11,211
	EES (kWh)	261	3,220
	REES (kWh)	0	10,844
Island (area-constrained)	**PV (kW)**	9,902	9,914
	EES (kWh)	11,402	10,976
	REES (kWh)	19,875	20,280

The different DER allocations of Table 5.5 produce different total project costs. For the ZNE scenarios, adding transformer constraints substantially increased cost. For our specific test case, the first year of operation total cost (including equipment capital cost and operational costs) for the ZNE scenario with no transformer constraints is about $3.5 million. When transformer constraints are added, this cost goes up to $3.81 million. Similarly, for the area-constrained ZNE case, the first-year cost is $3.57 million without transformer constraints and $5.07 million with transformer constraints. The need for battery energy storage adoption drives the cost increase. However, for the island scenario, since the initial storage adoption was already required for islanding, there is not a significant difference between costs before and after transformer constraints are applied; the total cost is $6.66 million without transformer constraints and $6.67 million with transformer constraints

5.4.3. Transformer versus Storage Investment Costs

To address the choice of installing storage instead of upgrading transformer infrastructure, we provide a brief analysis of costs for each option. In total, using the cost assumptions from Table 5.4, the annual electricity costs for the Oak View AEC ZNE scenario increase by over $1.5 million (this includes the annual amortized capital cost and also operation costs/revenue over one year). However, a simple cost exercise might show the value of adding this extra DER capacity. First, the total additional transformer capacity that would otherwise be needed to accommodate

the PV reverse power flows to achieve community ZNE is 6,565 kVA. Assuming a transformer replacement cost of $147/kVA (PG&E, 2016), the total cost of all replacements would be $965,055. However, with additional DER, the amount of revenue per kWh exported at the PCC increases from (from $0.17 to $0.26 per kWh). This happens because battery storage reduces grid imports (and in turn exports because of ZNE operation) at the PCC in 48% (from 8.58 GWh to 4.49 GWh). Simultaneously, REES performs arbitrage, that is, delayed export until peak cost periods. All of these effects and capabilities could become extremely valuable to the utility grid network that attempts to support very high renewable penetrations. The added flexibility inherent to battery storage will likely introduce possibilities for new and more valuable revenue streams, not yet considered here, building the case for a possible recovery of the investment throughout the project lifetime.

Additionally, with the added storage, the PV electricity used to directly power the AEC loads increases by 12%. Moreover, the reduced grid imports avoid a total of 7,040 $MTCO_2$ over 10 years, estimated considering the hourly grid emission factors for the CAISO grid in 2018 (CAISO, 2018). Moreover, before any DER deployment, 17.39 GWh is imported from the grid to meet the annual AEC demand. After PV and battery storage deployments, at best, the total grid electricity imports are reduced by 74% (to 4.49 GWh), and 5.94 GWh electricity is exported at the PCC back to the bulk system (due to the ZNE constraint) as renewable PV electricity. The total carbon emissions offset would consider both the time-resolved offset associated with utility imports and the marginal carbon benefit of exporting excess renewable generation back to the utility. The detailed analysis required to resolve a useful approximation of these emissions currently falls outside the scope of this work

From a technical perspective, locally deploying storage to prevent transformer overloads avoids extremely high reverse power flows, which guarantees that the “duck curve” effect (California Independent System Operator (CAISO), 2016) does not propagate upstream in the distribution system which would require infrastructure upgrades elsewhere. Extending this problem to include additional adjacent communities, connecting electrical infrastructure, and decisions surrounding infrastructure upgrades and community versus utility energy resources would begin to capture the various tradeoffs that must be considered as society moves to high renewable penetration. Moreover, the current analysis does not capture the cost benefits from the added resilience and reliability inherent to the local generation and storage. Lastly, as is shown for the

islanding scenario when storage is inevitably necessary, transformer constraints will provide valuable information on where to locate these assets, while the sole use of line and voltage constraints may not.

5.5. Summary

This chapter developed a mixed integer linear program for the optimal DER investment planning and operation of an advanced energy community microgrid, constrained by available physical space for rooftop solar PV deployment and also grid constraints with a novel technique to include transformer power constraints. We used a real-world test case, involving 31 customer loads modeled in *EnergyPlus*, to accurately represent the community aggregated load stock of residential, commercial, and industrial utility customers. We modeled operation goals typically desired for district systems such as Zero-Net-Energy and islanding as a microgrid during unplanned grid outages.

Regarding DER allocation in urban district systems, in order to meet ZNE or islanding goals within an AEC, our results show that:

- **In urban district systems, ZNE can only be accomplished at a community level;** large utility customers in the C&I sector most likely cannot entirely deploy enough PV to meet local electricity demand since they typically have high demand and there is a limited amount of space available for rooftop PV deployment at those sites. Therefore, to accomplish ZNE, the available area for PV installation in the residential sector needs to be leveraged to support the community energy goals.
- **Transformer overloads will likely occur as a result of high PV deployments in low voltage urban networks due to transformer sizes that were not designed to consider significant reverse power flow of PV electricity. Thus, including transformer constraints in the optimization problem formulation will provide a more accurate DER allocation;** the large amount of local solar PV required to meet ZNE is most times larger than what currently installed low-voltage utility distribution transformers can handle. Thus, the negative grid impacts associated with a high PV penetration will not only manifest as voltage and line ampacity margins being violated, which is the main focus of previous literature but also likely be accompanied by transformer overloads due to high reverse power flows (excess PV exported back to the grid).
- **It is possible to altogether remove transformer overloads while integrating high penetrations of solar PV into the AEC without any required transformer upgrades;** integrating transformer constraints into a MILP optimization to limit the power flows at the transformer level produces

entirely different optimal DER allocation and operation results. The main strategies to avoid overloads are deploying battery energy storage and also optimally re-distributing PV throughout the community.

- **Polygon relaxations are a practical linearization approach for transformer power flow constraints;** using polygon relaxations to capture the non-linear relationship between active and reactive power flows at the transformer showed adequacy in accuracy (errors below 1%), and computation tractability (run times of approximately 4 minutes), as well as a superior computational performance. When compared to comparable linearization methods such as piecewise linearization or linear interpolation, polygon relaxation run time is about six times faster.
- **The use of transformer constraints within DER investment planning, associated with the right battery storage allocation and dispatch, will effectively increase PV penetration as opposed to the use of practical rules, such as the "15%" rule.** Taking the ZNE, area-constrained scenario as an example, the total PV installed capacity over the entire community is 11,211 kW which is 1.7 times greater than the total installed transformer capacity of 6,500 kVA which shows an excellent potential for PV hosting capacity maximization beyond conservative rules of thumb.

6 Optimal DER Allocation in Meshed Microgrids with Grid Constraints

Highlights

- A novel linear decoupled power flow method is applied to a MILP for DER optimal allocation.
- The novel method has an improved accuracy for nodal voltage solution is improved for meshed networks
- As a result, the accuracy of the optimal DER allocation is improved.

6.1. Literature Review

The design of microgrids that enable reliable delivery of clean energy involves numerous modeling challenges that go beyond simple load and generation balancing. We refer to this design process as *DER optimal allocation problem*, which consists of determining the best (optimal) type, size, location, and dispatch of DER to meet a customer load. The problem is non-linear, highly constrained, multi-objective, mixed-integer, and multi-modal. Successful solution methods tend to reduce the complexity of this problem through omission or simplification of complex components, until a more tractable problem is obtained. The research community has identified many specific goals and constraints that are crucial to obtaining a cost-effective, accurate, and realistic design. One approach is centered on modeling the local electric utility infrastructure in place in order to design the DER system to work within current utility infrastructure and power quality constraints.

One big challenge is to linearize the highly non-linear power flow equations, which relate active and reactive power flows through a power system with voltage magnitudes and phase angles while maintaining sufficient accuracy. There is a vast body of work addressing this individual

effort (Akbari & Tavakoli Bina, 2016; Baran & Wu, 1989b; Coffrin & Hentenryck, 2013; Macedo, Montes, Franco, Rider, & Romero, 2016; Z. Yang, Bose, Xia, Zhong, & Kang, 2016), and amongst most notable achievements are the formulations proposed by Bolognani *et al.*(Bolognani & Zampieri, 2016) and the LinDistFlow(Baran & Wu, 1989a) equations.

Bolognani *et al.*(Bolognani & Zampieri, 2016) derived a linear approximation of the power flow equations with a bounded error starting from the relationship between apparent power, voltage, and current, formulated as nodal injections at PQ nodes (that is, nodes in which the active and reactive power are imposed, or known, and do not depend on nodal voltage). One of the main assumptions of this method is that the apparent power flow is sufficiently small, so its relationship with voltage is explicit. Moreover, in its simplified formulation (considered in this paper) shunt admittances are assumed negligible.

LinDistFlow(Baran & Wu, 1989a) simplifies a set of recursive branch flow equations for computing active (P), reactive (Q) powers, and voltages (V) across a radial network using the forward and backward updates method from known values at the sending/receiving feeder ends. First, in the backward update (that is, starting from the last branch in the network and moving towards the reference node) all real and reactive power branch flows are calculated from known load P and Q injection values. Then, in the forward update (starting from the reference node and moving towards the end of the circuit), branch voltage drops are calculated, and all nodal voltages and phase angles are updated. This approximation was explicitly developed for radial networks. One of its central assumptions is that the branch losses quadratic terms $R(P^2 + Q^2)/V^2$ and $X(P^2 + Q^2)/V^2$, where R and X are the branch resistance and reactance respectively, are small (and thus negligible) compared to the branch power flows. Even though the LinDistFlow equations have been widely used in a variety of models (Fachbereich, 2018; Klauber, 2016; Mashayekh et al., 2017; H. Wang et al., 2017) to calculate voltage and branch flows within an optimization model, we identify a clear drawback: it is not suitable for meshed networks.

Two benefits associated with meshed networks are increased reliability and more uniform voltage profiles resulting from the redundant power flow paths. Meshed grids architectures have been used in the medium voltage distribution level. One example is Consolidated Edison's underground meshed network in New York City. A common approach to a meshed grid network

in a microgrid is the typical ring bus architecture with N+1 level of redundancy. There are many microgrid projects, including notable examples from the DOE Smart Power Infrastructure Demonstration for Energy Reliability and Security (SPIDERS) program and the Renewable and Distributed Systems Integration (RDSI) program that use a meshed grid network. Amongst these projects are the Santa Rita Jail microgrid, in Alameda County, California,(Chevron Energy Solutions Company, 2014) Twenty Nine Palms military microgrid (Bose & Russel, 2012), Illinois Institute of Technology: Perfect Power Prototype(Award & Fc, 2014). Operational meshed microgrids include the Philadelphia Navy Yard (Kumar, 2015), Princeton University campus ("Princeton Microgrid," 2019), and the University of California San Diego campus(Washom, 2013).

The modeling challenge surrounding meshed networks stem from the fact that the concept of "upstream" and "downstream" power flow no longer applies. Recent literature with focus on meshed networks has revisited and expanded specific topics such as novel formulations for power flow(Bharti & Mala De, 2018; J. Yang et al., 2016), protection coordination(Bello et al., 2018), voltage and frequency control(Riverso, Sarzo, & Ferrari-Trecate, 2015), voltage regulation(Brandao, Pomilio, Caldognetto, Buso, & Tenti, 2016), and DER power management(Patterson & Geary, 2016). Moreover, a novel linearized power flow solution developed by Yang *et al.* (J. Yang et al., 2016), demonstrated superior accuracy and robustness when applied to meshed networks as compared to previous methods. The formulation does not depend on the radial topology of the network since it uses nodal injections as opposed to branch flows. Additionally, it is particularly interesting from an optimization standpoint because it decouples the relationship between voltage and phase angle, which typically gives rise to a quadratic problem formulation(J. Yang et al., 2016). The key improvements in the assumptions underlying the DLPF formulation are the inclusion of shunt suceptances, the voltage difference across buses and the conductance matrix G. In fact, the DLPF model is a generalization of Bolognani *et al.* (Bolognani & Zampieri, 2016) formulation, for meshed networks with PV (voltage controlled) nodes.

In this analysis, we use Yang *et al.* DLPF approach to implement voltage and branch kVA flow constraints (which we refer here to *grid constraints*) in the DER optimal allocation problem. While the DLPF formulation proposed by Yang *et al.* can be incorporated into a MILP optimization problem, it has not yet been formulated to do so. First, we compare the nodal

voltage and branch kVA flow solutions proposed by LinDistFlow and Bolognani *et al.*, against DLPF solutions for the radial and meshed benchmark 33-node systems. Then, we test the DER optimal allocation problem in a real-world 115-node meshed microgrid test case, comparing results when using either DLPF or LinDistFlow formulation for the linearized power flow while enforcing *grid constraints*.

6.2. Contributions

This chapter addresses the gap in the literature regarding the study of linearized power flow formulations applied to meshed networks within a mixed-integer linear optimization. To the best of our knowledge, all previous DER investment-planning studies that incorporate grid constraints assume radial circuits, which are indeed the vast majority of low voltage distribution feeders. Nonetheless, meshed microgrids and networked systems topologies will likely pose a challenge to the traditional way to implement a linearized power flow within a linear optimization, and so far, no study has proposed a suitable approach that is accurate for such systems.

The contributions of this chapter are:

- To leverage the novel decoupled linearized power flow formulation and implement it into a MILP optimization for DER investment planning.
- To quantify the impact on DER allocation when using a formulation that is not suitable for meshed networks.
- To compare the effects of stricter voltage constraints (ranging between 0.95 – 1.05 p.u) on DER optimal adoption.

6.3. Problem Formulation

This section summarizes the underlying equations that model the grid constraints as implemented in DERopt, an optimal DER allocation tool initially established in (R. J. Flores & Brouwer, 2018). All-electric network topology parameters, such as per unit branch resistances (r_{ij}), reactances (x_{ij}), base values for per unit calculations, and branch connections, follows the format of a MATPOWER (Zimmerman, Murillo-Sánchez, & Thomas, 2011) — an open-source MATLAB toolbox for solving the AC steady-state power flow problem — test case input file.

From this file, we calculate the sparse nodal admittance matrix Y. The constraints developed in this current work are implemented using the original DERopt formulation described in Chapter 5, section 5.2 such as energy balances and technology constraints, and also referred in (Novoa, Flores, & Brouwer, 2019).

The optimization algorithm is implemented in MATLAB(The MathWorks Inc., n.d.) R2015a using the YALMIP(Lofberg, 2005; Löfberg, 2019) R20181012 toolbox and CPLEX(IBM, 2017) v.12.8 for the MILP solver. The k-medoids methodology reduces our dataset to 36 representative days during the entire year; therefore, we simulate 864 hourly intervals. The hardware used is an Intel Xenon CPU E5-2680 v2 @2.80 GHz server with 20 cores, 40 threads, and 32 GB of RAM.

6.3.1. Notation

In this section, we define relevant model sets and subscripts used in the DLPF formulation. Additionally, Table 6.1and Table 6.2 provide a list and description of all model parameters and decision variables. Bold variables represent matrices (or vectors) that collect the *n* (nodal) values or *b* (branch) values for *t* (hourly) increments of the model decision variables.

The variables $\boldsymbol{\theta}, \boldsymbol{v}, \boldsymbol{p}$, and $\boldsymbol{q}$ are t-dimensional vectors which collect the decision variables for each time step (θ_t, v_t, p_t, and q_t), and are indicated in bold. Also, power flow variables are indexed by the sets *S*, the set of PV nodes, *L*, the set of PQ nodes, and *R*, the set of reference nodes.

- $t \in \mathrm{T}$: Set of hourly increments
- $n \in \mathrm{N}$: Set of nodes
- $i \in \mathrm{I}$: Set of "From" nodes
- $j \in \mathrm{J}$: Set of "To" nodes
- $b \in \mathcal{B}$: Set of branches
- $\lambda \in \Lambda$: Set of line segments for polygon relaxation
- *L*: Set of PQ nodes
- *S*: Set of PV nodes
- *R*: Set of reference (slack) nodes

Table 6.1 – Model Parameters

Parameter	Description	Units	Value
$\boldsymbol{Y}$	Nodal admittance matrix. $\mathbb{R}^{N\times N}$(sparse)	p.u.	Based on MATPOWER study case provided
$\boldsymbol{G}$	Nodal conductance matrix. $\mathbb{R}^{N\times N}$(sparse)	p.u.	Based on MATPOWER study case provided
$\boldsymbol{B}$	Nodal susceptance matrix. $\mathbb{R}^{N\times N}$(sparse)	p.u.	Based on MATPOWER study case provided
$\boldsymbol{B'}$	Nodal susceptance matrix without shunt elements. $\mathbb{R}^{N\times N}$(sparse)	p.u.	Calculated from *B*
$\boldsymbol{\theta}_0$	Initial voltage angle $\in \mathbb{R}^{(N-1)\times T}$	degree	Based on MATPOWER study case provided
$\boldsymbol{g_{ij}}$	Branch conductance matrix. Elements g_{ij} are entries $\in \mathbb{R}^{\mathcal{B}\times T}$	p.u.	Based on MATPOWER study case provided
$\boldsymbol{b_{ij}}$	Branch susceptance matrix. Elements b_{ij} are entries $\in \mathbb{R}^{\mathcal{B}\times T}$	p.u.	Based on MATPOWER study case provided
$\boldsymbol{\alpha}$	DLPF parameter matrix $\in \mathbb{R}^{(N-1)\times(N-1)}$ (sparse)	p.u.	$\frac{N}{L}$ (From (J. Yang et al., 2016))
$\boldsymbol{\beta}$	DLPF parameter matrix $\in \mathbb{R}^{(N-1)\times(N-1)}$ (sparse)	p.u.	$\frac{M}{H}$ (From (J. Yang et al., 2016))
$\boldsymbol{\tilde{H}}$	DLPF parameter matrix $\in \mathbb{R}^{(N-1)\times(N-1)}$ (sparse)	p.u.	$H-\alpha M$ (From (J. Yang et al., 2016))
$\boldsymbol{\tilde{L}}$	DLPF parameter matrix $\in \mathbb{R}^{(N-1)\times(N-1)}$ (sparse)	p.u.	$L-\beta N$ (From (J. Yang et al., 2016))
V_{base}	Base voltage for per-unit calculations	kV	12 /0.48 /0.120
S_{base}	Base apparent power for per-unit calculations	MVA	100
Z_{base}	Base impedance power for per-unit calculations	Ohms	1.44(12kV), 0.0023(480V), 0.0004(208)
$\underline{v}, \bar{v}$	Upper and lower voltage limit for voltage constraints	p.u.	0.95 p.u. and 1.05 p.u. respectively
$\boldsymbol{S_{ij_R}}$	Power Rating of branch connecting buses *i* and	p.u.	Based on power system topology
$\boldsymbol{\theta_\lambda}$	Angle of segment λ of polygon relaxation	degrees	Based on the number of polygon sides *L*
$\boldsymbol{\Lambda}$	Number of sides for polygon relaxation	n/a	22
$\boldsymbol{\epsilon}$	Approximation error for polygon relaxation	p.u.	<1%

Table 6.2 – Model decision variables

Decision Variable	Description	Units
$\boldsymbol{\theta}$	Nodal Voltage phase angle matrix. $\mathbb{R}^{N-1}$	degrees
$\boldsymbol{v}$	Nodal Voltage magnitude matrix. $\mathbb{R}^{N-1}$	p.u.
$\boldsymbol{p}$	Nodal Active power injection. $\mathbb{R}^{N-1}$	p.u.
$\boldsymbol{q}$	Nodal Reactive power injection. $\mathbb{R}^{N-1}$	p.u.
$\boldsymbol{p_{ij}}$	Branch active power flow. $\mathbb{R}^{N-1}$	p.u.
$\boldsymbol{q_{ij}}$	Branch reactive power flow. $\mathbb{R}^{N-1}$	p.u.
$\mathbf{s_{ij}}$	Branch apparent power flow. $\mathbb{R}^{N-1}$	p.u.

6.3.2. Decoupled Linearized Power Flow

We formulate the governing power flow equations using the original DLPF formulation presented in (J. Yang et al., 2016). Please refer to (J. Yang et al., 2016) for the original derivation of the DLPF model. Here, we summarize the resulting linearized power flow equations only. We adapt the DLPF formulation to a matrix format that can be implemented in a MILP optimization, *i.e.*, the power flow solution is calculated for every hourly interval *t*, which corresponds to each hourly interval at which the decision variables must be calculated, within the optimization timeframe. Thus, the DLPF constraints are implemented for each time step.

Equation (75) defines the conductance G and susceptance B matrices as the real and imaginary parts of the nodal admittance matrix Y_{BUS} , which collects the individual *i-j* admittance values. Equation (76) defines nodal voltage phase angles, $\boldsymbol{\theta}_{[S;L]}$, in degrees and Equation (76) (77) defines the matrix that collects all nodal voltage magnitudes, $\boldsymbol{v}_L$, in per-unit.Variables $\widetilde{\boldsymbol{H}}^{-1}, \widetilde{\boldsymbol{L}}^{-1}, \widetilde{\boldsymbol{p}}, \widetilde{\boldsymbol{q}}, \propto \boldsymbol{and}\ \boldsymbol{\beta}$ are time-invariant parameters, which only depend upon network topology (for the interested reader, the definition of these variables can be found in (J. Yang et al., 2016)) Variables. $\boldsymbol{p}_{[S;L]}$ and $\boldsymbol{q}_L$ collect the per-unit reactive and active power nodal injections, which equal transformer injections, as defined by Equation (78) .Variables $\boldsymbol{P}_T$ $\boldsymbol{Q}_T$ collect transformer nodal injections ($P_{\mathrm{T}_{x_t}}$.and $Q_{\mathrm{T}_{x_t}}$).

$$\boldsymbol{Y}_{BUS} = \boldsymbol{G} + j\boldsymbol{B} \tag{75}$$

$$\boldsymbol{\theta}_{[S;L]} = \widetilde{\boldsymbol{H}}^{-1}\left[\boldsymbol{p}_{[S;L]} + \widetilde{\boldsymbol{p}} - \boldsymbol{\alpha}(\boldsymbol{q}_L + \widetilde{\boldsymbol{q}})\right] \tag{76}$$

$$\boldsymbol{v}_L = \tilde{\boldsymbol{L}}^{-1}(\boldsymbol{q}_L + \widetilde{\boldsymbol{q}}) - \boldsymbol{\beta}\,(\boldsymbol{p}_{[S;L]} + \widetilde{\boldsymbol{p}}\,) \tag{77}$$

$$\boldsymbol{p}_{[S;L]} = \boldsymbol{P}_{T_x}\ ,\ \boldsymbol{q}_L = \boldsymbol{Q}_{T_x} \tag{78}$$

$$\boldsymbol{\alpha} = \frac{\boldsymbol{N}}{\boldsymbol{L}} = \frac{\boldsymbol{G}_{[S;L],L}}{-\boldsymbol{B}_{L,L}}, \qquad \boldsymbol{\beta} = \frac{\boldsymbol{M}}{\boldsymbol{H}} - \frac{\boldsymbol{G}_{[L;S],R}}{\boldsymbol{B}'_{[S;L],[S;L]}} \tag{79}$$

$$\widetilde{\boldsymbol{H}} = \boldsymbol{H} - \boldsymbol{\alpha}\boldsymbol{M}\ ,\quad \tilde{\boldsymbol{L}} = \boldsymbol{L} - \boldsymbol{\beta}\boldsymbol{N} \tag{80}$$

$$\widetilde{\boldsymbol{p}} = \begin{bmatrix} \boldsymbol{B}'_{S,R} & -\boldsymbol{G}_{S,R} & -\boldsymbol{G}_{S,S} \\ \boldsymbol{B}'_{L,R} & -\boldsymbol{G}_{L,R} & -\boldsymbol{G}_{L,S} \end{bmatrix} \begin{bmatrix} \boldsymbol{\theta}_R \\ \boldsymbol{v}_R \\ \boldsymbol{v}_S \end{bmatrix} \tag{81}$$

$$\widetilde{\boldsymbol{q}} = \begin{bmatrix} \boldsymbol{G}_{L,R} & \boldsymbol{B}_{L,R} & \boldsymbol{B}_{L,S} \end{bmatrix} \begin{bmatrix} \boldsymbol{\theta}_R \\ \boldsymbol{v}_R \\ \boldsymbol{v}_S \end{bmatrix} \tag{82}$$

$$\boldsymbol{p}_{\boldsymbol{ij}} = \left(\boldsymbol{v}_i - \boldsymbol{v}_j\right)\boldsymbol{g}_{\boldsymbol{ij}} - (\boldsymbol{\theta}_i - \boldsymbol{\theta}_j)\boldsymbol{b}_{\boldsymbol{ij}} \tag{83}$$

$$\boldsymbol{q}_{\boldsymbol{ij}} = (\boldsymbol{v}_i - \boldsymbol{v}_j)(-\boldsymbol{b}_{\boldsymbol{ij}}) + (\boldsymbol{\theta}_i - \boldsymbol{\theta}_j)\boldsymbol{g}_{\boldsymbol{ij}} \tag{84}$$

$$g_{ij} = \frac{r_{ij}}{r_{ij}^2 + x_{ij}^2}\ , b_{ij} = \frac{x_{ij}}{r_{ij}^2 + x_{ij}^2} \tag{85}$$

6.3.3. Voltage Constraints

Equation (86) limits all nodal voltages, at time *t*, to an upper and lower per-unit bound. We use the voltage bounds suggested by the ANSI C84.1 standard(ANSI, 2005).

$$\underline{v} \le v_t \le \bar{v} \text{ (per unit)} \tag{86}$$

6.3.4. Branch kVA Constraints

Similar to Chapter 5, where non-linear the transformer capacity limits, we perform a polygon relaxation of the apparent power circle of branch kVA $\boldsymbol{s_{ij}^2 = p_{ij}^2 + q_{ij}^2}$, A second circle with radius s_{ij} smaller than the branch rated power capacity (S_{ij_R}), that is, $s_{ij} < S_{ij_R}$, can be inscribed within the polygon. In this case, the maximum s_{ij} is defined by $s_{ij} = S_{ij_R} \, cos\left(\frac{\pi}{\Lambda}\right)$, where increasing the number of sides Λ decreases the difference between maximum s_{ij} and rated S_{ij_R}. Considering that the error is defined by the difference between s_{ij} and S_{ij_R} is defined by Equation (88), the absolute error can be reduced below 1% by setting polygon sides Λ to 22. Using this approximation, power through a branch can be written as Equation(89), and implemented into the optimization model as Equation (90) For simplifying notation, the subscript *t* is omitted here. Nonetheless, the polygon constraints are applied to every time step.

$$\boldsymbol{s_{ij}^2 = p_{ij}^2 + q_{ij}^2} \tag{87}$$

$$\boldsymbol{\epsilon = S_{ij_R} - s_{ij} = S_{ij_R}}\left(1 - cos\left(\frac{\pi}{\Lambda}\right)\right) \rightarrow \Lambda \geq \left(\frac{\pi}{arccos\left(1-\frac{\epsilon}{S_{ij_R}}\right)}\right) \tag{88}$$

$$\boldsymbol{s_{ij} = p_{ij}} cos\,(\boldsymbol{\theta_\lambda}) + \boldsymbol{q_{ij}} sin\,(\boldsymbol{\theta_\lambda}) \quad , \quad \boldsymbol{\theta_\lambda} = \frac{\pi}{\Lambda} + k\left(\frac{2\pi}{\Lambda}\right),\ \lambda = 0,1,\dots,\Lambda - 1 \tag{89}$$

$$\boldsymbol{s_{ij}} \geq \left[\cos(\boldsymbol{\theta_\lambda}) \ \sin(\boldsymbol{\theta_\lambda})\right] \begin{bmatrix} \boldsymbol{p_{ij}} \\ \boldsymbol{q_{ij}} \end{bmatrix} \tag{90}$$

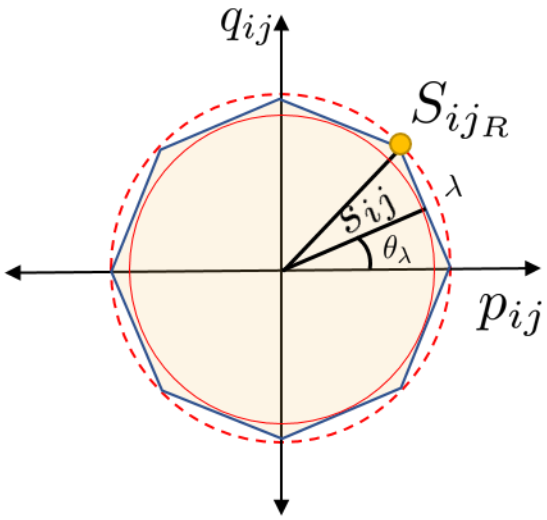

Figure 6.1 – Polygon relaxation for branch kVA power flows (s_{ij}). p_{ij} and q_{ij} are branch active and reactive flows respectively. A polygon of Λ sides is inscribed in the complex power circumference (dashed line) that defines the branch kVA flow limit according to its rated power S_{ij_R} . The k sides of the polygon, and respective angles θ_λ are used to calculate the approximated apparent power limit : $s_{ij} = S_{ij_R} \cos\left(\frac{\pi}{\Lambda}\right)$, which is the radius of the circumference inscribed within the Λ-sided polygon (solid red line). Equation (72) defines the error of this approximation.

6.4. Test Cases

This section describes the various model inputs required for the comparison of the different ACPF linearization methods

6.4.1. Radial and Meshed Test Circuits

We use as test circuits the radial IEEE-33 node and an adapted meshed version, as proposed in Ref (Baran & Wu, 1989a). This circuit is chosen due to the large body of work that has previously examined it as well as the ease of converting it to a multi-mesh system. The circuit is a 12.4 kV primary radial distribution feeder with 33 nodes, the total loading of 3.7 MW/2.3 MVar, the official test case loading,(0.85 lagging average power factor), and a maximum R/X ratio of 3.03. For a meshed test case benchmark, five looping branches are added to the radial feeder. Figure 6.2 shows the schematics of the feeder radial and meshed topologies. For complete branch impedance and nodal injection values, the reader can refer to Ref (Baran & Wu, 1989a).

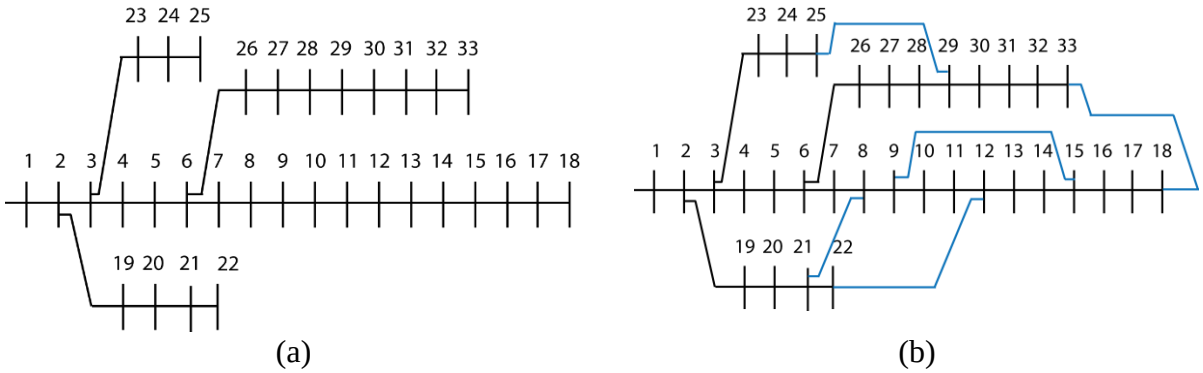

Figure 6.2 – (a) Radial 33-node feeder test case. (b) Adapted meshed 33-node network test case, a hypothetical 12.4 kV system with 33 nodes and 32 branches for the radial case plus five looping branches for the meshed case. Total loading is 3.7 MW/2.3 MVar. The maximum R/X ratio is 3.03.

6.4.2. Real World Meshed Microgrid Circuit

The purpose of this circuit is to represent a real microgrid system. Therefore, we use the real-world distribution power system introduced in Chapter 4 and load and PV time-series data detailed in Chapter 5. Node 1 is the slack node and represents the PCC with the wide-area electricity grid. We assume a balanced, 3-phase power system. The primary service voltage is 12.47 kV, and the secondary voltages are 480 V for C&I customers and 208 V for residential customers. There are 115 nodes, 31 transformers that serve load clusters, and 117 branches. Of the 117 branches. Three are looping branches. The maximum R/X ratio is 3.5 for primary circuits and 5.5 for secondary circuits. Figure 6.3 shows the schematics of the circuit topology.

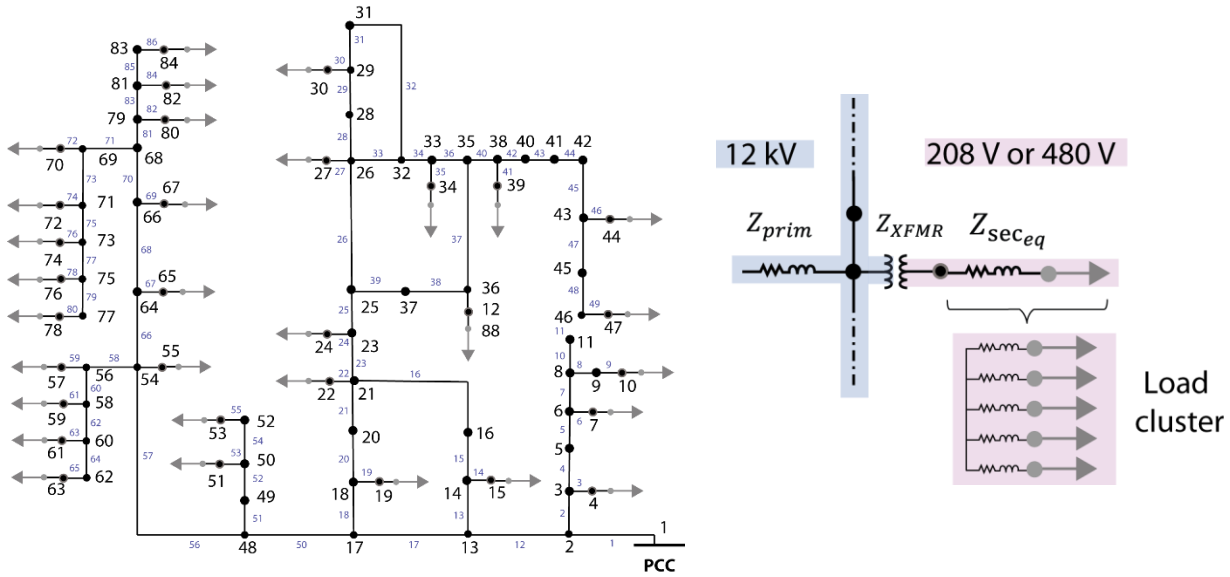

Figure 6.3 – Test case topology, based on a real-world power system modeled as 115 nodes, 31 of which are transformers that serve clusters of industrial, commercial, and residential loads. The primary voltage is 12.47 kV, and secondary voltages are 480 V, and 208 V. Node 1 is the PCC with the wide-area grid.

To capture the worst-case voltage drop possible, we extend our test case to include secondary circuits. Hence, we model each distribution transformer from which secondary lines (line drops) extend out to the customer loads. We model transformers as per unit impedances connected in series between a primary (higher voltage) and a secondary (lower voltage) node. We use typical values(Eaton & Cooper Industries, n.d.) for distribution transformer equivalent per-unit impedances. To simplify the analysis, we aggregate customer loads on the same transformer into a single (constant PQ) load cluster. Each load cluster connects to the secondary of the transformer through an equivalent line drop circuit. We assume transformer kVA rated power values are just above the maximum peak load of its load cluster and place all load cluster at the end of the secondary conductors. We assume an average of five customers per transformer; therefore, we divide the equivalent line drop circuit impedance by five. Finally, we assume the length of the secondary conductor is 65 feet. We assume a 0.9 lagging power factor for residential customers and 0.8 lagging power factor for C&I customers. The primary lines conductors used are assumed to be in overhead configuration, using ACSR aluminum conductors with 4 AWG (R=2.17 ohm/mile, X=0.61 ohm/mile) and secondary line drops are assumed to be 6 AWG (R=3.46 ohm/mile, X=0.63 ohm/mile) (CME Wire and Cable, 2016) as per NEC conductor size minimum requirements for overhead spans and service drops (Articles 225.6(A)(2) and 230.23(B), respectively)(National Fire Protection Association, 2014). The ampacities assumed for these conductors are 127 A and 101 A, respectively, based on a covered conductor in free air at ambient 40°C (104°F), according to NEC Table 310.15(B)(21)(National Fire Protection Association, 2014).

6.4.3. Assumptions on DER Technology and Cost

The ultimate goal of this work is to improve the methods for modeling power flows typically involved in the DER investment planning and dispatch problem. Although the quantity of available DER is extensive, without loss of generality, we assume the DER technology available are renewable solar PV and electrical battery storage.

We assume that the initial cost of solar is $2,000 per kW(Lazard, 2016), that ongoing operations and maintenance costs are $0.001(R. J. Flores & Brouwer, 2018) per kWh, and that the solar PV

panel has a nominal electrical conversion efficiency of 20%(R. J. Flores & Brouwer, 2018). For the electrical battery energy storage, we assume a generic battery type that has an initial cost of $600(Lazard, 2018b) per kWh, operations and maintenance cost of $0.001(R. J. Flores & Brouwer, 2018a) per kWh discharged, has a power to energy ratio of four, and has a charging and discharging efficiency of 90%(R. J. Flores & Brouwer, 2018). We assume the system is deployed in the CAISO territory, where the economic value streams available to the battery change depend upon the charging source. Note that, if a battery is exclusively charged by onsite renewables, then it can discharge to offset utility imports or export back to the grid at any time under net energy metering rates. However, if a battery is partially or wholly charged using grid electricity, it is ineligible to export any electricity back to the grid.

6.5. Results and Discussion

In this section, we perform a validation of the DLPF method against the exact AC power flow (ACPF) solution and provide a comparison between commonly used linearized power flow methods proposed in the literature for meshed and radial test-circuits. We follow by testing the DLPF formulation with our DER optimal allocation model DERopt to constrain voltages, and branch kVA flows.

The MATLAB toolbox for power flow calculations, MATPOWER(Zimmerman et al., 2011), is used to provide the benchmark for the exact ACPF solution. The other linearization methods were implemented in MATLAB using algorithms available at public GitHub repositories (LinDistFlow(Schweitzer, 2018), Bolognani *et al.* (Bolognani, 2014) and steady-state DLPF(J. Yang, 2016)). We use as simulation platform the Intel Xenon CPU E5-2680 v2 @2.80 GHz server with 20 cores, 40 threads, and 32 GB of RAM. We implement all formulations in MATLAB R2015a (The MathWorks Inc., n.d.), and for the MILP optimization, we use YALMIP R20181012 toolbox (Lofberg, 2005; Löfberg, 2019) and CPLEX v.12.8 (IBM, 2017) for the MILP solver.

6.5.1. DLPF validation and comparison with other linearization techniques for radial and meshed network

The goals of this section are to (1) validate DLPF against the exact ACPF solution and (2) to demonstrate the improved accuracy of the DLPF method to calculate nodal voltage magnitudes and branch flows in a meshed network. For this, we compare the steady-state DLPF formulation against (1) the full AC power flow solution, calculated using MATPOWER (2) the formulation proposed in Bolognani *et al.* and (3) LinDistFlow. We use the test feeder proposed in Ref (Baran & Wu, 1989a) and described in Section 6.4.1 as the benchmark. Starting with the IEEE-33 node radial feeder, Figure 6.4 presents the results of the comparison between methods. The voltage profiles (Figure 6.4a.) of the linearized methods match quite closely with the exact solution. Note that all linearized methods overestimate the true voltage value, which translates into a conservative constraint if the goal is to limit over-voltages. The errors in Figure 6.4b. are the percent difference between the approximated solution and the exact AC power flow solution. Figure 6.4b shows that the voltage magnitude error for all methods falls below 1% for all linearization methods, indicated a high degree of accuracy for voltage estimation. As expected, the voltage error increases with distance from the slack node, as the growing impedance will increase the approximation error of the simplifying assumptions. This echoes the results shown in (Mashayekh et al., 2017). The LinDistFlow solution is the most accurate and produces a maximum error of 0.02844 p.u., which is very close to the 0.028 p.u. upper bound approximation error estimated in (Fachbereich, 2018). This demonstrates the merit of using LinDistFlow for this particular application.

Figure 6.4.c compares branch power flows (apparent power: $S = P + jQ$). Equations (83) and (84) define the DLPF branch power solution. Since Bolognani *et al.* does not provide a formulation for power flow, we use Equations (83) and (84) to calculate the branch power flows for that method, taking the voltages and phase angle solutions as inputs. All linearized solutions show similar degrees of accuracy, with some deviations for Bolognani *et al.*'s method. The errors lie within 5% of the true value, mostly due to the assumption across all methods of lossless lines. This assumption leads to the underestimation of power flows necessary to meet the load. Branch flow errors increase at higher power flows (higher current), which happen most frequently at the nodes closer to the slack node. While LinDistFlow achieves the most accurate linearization for this radial test case, all methods perform with a similar error.

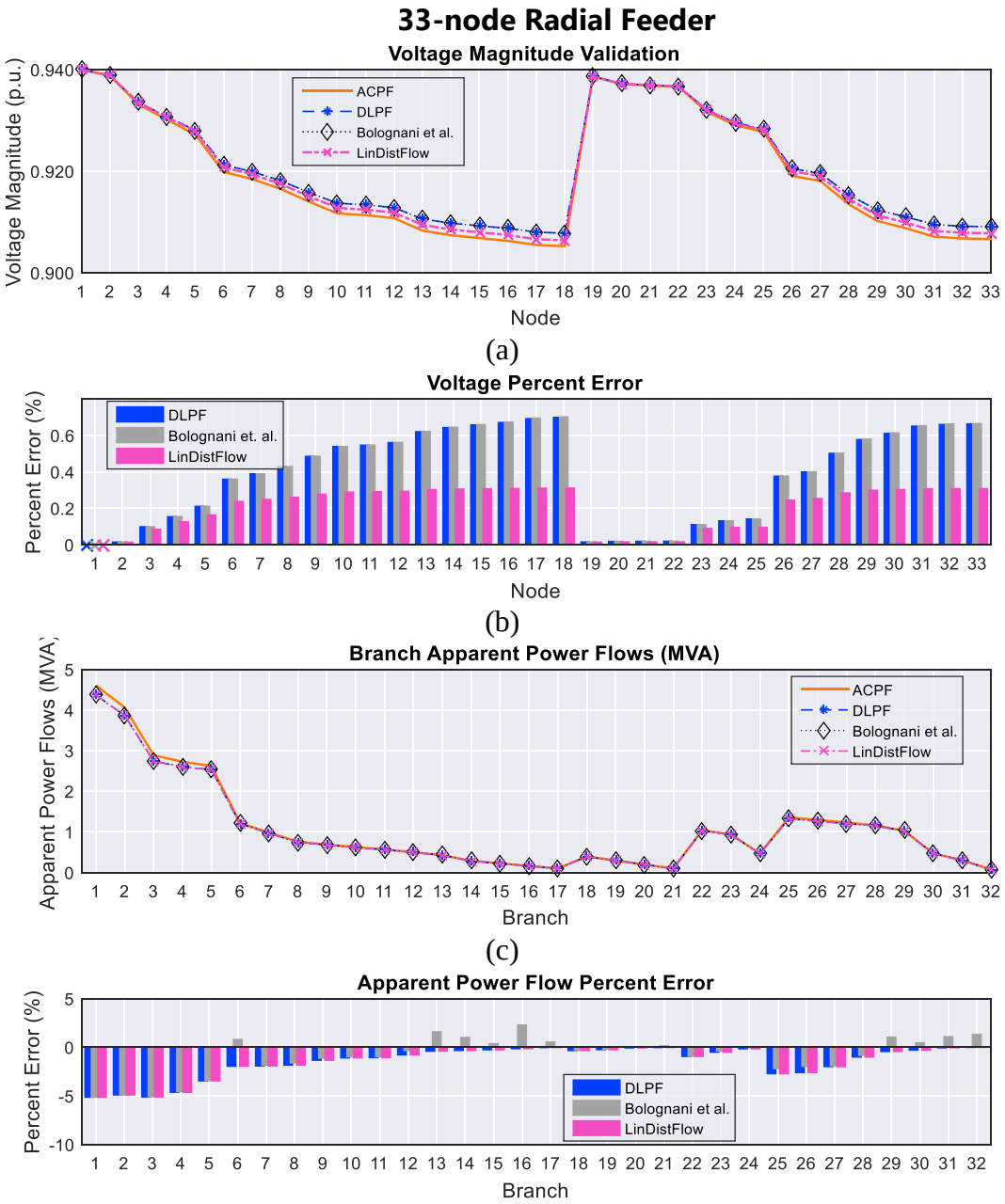

*Figure 6.4 – The (a) Voltage Magnitude and (b) Voltage Percent Error at each node of the **radial** 33-node case comparing the full AC power flow (ACPF), DLPF, Bolognani, et al., and LinDistFlow solutions. As Bolognani et al. do not provide a power flow solution, we use the angle and voltage solutions in the DLPF formulation. An X indicates errors smaller than 0.1%*

.Figure 6.5 shows the results of the same comparison but using the meshed network benchmark. Regarding voltage magnitude, we see in Figure 6.5a how the LinDistFlow solution starts to deviate significantly from the true voltage value, with a much more significant percent error, underestimating true voltage values by over 3%. Note that even though a 3% error might seem small, a 3% per unit difference can be significant given that ANSI C.84(ANSI, 2005) standard margins for unacceptable voltage levels are in the range of ±5% from the nominal value. The

DLPF solution, on the other hand, overestimates true voltage slightly for this test case. Nonetheless, the DLPF and Bolognani *et al* solutions demonstrate higher accuracy for voltage magnitudes. Regarding branch power flows, the LinDistFlow solution overestimates the true value by 3 MVA at the point of common coupling. These results are reasonable considering the underlying assumptions made during linearization of the AC power flow equations. This validation shows that the DLPF formulation can achieve higher levels of accuracy for meshed networks, and comparable accuracy to LinDistFlow for radial networks.

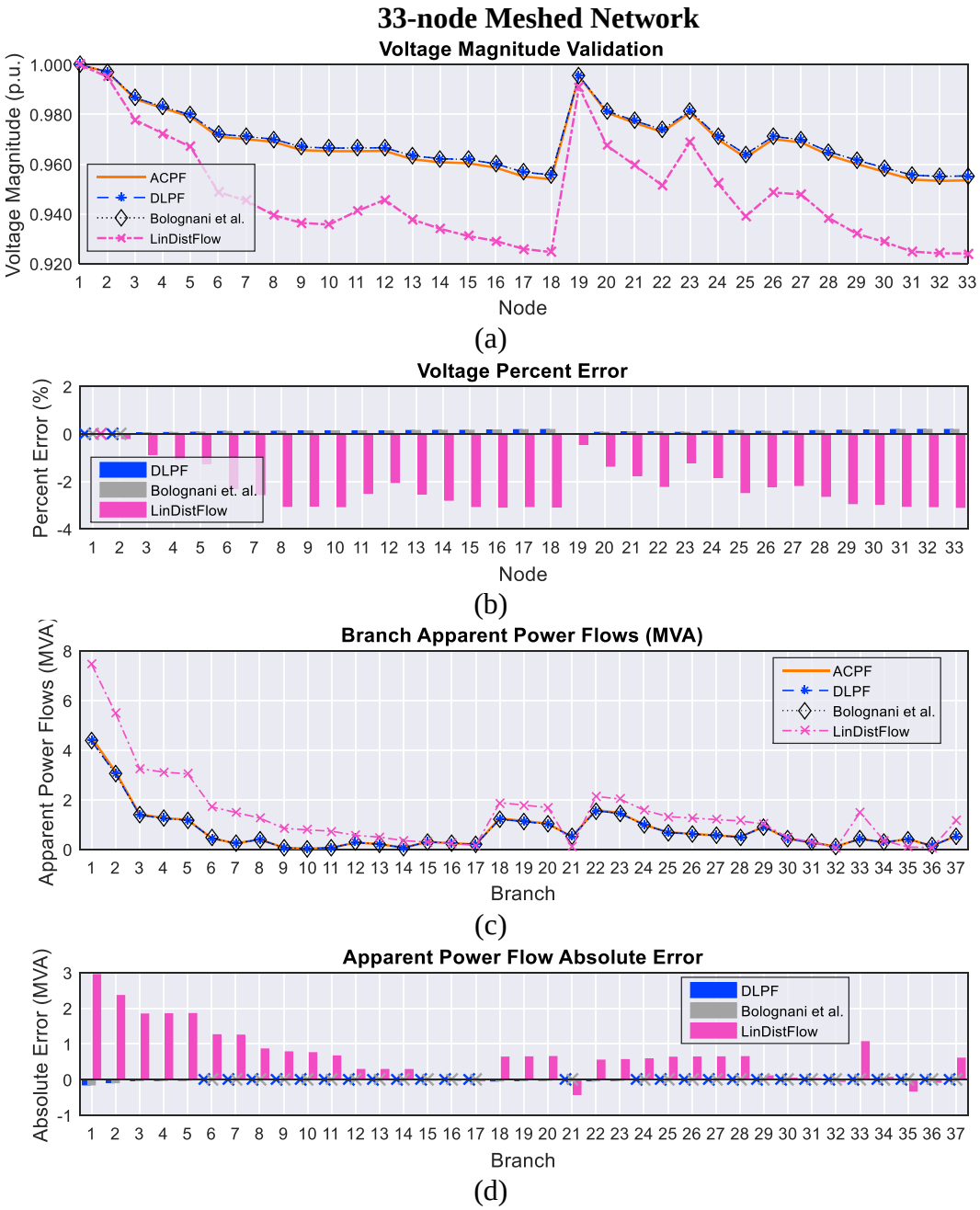

*Figure 6.5 – The (a) Voltage Magnitude and (b) Voltage Percent Error at each node of the **meshed** 33-node case comparing the full AC power flow (ACPF), DLPF, Bolognani et al., and LinDistFlow solutions. An X indicates errors smaller than 0.1%. As Bolognani et al. does not provide a power flow solution, we use the angle and voltage solutions in the DLPF formulation*

6.5.2. Meshed microgrid test case

The goal of this section is to validate the DLPF performance when applied to our third benchmark case. Since we are interested in investigating over voltages caused by high PV penetration and reverse power flows, we simulate a steady-state, worst-case injection that

represents an extreme solar PV and load scenario that totals to a 6.2 MW export (negative nodal injections) back to the grid. The total export is distributed evenly across all transformer nodes. We also simulate a total reactive power import of 3.1 MVar, which corresponds to a 0.89 lagging power factor. The magnitude of the MW exports reflects a high PV penetration scenario (above 200% of peak load), while the magnitude of the MVar imported reflect each building assumed power factor and reactive demand.

Figure 6.6 shows the comparison results. Regarding voltage (Figure 6.6.a), note how the LinDistFlow solution progressively worsens at the looped branches while DLPF and Bolognani *et al.* solutions again, slightly overestimate voltages. Errors (Figure 6.6.b) are kept below 5% for DLPF and Bolognani *et al.,* while LinDistFlow errors reach -15% at nodes that are found along and at the end of looped circuits. As expected (Figure 6.6.c), LinDistFlow also has the worse branch kVA flow accuracy, both overestimating and underestimating kVA flows at different branches. We omit LinDistFlow solution in the absolute/percent error comparisons of Figure 6.6.c and Figure 6.6.d since it was significantly higher than the other errors. DLPF solution tends to overestimate kVA flows by less than 5% (0.4 MVA max), while Bolognani *et al.* solutions tend to underestimate kVA flows by a maximum of 12% in certain branches.

The test case used here is a real distribution circuit. In this instance, the DLPF is able to produce a more accurate solution. During simulations, we noticed that Bolognani *et al.* performance deteriorated with higher reactive power flows, that is, when operating at a lower 0.70 lagging power factor, the maximum absolute voltage error went from 0.0364 p.u. to 0.0637 p.u., whereas the DLPF solution kept a good performance; its absolute voltage error went from 0.0215 p.u.to 0.0287 p.u.

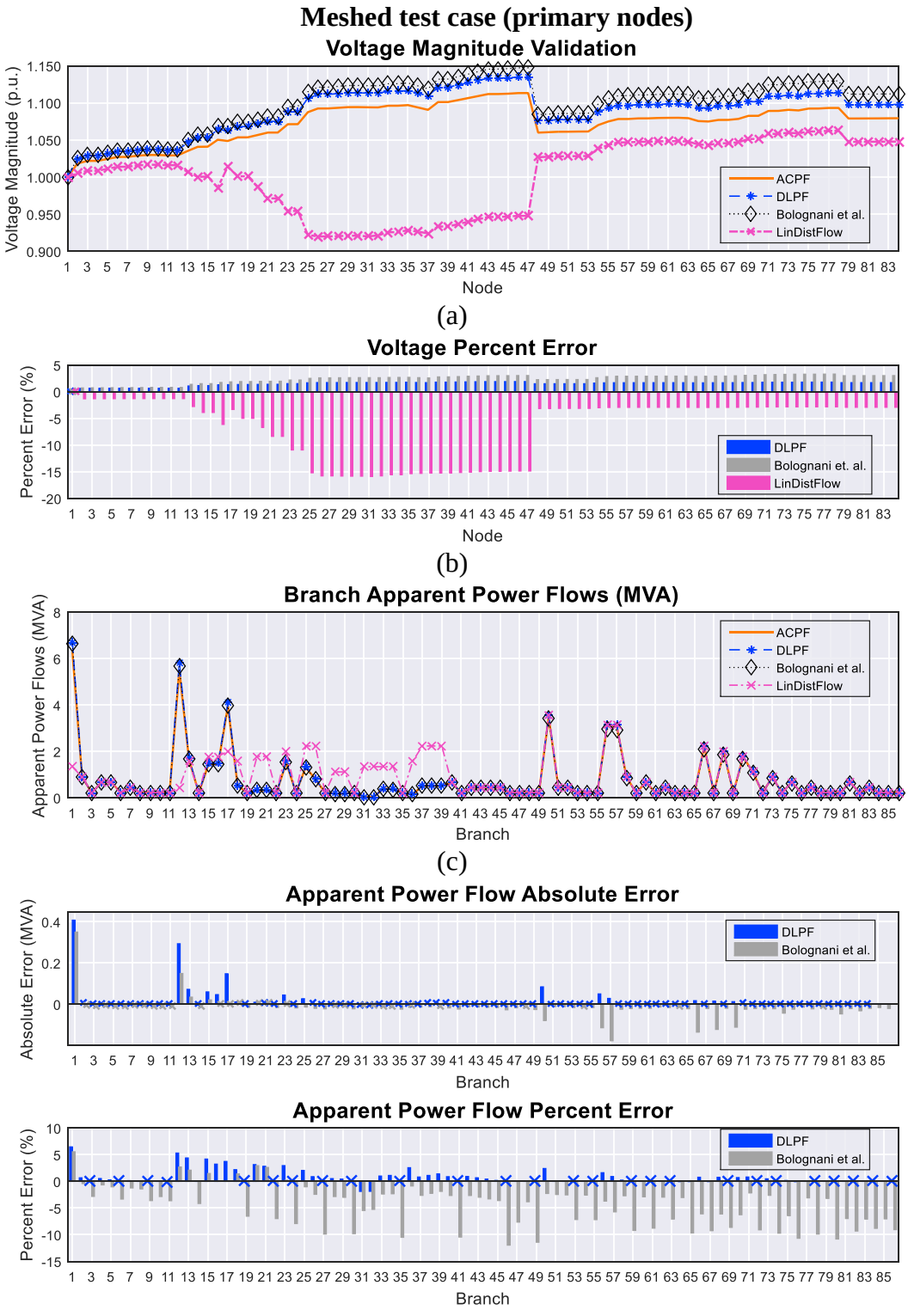

*Figure 6.6 – The (a) Voltage Magnitude and (b) Voltage Percent Error at each primary (12 kV) node of the **meshed network** case comparing the full AC power flow (ACPF), DLPF, Bolognani et al., and LinDistFlow solutions. Errors smaller than 0.1% are indicated by an X.*

6.5.3. DERopt solution with grid constraints for a meshed microgrid

The goal of this section is to compare results found by our MILP optimization model for DER allocation for a base case (DERopt without any voltage or power flow grid constraints) versus using either DLPF or LinDistFlow as the load flow formulation. We selected these two AC power flow approximations due to their accuracy when analyzing meshed and radial circuits, respectively.

The primary result of this section is how the optimal DER allocation solution changes depending upon the load flow formulation. The optimization minimizes investment cost while meeting a yearly zero-net-energy constraint, *i.e.*, total imports must be less than or equal to total exports by the end of the year. Also, PV adoption is constrained by the physical area (rooftop) available for installation. For more details on DERopt formulation, we direct the reader to (R. J. Flores & Brouwer, 2018)(R. J. Flores & Brouwer, 2018b; Novoa et al., 2019). For the comparison, we use the 115-node meshed network system presented in Section 6.5.2 as the test case. The grid constraints considered are nodal voltage and branch kVA flow limits, which were presented in Section 6.3.3 and 6.3.4, respectively. Therefore, the optimal DER allocation and dispatch solution will always respect the local electric power system infrastructure limits while achieving ZNE at the least possible cost.

The base case adopts DER (10,577 kW PV and 120 kWh of EES). Figure 6.7 shows the post-processed ACPF voltage profiles for this solution. Each curve represents the voltage profile calculated at a given time-step over the optimization timeframe**.** The markers indicate the worst case under-voltage (UV) and over-voltage (OV) – both true and linearized - over the optimization timeframe. The solid and dotted black lines highlight days in winter and summer, respectively, at 1 PM and 6 PM. For the base case, voltages range between 0.887 - 1.187 p.u. These extreme values occur at the same secondary node (node 88), which hosts 1,552 kW of PV and no EES. The worst UV occurs at an evening peak in October, and the worst OV occurs at solar max output at 1 PM in August. As shown by other DER interconnection modeling efforts (Mead, Donde, Garnett, & (PG&E), 2015; NREL & SolarCity, 2016), most of the voltage issues occur at the lower voltage, secondary circuits. These results show the expected outcome of poor power quality when neglecting utility infrastructure during DER allocation.

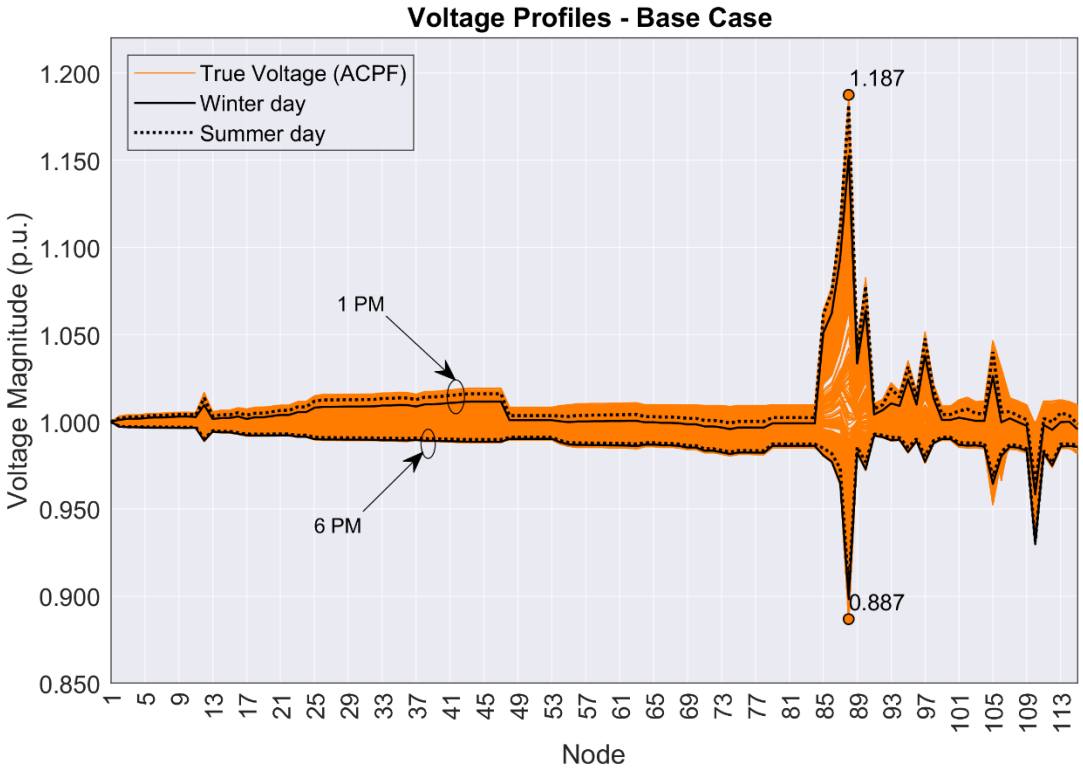

Figure 6.7 – Base Case. Voltages range between 0.887 – 1.187 p.u. Markers indicate the worst case under voltage and over voltage over the optimization timeframe. Solid and dotted black lines highlight days in winter and summer, respectively, at 1 PM and 6 PM.

After testing the base case, we implement the linearized AC power flow constraints. The first constraint tested prevents only over-voltages. Thus, voltage can only be 5% above its nominal value, or $V \leq 1.05$ p.u. The second voltage constraint tested assumes the stricter ANSI Range A(ANSI, 2005) voltage limits, which also limit under-voltages; thus, voltage is only allowed to be ± 5% its nominal value, or $0.95 \leq V \leq 1.05$ p.u.

Table 6.3 summarizes results and compares differences in DER (PV, EES, and REES) adoption when using either DLPF or LinDistFlow load flow formulations for the different voltage constraints simulated.

To meet only OV constraints, *i.e.*, $V \leq 1.05\ p.u.$, DLPF recommends a 10,857 kW solar PV system, while LinDistFlow recommended a 10,771 kW system, which is 0.8% smaller. Regarding energy storage, DLPF recommends a combined capacity (EES and REES) of 6,004 kWh, while LinDistFlow recommends a 4,308 kWh system, which is 28.3% smaller.

To meet the stricter voltage limits $0.95 \leq V \leq 1.05\ p.u.$, *i.e.,* limiting both over and under-voltages, the DLPF solution recommends 11,052 kW of solar PV, while the LinDistFlow solution recommends 10,953 kW, which is 8.96% smaller. Regarding battery energy storage, the DLPF solution recommends a combined capacity of 11,006 kWh while the LinDistFlow solution recommends 8,887 kWh, which is 19.3% smaller.

Therefore, the LinDistFlow solution underestimates both PV and the total battery storage capacity needed to meet voltage constraints; it also suggests a higher share of the battery be strictly REES.

Table 6.3 –DER adoption DLPF vs. LinDistFlow for the base case and two different voltage constraints. Percentages show the percentual difference between LinDistFlow solution and DLPF solution.

DER total adoption	*Base Case*	$V \leq 1.05$		$0.95 \leq V \leq 1.05$	
	No V constraints	**DLPF**	**LinDistFlow**	**DLPF**	**LinDistFlow**
PV (kW)	10,577	10,857	10,771(-0.8%)	11,052	10,953(-8.95%)
EES (kWh)	120	3,536	3,216 (-9.95%)	8,767	7,760 (-11.5%)
REES (kWh)	0	2,468	1,092(-55.8%)	2,239	1,127(-49.7%)
Total Storage (kWh)	120	6,004	4,308(-28.3%)	11,006	8,887(-19.3%)

To understand the underlying reasons for the results above, we look at the ability of each method to accurately approximate nodal voltage and branch power flows. We simulate the first constraint that prevents OV greater than 1.05 p.u. Figure 6.7 compares the linearized voltage profiles calculated using DLPF and LinDistFlow against the exact (post-processed) true voltage solution, or ACPF, calculated using MATPOWER. The DLPF voltage profiles for the entire optimization timeframe and for only a single time step (solid and dotted black lines), shown in Figure 6.7show an accurate linear approximation for voltage magnitude. The linearized voltage solutions range between 0.873 - 1.050 p.u. while the true (ACPF) voltage values range between 0.851 - 1.048 p.u. Recall that the base case (no voltage constraints) maximum OV reaches 1.179 p.u.; thus DLPF was effective in limiting OV. We note that the DLPF solution always suggests that the voltage at a given node is higher than the true voltage, or over-voltages are overestimated and under-voltages are underestimated. Thus, DLPF always captures and limit OV events but may be unable to capture and limit UV events.

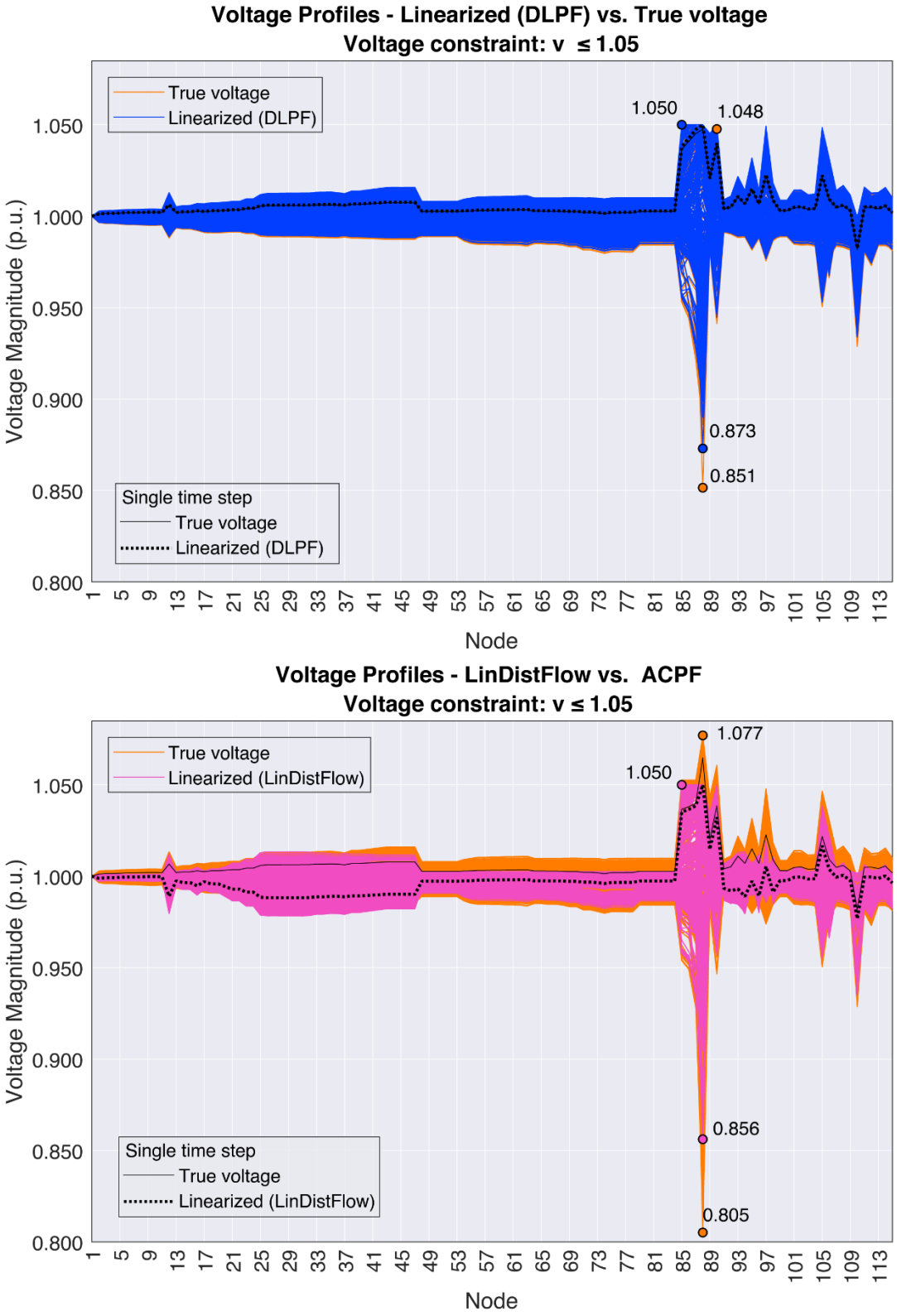

Figure 6.8 – Comparison of the voltage magnitude solution using DLPF (top) and LinDistFlow (bottom) against the ACPF (post-processed) true voltage solution. Each curve represents the voltage profile at a given time-step over the optimization timeframe. Markers indicate the worst case UV and OV (true and linearized) over the optimization timeframe. Solid and dotted black lines highlight the true and linearized voltages, respectively, at a given time step.

The LinDistFlow voltage profiles, however, differ significantly from the true voltage solution across the meshed nodes, as shown in Figure 6.8. One can observe this difference over a single time step — the true voltage is plot as a solid line, and the LinDistFlow solution is plot as a dotted line. The linearized voltage solutions range between 0.856 – 1.050 p.u. while the true voltage solution values range between 0.805 – 1.077 p.u. Therefore, LinDistFlow underestimates over-voltages and overestimates under-voltages across meshed nodes.

We then simulate the full ANSI Range A voltage limits of 0.95 – 1.05 p.u. to test the stricter voltage constraints. Figure 6.9 shows that for both DLPF and LinDistFlow, the linearized voltage solution ranges between 0.95 and 1.05 p.u.; however, the true voltage solution ranges, for DLPF, from 0.947 to 1.048 p.u., while for LinDistFlow, from 0.932 to 1.077 p.u. Therefore, neither DLPF nor LinDistFlow are able to capture and prevent UV below the 0.95 p.u. constraint. However, DLPF is still effective in preventing the OV in this particular case, while LinDistFlow exceeds the OV constraint by 0.022 p.u., or 2.2%.

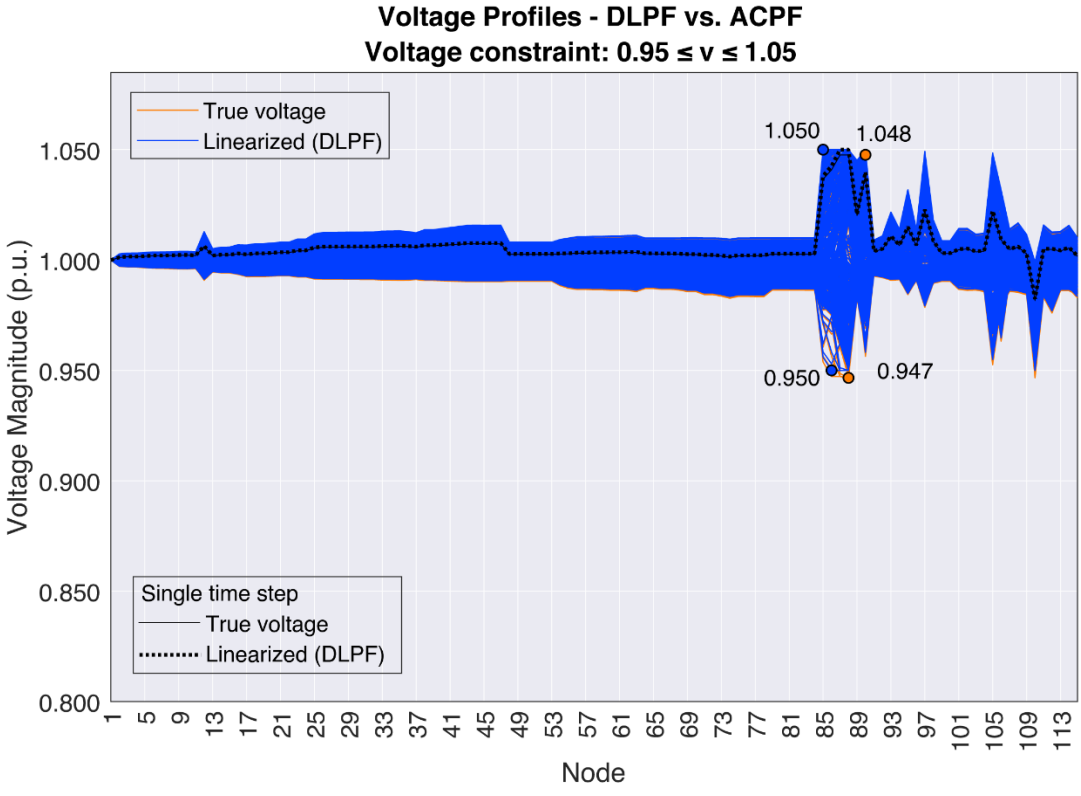

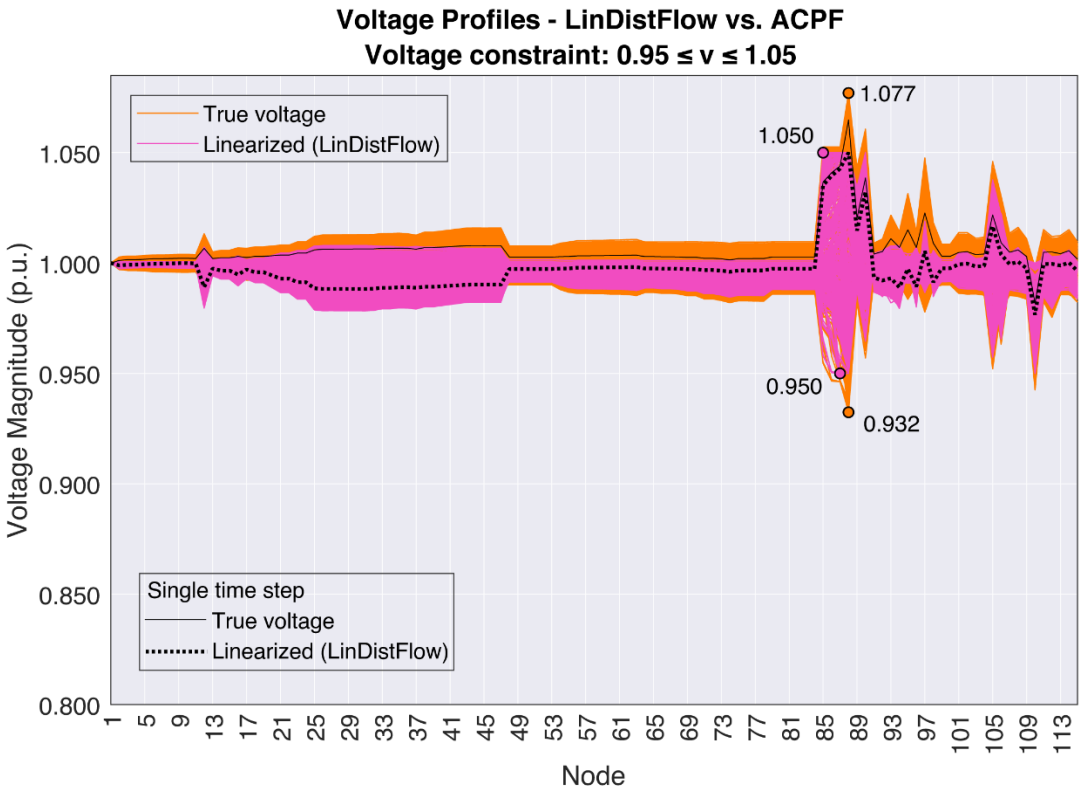

Figure 6.9 – Comparison of the voltage magnitude solution using DLPF (top) and LindistFlow (bottom) against e ACPF (post-processed) true voltage solution. Each curve represents the voltage profile at a given time step over the optimization timeframe. Markers indicate the worst case UV and OV (true and linearized) over the optimization timeframe. Solid and dotted black lines highlight the true and linearized voltages, respectively, at a given time step.

From the results of Table 6.3 we can also investigate the effects of voltage constraints in the optimal DER allocation. Strictly looking at the DLPF solution, compared to the base case, constraining OV causes a 2% increase in solar capacity and the combined battery storage capacity increases by 50-fold. If under voltages are also to be limited, the PV capacity increases by 2.7% from the base case, and total storage capacity increases by nearly two-fold from the OV limit case. Therefore, voltage constraints suggest a need for slightly more solar PV and significantly larger storage capacity when compared to the base case.

Regarding branch kVA power flows, Figure 6.10 compares solutions for the DLPF and LinDistFlow, and the true, post-calculated ACPF solution. Each curve shows the kVA power flows at all branches for a given time step. Solid and dotted black lines highlight true and linearized, respectively, branch kVA flows at a single given time step. Markers show the worst case (maximum) true and linearized kVA branch flows. For both DLPF and LinDistFlow, the true worst-case kVA flow happens at the node closest to the PCC, the branches with the highest power flow magnitude. Both approximation methods underestimate kVA flows (which is

expected form the underlying assumption of lossless lines), but DLPF is closer to predicting the correct solution than LinDistFlow. Nonetheless, both DLPF and LinDistFlow underestimate true kVA branch flows, which indicates that the solution does not respect branch kVA limits imposed, and the model likely needs to include a safety margin.

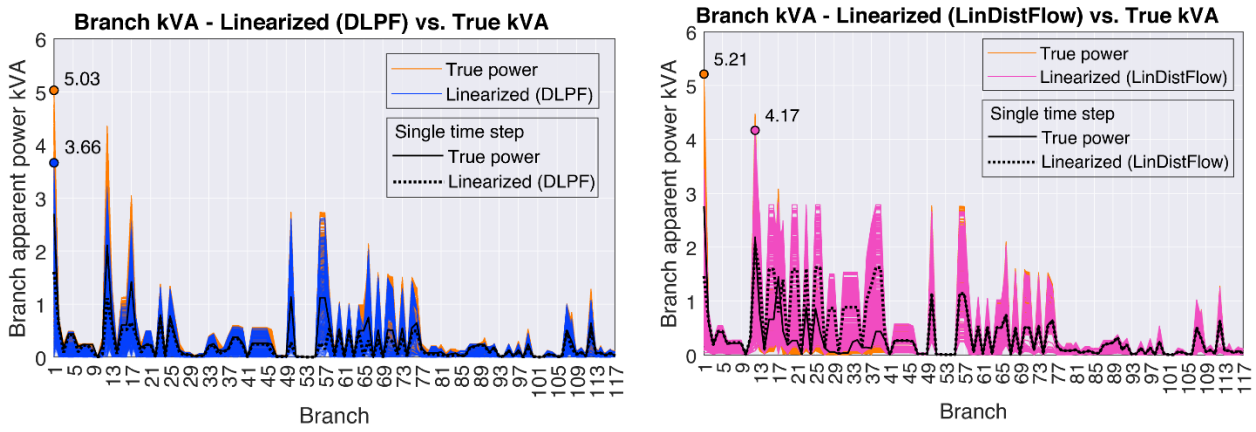

Figure 6.10 – Comparison of branch kVA power flows for DLPF (a) and LinDistFlow(B) solutions, compared to the true, post-calculated branch kVA power flow. Each curve shows the kVA power flows at all branches for a given time step. Markers indicate the worst case kVA power flows (true and linearized) over the optimization timeframe. Solid and dotted black lines highlight true and linearized, respectively, branch kVA flows at a single given time step.

The run times for both implementations varied between 70 minutes to 3 hours, depending on the number of constraints. The base case (no voltage or branch constraints) ran in 150 seconds. The LinDistFlow solution with only overvoltage constraints ran in 70 minutes while the DLPF solution took 85 minutes. For the full voltage constraints, the LinDistFlow solution took 83 minutes while the DLPF solution took 185 minutes. The optimality gap between the optimal and integer solution was limited to 0.4% in all runs.

6.6. Summary

This chapter developed a new approach to model the linearized power flow in a MILP for DER optimal allocation and dispatch to minimize cost. We provided a validation of the DLPF voltage magnitude and branch kVA power solutions against LinDistFlow and ACPF for a meshed benchmark network. We then formulated the DER allocation and dispatch problem as a MILP and used DLPF and LinDistFlow to model voltage and branch kVA flow constraints.

Our results show that:

- **For radial circuits, LinDistFlow is the most accurate linearization method**. Considering voltage magnitude, all linearized methods achieve a high degree of accuracy for voltage estimation: for our steady-state validation, linearization errors lie within 1% of the true value. For branch kVA flows, the errors lie within 5% of the true value.
- **For meshed networks, DLPF is the most accurate linearization method**. At the loops, LinDistFlow underestimates true voltage values, which occurred in both our steady-state validation and within our dynamic MILP optimization. Bolognani *et al.* approximation errors have the same order of magnitude, but slightly higher.
- The use of LinDistFlow within a DER optimization for a meshed network with voltage constraints may lead to undersized optimal PV and battery systems. The LinDistFlow solution will underestimate both OV and UV. Thus, it is not able to fully capture the magnitude of over and under voltages, and as a result, recommending undersized PV and battery systems.
- The DLPF solution is effective for limiting overvoltages, but might not capture under voltages. The DLPF solution slightly overestimates overvoltages (conservative) and underestimates under voltages (not strict enough).

7 Optimal solar inverter sizing considering Volt-Var droop-control and PQ control for voltage regulation

Highlights

- A MILP optimization for inverter sizing minimizes voltage deviations in a ZNE microgrid
- Smart inverter Volt-Var and optimal PQ functions are modeled within a linear optimization
- A novel linear approach to minimize the absolute voltage deviations is introduced
- An approximated model for AC/DC inverter sizing model was abstracted from simulations

7.1. Literature review

The low voltage electric distribution grid is being required to interconnect an increasing number of distributed energy resources such as solar photovoltaics. As a result, in moments of low load and high PV generation, reverse power flow — and subsequent overvoltages — threaten the local power quality. Reactive power support (by injecting or absorbing Vars) is a useful technique for controlling voltage excursions, and system operators have historically used Capacitor banks and Static Var Controllers (SVCs) for this end. However, they usually allow for only fixed-step Var increments and often operate at slower time scales, which can lead to over or under-voltage compensation (Thompson, Martini, & Seeley, n.d.).

A more effective way to provide reactive power support and local voltage control is by leveraging the potential of existing DER-interfacing power inverters to control Var absorption and injection. This method has only started to be considered in the U.S. somewhat recently since early grid interconnection standards, such as the IEEE 1547-2003 (IEEE, 2003), strictly prohibited the DER from regulating local voltage actively. There have been several initiatives started mostly by professionals in the utility sector to update such regulations. In California, the Smart-Inverter Working Group (SIWG) worked with the California Public Utilities Commission (CPUC) to update California interconnection standard, Rule 21, to accommodate and make advanced smart-inverter functions mandatory for new projects. A revision to Rule 21 (California Energy Commission, 2014) states that all new inverters interconnecting DER must have smart-inverter capabilities, *i.e.*, be equipped with a set of control functions that enable the local control active and reactive power. California's updated Rule 21 also drove the review process to the widely-used IEEE 1547-2003 interconnection standard, now in a most updated version, IEEE 1547-2018 (IEEE, 2018). Per the new standard, a category framework is established for voltage regulation (Category A and B) and disturbance ride-through requirements and (Category I, II, and III). Depends on the category, the DER inverter is required to absorb/inject, a certain percentage of its nameplate kVA.

Smart-inverters and their advanced control functions can play a crucial role in facilitating the penetration of renewable solar PV into the electric grid and the hosting capacity, *i.e.*, how much solar PV any given feeder can accommodate before causing an overvoltage (EPRI et al., 2015), of distribution feeders (NREL & Schauder, 2014). The relationship between voltage, DER active and reactive power consumption and generation, and network impedance is well known: the consumption of active power and/or consumption of reactive power (inductive Vars) locally reduces voltage. Conversely, the generation of active power and/or injection of reactive power (capacitive Vars) will locally raise voltage proportionally to system resistive and reactive impedances (Marra, Fawzy, Bulo, & Blažič, 2012; Smith, Sunderman, Dugan, & Seal, 2011). Therefore, smart-inverters can regulate voltage by (1) controlling the local reactive power, (2) controlling the local active power output, which poses the clear drawback of hindering the full utilization of PV assets, (3) leveraging co-located battery energy storage to store surplus generation, or (4) a combination of the above. Nonetheless, as already observed in previous studies (Alyami, Wang, Wang, Zhao, & Zhao, 2014), low voltage distribution systems are more

resistive than reactive, usually referred to as having a high R/X ratio, due to the short length of its circuits. Therefore, regulating the real power output in these types of networks is a very effective way of managing voltage.

Another current challenge involving DER integration to the grid is to allocate, *i.e.*, to assign an amount of a resource to a particular recipient node, commonly known as the process of "sizing and siting" these resources into the existing electric distribution grid. Thus, the types of DER (solar, storage, demand response) as well as their allocation within the grid network, and their operation has to be carefully chosen to meet customer demand without creating power quality issues and hindering system reliability.

In this context, this chapter proposes the optimal sizing of smart-inverters that are equipped with typical advanced functions such as Volt-Var-Optimization (VVO), to increase the PV hosting capacity of a community microgrid required to have a high penetration of solar PV to meet Zero-Net-Energy.

The goals of this chapter are (1) determine the optimal solar PV portfolio, size, and location within a real-world, ZNE urban electric distribution system (2) implement smart-inverter Volt-Var and PQ control function into the existing optimization framework to (3) optimally size the interfacing inverter while (4) minimizing cost and voltage deviations while (4) considering physical, electrical power system constraints. We then quantify power quality improvements in voltage.

The smart-inverter droop-control functions considered in the last analysis were initially proposed in the "ERPI, Common Functions for Smart Inverters – Phase 3" report (Electric Power Research Institute (EPRI), 2014).

7.1.1. Related Work

Many authors have explored novel methods for voltage regulation and control for high penetration of DER, their effectiveness, their impact on the network, and their interoperability with existing network devices.

One method is by the use of droop control curves programmed in DER inverters, known as "smart-inverter functions". The Volt-Watt and Volt-Watt, for example, define active and reactive power injections as piecewise linear functions of voltage and are a standard set of autonomous functions applied to voltage control.

A widely used approach to voltage control with a solar PV DER is the Volt-Watt function – active power curtailment based on local voltage – which uses the inverter rated apparent power as the static reference for the droop-based active power curtailment. (Luthander, Lingfors, & Widén, 2017) implemented a fixed-slope Volt-Watt control that was effective in removing all overvoltages in a three-phase 10 kV/400V distribution test system with a 100% PV penetration at the expense of a 31% reduction of the total PV generation. Dynamic approaches, on the other hand, use the inverter operation points at the time the overvoltage occurs as the reference for curtailment. (Y. Wang, Zhang, Li, Xiao, & Abdollahi, 2012) described a dynamic Volt-Watt control that curtails active power by predicting the resulting voltage variation using a Thevenin equivalent circuit at the point of injection. The method continually updated the droop-control curve slopes, and completely prevented overvoltages in the IEEE 34-bus test case. (Alyami et al., 2014) proposed a dynamic Volt-Watt control that does not require global system information, which eliminated overvoltages in the IEEE-13 bus system.

The Volt-Var function – Var output based on local voltage – is another common smart-inverter droop control strategy that regulates local reactive power absorption or injection. (Smith et al. 2011) demonstrated a static Volt-Var function, which provided adequate voltage support for a 12 kV circuit with 450 inverters operating in parallel. (Jahangiri and Aliprantis 2013) proposed a distributed control strategy for a dynamic Volt-Var function that avoids instabilities caused by the interactions of a large number of inverters operating in parallel. In that previous work, the proposed distributed control scheme mitigated overvoltages successfully in simulations of realistic distribution feeders with high (50%) smart-inverter penetration. (Seuss et al. 2015), showed a Volt-Var control that improved hosting capacity in a 12.47 kV distribution feeder by 72% (from 600 to 900 kVA). The author also points out that, at voltage-constrained buses, the Volt-Var control only improves the hosting capacity until a line thermal constraint is hit due to the injection of extra reactive currents, which may be even more challenging in distribution systems with a low X/R ratio. (Turitsyn et al. 2011) also points out the increased losses due to Volt-Var control.

One other method is the optimization of reactive power dispatch in a Volt-Var Optimization (VVO). (Farivar, Neal, Clarke, & Low, 2012) proposed an optimal inverter reactive power dispatch that was able to mitigate rapid and significant voltage fluctuations caused by a 5 MW PV deployment in a 12 kV, 56-node radial rural distribution feeder in Southern California.

Another VVO method to dispatch inverter Var resources was proposed by (Arnold et al., 2016), where a linearized optimal power flow formulation (LinDistFlow) was effective in limiting the voltage to +-5% bounds while minimizing voltage imbalance between phases in the radial IEEE 13 node test feeder.

Some authors extended the optimal Var control to both optimal Var and Watt control (or active power curtailment), which we refer here as *optimal inverter PQ control*. (Su, Masoum, & Wolfs, 2014) proposed an optimal PQ control strategy to minimize generation cost, losses, and voltage imbalance. The authors extended the analysis to single-phase inverters, which, when optimally dispatched, removed overvoltage and phase voltage imbalances in a 101 node three-phase, four-wire 22 kV/415V/240 V low voltage distribution feeder in Perth, Australia, with 39% solar PV penetration. (Sepehry, Heidari Kapourchali, Aravinthan, & Jewell, 2019) showed a similar optimal inverter PQ dispatch strategy, using a linearized unbalanced power flow, which minimized cost and wind curtailment while meeting power quality operational grid constraints in the radial IEEE-37 and IEEE-60 bus test cases. (Dall'Anese, Dhople, Johnson, & Giannakis, 2014) optimized inverter PQ dispatch in a 12-node residential low voltage (LV) test feeder with pre-selected inverter deployments to minimize losses, curtailment cost, and flat out the voltage profile. In that early work, the authors noted that inverters at the end of the feeder curtailed more active power and absorbed more reactive power to regulate voltage as compared to the other inverters.

Therefore, having PQ control does not provide a fair share between inverters of the burden of regulating system voltage by providing reactive power compensation and/or active power curtailment. As noted, inverters located at nodes with high impedance will be taxed with more regulation (Collins & Ward, 2015; Dall'Anese et al., 2014; Marra et al., 2012; Turitsyn, Šulc, Backhaus, & Chertkov, 2011). Droop-control strategies are usually employed to guarantee a more equal share of voltage regulation, and we will explore to what extent this regulation is distributed equally amongst inverters in our simulations.

The literature has shown successful use of different smart-inverter functions to mitigate overvoltages and, in turn, increase a feeder's voltage-based hosting capacity. However, the optimal choice of inverter size (kVA) is still a standing research question. Most inverters are set to operate in droop control with watt-priority, *i.e.*, reducing reactive power output to meet the maximum rated active power output. Thus, in watt-priority mode, the inverter kVA capability

limits its ability to provide reactive power regulation, especially in instances where the inverter size margin (*i.e.*, the inverter capacity beyond DER nameplate) is tight, and the DER is at full active power output. In a study led by the utility PG&E (Mead et al., 2015), it was shown that droop-controlled smart-inverters on the secondary (low voltage side) of a typical distribution feeder with high PV penetration had limited effect on reducing high voltage conditions due to an inverter capacity limitation for reactive power injection. In this previous study, the inverters were slightly undersized – a common practice in large-scale deployments, namely inverter *clipping*. (Seuss, Reno, Broderick, & Grijalva, 2015) also demonstrated a case where the inverter did not have enough capacity for reactive power injection to remove all overvoltages violations in a 12.4 kV feeder with a 1.3 X/R ratio. The previous study also performed a sensitivity analysis to explore the role of inverter sizing and Volt-Var control potential and showed that the best inverter size, *i.e.*, the size that will maximize the PV hosting capacity before reaching the point of diminishing returns, varied for one feeder to another, and ranged from 121% to 135%.

In the literature, there is not a clear consensus on how much inverter capacity beyond or below DG nameplate is needed, and many authors have judiciously assumed different values. For example, (Abate, McDermott, Rylander, & Smith, 2015; Dall'Anese et al., 2014; Farivar et al., 2012; Rylander, Li, Smith, & Sunderman, 2016; Rylander et al., 2017; Schultis, 2019; Smith et al., 2011; Turitsyn et al., 2011) assumed a 10% oversizing margin, which is the equivalent of allowing a reactive power injection with a power factor of 0.90 lagging, even during peak active power production. (Jafari, Olowu, & Sarwat, 2019) oversized inverters by 15%, (EPRI et al., 2015; Seuss et al., 2015) oversized inverters by 20%, and (Su et al., 2014) oversized the inverters by 60%. Authors in (Jahangiri & Aliprantis, 2013; Sepehry et al., 2019), assumed the inverter rating matches the DG rated capacity, while in (Ding et al., 2016; Stetz, 2014) the inverters were undersized by up to 10% below DG rated capacity.

Ideally, for each control function, there would be one global inverter size margin that is effective in all situations. However, the amount of reactive power necessary for a given compensation strategy to be useful is shown to be strongly related to the electric power system characteristics such as feeder R/X (resistance versus reactance) ratio, source impedance, and PV penetration levels (EPRI et al., 2015; Rylander et al., 2017; Seuss et al., 2015; Smith et al., 2011; Su et al., 2014). Therefore, the optimal inverter size margin is likely location/feeder-specific. One recent study by (Ali, Raisz, & Mahmoud, 2019) proposed an optimization-based method to oversize

inverter capacity. However, it did not consider a droop-control strategy, nor a fair sharing of regulation amongst inverters.

The previous discussion points to a gap identified in literature regarding the lack of studies that optimally size inverters that use voltage-reactive power droop-control within an optimal DER allocation (size and site) problem.

7.1.2. Contributions

- Include smart inverter Volt/Var droop-control and optimal *PQ control* functions in a MILP optimization formulation for the *DER allocation problem.* By introducing a novel linearization approach.
- Optimally size inverters for minimizing voltage deviations in a low voltage distribution feeder with a high PV penetration. A novel approach to minimize the absolute voltage deviations is introduced in the objective function
- Model and compare optimal AC/DC inverter sizing for inverter PQ and droop-control strategies.

7.2.Notation

We define below relevant model sets and the subscripts defined in this chapter regarding smart inverter integration into the model. We assume the reader is familiar with the previous DERopt model sets and decision variables. For reference see the notation sessions on Chapters 4 and 5. Table 7.1 and Table 7.2 provide a list and description of new model parameters and decision variables.

- $t \in T$: Set of hourly increments
- $n \in N$: Set of nodes
- $i \in I$: Set of "From" nodes
- $j \in J$: Set of "To" nodes
- $b \in \mathcal{B}$: Set of buildings
- $\lambda \in \Lambda$: Set of line segments for polygon relaxation
- $x \in X$: Set of transformers
- $h \in H$: Set of inverters
- L: Set of PQ nodes

- *S*: Set of PV nodes
- *R*: Set of reference (slack) nodes

Table 7.1 – Model decision variables

Decision Variable	Description	Units
$\bar{S}_{\text{inv}_b}$	Inverter adoption at building *b*	kV
$P_{\text{Inv}_{h_t}}$, $Q_{\text{Inv}_{h_t}}$, $S_{\text{Inv}_{h_t}}$	Active, Reactive, and Apparent Power flows through inverter *h* at hour *t*	kW/ kVar/ kVA
$Q_{\text{inv}_{\text{BLDG}}}$	Building reactive power demand	kVA
$Q_{ind_{h,t}}$	Inductive Reactive Power absorbed by inverter h at hour t	kVar
$Q_{cap_{h,t}}$	Capacitive Reactive Power injected by inverter h at hour t	kVar
$\boldsymbol{\theta}$	Nodal Voltage phase angle matrix. $\mathbb{R}^{N-1}$	degrees
$\boldsymbol{v}$	Nodal Voltage magnitude matrix. $\mathbb{R}^{N-1}$	p.u.
$\boldsymbol{p}$	Nodal Active power injection. $\mathbb{R}^{N-1}$	p.u.
$\boldsymbol{q}$	Nodal Reactive power injection. $\mathbb{R}^{N-1}$	p.u.
q_{anc}	Linearized reactive power regulation for Volt-Vat curve	p.u.

Table 7.2 – List of parameters used in DERopt

Parameter	Description	Units	Value
ω	Weight for penaltty function	N/A	1 for PQ control 1,000 for Volt-Var control
v_1, v_2, v_3, v_4	Volt-Var inverter voltage curve settings	p.u.	0.90, 0.97, 1.03, 1.1
q_1, q_2, q_3, q_4	Volt-Var inverter Var curve settings	p.u. (Var)	0.60, 0, 0, -0.60
m_{cap}, m_{ind}	Volt-Var curve slopes	N/A	Dedepnds upon Volt-Var curve

7.3.Problem Formulation

We extend the Building Energy Hub concept presented in Chapter 5 and in (Novoa et al., 2019) to include an interfacing DER inverter. The schematics in Figure 7.1 illustrates a building energy

hub, which includes the building load ($BLDG_b$) the local DER adopted (PV_b , EES_b, $REES_b$), and the interfacing inverter (Inv_b), which connects the direct current DER to the building AC loads and a distribution transformer (T_x). Each distribution transformer connects one or a cluster of building energy hubs to the AC low voltage electric grid network. DERopt optimally sizes the interfacing inverter ($\bar{S}_{\mathrm{inv}_b}$) accommodate the active net power flows from PV generation, battery storage charging and discharging, and also the necessary reactive power flows to provide voltage local support. Equations (91) and (92) provide the active and reactive power balances within the building energy hub. Each building load P_{BLDG} can be fed by a mix of power imported to the hub (P_{import}), PV generation ($P_{\mathrm{PV}_{\mathrm{BLDG}}}$), and any battery power ($P_{\mathrm{EES}_{\mathrm{dch}}}$, $P_{\mathrm{REES}_{\mathrm{dch}}}$). The building reactive power demand (is calculated at a fixed power factor from the active power demand, thus, Q_{BLDG} = $\mathrm{P}_{\mathrm{BLDG}}\arctan(PF)$.The building reactive demand can be met by grid imports (Q_{import}) or by reactive power produced by the inverter ($Q_{\mathrm{inv}_{\mathrm{BLDG}}}$). Equation (93) constrains all PV power generation, that is, the PV generation to meet building loads ($P_{\mathrm{PV}_{\mathrm{BLDG}}}$) and the PV generation exported for revenue under the NEM and wholesale markets ($P_{PV_{NEM}}$, P_{PV_W}) to the PV system rated power ($\bar{S}_{\mathrm{PV}_b}$) times the normalized local insolation (I). Note that equation (93) calculates the value of the decision variable ($\bar{S}_{\mathrm{PV}_b}$) and since it is an inequality, it allows for power curtailment. We adopt the *load convention* for all power flow throughout the entire hub; therefore, positive values mean import, and negative values mean export. All variables described above have positive values. Equations (94) and (95) calculate the *net* real and reactive power flows through the inverter ($P_{\mathrm{inv}_{t,b}}$, $Q_{\mathrm{inv}_{t,b}}$), therefore these variables can assume either a positive (import) or negative (export) value, and using this modeling approach, the inverter cannot import and export power at the same time. The only active power import through the inverter happens when EES charges using grid power ($P_{\mathrm{EES}_{\mathrm{ch}}}$) and all other power flows regarding PV generation (PV_{BLDG}, PV_{NEM}, PV_W) and battery discharge ($P_{\mathrm{EES}_{\mathrm{dch}}}$, $P_{\mathrm{REES}_{\mathrm{dch}}}$, $P_{\mathrm{REES}_{\mathrm{NEM}}}$) are exports. Regarding reactive power flows, the inverter can meet part (or all) of the reactive building load ($Q_{\mathrm{inv}_{\mathrm{BLDG}}}$) or also provide ancillary services (Q_{anc}) such as when a smart-inverter has a Volt-Var droop-control curve implemented. Q_{anc} can assume either a positive or negative value. A positive value indicates that inductive reactive power is absorbed by the inverter and a negative value, capacitive reactive power being injected. By this modeling approach, the inverter cannot provide both capacitive and reactive compensation at the same time, which makes physical

sense. The variable Q_{anc} can be broken down into two positive quantities: Q_{cap} and Q_{ind}. Such as $Q_{\text{anc}} = Q_{\text{ind}} - Q_{\text{cap}}$ Equations (96) and (97) calculate the *net* real and reactive power flows through the transformer T_x, P_{T_x} and Q_{T_x} respectively . These *net* flows take into account grid imports (P_{import}, Q_{import}), renewable power exports ($P_{PV_{NEM}}$, P_{PV_W}, $P_{\text{REES}_{\text{NEM}}}$), and inverter ancillary services (Q_{anc}, Q_{cap}, Q_{ind}), as illustrated in Figure 7.1.

We note that even though battery storage is defined here, this analysis does not consider the adoption of battery energy storage since we want to focus on the sole ability of smart inverters to locally regulate voltages.

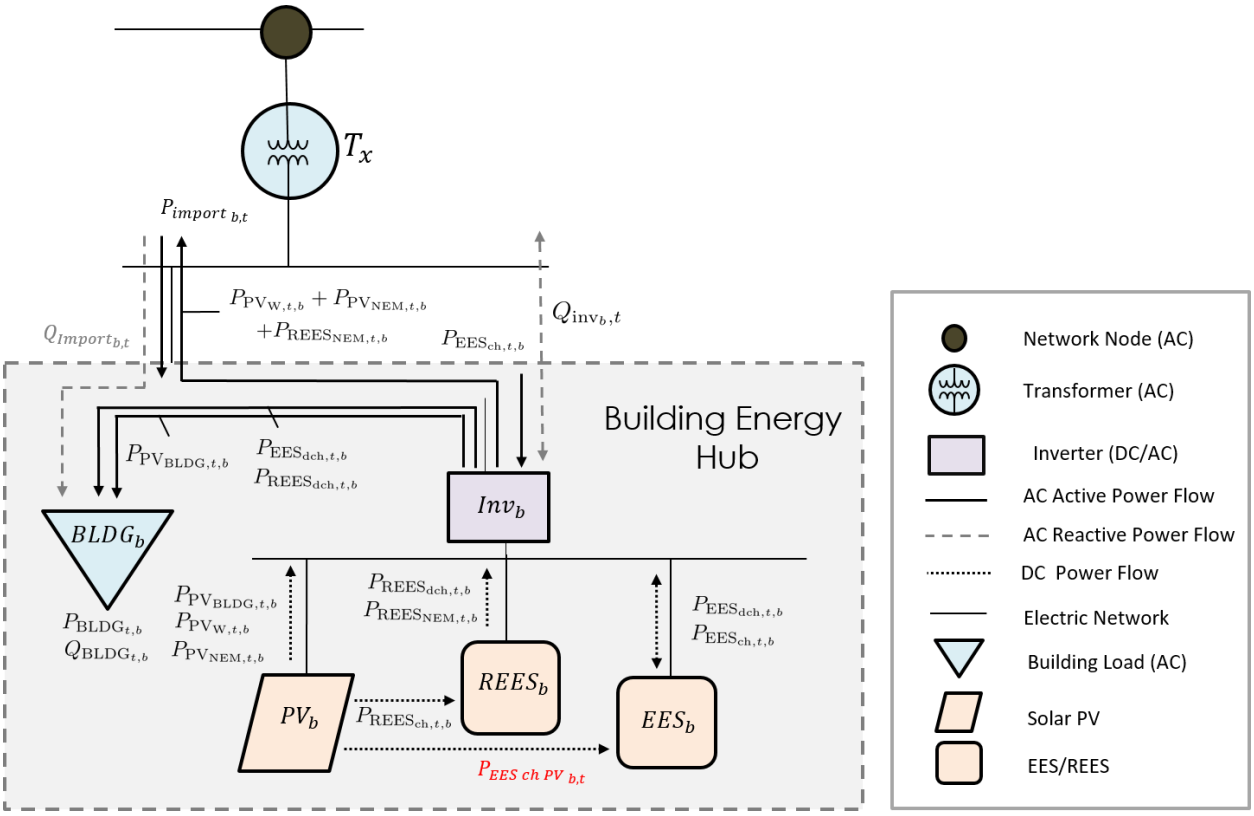

Figure 7.1 – Schematic of one Building Energy Hub used in the multi-node approach. Transformer T_x is one node, to which a cluster of buildings and adopted DER (PV_b , EES_b, $REES_b$) are connected. Inverter Inv_b connects the DER adopted at building b to the AC side of the distribution system.

$$P_{\text{import}_{t,b}} + P_{\text{PV}_{\text{BLDG},t,b}} + P_{\text{EES}_{\text{dch},t,b}} + P_{\text{REES}_{\text{dch},t,b}} = P_{\text{BLDG}\,t,b} + P_{\text{EES}_{\text{ch},t,b}} \quad (91)$$

$$Q_{\text{import}_{t,b}} = \text{P}_{\text{BLDG}}\arctan(PF) - Q_{\text{invBLDG}_{t,b}} \quad (92)$$

$$P_{\text{PV}_{\text{BLDG},t,b}} + P_{\text{PV}_{\text{NEM},t,b}} + P_{\text{PV}_{W,t,b}} + P_{\text{EES}_{\text{chPV},t,b}} + P_{\text{REES}_{\text{ch},t,b}} \leq I_t S_{\text{PV}_b} \quad (93)$$

$$P_{\text{inv}_{t,b}} = P_{\text{EES}_{\text{ch},t,b}} - P_{\text{EES}_{\text{dch},t,b}} - P_{\text{REES}_{\text{dch},t,b}} - P_{\text{REES,NEM}_{dch,t,b}} - P_{\text{PV}_{\text{BLDG},t,b}} - P_{\text{PV}_{\text{NEM},t,b}} - P_{\text{PV}_{\text{W},t,b}} \quad (94)$$

$$Q_{\text{inv}_{t,b}} = -Q_{\text{invBLDG}_{t,b}} + Q_{\text{anc}_{t,\text{b}}} \quad (95)$$

$$P_{\text{T}_{x_t}} = \sum_{j \in J_k} P_{\text{import}_j} - P_{\text{PVNEM}_j} - P_{\text{PV W}_j} - P_{\text{REES dch NEM}_j} \quad (96)$$

$$Q_{T_{x_t}} = \sum_{c \in \mathcal{C}_x} Q_{\text{import}_c} + Q_{\text{anc}_c} \quad (97)$$

7.3.1. Zero-Net-Energy Operation

The Zero Net Energy operation is formulated using the same Equations defined in Chapter 5, section 5.2.3 and omitted here for brevity.

7.3.2. Decoupled Linearized Power Flow

We formulate the governing power flow equations using the decoupled linearized power flow formulation introduced in Chapter 6, session 6.3.2 and we omit it for brevity.

7.3.3. Inverter Constraints

7.3.4. Polygon Relaxation

The inverter rated power capacity $\bar{S}_{\text{inv}}$ limits the amount of current (equivalently, the amount of power) it can inject into the grid. The industry expresses power ratings in kilovolt-amperes (kVA), i.e., the vectorial sum of the active P_{inv} (kW) and reactive Q_{inv} (kVAr) power injections; Equation (98) shows this relationship. Therefore, the inverter apparent power injection at any given time S_{inv} can't exceed its power rating $\bar{S}_{inv}$

$$S_{inv} = \sqrt{P_{inv}^2 + Q_{inv}^2} \leq \bar{S}_{inv} \quad (98)$$

Equation (98) dictates inverter power flows; however, a MILP formulation cannot directly capture non-linearities. Thus, we perform a polygon relaxation of the apparent power circle, as shown in Figure 7.2 and formulated by the constraints in equations (99) through (102). Equation (102) defines the approximation error, which is the difference between s and $\bar{S}$. For our particular problem, we can reduce the absolute error below 1% by setting the number of polygon sides Λ to 22. Using this approximation, power through an inverter can be written as equation (100), and implemented into the MILP optimization as equation (101). Equation (99) obtains the optimal value for the inverter size ($\bar{S}_{inv}$) decision variable.

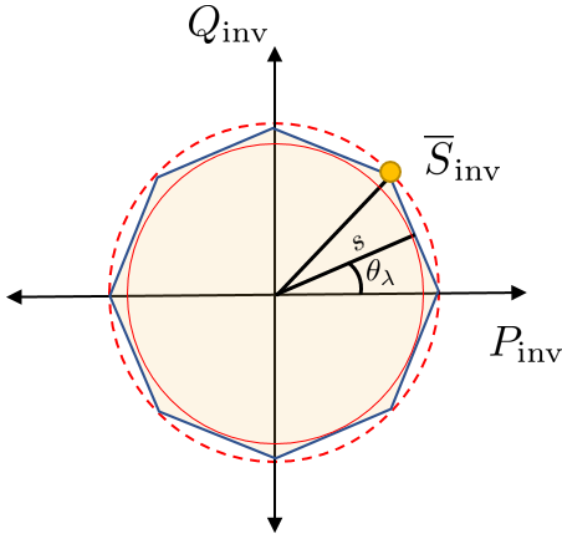

Figure 7.2 – Depiction of the polygon relaxation constraints and operating regions for the inverter (shaded in yellow).

$$s = \bar{S}_{inv} cos\left(\frac{\pi}{\Lambda}\right) \tag{99}$$

$$s = P_{inv}\cos(\theta_\lambda) + Q_{inv}\sin(\theta_\lambda), \tag{100}$$

$$\theta_\lambda = \frac{\pi}{\Lambda} + \lambda\left(\frac{2\pi}{\Lambda}\right) \qquad \lambda = 0,1,\dots,\Lambda - 1$$

$$s \geq \begin{bmatrix}\cos(\theta_\lambda) & \sin(\theta_\lambda)\end{bmatrix}\begin{bmatrix}P_{inv}\\ Q_{inv}\end{bmatrix} \tag{101}$$

$$\epsilon = \bar{S}_{inv} - s = \bar{S}_{inv}\left(1 - \cos\frac{\pi}{\Lambda}\right) \tag{102}$$

$$\Lambda \geq \frac{\pi}{\arccos\left(1 - \frac{\epsilon}{\bar{S}_{inv}}\right)}$$

7.3.5. *Inverter Droop Control (Volt-Var)*

The inverter static *Volt-Var* droop-control curve is illustrated in Figure 7.3. The per-unit reactive power injection/absorption (q) varies as a linear function of the per-unit voltage at the inverter terminals (v). This curve is defined by four points, or v-q pairs, namely the *inverter settings*. A dead band between points v_2 and v_3 is the region where no reactive power compensation occurs. The inverter settings used here are based upon the settings recommended by the IEEE-1547 2018 standard for Category A, except for the reactive power absorption limit was increased from 44% to 60% to improve voltage compensation capacity. The settings used are shown in Table 7.3
We assumed the inverters operate in *Q- priority*, that is, active power is curtailed in favor of accommodating the necessary reactive power compensation, that is: $P_{inv} = \sqrt{S_{inv}^2 - Q_{inv}^2}$. This behavior is modeled by the inequality constraint on equation (93) and the equality constraint of equations (95) and (105). Nonetheless, as recommended by IEEE-1547, the maximum compensation an inverter will produce can only go up to 44% of its capacity (0.44 per-unit). Equation (104) calculates the curve fixed (pre-defined) slope.

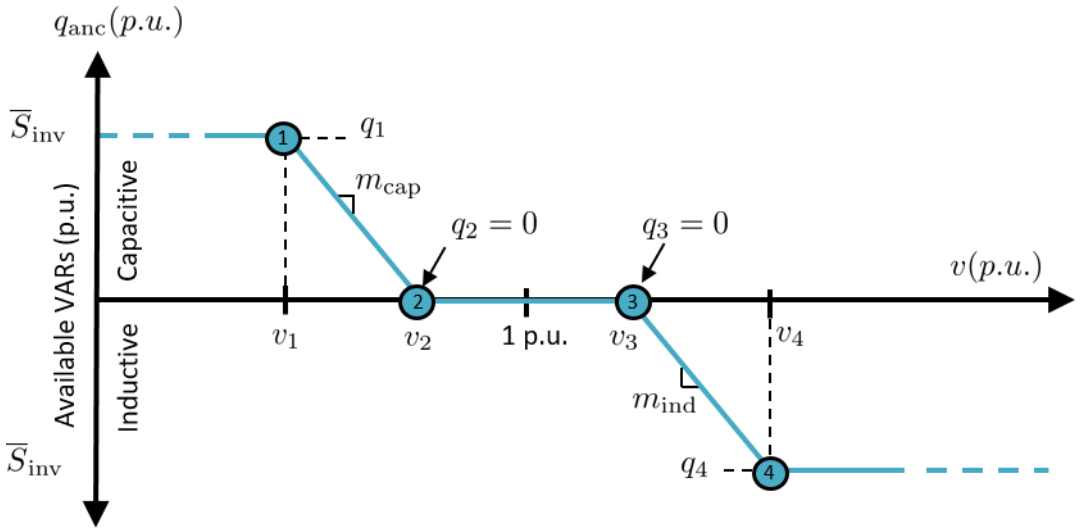

Figure 7.3 – Volt-Var droop control curve. The curve is defined by four points, or v-q pairs, that define the reactive power outputq_{anc} as a function of the voltage v at the inverter terminals

Table 7.3 – Volt-Var inverter settings

Volt-Var droop-control parameter	Value (p.u.)
v_1	0.90
v_2	0.97
v_3	1.03
v_4	1.1
q_1	0.60
q_2	0
q_3	0
q_4	-0.60

$$q_{anc} = \begin{cases} q_1 & , if\ v < v_1 \\ m_{cap}(v - v_2) & , if\ v_1 < v < v_2 \\ 0 & if\ v_2 < v < v_3 \\ m_{ind}(v - v_3) & if\ v_3 < v < v_4 \\ q_4 & if\ v > v_4 \end{cases} \quad (103)$$

$$m_{cap} = \frac{q_2 - q_1}{v_2 - v_1}, \qquad m_{ind} = \frac{q_4 - q_3}{v_4 - v_3} \quad (104)$$

$$Q_{anc} = -q_{anc}\bar{S}_{inv} \quad (105)$$

$$f^a(q_{anc}, \bar{S}_{inv},) \quad (106)$$

Equation (105) is, however, non-linear when both q_{anc} and $\bar{S}_{inv}$ are decision variables, i.e., when we are interested in sizing the inverter. The challenge of modeling Volt-Var behavior in a MILP model requires a novel approach to linearize this relationship. We then devise a method that takes advantage of the linearity of the feasible region. Thus, we model equation (105) as a piecewise-linear approximation of a surface, which is a function of two variables, *i.e.*, $f^a(q_{anc}, \bar{S}_{inv})$, Figure 7.4 illustrates the piece-wise linear surface. We then calculate the inverter reactive power Q_{anc} by interpolating between points in the feasible surface. We use the solver's built-in linear interpolation function, which creates SOS2 sets. This linearization could have been

modeled directly, using binary variables and appropriate auxiliary SOS constraints. We chose to use the built-in function since it produces a model with pure SOS2 sets, which the branch-and-cut algorithm can process and solve more efficiently and faster as opposed to processing binary sets. Also, the surface in Figure 7.4 has a high number of breakpoints (fine mesh grid) for illustrational purposes, in reality, to minimize problem scale, the surface is implemented using a much sparse mesh grid that only uses the inverter settings voltage points, *i.e.*, $v_i = [v_1, v_2, v_3, v_4]$ and two inverter size limits $s_i = [0, \bar{S}_{inv_{max}}]$ where $\bar{S}_{inv_{max}}$ is assumed based upon the order of magnitude of the maximum PV adoption in the *Baseline* scenario. Nonetheless, the solver function also performs linear extrapolation when necessary.

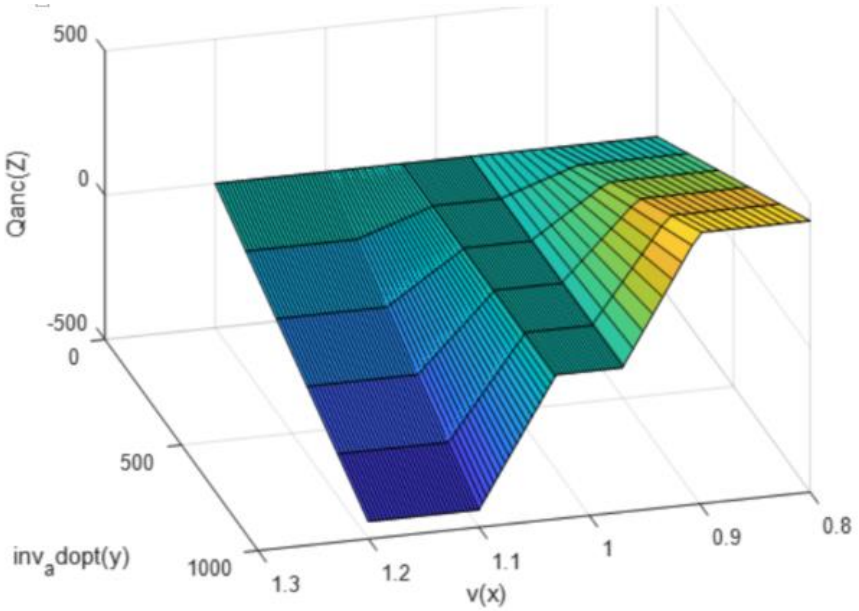

Figure 7.4 – Piece-wise linearization of a function of tow variables, $Q_{anc} = -q_{anc}\bar{S}_{inv}$. As the inverter size increases, so does the ability of the inverter to provide more reactive compensation (Q_{anc}).

7.3.6. Inverter PQ control

In this inverter control mode, the per-unit active and reactive power injection/absorption (P_{inv}, Q_{inv}) vary freely (unconstrained). The inverter capacity S_{inv} is determined according to Equations (99) and (100)

7.3.7. MILP Formulation

7.3.8. Objective Function

The objective function used here $G(x)$adds to the already defined cost function $J(x)$, defined in Chapter 5, Equation (47), which captures the costs associated with purchase and sale of energy, the cost associated with demand charges, and the cost associated with purchasing and operating the adopted DER. We add to the existing objective function e cost of purchasing the interfacing DER inverter. Therefore, the model will drive inverter adoption the minimum necessary to meet system constraints. The voltage deviation penalty parameter $\Delta_v$aims to drive system voltages closer to 1 p.u. and it is described below

$$G(x) = \quad J(x) + \ C_{\text{cap}}^{\text{inv}} S_{inv_b} + \Delta_v \tag{107}$$

The voltage deviation penalty term Δ_v aims to capture the sum (of the absolute values) of all hourly voltage deviations (from 1 p.u.) across all system nodes, *i.e.*, $|1 - \boldsymbol{v}|$, where the boldface vector $\boldsymbol{v} \in \mathbb{R}^{SxT}$ collects all nodal voltages for the optimization timeframe. However, since the absolute value is a non-linear function: $|1 - v| = \sqrt{(1 - v)^2}$, We cannot directly implement it into the MILP. Hence, a mathematical artifice, namely the decision variable $\boldsymbol{\delta} \in \mathbb{R}^{SxT}$ is used to linearize the absolute voltage deviation as follows: two constraints described by equations (108) and (109) are added to the model formulation and Equation (110), which describes the sum of all individual $\boldsymbol{\delta}$ terms (Δ_v) is added to the objective function preceded with a weight ω. Therefore, the minimzation of Δ_v (and consequently) will drive the individual nodal voltages v towards 1 p.u. The weight ω assumed for PQ control is 1 and for Volt-Var control, 1,000 in order to drive adequate voltage regulation.

$$\boldsymbol{\delta} \geq \ 1 - \boldsymbol{v} \tag{108}$$

$$\boldsymbol{\delta} \geq \ -(1 - \boldsymbol{v}) \tag{109}$$

$$\Delta_v = \ \omega \sum_{i=1}^{S} \sum_{t=1}^{T} \boldsymbol{\delta} \tag{110}$$

The objective function is thus minimized subject to a set of equality and inequality constraints, and also integer constraints, lower l and upper u bounds, which limit strictly positive variables and Big M limits.

The MILP optimization problem is given by the following functions and constraints: Where $G(x)$ is the objective function and A and B are the respective coefficient variables for x continuous decision variables and y integer decision variables. The problem is subjected to linear equality and inequality constraints, l and u upper and lower bounds, and integer constraints on y.

$$\begin{aligned} \textbf{min} \quad & G(x) && (107) \\ \boldsymbol{s.t.} \quad & Ax + By \leq b && (76),(77),(86),(91)\text{-}(97),\ (99)\text{-}\ (103),(105),(106) \\ & l \leq x \leq u && \text{*specific to each variable} \\ & y \in \mathbb{Z}^n \\ & y \geq 0 \end{aligned} \tag{111}$$

7.4. Test Case and Assumptions

We use the test case introduced in Chapters 5 and 6, the Oak View microgrid. All assumptions for circuit topology, technology cost, electrical demand, and PV resources are the same. Inverter cost is assumed to be $150/kW based on current market research for inverters up to 6 kVA.

To pursue a tractable optimization, we perform a worst-case type analysis, where we only simulate the day (24-hours) in the year flagged with the worst (maximum) RPF. Therefore, our design results indicate the inverter size that can provide support to the worst RPF event in the year. The worst-case RPF day was identified by scaling up the normalized PV annual generation profile to just above the local peak load (3111.6 kW), calculating the net-load (load minus generation), and identifying the hour with the most negative net-load. For our test system, the worst-case RPF happens on a Sunday in March, a sunny, clear day in spring with mild temperatures and low load.

A detailed list of all building load maximum demand, total energy demand, the associated transformer, and its power rating, and building power factor is presented in Chapter 6. We also assume smart-inverters are adopted in 7 out of the 31 building nodes. The other inverters are assumed to be standard inverters, with no reactive power output. Figure 5.5 shows a schematics

of the circuit topology. We represent loads as triangles, building numbers in red, primary node numbers in black and secondary node numbers in blue.

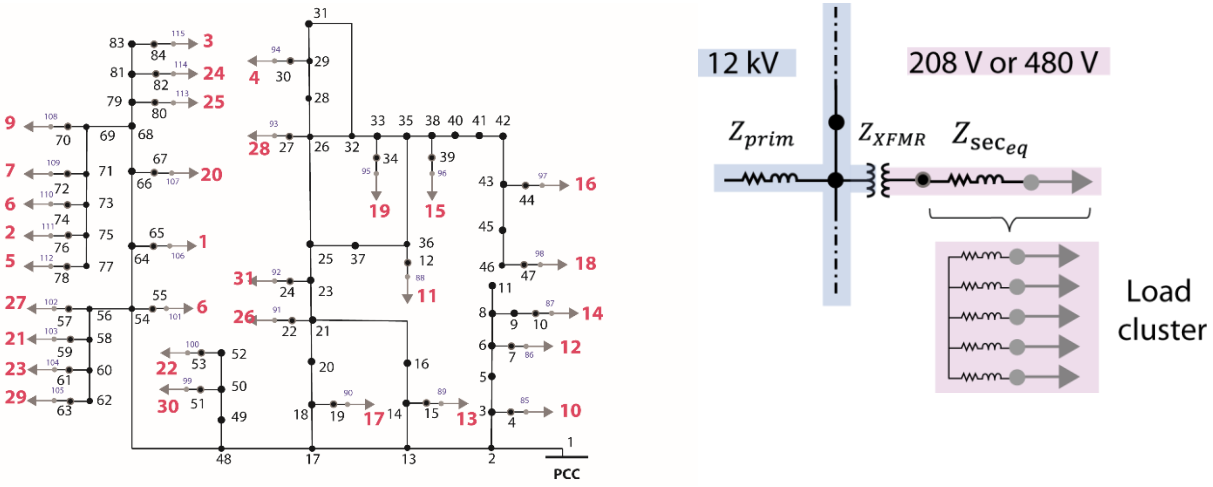

Figure 7.5 – Meshed benchmark case based on a real-world power system (left) and modeled as 115 nodes, 31 of which are transformers that serve clusters of industrial, commercial, and residential loads. We represent loads as triangles, building numbers in red, primary node numbers in black and secondary node numbers in blue. Node 1 is the PCC with the wide-area grid. (right) The primary voltage is 12.47 kV, and secondary voltages are 480 V or 208 *V, depending upon customer type. Each transformer is modeled as a series impedance (Z_{XFMR}) with the secondary line drop equivalent impedance ($Z_{sec_{eq}}$), which represents five customers aggregated in parallel in a load cluster.*

7.4.1. Scenarios

The goal of this chapter is to use our MILP optimization to determine the optimal inverter size (kVA) for pre-defined smart-inverter locations within the test-case under two different smart inverter control strategies. We are interested in analyzing the challenging cases of large PV deployments. Therefore, for all simulations, the test case is constrained to be Zero-Net-Energy, defined as able to produce as much electricity as demand over one *day*, or 24 hours.

In the *Baseline* scenario, the DER allocation problem is simulated to meet ZNE constraints with conventional inverters, i.e., inverters without smart-inverter features. There are no other constraints limiting voltage magnitudes or power flows through transformers, nodes, or feeders; in other words, the system power quality is not actively controlled.

In the *Optimal PQ* scenario, solar PV smart-inverters will be optimally sized to provide over-voltage support to the *Baseline* scenario. All inverters can produce and absorb P and Q freely.

In the *Volt-Var* scenario, we simulate the *Baseline* solar PV allocation, and we apply a droop-control *Volt-Var* function to seven pre-defined inverter locations. The locations chosen are the

seven buildings with higher overvoltages recorded over the optimization timeframe. The other inverters are assumed to be standard inverters.
A summary of all scenarios is given below:

- **Baseline:** Solar PV allocation problem for a ZNE test case with standard inverters (no local reactive power control)
- **Optimal PQ:** Baseline solar PV allocation. All inverters inject/absorb an unconstrained amount of active (P) and reactive (Q) power.
- **Droop control (*Volt-Var*):** Baseline solar PV allocation. Reactive power output is a function of voltage, following a droop-control function at seven pre-defined locations at buildings 1, 10, 11, 12, 14, 16, and 17. Remaining inverters are standard inverters.

The optimization algorithm is implemented in MATLAB R2015a (The MathWorks Inc., n.d.) using the YALMIP R20181012 toolbox (Lofberg, 2005; Löfberg, 2019) and CPLEX v.12.8 (IBM, 2017) for the MILP solver. The worst-case analysis reduces our dataset to 24 hourly intervals. The hardware used for the optimization is an Intel Xenon CPU E5-2680 v2 @2.80 GHz server with 20 cores, 40 threads, and 32 GB of RAM. Simulation times are no longer than 30 seconds.

7.5. Results and Discussion

7.5.1. Baseline

The *Baseline* scenario adopts 5,090 kW of solar PV and a total inverter capacity of 4,227 kVA (*i.e.*, AC/DC ratio <1). Figure 7.6a. shows the resulting post-processed true AC voltage profiles. Each curve represents the voltage profile at a given hour over the optimization timeframe (24 hours)**.** The markers indicate the worst-case under voltage and over voltage recorded. The dotted black lines highlight the voltage profile at 1 PM and 8 PM. The *Baseline* voltages range between 0.94 - 1.07 p.u. These extreme values occur at building 11 (located at the secondary node 88), which hosts a large 404 kW PV system. The lowest voltage occurs at 8 PM, and the highest voltage occurs at 2 PM. Similarly to the results of other DER interconnection modeling efforts (Mead et al., 2015; NREL & SolarCity, 2016), the worst voltages here occur at the secondary nodes. Our results show the expected outcome of poor power quality when large PV systems are

deployed into the existing grid infrastructure. We aim to overcome with both optimal PQ and Volt-Var droop control.

7.5.2. Optimal PQ control and Volt-Var droop-control

In the *Optimal PQ* scenario, all inverters are allowed to perform PQ control locally. In these inverter nodes, unconstrained active and reactive power injections will regulate voltage. In the *Volt-Var* scenario, smart inverters are installed in seven pre-defined building nodes (11, 14, 1, 17, 12, 10, 16). To drive voltage regulation, a penalty for voltage deviation from 1 p.u., as described in section 5.2.2, is introduced in the objective function. Figure 7.6.b shows the resulting post-processed true AC voltage profiles for the *Optimal PQ and Volt-Var* control scenarios. The min/max voltage values occur at buildings 11 and 14 (at secondary nodes 88 and 87, respectively). Building 14 hosts 336 kW of solar PV. For both controls, the min/max per unit voltages are the same, 0.94 /1.05 per unit. However, the average standard deviation for PQ control is the lowest ($\bar{\sigma} = 0.0039$) followerd by Volt-Var ($\bar{\sigma} = 0.0048$). Therefore, on the voltage controlled methods, there is less voltage dispersion compared to Baseline ($\bar{\sigma} = 0.0052$), in other words, the voltages are overall closer to 1 per-unit.

Compared to the *Baseline*, the maximum overvoltage is now compliant with the ANSI C.84 1.05 p.u. limit. The minimum voltage 0.94 is still below the recommended ANSI C84 limit of 0.95 p.u. — inverter controls did not assist with under voltages. That happens because the worst under voltages occur at 8 PM, which is outside the PV generation window. At this time, the inverter is idle because there is no PV generation (DC voltage). An alternative to regulating evening under-voltages would be to co-locate DC-coupled battery energy storage. Nonetheless, as under voltages are not usually the limiting factor for PV deployments, the reactive power control efforts here will target overvoltages during the PV generation window.

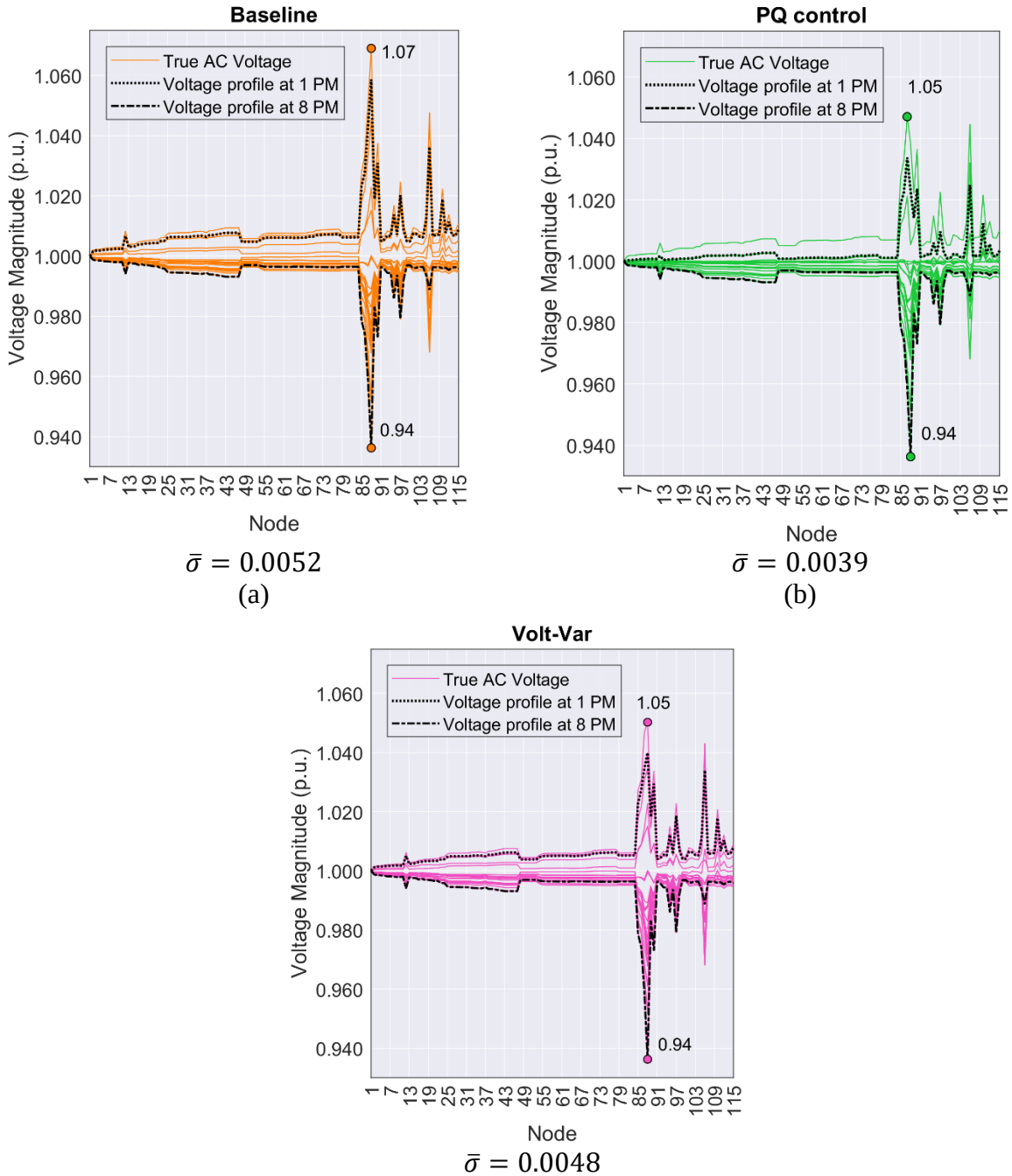

Figure 7.6 – a) Baseline scenario. b) PQ control scenario. c) Volt-Var scenario Markers indicate the worst case under and overvoltages. Solid and dotted black lines highlight the voltage profile at 1 PM and 8 PM.

Figure 7.7 compares the inverter dynamics at buildings 11 and 14 for the *Baseline*, *PQ*, and *Volt-Var* droop control. The dynamics include the inductive reactive power absorption, Q_{ind}, and capacitive reactive power injection, Q_{cap}, both shown as positive bars. The inverter net active

and reactive power flows are also shown by P_{inv} and Q_{inv}, respectively, those can assume positive or negative values, with the positive sign convention indicating power absorbed by the inverter and negative indicating power injected by the inverter. S_{inv} is the absolute value of the inverter apparent power throughput, and its maximum value dictates the inverter capacity, in kVA. $Q_{\text{inv}_{\text{bldg}}}$ is the building inductive reactive power demand that is supplied by the inverter. Q_{import} is the building inductive reactive power demand that is supplied by the grid. The solar PV (DC) production indicates solar PV power generated (DC voltage present) at the inverter. The per-unit voltage hourly variation is shown in the secondary axis.

At both buildings, for the *Baseline* case, voltages rise during the PV generation window, and sag otherwise during the evening and morning due to the building load demand, in an "inverse duck curve" trend. In both PQ and Volt-Var control, there is a clear correlation between solar PV production, voltage rise, and inverter Q_{ind} regulation. Similarly, there is a correlation between lower morning/evening voltage sags (due to the building load power demand) and inverter Q_{cap} regulation. Also, none of the inverter controls use active power curtailment as a voltage regulation strategy. This happens because of the ZNE constraints, which make active power generation to be prioritized in order to meet ZNE.

At Building 14, the AC/DC ratio is < 1. Therefore, there is not much room to absorb inductive reactive power during peak PV generation hours. Thus, there is a clear drop-in Q_{ind} proportional to solar PV active power generation, (notice the "V shape" of the Q_{ind} bars) to give priority to PV active power output by the inverter. At building 11, since the AC/DC ratio is >1, this is not a problem. We will discuss the optimal AC/DC ration and inverter sizing in the following section.

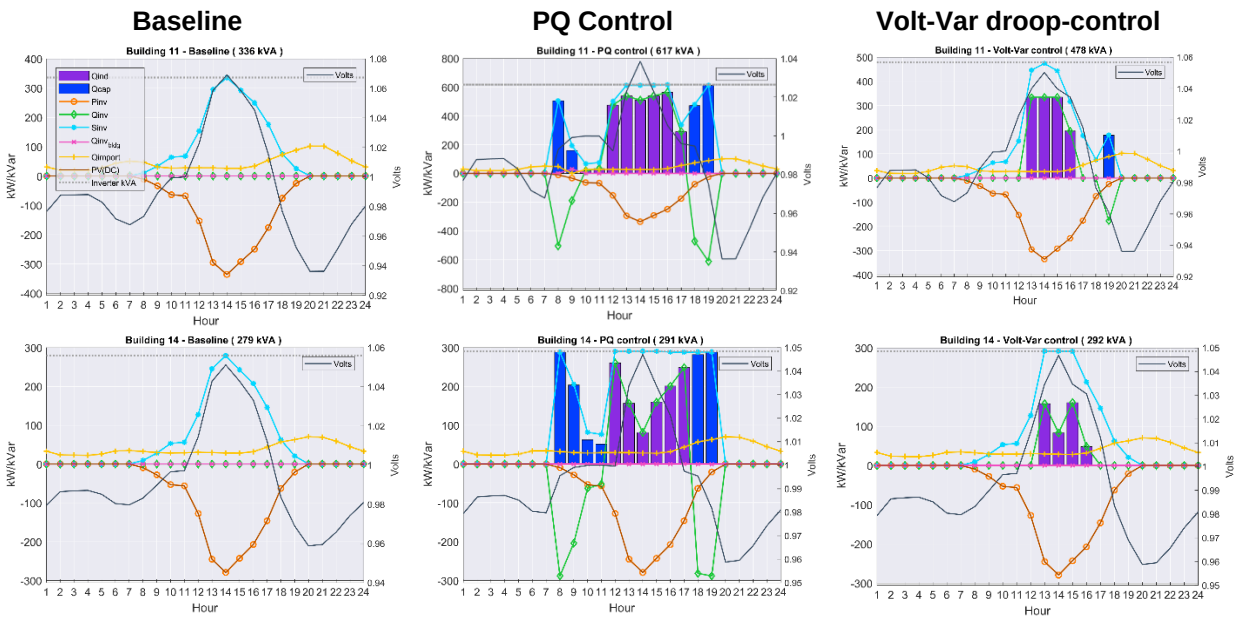

Figure 7.7 – Inverter dynamics at buildings 11 and 14. Baseline versus PQ control and Volt-Var Sinv, Pinv, and Qinv are the net apparent, active, and reactive power flow through the inverter. Qelec is the reactive power used by the building; Qind and Qcap are inverter induction (absorption) and capacitive (injection) controls. Qimport is the reactive power imported from the grid. PV is the DC solar generation. Inverter kVA is the inverter capacity. Voltage in per-unit is plot on the secondary axis to the left.

7.5.3. Inverter sizing and optimal AC/DC ratio

Here we compare the optimal inverter sizing, or AC/DC ratio, for each scenario and attempt to find a correlation between the maximum *Baseline* over-voltage value at a given inverter location and the optimal inverter AC/DC ratio. The inverter AC/DC ratio is simply the inverter capacity, in kVA, divided by the solar PV system DC rating, in kW. Inverter AC/DC ratios were calculated for all inverters for the different scenarios; we provide these data in

Table 3, in the Appendix.

For the *Baseline,* the same optimal AC/DC ratio of 0.83 is used for all inverters, and this occurs because of the assumed solar PV generation profiles used for all buildings. In this profile, the PV system does not generate 100% of the DC nameplate power due to expected generation losses. Therefore, the *Baseline* inverter is sized to be just large enough to accommodate the solar PV generation output. For the *PQ control* scenario, we observe that only two buildings (11 and 14) require an inverter AC/DC ratio beyond the *Baseline*. The inverter at building 11 adopts an optimal AC/DC ratio of 1.53, and the inverter at building 14, 0.87. All other inverters did not require a kVA capacity beyond *Baseline* because the voltages at those locations did not extend far from 1 per unit in order to drive regulation. For *Volt-Var* control, on the other hand, 5 out of 7 inverter locations (building 1, 11, 12, 14, and 17) adopted an inverter AC/DC ratio beyond *Baseline*. This happens because, in droop-control, any voltage deviation will drive voltage regulation. However, we note that the AC/DC oversize is less on a droop-control model, and will be dictated by the Volt-Var curve limit points and slope.

We want to find a correlation between the inverter AC/DC ratio and a local variable, such as voltage. We use MATLAB's `corrcoef()` function to calculate the R values between variable pairs, and we find a reasonable linear correlation between AC/DC ratio and maximum nodal overvoltages (R = 0.649 for *PQ control* and R = 0.7351 for *Volt-Var* control). For *Volt-Var,* we only use 7 data points, corresponding to the nodes of the seven pre-defined inverter locations. We then attempt to find a curve fit, using MATLAB's `fit()` function and choosing the *power2* as the fit model, which assumes the equation of the form $Y = ax^b + c$. Where $a, b,$ and c are the fitness coefficients. The resulting fitted curve, goodness of fit, and model are shown in Figure 7.8, where Y is the inverter AC/DC ratio (for their *PQ control* or *Volt-Var control*), and x is the node's maximum over voltage at *Baseline.* R^2 is the determination coefficient, RMS_{error} is the root mean squared error (standard error), and. coefficients are calculated with (with 95% confidence bounds)

Curve fit model: $Y = ax^b + c$

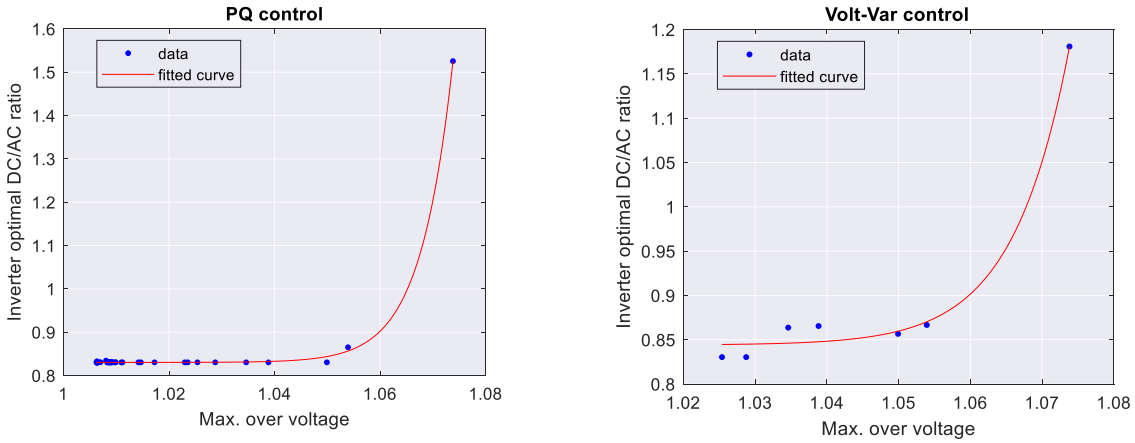

$a = 2.641\text{e} - 06$
$b = 175.3$
$c = 0.8303$
$R^2 = 0.99939$
$RMS_{error} = 0.003188$

$a = 2.02\text{e} - 05$
$b = 136.5$
$c = 0.844$
$R^2 = 0.98872$
$RMS_{error} = 0.01629$

Figure 7.8 – Optimal AC/DC ratio vs. maximum nodal over voltage curve fit for PQ control and Volt-Var using the power2 MATLAB curve fit model.

7.6. Summary

In this chapter, a new approach to model inverter Volt-Var droop-control and PQ control within a MILP for optimal DER allocation and dispatch to minimize cost and minimize voltage deviation was developed. We provide a comparison of the optimal inverter sizes for inverters with Volt-Var droop control and optimal PQ control.

Our results show that:

- **Volt-Var droop-control and optimal PQ control are effective strategies to regulate the voltage to be within the compliant upper level of 1.05 p.u of a ZNE microgrid.** Especially when active power curtailment is not feasible since the system needs to meet ZNE (and therefore export a lot of solar PV generation). Because voltage control only occurs during the PV generation window (when DC voltage is present), the control methods were not able to eliminate under-voltages that occur in the evening.

- **If there are no voltage regulation needs, the optimal AC/DC ratio will be <1. Optimal PQ recommends a larger inverter size than Volt-Var droop control for the same node.** The maximum oversize needed to be 1.53 for optimal PQ and 1.18 for Volt-Var droop control. Optimal PQ control will recommend a larger inverter size than droop control for the same node because reactive power output is only limited by inverter capacity and to minimize voltage deviations, it will maximize reactive power control.
- **The optimal inverter AC/DC ratio is location-dependent and is correlated to the maximum Baseline overvoltage (without regulation) at that inverter location.**

  From our optimization model solution, we derived an approximated practical model for inverter sizing when operating either with at Volt-Var droop control or optimal PQ. choosing the *power2* as the fit model, which assumes the equation of the form $Y = ax^b + c$, where Y is the inverter oversizing and x, is the maximum baseline overvoltage.

8 Conclusions

The main takeaways from this work, separated by chapter are as follows:

Chapter 3, demonstrated the ability of an inverter-connected baseload DER to locally reduce line losses and provide local voltage support in a real-world transmission (500/230/66 kV) power system that is generation-constrained. It showed that:

- **The best DER placement is at the weakest point in the system**, at the end of the circuit, at the lowest voltage bus.
- **In systems with long lines, reactive power injection is, in fact, more effective to raise voltage profiles than active power injection.** The combined active/reactive power injection scenario is found to be most attractive for voltage regulation; thus, the 0.7 leading PF case shows an overall better voltage regulation for the entire system. Operating at a 0.7 leading power factor also improved system voltage stability

Chapter 4 developed an urban microgrid test case that is representative of a real-world power system. It also identified potential challenges associated with grid integration of large-scale PV deployments into that existing system:

- **There are locations in the feeder more prone to challenges in hosting DER**: impacts on the 66 kV level are negligible while on the lower voltage 480, 277 V, 208 V or 120, 240 V level, at secondary buses, transformer and cable overloads occurred as well as over voltages. These impacts are extremely locational: over voltages are exacerbated as PV is deployed further away from the substation. Line overloads are more likely to happen at the head of the feeder
- **The challenging approach of judiciously siting and sizing of battery storage points to the lack of an integrated tool to optimize all DER allocation simultaneously** while considering system dynamic (time-series) operation and the

resultant power flows, voltages, and branch currents at the electric grid network. Ideally, the optimization suite would simultaneously account for all constraints and compute a unique final solution. These results drove the development of such an optimization model, a MILP for DER optimal allocation, namely DERopt.

- **Utility distribution transformer overloads are a significant negative impact of large deployments of solar PV**. These results drove the development of novel t*ransformer constraints* to limit the reverse power flow at the transformer level (limiting the total apparent power injection at that node). These novel constraints were discussed in Chapter 5
- **Over voltage excursions during midday are another major limiting factor to large PV deployments,** point to the need for a linearized power flow formulation that is also suitable for meshed networks to accurately describe (and limit) the impact of these deployments. This results drove the development of a linearized decoupled power flow formulation that can be integrated into a MILP, as described in Chapter 6

Chapter 5 proposed a Mixed Integer Linear Program optimization to decide the best DER portfolio, allocation, and dispatch, for an AEC microgrid that achieves ZNE and islanding while respecting electrical grid operational constraints, with a focus on distribution transformer overloads. It used the same real-world test case of Chapter 4, with time-series loads modeled in *EnergyPlus*, to accurately represent the community aggregated load stock of residential, commercial, and industrial utility customers. It modeled operation goals typically desired for district systems such as Zero-Net-Energy and islanding as a microgrid during unplanned grid outages. A novel **polygon relaxation was used as a practical linearization approach for transformer power flow constraints;** using polygon relaxations to capture the non-linear relationship between active and reactive power flows at the transformer showed adequate accuracy (errors below 1%), and computation tractability, as well as superior computational performance. When compared to comparable linearization methods such as piecewise linearization or linear interpolation, polygon relaxation run time is about six times faster Polygon relaxations are a versatile tool can also be used to limit branch kVA flows to their allowed thermal limit.

- **Effective strategies to avoid transformer overloads are careful sizing and siting of battery energy storage** behind those transformers and also optimally re-distributing PV throughout the community, which increased the ability of the electric infrastructure to support a PV deployment that is 1.7 times larger than the existing transformer capacity without the need for infrastructure upgrades.
- **The use of transformer constraints within DER investment planning, associated with the right battery storage allocation and dispatch, increases PV penetration as opposed to the use of practical rules, such as the "15%" rule**. Taking the ZNE, area-constrained scenario as an example, the total PV installed capacity over the entire community is 11,211 kW which is 1.7 times greater than the total installed transformer capacity of 6,500 kVA, which shows an excellent potential for PV hosting capacity maximization beyond conservative rules of thumb.
- **ZNE can be accomplished at a community level in urban district systems,** large utility customers in the C&I sector most likely cannot entirely deploy enough PV to meet local electricity demand since they typically have high demand and there is a limited amount of space available for rooftop PV deployment at those sites. Therefore, to accomplish ZNE, the available area for PV installation in the residential sector needs to be leveraged to support the community energy goals.

Chapter 6 described and validated a new approach to model the linearized AC power flow in a MILP. The approach used the Decoupled Linearized Power Flow (J. Yang et al., 2016). DLPF demonstrated the advantage of being suitable for meshed networks, while the majority of current models use LinDistFlow, which is only suitable for radial networks. The DLPF voltage magnitude and branch power (in kVA) solutions were validated against LinDistFlow and the true AC power flow (ACPF) solution for a meshed benchmark network, a 33-node system. Then, we integrated the DLPF formulation into our MILP. Both DLPF and LinDistFlow were used to model constraints on the electric power network infrastructure that limits voltages to ANSI C84 standard limits.

The main takeaways were:

- **For radial circuits, LinDistFlow is the most accurate linearization method**, while **for meshed networks, DLPF is the most accurate linearization method** Overall,

all linearization methods evaluated performed a good linearization at radial circuits (voltage errors lied within 1% of the true value and branch kVA flows errors lied within 5% of the true value). However, at the loops, LinDistFlow underestimates true voltage values. Bolognani *et al.* approximation errors had the same order of magnitude, but slightly higher.

- **The use of LinDistFlow within a DER optimization for a meshed network with voltage constraints may lead to undersized optimal PV and battery systems**. The LinDistFlow solution underestimated both overvoltage and undervoltage. Thus, it is not able to fully capture the magnitude of over and under voltages, and as a result, recommending undersized PV and battery systems.
- **The DLPF solution was effective for limiting overvoltages, but would not capture under voltages**. The DLPF solution slightly overestimated overvoltages (conservative) and underestimated under voltages (not strict enough).
- **Both DLPF and LinDistFlow underestimate branch kVA power flows by up to 2 MW**. Both solutions were found not to be able to capture the true branch kVA flow due to the underlying assumption of lossless lines, which may lead to line overloading for practical systems. It is suggested that a safety margin should be included, reducing the quantity of power that can flow through individual power lines.

Chapter 7 developed a new approach to model inverter Volt-Var droop-control and optimal PQ control within a MILP, then applied these models into an optimal DER investment planning to optimally size inverters that can provide voltage support for a microgrid with high PV penetration. Inverters were solely capable of removing all over voltage issues by controlling local reactive power. Controlling reactive power is preferred since active power curtailment would compromise the meeting of ZNE operation, where solar PV exports a highly necessary. Inverter oversizing proved to be location-dependent and control-mode dependent. A correlation between inverter AC/DC ratio and maximum nodal over-voltage was fond. A curve fit model for optimal inverter sizing was then provided for each control strategy Volt-Var droop control and optimal PQ control. We used the *power2* as the fit model unction in MATLAB, which assumes the equation of the form $Y = ax^b + c$ where Y is the inverter oversizing and x is the maximum. baseline overvoltage.

Overall, the current aggressive (and much needed) global decarbonization agenda and the current incentive-driven favorable techno-economic feasibility of renewable solar PV coupled with battery storage will drive an ever-increasing adoption of such systems. These ambitious deployment levels will require DER to be integrated within the current urban space, likely at the distribution level feeders. The challenges of this integration are many and will require careful consideration of the existing power system infrastructure equipment and local power quality. In parallel, the cost-effectiveness of such deployments is still the main focus of project owners and stakeholders. Optimal DER investment planning optimization tools, especially MILPs to minimize overall project cost, are becoming gradually popular for achieving feasible microgrid design at the least-cost. This research work was entirely motivated by the identification of existing gaps in the current sate-of-the art optimization tools: no previous tool was able to simultaneously optimize DER allocation while considering distribution power transformer infrastructure, for instance. No tools also employed a suitable AC power flow solver for meshed microgrid networks. Moreover, smart-inverter inverter technology was often not leveraged to provide local voltage control and increase PV hosting capacity. This work addresses these gaps by proposing novel approaches such as polygon relaxations, the integration of the novel linear DLPF AC power flow, and the linearization of smart-inverter functions. The resulting tool optimizes DER allocation for a 115-node microgrid that achieves ZNE over one year period. Future work points to the need for even more detailed power system modeling, such as individual phasing, transformer automatic TAP changers, and existing power system protection equipment, for instance, while keeping the model tractable and feasible for an increased number of nodes and meshes. By taking some of these aspects into account, there is still a great potential in increasing the optimality of such designs.

REFERENCES

Abate, S. R., McDermott, T. E., Rylander, M., & Smith, J. (2015). Smart inverter settings for improving distribution feeder performance. *IEEE Power and Energy Society General Meeting*, *2015-Septe*, 1–5. https://doi.org/10.1109/PESGM.2015.7286560

Abdel-Akher, M., Ali, a. a., Eid, a. M., & El-Kishky, H. (2011). Optimal size and location of distributed generation unit for voltage stability enhancement. *2011 IEEE Energy Conversion Congress and Exposition*, 104–108. https://doi.org/10.1109/ECCE.2011.6063755

Abdi, H., Beigvand, S. D., & Scala, M. La. (2017). A review of optimal power flow studies applied to smart grids and microgrids. *Renewable and Sustainable Energy Reviews*, *71*(May 2015), 742–766. https://doi.org/10.1016/j.rser.2016.12.102

AES California. (n.d.). Facilities: Huntington Beach | AES California. Retrieved December 12, 2016, from http://www.aescalifornia.com/facilities/huntington-beach

AES Uses Synchronous Condensers for Grid Balancing. (n.d.). Retrieved December 12, 2016, from http://www.powermag.com/aes-uses-synchronous-condensers-for-grid-balancing/?pagenum=1

Ahmadi, H., Member, S., & Mart, J. R. (2015). *Linear Current Flow Equations with Application to Distribution Systems Reconfiguration*. *30*(4), 2073–2080.

Akbari, T., & Tavakoli Bina, M. (2016). Linear approximated formulation of AC optimal power flow using binary discretisation. *IET Generation, Transmission & Distribution*, *10*(5), 1117–1123. https://doi.org/10.1049/iet-gtd.2015.0388

Ali, A., Raisz, D., & Mahmoud, K. (2019). Optimal oversizing of utility-owned renewable DG inverter for voltage rise prevention in MV distribution systems. *International Journal of Electrical Power and Energy Systems*, *105*(June 2018), 500–513. https://doi.org/10.1016/j.ijepes.2018.08.040

Alrashidi, M. R., & Alhajri, M. F. (2011). Optimal planning of multiple distributed generation sources in distribution networks: A new approach. *Energy Conversion and Management*, *52*(11), 3301–3308. https://doi.org/10.1016/j.enconman.2011.06.001

Alturki, M., Khodaei, A., Paaso, A., & Bahramirad, S. (2018). Optimization-based distribution grid hosting capacity calculations. *Applied Energy*, *219*(September 2017), 350–360. https://doi.org/10.1016/j.apenergy.2017.10.127

Alyami, S., Wang, Y., Wang, C., Zhao, J., & Zhao, B. (2014). Adaptive real power capping method for fair overvoltage regulation of distribution networks with high penetration of PV systems. *IEEE Transactions on Smart Grid*, *5*(6), 2729–2738. https://doi.org/10.1109/TSG.2014.2330345

Angelim, J. H., & Affonso, C. M. (2016). Impact of distributed generation technology and location on power system voltage stability. *IEEE Latin America Transactions*, *14*(4), 1758–1764. https://doi.org/10.1109/TLA.2016.7483512

ANSI. (2005). *ANSI Std C84.1-1995 (R2005) , Electric Power Systems and Equipment - Voltage Ratings (60 Hertz)*.

Arabali, A., Ghofrani, M., Bassett, J. B., Pham, M., & Moeini-Aghtaei, M. (2017). Chapter 7 - Optimum Sizing and Siting of Renewable-Energy-based DG Units in Distribution Systems. In *Optimization in Renewable Energy Systems*. https://doi.org/10.1016/B978-0-08-101041-9.00007-7

Archimedes (ed.Heath). (1897). *Works of Archimedes*. Cambridge University Press.

Arnold, D. B., Sankur, M., Dobbe, R., Brady, K., Callaway, D. S., & Meier, A. Von. (2016). Optimal Dispatch of Reactive Power for Voltage Regulation and Balancing in Unbalanced Distribution

Systems. *IEEE Transactions on Power Systems*, *31*(4), 2903–2913. https://doi.org/10.1109/TPWRS.2015.2451519

Award, D. O. E., & Fc, N. D. E. (2014). *Perfect Power Prototype for Illinois Institute of Technology Final Technical Report*.

Babacan, O., Torre, W., & Kleissl, J. (2017). Siting and sizing of distributed energy storage to mitigate voltage impact by solar PV in distribution systems. *Solar Energy*, *146*, 199–208. https://doi.org/10.1016/j.solener.2017.02.047

Baran, M. E., & Wu, F. F. (1989a). Network reconfiguration in distribution systems for loss reduction and load balancing. *IEEE Transactions on Power Delivery*, *4*(2), 1401–1407.

Baran, M. E., & Wu, F. F. (1989b). Optimal Sizing of Capacitors Placed on a Radial Distribution System. *IEEE Transactions on Power Delivery*, *4*(1), 735–743.

Barelli, L., Bidini, G., & Ottaviano, A. (2016). Solid oxide fuel cell modelling: Electrochemical performance and thermal management during load-following operation. *Energy*, *115*, 107–119. https://doi.org/10.1016/j.energy.2016.08.107

Basu, A. K., Bhattacharya, A., Chowdhury, S., & Chowdhury, S. P. (2012). Planned scheduling for economic power sharing in a CHP-based micro-grid. *IEEE Transactions on Power Systems*, *27*(1), 30–38. https://doi.org/10.1109/TPWRS.2011.2162754

Bauen, A., Hart, D., & Chase, A. (2003). Fuel cells for distributed generation in developing countries - An analysis. *International Journal of Hydrogen Energy*, *28*(7), 695–701. https://doi.org/10.1016/S0360-3199(02)00248-3

Bello, M., Maitra, A., Dugan, R., McGrail, M., Reid, A., & Rodrigo, R. (2018). Protection coordination considerations for a highly meshed urban microgrid. *2018 IEEE Power and Energy Society Innovative Smart Grid Technologies Conference, ISGT 2018*, 1–5. https://doi.org/10.1109/ISGT.2018.8403351

Bharti, D., & Mala De. (2018). A New Graph Theoretic Power Flow Framework for Microgrid. *WIECON-ECE 2017 - IEEE International WIE Conference on Electrical and Computer Engineering 2017*, (December), 137–140. https://doi.org/10.1109/WIECON-ECE.2017.8468900

Bischoff, M. (2006). Large stationary fuel cell systems: Status and dynamic requirements. *Journal of Power Sources*, *154*(2), 461–466. https://doi.org/10.1016/j.jpowsour.2005.10.027

Bollen, M., & Hassan, F. (2011). *Integration of Distributed Generation in the Power System*. Hoboken, New Jersey: John Wiley & Sons, Inc.

Bolognani, S. (2014). approx-pf - approximate linear solution of power flow equations in power distribution networks. Retrieved from GitHub website: http://github.com/saveriob/approx-pf

Bolognani, S., & Zampieri, S. (2016). On the existence and linear approximation of the power flow solution in power distribution networks. *IEEE Transactions on Power Systems*, *31*(1), 163–172. https://doi.org/10.1109/TPWRS.2015.2395452

Borges, C. L. T., & Falcão, D. M. (2006). Optimal distributed generation allocation for reliability, losses, and voltage improvement. *International Journal of Electrical Power and Energy Systems*, *28*(6), 413–420. https://doi.org/10.1016/j.ijepes.2006.02.003

Bose, S., & Russel, M. (2012). The Microgrid solutin at Twenty-Nine Palms. Retrieved from https://slideplayer.com/slide/1638874/

Brandao, D. I., Pomilio, J. A., Caldognetto, T., Buso, S., & Tenti, P. (2016). Coordinated control of distributed generators in meshed low-voltage microgrids: Power flow control and voltage regulation. *Proceedings of International Conference on Harmonics and Quality of Power, ICHQP*, *2016-*

Decem(Mc), 249–254. https://doi.org/10.1109/ICHQP.2016.7783458

CAISO. (2018). Greenhouse Gas Emission Tracking Report - Total hourly GHG emissions to serve ISO load. Retrieved from http://www.caiso.com/market/Pages/ReportsBulletins/RenewablesReporting.aspx#ghgreport%0A

California Energy Commission. (2014). *CA Rule 21 Smart Inverter Update*.

California Independent System Operator (CAISO). (2016). What the duck curve tells us about managing a green grid. Retrieved from https://www.caiso.com/documents/flexibleresourceshelprenewables_fastfacts.pdf

California ISO. (2016). *2015-2016 Transmission Plan*.

Carpentier, J. (1979). Optimal power flows. *International Journal of Electrical Power & Energy Systems*, *1*(1), 3–15. https://doi.org/10.1016/0142-0615(79)90026-7

Chanda, S., & De, A. (2014). A multi-objective solution algorithm for optimum utilization of Smart Grid infrastructure towards social welfare. *International Journal of Electrical Power and Energy Systems*, *58*, 307–318. https://doi.org/10.1016/j.ijepes.2014.01.029

Chen, H., Chen, J., Shi, D., & Duan, X. (2006). Power flow study and voltage stability analysis for distribution systems with distributed generation. *2006 IEEE Power Engineering Society General Meeting*, 8 pp. https://doi.org/10.1109/PES.2006.1709198

Chen, P., Member, S., Malbasa, V., & Kezunovic, M. (2013). Analysis of Voltage Stability Issues with Distributed Generation Penetration in Distribution Networks. *North American Power Symposium (NAPS)*, 1–6.

Chevron Energy Solutions Company. (2014). *CERTS Microgrid demonstration with large-scale energy storage and renewables at Santa Rita Jail*. 214.

Chiradeja, P., & Ramakumar, R. (2004). An approach to quantify the technical benefits of distributed generation. *IEEE Transactions on Energy Conversion*, *19*(4), 764–773. https://doi.org/10.1109/TEC.2004.827704

Christos, A. (2016). *Investigation of the distribution grid hosting capacity for distributed generation and possible improvements by SmartGrid technologies*. Retrieved from https://www.ethz.ch/content/dam/ethz/special-interest/itet/institute-eeh/power-systems-dam/documents/SAMA/2016/Antonakopoulos-MA-2016.pdf

CME Wire and Cable. (2016). *ACSR Aluminum Conductor Steel Reinforced Bare Overhead Concentric Lay Stranded Conductors ASTM B232*. Retrieved from http://www.cmewire.com/catalog/sec03-bac/bac-07-acsr.pdf

Coffrin, C., & Hentenryck, P. Van. (2013). *A Linear-Programming Approximation of AC Power Flows*. 1–13.

Collins, L., & Ward, J. K. (2015). Real and reactive power control of distributed PV inverters for overvoltage prevention and increased renewable generation hosting capacity. *Renewable Energy*, *81*, 464–471. https://doi.org/10.1016/j.renene.2015.03.012

Conforti, M., Cornuéjols, G., & Zambelli, G. (2014). *Integer Programming*. https://doi.org/10.1007/978-3-319-11008-0

Cragg, C. T. (1996). Changing nature of the power generation market - does it create opportunities for fuel cells? *Journal of Power Sources*, *61*(1–2), 1–6. https://doi.org/10.1016/S0378-7753(96)02331-2

Curtin, S., & Gangi, J. (2015). *Fuel Cell Technologies Market Report 2015*.

Dall'Anese, E., Dhople, S. V., Johnson, B. B., & Giannakis, G. B. (2014). Optimal Dispatch of Photovoltaic Inverters in Residential Distribution Systems. *IEEE Transactions on Sustainable*

Energy, *5*(2), 487–497. https://doi.org/10.1109/TSTE.2013.2292828

Das, S., Das, D., & Patra, A. (2014). Operation of Solid Oxide Fuel Cell based Distributed Generation. *Energy Procedia*, *54*, 439–447. https://doi.org/10.1016/j.egypro.2014.07.286

Ding, F., Pratt, A., Bialek, T., Bell, F., McCarty, M., Atef, K., … Gotseff, P. (2016). Voltage support study of smart PV inverters on a high-photovoltaic penetration utility distribution feeder. *2016 IEEE 43rd Photovoltaic Specialists Conference (PVSC)*, 1375–1380. https://doi.org/10.1109/PVSC.2016.7749840

Domínguez-Muñoz, F., Cejudo-López, J. M., Carrillo-Andrés, A., & Gallardo-Salazar, M. (2011). Selection of typical demand days for CHP optimization. *Energy and Buildings*, *43*(11), 3036–3043. https://doi.org/10.1016/j.enbuild.2011.07.024

Dufour, A. U. (1998). Fuel cells – a new contributor to stationary power. *Journal of Power Sources*, *71*(1–2), 19–25. https://doi.org/10.1016/S0378-7753(97)02732-8

Eaton, & Cooper Industries. (n.d.). *Short-Circuit Current Calculations Basic Point-to-Point Calculation Procedure*. Retrieved from http://www.cooperindustries.com/content/dam/public/bussmann/Electrical/Resources/solution-center/technical_library/BUS_Ele_Tech_Lib_Electrical_Formulas.pdf

Ehsan, A., & Yang, Q. (2017). Optimal integration and planning of renewable distributed generation in the power distribution networks: A review of analytical techniques. *Applied Energy*, *210*(July 2017), 44–59. https://doi.org/10.1016/j.apenergy.2017.10.106

Ehsan, A., & Yang, Q. (2019). Scenario-based investment planning of isolated multi-energy microgrids considering electricity, heating and cooling demand. *Applied Energy*, *235*(July 2018), 1277–1288. https://doi.org/10.1016/j.apenergy.2018.11.058

Electric Power Research Institute (EPRI). (2014). *Common Functions for Smart Inverters, Version 3*. https://doi.org/Report 3002002233,

Electric Power Research Institute (EPRI). (2015). *Alternatives to the 15% Rule: Modeling and Hosting Capacity Analysis of 16 Feeders*. Palo Alto, CA.

Electric Power Research Institute (EPRI). (2016). *Grid Integration of Zero Net Energy Communities - Final Report* (Vol. 2021). Palo Alto, CA.

Electric Power Research Institute (EPRI). (2017). *An Overview of Advanced Energy Communities*.

EPRI; APS. (2017). *Arizona Public Service Solar Partner Program - Research Results*.

EPRI, Smith, J., & Rogers, L. (2015). *Smart Grid Inverters To Support Photovoltaics in New York Distribution Systems*.

Erdal, M. (2015). *Optimal Thrust Allocation for Dynamic Positioning Systems using Linear Programming and Quadratic Programming*. (June).

Fachbereich, V. (2018). *A Concept of Distributed Energy Management Systems with Fully Decentralized Primary Control Strategies for Microgrids*. (April).

Falke, T., Krengel, S., Meinerzhagen, A.-K., & Schnettler, A. (2016). Multi-objective optimization and simulation model for the design of distributed energy systems. *Applied Energy*, *184*, 1508–1516. https://doi.org/10.1016/j.apenergy.2016.03.044

Farivar, M., Neal, R., Clarke, C., & Low, S. (2012). Optimal inverter VAR control in distribution systems with high PV penetration. *IEEE Power and Energy Society General Meeting*, 1–7. https://doi.org/10.1109/PESGM.2012.6345736

Flores, R., & Brouwer, J. (2017). Optimal Design of a Distributed Energy Resources System That Minimizes Cost While Reducing Carbon Emissions. *ASME 2017 11th International Conference on*

Energy Sustainability.

Flores, R. J. (2016). *Costs and Operating Dynamics of Integrating Distributed Energy Resources in Commercial and Industrial Buildings with Electric Vehicle Charging [DISSERTATION]*.

Flores, R. J., & Brouwer, J. (2018a). Optimal design of a distributed energy resource system that economically reduces carbon emissions. *Applied Energy*, *232*(September), 119–138. https://doi.org/10.1016/j.apenergy.2018.09.029

Flores, R. J., & Brouwer, J. (2018b). Optimal design of a distributed energy resource system that economically reduces carbon emissions. *Applied Energy*, *232*, 119–138. https://doi.org/10.1016/j.apenergy.2018.09.029

Flores, R., Novoa, L., Brouwer, J., Jordan Raffo, Maclay, J., Graham, A., … Silverman, R. (2018). *Huntington Beach Advanced Energy Community Blueprint*. Retrieved from https://www.energy.ca.gov/2019publications/CEC-500-2019-047/CEC-500-2019-047.pdf

Folsom Labs. (2017). *Helioscope [Software]*. San Francisco, CA.

Gholami, A., Shekari, T., & Grijalva, S. (2019). Proactive Management of Microgrids for Resiliency Enhancement: An Adaptive Robust Approach. *IEEE Transactions on Sustainable Energy*, *10*(1), 470–480. https://doi.org/10.1109/TSTE.2017.2740433

Gil, H. A., El Chehaly, M., Joos, G., & Cañizares, C. (2009). Bus-based indices for assessing the contribution of DG to the voltage security margin of the transmission grid. *2009 IEEE Power and Energy Society General Meeting, PES '09*, 1–7. https://doi.org/10.1109/PES.2009.5275276

Google Inc. (2017). *Google Earth v.7.1.7.2606 [Software]*. Retrieved from https://www.google.com/earth/download/gep/agree.html

Grainger, J. J., & Stevenson, W. D. (1994). *Power System Analysis*.

Grover-Silva, E., Girard, R., & Kariniotakis, G. (2018). Optimal sizing and placement of distribution grid connected battery systems through an SOCP optimal power flow algorithm. *Applied Energy*, *219*(April 2017), 385–393. https://doi.org/10.1016/j.apenergy.2017.09.008

Grover-Silva, E., Heleno, M., Mashayekh, S., Cardoso, G., Girard, R., & Kariniotakis, G. (2018). A stochastic optimal power flow for scheduling flexible resources in microgrids operation. *Applied Energy*, *229*(609687), 201–208. https://doi.org/10.1016/j.apenergy.2018.07.114

Harrison, G.P., & Wallace, A. R. (2005). Optimal power flow evaluation of distribution network capacity for the connection of distributed generation. *IEE Proceedings-Generation, Transmission and …*, *151*(3), 201–212. https://doi.org/10.1049/ip-gtd

Harrison, Gareth P, Piccolo, A., Siano, P., & Wallace, A. R. (2007). Distributed Generation Capacity Evaluation Using Combined Genetic Algorithm and OPF. *International Journal of Emerging Electric Power Systems*, *8*(2), 750–757. https://doi.org/10.2202/1553-779X.1517

Hatziargyriou, N. (2014). Microgrid: Architectures and Control - Chapter 1 - The Microgrid Concept. In I. Press (Ed.), *Microgrids: Architecture and Control*. Wiley.

Hessenius, C. A., Ang, A., & Hamilton, S. (2006). Fuel cells: A utilities perspective. *Journal of Power Sources*, *158*(1), 436–445. https://doi.org/10.1016/j.jpowsour.2005.09.049

HOMER Energy LLC. (2017). *HOMER Pro v.3.9.2 [Software]*. Retrieved from https://www.homerenergy.com/homer-pro.html

Huang, W., Zhang, N., Yang, J., Wang, Y., & Kang, C. (2017). Optimal Configuration Planning of Multi-Energy Systems Considering Distributed Renewable Energy. *IEEE Transactions on Smart Grid*, *3053*(c), 1–12. https://doi.org/10.1109/TSG.2017.2767860

IBM. (2017). *CPLEX*. Retrieved from https://www.ibm.com/analytics/cplex-optimizer

IEEE. (2003). IEEE 1547-2003, Standard for Interconnecting Distributed Resources with Electric Power Systems. In *Test* (Vol. 2003). https://doi.org/10.1109/IEEESTD.2002.94130

IEEE. (2018). IEEE Std. 1547-2018 (Revision of IEEE Std 1547-2003) Standard for Interconnection and Interoperability of Distributed Energy Resources with Associated Electric Power Systems Interfaces. *IEEE Std 1547-2018 (Revision of IEEE Std 1547-2003)*, pp. 1–138. https://doi.org/10.1109/IEEESTD.2018.8332112

Ismael, S. M., Abdel Aleem, S. H. E., Abdelaziz, A. Y., & Zobaa, A. F. (2019). State-of-the-art of hosting capacity in modern power systems with distributed generation. *Renewable Energy*, *130*, 1002–1020. https://doi.org/10.1016/j.renene.2018.07.008

Jafari, M., Olowu, T. O., & Sarwat, A. I. (2019). Optimal Smart Inverters Volt-VAR Curve Selection with a Multi-Objective Volt-VAR Optimization using Evolutionary Algorithm Approach. *2018 North American Power Symposium, NAPS 2018*, 1–6. https://doi.org/10.1109/NAPS.2018.8600542

Jahangiri, P., & Aliprantis, D. C. (2013). Distributed Volt/VAr control by PV inverters. *IEEE Transactions on Power Systems*, *28*(3), 3429–3439. https://doi.org/10.1109/TPWRS.2013.2256375

Klauber, C. (2016). *Advanced Modeling and Computational Methods for Distribution System State Estimation*. Retrieved from https://www.ideals.illinois.edu/bitstream/handle/2142/95400/KLAUBER-THESIS-2016.pdf?sequence=1&isAllowed=y

Kroposki, B., Sen, P. K., & Malmedal, K. (2013). Optimum sizing and placement of distributed and renewable energy sources in electric power distribution systems. *IEEE Transactions on Industry Applications*, *49*(6), 2741–2752. https://doi.org/10.1109/TIA.2013.2262661

Krumdieck, S., Page, S., & Round, S. (2004). Solid oxide fuel cell architecture and system design for secure power on an unstable grid. *Journal of Power Sources*, *125*(2), 189–198. https://doi.org/10.1016/j.jpowsour.2003.07.011

Kumar, J. (2015). Alstom Microgrid system for Philadelphia Navy Yard. Retrieved from https://www.nrel.gov/esif/assets/pdfs/agct_day3_kumar.pdf

Kurtz, E. B., Shoemaker, T. M., & Mack, J. E. (Engineer). (1997). *The lineman's and cableman's handbook*. 18-8 through 18-15.

Kwasinski, A., Weaver, W., & Balog, R. S. (2017). *Microgrids and Other Local Area Power and Energy Systems*. Cambridge: Cambridge University Press.

Lazard. (2016). *Lazard's Levelised Cost of Energy Analysis - version 10.0*. Retrieved from https://www.lazard.com/media/438038/levelized-cost-of-energy-v100.pdf

Lazard. (2018a). *Lazard's Levelized Cost of Energy Analysis - version 12.0*. (November), 0–19. Retrieved from https://www.lazard.com/media/450784/lazards-levelized-cost-of-energy-version-120-vfinal.pdf

Lazard. (2018b). *Levelized Cost of Storage Analysis - version 4.0*. (November). https://doi.org/10.1097/01.psy.0000529859.93952.b1

Li, B., Roche, R., Paire, D., & Miraoui, A. (2017). Sizing of a stand-alone microgrid considering electric power, cooling/heating, hydrogen loads and hydrogen storage degradation. *Applied Energy*, *205*(August), 1244–1259. https://doi.org/10.1016/j.apenergy.2017.08.142

Lofberg, J. (2005). *YALMIP : a toolbox for modeling and optimization in MATLAB*. 284–289. https://doi.org/10.1109/cacsd.2004.1393890

Löfberg, J. (2019). *YALMILP*. Retrieved from https://yalmip.github.io/

Luthander, R., Lingfors, D., & Widén, J. (2017). Large-scale integration of photovoltaic power in a

distribution grid using power curtailment and energy storage. *Solar Energy*, *155*, 1319–1325. https://doi.org/10.1016/j.solener.2017.07.083

Macedo, L. H., Montes, C. V., Franco, J. F., Rider, M. J., & Romero, R. (2016). MILP branch flow model for concurrent AC multistage transmission expansion and reactive power planning with security constraints. *IET Generation, Transmission and Distribution*, *10*(12), 3023–3032. https://doi.org/10.1049/iet-gtd.2016.0081

Mahmud, M. A., Hossain, M. J., & Pota, H. R. (2011). Analysis of Voltage Rise Effect on Distribution Network with Distributed Generation. *IFAC Proceedings Volumes*, *44*(1), 14796–14801. https://doi.org/10.3182/20110828-6-IT-1002.01305

Mansini, R., Ogryczak, W., & Speranza, M. G. (2015). Linear and mixed integer programming for portfolio optimization. In Springer (Ed.), *Linear and Mixed Integer Programming for Portfolio Optimization*. https://doi.org/10.1007/978-3-319-18482-1

Marra, F., Fawzy, Y. T., Bulo, T., & Blažič, B. (2012). Energy storage options for voltage support in low-voltage grids with high penetration of photovoltaic. *IEEE PES Innovative Smart Grid Technologies Conference Europe*, 1–7. https://doi.org/10.1109/ISGTEurope.2012.6465690

Mashayekh, S., Stadler, M., Cardoso, G., & Heleno, M. (2016). A mixed integer linear programming approach for optimal DER portfolio, sizing, and placement in multi-energy microgrids. *Applied Energy*, *187*, 154–168. https://doi.org/10.1016/j.apenergy.2016.11.020

Mashayekh, S., Stadler, M., Cardoso, G., Heleno, M., Chalil Madathil, S., Nagarajan, H., … Wang, J. (2017). Security-Constrained Design of Isolated Multi-Energy Microgrids. *IEEE Transactions on Power Systems*, (September). https://doi.org/10.1109/TPWRS.2017.2748060

McDonald, A. N. (2017). *Method for Calibrating Community Scale Energy Demand using Whole Building Simulation Tools for Advanced Energy Community Planning*.

Mead, J., Donde, V., Garnett, J., & (PG&E). (2015). *Advanced Control Technologies for Distribution Grid Voltage and Stability With Electric Vehicles and Distribute Generation*.

Morvaj, B., Evins, R., & Carmeliet, J. (2016). Optimization framework for distributed energy systems with integrated electrical grid constraints. *Applied Energy*, *171*, 296–313. https://doi.org/10.1016/j.apenergy.2016.03.090

National Fire Protection Association. (2014). *NFPA 70: National Electrical Code (NEC) 2014* (2014th ed., Vol. 70). Quincy, Massachusetts: NFPA.

Novoa, L., Flores, R., & Brouwer, J. (2019). Optimal renewable generation and battery storage sizing and siting considering local transformer limits. *Applied Energy*, *256*. https://doi.org/10.1016/j.apenergy.2019.113926

NREL. (n.d.). NSRDB: 1991- 2005 Update: TMY3. Retrieved October 22, 2017, from http://rredc.nrel.gov/solar/old_data/nsrdb/1991-2005/tmy3/

NREL, & Schauder, C. (2014). Advanced Inverter Technology for High Penetration Levels of PV Generation in Distribution Systems. In *Nrel*. https://doi.org/NREL/SR-5D00-60737

NREL, & SolarCity. (2016). Photovoltaic Impact Assessment of Smart Inverter Volt-VAR Control on Distribution System Conservation Voltage Reduction and Power Quality. In *National Renewable Energy Laboratory*. Retrieved from https://www.nrel.gov/docs/fy17osti/67296.pdf

Operation Technology Inc. (2017). *Electric Transient Analysis Program (ETAP) v.16.00 [Software]*.

Palmintier, B., Broderick, R., Mather, B., Coddington, M., Baker, K., Ding, F., … Bharatkumar, A. (2016). *On the Path to SunShot: Emerging Issues and Challenges in Integrating Solar with the Distribution System*. https://doi.org/NREL/TP-5D00-6533, SAND2016-2524

Patterson, B. T., & Geary, D. E. (2016). Real-Time transactional power management in a microgrid mesh network: The enernet. *INTELEC, International Telecommunications Energy Conference (Proceedings)*, *2016-Novem*, 1–7. https://doi.org/10.1109/INTLEC.2016.7749106

Pesaran H.A, M., Huy, P. D., & Ramachandaramurthy, V. K. (2017). A review of the optimal allocation of distributed generation: Objectives, constraints, methods, and algorithms. *Renewable and Sustainable Energy Reviews*, *75*(October 2016), 293–312. https://doi.org/10.1016/j.rser.2016.10.071

PG&E. (2016). *Transformer Unit Cost data sheet received from Utility Distribution Planner*.

Prakash, P., & Khatod, D. K. (2016). Optimal sizing and siting techniques for distributed generation in distribution systems: A review. *Renewable and Sustainable Energy Reviews*, *57*, 111–130. https://doi.org/10.1016/j.rser.2015.12.099

Princeton Microgrid. (2019). Retrieved from https://facilities.princeton.edu/node/1486

Qiu, J., Zhao, J., Yang, H., Wang, D., & Dong, Z. Y. (2018). Planning of solar photovoltaics, battery energy storage system and gas micro turbine for coupled micro energy grids. *Applied Energy*, *219*(June 2017), 361–369. https://doi.org/10.1016/j.apenergy.2017.09.066

Ranjan, R., & Das, D. (2003). Voltage Stability Analysis of Radial Distribution Networks. *Electric Power Components and Systems*, *31*(1), 501–511. https://doi.org/10.1080/15325000390127011

Ren, H., & Gao, W. (2010). A MILP model for integrated plan and evaluation of distributed energy systems. *Applied Energy*, *87*(3), 1001–1014. https://doi.org/10.1016/j.apenergy.2009.09.023

Ren, H., Zhou, W., Nakagami, K., Gao, W., & Wu, Q. (2010). Multi-objective optimization for the operation of distributed energy systems considering economic and environmental aspects. *Applied Energy*, *87*(12), 3642–3651. https://doi.org/10.1016/j.apenergy.2010.06.013

Rezaee Jordehi, A. (2016). Allocation of distributed generation units in electric power systems: A review. *Renewable and Sustainable Energy Reviews*, *56*, 893–905. https://doi.org/10.1016/j.rser.2015.11.086

Riverso, S., Sarzo, F., & Ferrari-Trecate, G. (2015). Plug-and-Play Voltage and Frequency Control of Islanded Microgrids with Meshed Topology. *IEEE Transactions on Smart Grid*, *6*(3), 1176–1184. https://doi.org/10.1109/TSG.2014.2381093

Rylander, M., Li, H., Smith, J., & Sunderman, W. (2016). Default volt-var inverter settings to improve distribution system performance. *IEEE Power and Energy Society General Meeting*, *2016-Novem*, 1–5. https://doi.org/10.1109/PESGM.2016.7741947

Rylander, M., Reno, M. J., Quiroz, J. E., Ding, F., Li, H., Broderick, R. J., … Smith, J. (2017). Methods to determine recommended feeder-wide advanced inverter settings for improving distribution system performance. *2017 IEEE 44th Photovoltaic Specialist Conference, PVSC 2017*, 1–6. https://doi.org/10.1109/PVSC.2017.8366289

Santos, S. F., Fitiwi, D. Z., Shafie-khah, M., Bizuayehu, A. W., & Catalão, J. P. S. (2016). Optimal sizing and placement of smart-grid-enabling technologies for maximizing renewable integration. In *Smart Energy Grid Engineering*. https://doi.org/10.1016/B978-0-12-805343-0.00003-6

Schultis, D.-L. (2019). Comparison of Local Volt/var Control Strategies for PV Hosting Capacity Enhancement of Low Voltage Feeders. *Energies*, *12*(8), 1560. https://doi.org/10.3390/en12081560

Schwaegerl, C., Bollen, M. H. J., Karoui, K., & Yagmur, A. (2005). Voltage control in distribution systems as a limitation of the hosting capacity for distributed energy resources. *CIRED 2005: 18th International Conference And Exhibition on Electricity Distribution*, (June), 6–9. Retrieved from https://vpn.upc.edu:11001/articleDetails.jsp?arnumber=5427947

Schweitzer, E. (2018). Lossless DistFlow implementation. Retrieved from GitHub website:

https://github.com/eranschweitzer/distflow

Sepehry, M., Heidari Kapourchali, M., Aravinthan, V., & Jewell, W. (2019). Robust Day-Ahead Operation Planning of Unbalanced Microgrids. *IEEE Transactions on Industrial Informatics*, *PP*(c), 1–1. https://doi.org/10.1109/tii.2019.2895080

Seuss, J., Reno, M. J., Broderick, R. J., & Grijalva, S. (2015). Improving distribution network PV hosting capacity via smart inverter reactive power support. *IEEE Power and Energy Society General Meeting*, *2015-Septe*(1), 0–4. https://doi.org/10.1109/PESGM.2015.7286523

Singh, D., Singh, D., & Verma, K. S. (2009). Multiobjective optimization for DG planning with load models. *IEEE Transactions on Power Systems*, *24*(1), 427–436. https://doi.org/10.1109/TPWRS.2008.2009483

Smith, J. W., Sunderman, W., Dugan, R., & Seal, B. (2011). Smart inverter volt/var control functions for high penetration of PV on distribution systems. *2011 IEEE/PES Power Systems Conference and Exposition, PSCE 2011*, 1–6. https://doi.org/10.1109/PSCE.2011.5772598

Solar, C. (2017). *Canadian Solar CS6X-325 P Data Sheet*. Retrieved from https://www.canadiansolar.com/fileadmin/user_upload/downloads/datasheets/v5.5/Canadian_Solar-Datasheet-MaxPower-CS6X-P-v5.51en.pdf

Solar Pro, & Berdner, J. (2008). From kW to MW: System Design Considerations. Retrieved January 1, 2017, from https://solarprofessional.com/articles/design-installation/from-kw-to-mw-system-design-considerations#.WfrabBNSwWo

Southern California Edison. (2016). *Distribution Resources Plan (DRP) - Demo A and Demo B Final Reports*. (626).

Southern California Edison. (2019). Schedule TOU-D TIME-OF-USE DOMESTIC.

Southern California Edison (SCE). (2016a). *Distributed Energy Resource Interconnection Map (DERiM)*. Retrieved from http://www.energy.ca.gov/distgen/equipment/equipment.html

Southern California Edison (SCE). (2016b). *Distributed Energy Resource Interconnection Map (DERiM)*. Retrieved from http://www.energy.ca.gov/distgen/equipment/equipment.html

Stadler, M., Groissböck, M., Cardoso, G., & Marnay, C. (2014). Optimizing Distributed Energy Resources and building retrofits with the strategic DER-CAModel. *Applied Energy*, *132*, 557–567. https://doi.org/10.1016/j.apenergy.2014.07.041

Stetz, T. (2014). *Autonomous Voltage Control Strategies in Distribution Grids with Photovoltaic Systems: Technical and Economic Assessment*. Retrieved from https://www.researchgate.net/publication/275341268_Autonomous_Voltage_Control_Strategies_in_Distribution_Grids_with_Photovoltaic_Systems_-_Technical_and_Economic_Assessment

Su, X., Masoum, M. A. S., & Wolfs, P. J. (2014). Optimal PV inverter reactive power control and real power curtailment to improve performance of unbalanced four-wire LV distribution networks. *IEEE Transactions on Sustainable Energy*, *5*(3), 967–977. https://doi.org/10.1109/TSTE.2014.2313862

Sultana, U., Khairuddin, A. B., Aman, M. M., Mokhtar, A. S., & Zareen, N. (2016). A review of optimum DG placement based on minimization of power losses and voltage stability enhancement of distribution system. *Renewable and Sustainable Energy Reviews*, *63*, 363–378. https://doi.org/10.1016/j.rser.2016.05.056

Tarman, P. B. (1996). Fuel cells for distributed power generation. *Journal of Power Sources*, *61*, 87–89.

Tesla. (2017). *Tesla Power Pack 2 Data Sheet*. Retrieved from https://www.tesla.com/powerpack

Tesla. (2019). Powerwall Technical Specs. Retrieved from https://www.tesla.com/powerwall

The MathWorks Inc. (n.d.). *MATLAB v.2011a*. Retrieved from

https://www.mathworks.com/products/matlab.html

Thompson, M., Martini, T., & Seeley, N. (n.d.). Wind Farm Volt/VAR Control Using a Real-Time Automation Controller. *SEL POWERMAX Papers*.

Toonssen, R., Woudstra, N., & Verkooijen, A. H. M. (2009). Decentralized generation of electricity from biomass with proton exchange membrane fuel cell. *Journal of Power Sources*, *194*(1), 456–466. https://doi.org/10.1016/j.jpowsour.2009.05.044

Turitsyn, K., Šulc, P., Backhaus, S., & Chertkov, M. (2011). Options for control of reactive power by distributed photovoltaic generators. *Proceedings of the IEEE*, *99*(6), 1063–1073. https://doi.org/10.1109/JPROC.2011.2116750

U.S.Department of the Interior Bureau of Reclamation - Facilities Enineering Branch. (2000). *Permissible Loading of Oil-Immersed Transformers and Regulators* (Vol. 1–5, pp. 1–25). Vol. 1–5, pp. 1–25. Retrieved from https://www.usbr.gov/power/data/fist/fist1_5/vol1-5.pdf

Varikuti, R., & Reddy, M. D. (2009). Optimal Placement of DD Units Using Fuzzy and Real Coded Genetic Algorithm. *Journal of Theoretical and Applied Information Technology*, 145–151.

von Appen, J., Braun, M., Stetz, T., Diwold, K., & Geibel, D. (2013). Time in the Sun: The Challenge of High PV Penetration in the German Electric Grid. *IEEE Power & Energy Magazine*, (February), 55–64. https://doi.org/10.1109/MPE.2012.2234407

Wang, H., Huang, Y., He, H., Lv, C., Liu, W., & Khajepour, A. (2017). Energy Management of Hybrid Electric Vehicles. In *Modeling, Dynamics, and Control of Electrified Vehicles*. https://doi.org/10.1016/B978-0-12-812786-5.00005-7

Wang, Y., Zhang, P., Li, W., Xiao, W., & Abdollahi, A. (2012). Online overvoltage prevention control of photovoltaic generators in microgrids. *IEEE Transactions on Smart Grid*, *3*(4), 2071–2078. https://doi.org/10.1109/TSG.2012.2222679

Wang, Z., Chen, B., Wang, J., Kim, J., & Begovic, M. M. (2014). Robust optimization based optimal DG placement in microgrids. *IEEE Transactions on Smart Grid*, *5*(5), 2173–2182. https://doi.org/10.1109/TSG.2014.2321748

Washom, B. (2013). *Enabling Renewable Energy , Energy Storage , Demand Response , and Energy Efficiency With a Community - Based Master Controller - Optimizer*.

White, D. (2016). *Important Factors for Early Market Microgrids: Demand Response and Plug-in Electric Vehicle Charging*. Univeristy of California, Irvine.

Williams, M. C., Strakey, J. P., & Singhal, S. C. (2004). U.S. distributed generation fuel cell program. *Journal of Power Sources*, *131*(1–2), 79–85. https://doi.org/10.1016/j.jpowsour.2004.01.021

Williams, Mark C., & Maru, H. C. (2006). Distributed generation-Molten carbonate fuel cells. *Journal of Power Sources*, *160*(2 SPEC. ISS.), 863–867. https://doi.org/10.1016/j.jpowsour.2006.05.019

Yang, J. (2016). A linear power flow model. Retrieved from GitHub website: https://github.com/Jingwei-THU/linear-power-flow

Yang, J., Zhang, N., Kang, C., & Xia, Q. (2016). A State-Independent Linear Power Flow Model with Accurate Estimation of Voltage Magnitude. *IEEE Transactions on Power Systems*, *8950*(c), 1–1. https://doi.org/10.1109/TPWRS.2016.2638923

Yang, Y., Zhang, S., & Xiao, Y. (2015a). An MILP (mixed integer linear programming) model for optimal design of district-scale distributed energy resource systems. *Energy*, *90*, 1901–1915. https://doi.org/10.1016/j.energy.2015.07.013

Yang, Y., Zhang, S., & Xiao, Y. (2015b). Optimal design of distributed energy resource systems coupled with energy distribution networks. *Energy*, *85*, 433–448.

https://doi.org/10.1016/j.energy.2015.03.101

Yang, Z., Bose, A., Xia, Q., Zhong, H., & Kang, C. (2016). Optimal power flow based on successive linear approximation of power flow equations. *IET Generation, Transmission & Distribution*, *10*(October), 3654–3662. https://doi.org/10.1049/iet-gtd.2016.0547

Zakeri, B., & Syri, S. (2015). Electrical energy storage systems: A comparative life cycle cost analysis. *Renewable and Sustainable Energy Reviews*, *42*, 569–596. https://doi.org/10.1016/j.rser.2014.10.011

Zhang, B. (2013). *Control and Optimization of Power Systems with Renewables : Voltage Regulation and Generator Dispatch*. University of California, Berkeley.

Zimmerman, R. D., Murillo-Sánchez, C. E., & Thomas, R. J. (2011). MATPOWER: Steady-state operations, planning, and analysis tools for power systems research and education. *IEEE Transactions on Power Systems*, *26*(1), 12–19. https://doi.org/10.1109/TPWRS.2010.2051168

APPENDIX

Table 1 – Comparison of existing literature on the topic of DER optimal allocation, with a MILP considering power system constraints

Author	**Type**	**Technology**		**Grid Constraints**			**Objective (minimize)**	**Power Flow Method**	**Test System**
		Storage	Smart Inverter	Line Capacity	DG Capacity	Voltage			
Yang, Y. *et. al.* (2015)	MILP			X	X		Cost	Not formal power flow	4 nodes (Meshed)
Mashayekh, S. *et. al.* (2016)	MILP	X		X	X	X	Cost	Bolognani *et. al.*	5 nodes (Meshed)
Morvaj, B. *et. al.* (2016)	MILP	X		X	X	X	Cost + Emissions	Linear approximation of ACPF	7 nodes (Radial)
Santos, S. *et. al.* (2016)	MILP	X		X	P and Q limits separately	X	(max) Hosting capacity + Cost	Piecewise - linear ACPF	IEEE 41-node (Radial)
Arnold, D. *et. al.* (2016)	MILP		PQ control	X	X	X	Voltage deviation	LinDistFlow	IEEE 13-node (Radial)
Mashayekh , S. *et. al.* (2017)	MILP	X		X	X	X	Cost + Emissions	LinDistFlow	19 nodes (Radial)
Zou, G. *et.al.* (2018)	MILP	X		X	X	X	Cost	LinDistFlow	IEEE 33-node (Radial)
Gholami, A. *et. al.* (2019)	MILP	X		X	X	X	Cost	Piecewise - linear ACPF	IEEE 33-node (Radial)
Sepehry, M. *et. al.* (2019)	MILP	X	PQ control	X	X	X	Cost and wind curtailment	Piecewise - linear ACPF	IEEE 60-node (Radial)
This study	MILP	X	PQ control / droop control	X	X	X	Cost + Voltage Deviations	DLPF	115-node (Meshed) real-world microgrid

Table 2 – Building DER allocation for all scenarios

#	ZNE			ZNE+TC			ZNE+area			ZNE+area+TC			Island+area			Island+area+TC		
BDG	PV	EES	REES	PV	EES	REES	PV	EES	REES	PV	EES	REES	PV	EES	REES	PV	EES	REES
1	1152	0	0	1523	0	0	1296	0	0	1296	0	0	1296	2328	2445	1296	2250	2758
2	58	0	0	61	0	0	101	0	0	175	0	354	221	79	428	221	92	211
3	253	0	0	245	0	0	18	0	0	18	0	0	18	528	55	18	528	55
4	45	0	0	43	0	0	73	0	0	120	0	241	210	54	298	210	72	302
5	11	0	0	442	0	0	227	0	0	227	0	0	227	784	883	227	780	857
6	894	0	0	2766	0	0	489	0	0	489	0	0	489	6191	1077	489	5774	1258
7	5	0	0	7	0	0	13	0	0	58	0	46	58	13	62	58	15	73
8	60	0	0	54	13	0	142	0	0	198	0	0	198	109	528	198	86	591
9	54	0	0	55	0	0	88	0	0	168	13	319	251	66	360	251	87	299
10	478	0	0	230	169	0	482	0	0	573	321	1268	0	0	0	301	67	835
11	2222	0	0	1096	656	198	1552	0	0	1552	424	1907	1422	302	3736	1503	324	3892
12	582	0	0	299	148	0	588	0	0	647	390	1064	647	159	1837	451	104	1343
13	350	0	0	172	114	13	306	0	0	306	192	422	306	76	885	225	53	706
14	917	0	0	453	312	15	925	0	0	1011	646	1914	942	188	2562	601	132	1556
15	36	0	0	36	0	0	9	0	0	9	0	0	0	0	0	9	0	0
16	901	0	0	446	292	15	801	0	0	801	499	1078	83	15	199	601	118	1327
17	625	0	0	316	178	0	613	0	0	613	387	864	613	128	1612	451	105	1359
18	66	0	0	39	0	0	58	0	0	58	29	28	58	16	192	58	13	139
19	502	0	0	236	169	13	446	0	0	446	297	688	420	88	1109	301	72	840
20	17	0	0	56	0	0	149	0	0	149	0	270	149	0	0	149	13	197
21	29	0	0	33	0	0	37	0	0	37	0	0	37	13	109	37	13	117
22	10	0	0	12	0	0	15	0	0	15	0	0	15	13	27	15	13	33
23	49	0	0	52	0	0	45	0	0	45	0	0	45	40	177	45	38	185
24	31	0	0	37	0	0	50	0	0	50	0	0	50	0	0	50	0	0
25	89	0	0	104	0	0	111	0	0	111	0	0	111	37	359	111	35	382
26	29	0	0	36	0	0	41	0	0	41	0	0	41	0	0	41	0	0
27	90	0	0	118	0	0	142	0	0	142	0	0	142	51	388	142	49	396
28	124	0	0	159	0	0	251	0	0	341	0	329	341	89	372	341	101	446
29	876	424	0	1515	476	0	1436	261	0	1436	20	0	1436	0	0	1436	0	0
30	10	0	0	12	0	0	15	0	0	15	0	0	15	0	0	15	0	0
31	17	0	0	34	0	0	59	0	0	62	0	51	62	34	176	62	41	125
Total	10585	424	0	10686	2528	254	10580	261	0	11211	3220	10844	9902	11402	19875	9914	10976	20280

Table 3 – Inverter capacity comparison, at each building, for all scenarios. Highlighted rows indicate the even inverter locations for Volt-Var droop control

BLDG #	Solar PV Installed (kW)	Inverter capacity *Baseline* (kVA)	Inverter capacity *PQ control* (kVA)	Inverter capacity *Droop-control* (kVA)
1	1,846	0.83	0.83	0.86
2	22	0.83	0.83	
3	97	0.83	0.83	
4	18	0.83	0.83	
5	155	0.83	0.83	
6	385	0.83	0.83	
7	4	0.83	0.83	
8	86	0.83	0.83	
9	21	0.83	0.83	
10	176	0.83	0.83	0.83
11	405	0.83	1.53	1.18
12	212	0.83	0.83	0.86
13	128	0.83	0.83	
14	336	0.83	0.87	0.87
15	7	0.83	0.83	
16	329	0.83	0.83	0.83
17	228	0.83	0.83	0.87
18	24	0.83	0.83	
19	183	0.83	0.83	
20	16	0.83	0.83	
21	11	0.83	0.83	
22	3	0.83	0.83	
23	2	0.83	0.83	
24	6	0.83	0.83	
25	26	0.83	0.83	
26	19	0.83	0.83	
27	44	0.83	0.83	
28	20	0.83	0.83	
29	257	0.83	0.83	
30	3	0.83	0.83	
31	20	0.83	0.83	